2017

Insights into the Assembly of Arctic Alaska: Provenance and Geochemical Data from the Doonerak Fenster and Endicott Mountains Allochthon

William Patrick Frier

Insights into the assembly of Arctic Alaska: Provenance and geochemical data from the Doonerak fenster and Endicott Mountains allochthon

William Patrick Frier

Thesis submitted
to the Eberly College of Arts and Sciences
at West Virginia University

In partial fulfillment of the requirements for the degree of

Masters of Science in
Geology

Jaime Toro, Ph.D., Chair
Helen Lang, Ph.D.
Kenneth Brown, Ph.D.

Department of Geology and Geography

Morgantown, West Virginia
2017

Keywords: Arctic Alaska Terrane, Doonerak Fenster, Arctic Alaska Chukotka Microcontinent, Endicott Mountains Allochthon, Provenance, Detrital Zircon, Geochronology, Geochemistry, Major Elements, Trace Elements, Rare Earth Elements

ABSTRACT

INSIGHTS INTO THE ASSEMBLY OF ARCTIC ALASKA: PROVENANCE AND GEOCHEMICAL DATA FROM THE DOONERAK FENSTER AND ENDICOTT MOUNTAINS ALLOCHTHON

William Patrick Frier

The Doonerak fenster of the central Brooks Range contains the Apoon assemblage, a suite of Early Paleozoic mafic-to-intermediate volcanic and siliciclastic rocks. The fenster exposes deep structural levels of the Brooks Range between regions of Laurentian and non-Laurentian origin in Arctic Alaska. During the Mesozoic to Cenozoic formation of the Brooks Range, Upper Devonian to Triassic siliciclastic and carbonate rocks of the Endicott Mountains allochthon were thrusted northward and juxtaposed over the top of this volcanic suite.

New geochemical data indicates that the Apoon assemblage formed as part of an island arc complex. The assemblage contains basaltic-to-andesitic rocks with diverse textures, including pillow basalts and cross-cutting dikes and sills. Enrichment in large ion lithophile elements (e.g. Cs, Rb, Ba, Th), depletion in high field strength elements (e.g. Nb, P, Zr, Ti), and chondrite-normalized rare-earth element (REE) trends within the Apoon volcanics are consistent with formation in an island arc setting and corroborate previous work.

Detrital zircon spectra from volcaniclastic portions of the Apoon assemblage show a prominent unimodal 440-530 Ma population centered on 504 Ma with only minor populations potentially derived from Laurentia. The siliciclastic units unconformably overlying the Apoon assemblage (Ellesmerian sequence) and those of the Endicott Mountains allochthon mostly lack detritus from this 504 Ma population and are instead dominated by 400-440 Ma populations centered on ~420 Ma. While this is dissimilar from the Apoon assemblage, detritus of this age is common in rocks of the Canadian Arctic, Svalbard, and eastern Greenland and is associated with the Caledonian orogeny.

The coexistence of Caledonian detritus alongside 800 - 550 Ma populations within samples from the northern margin of the fenster also indicates a connection to the Timanian orogen of northern Baltica. The youngest portions of the Apoon assemblage also show significant Laurentian and Caledonian age detritus. This shift in provenance could be explained by the closure of an oceanic basin, providing newly integrated sediment pathways. Collectively, evidence presented here indicates that the Apoon assemblage formed as part of an island arc, which initially formed in a relatively isolated geographic position and received detritus from mostly proximal sources (single unimodal 504 Ma population). This arc progressively approached and eventually docked onto the margin of northwest Laurentian during closure of the northernmost Iapetus Ocean, eventually amalgamating regions of Laurentian and non-Laurentian origin. Thus, the Doonerak fenster preserves an island arc complex and marks the location of a Paleozoic suture between Laurentian and non-Laurentian portions of Arctic Alaska.

ACKNOWLEDGEMENTS

Foremost among those I would like to thank is my advisor, Dr. Jaime Toro. Jaime is a passionate teacher, encouraging advisor, caring family man, and genuinely good person. He pushes his advisees to think for themselves and places them in environments that encourage them to develop the skills needed to be successful as students of both geology and life. He is pleasant to be around and approaches life with an attitude that is simultaneously easy-going, hardworking, and contagiously positive. He also plays soccer well and makes great book suggestions.

I owe significant credit to Benjamin Johnson, my office mate and pseudo-advisor. Ben is an extremely generous and kind man. He shared his ideas and experiences with me without complaint, even when I blatantly interrupted his work. Over the past few years, Ben helped me see a path toward completing the document you are now reading all while working to complete his own PhD. His wit and sharp intellect also made our cave-like basement office an engaging and fun place to work. He and his partner, Patricia, are fine people who deserve the best.

Greg Hammond joined me in the Brooks Range as my field assistant before starting his own master's project, focused on the deformational and thermal history of rocks in the vicinity of Doonerak. I feel like I got to know a different side of Greg during our one-on-one fourteen day stint under Alaska's midnight sun. He is an interesting man whom I'm sure will be very successful in life. I wish him the best as he continues to think about the Doonerak fenster.

Drs. Helen Lang and Kenny Brown were kind enough to share their intellect and provide useful critiques as committee members. Helen and Kenny both exhibit unique and fun senses of humor. Helen is a signpost of our department, respected by all who know her, and a pleasure when our department goes to the pub on Fridays. Kenny (of Earth C130) was extremely kind, humorous, passionate, and selfless as he helped me understand geochemistry. I also served as his TA, which was a fun and educational experience for me as well as our students.

Dr. David Barbeau of the University of South Carolina assisted with all aspects of the detrital zircon LA-ICP-MS analysis. Dave is an extremely nice guy and he was a huge help with the DZ data acquisition and processing. He is a laser ablation guru. One DZ sample (J1415) was provided by Justin Strauss, a friend and colleague of Ben's, who is also a great guy.

A. Rizzo, C. Khoury, P. Goodling, and G. Morris helped remind me of my real path. Thanks is also due to many WVU grad students for being encouraging and passionate friends in the department. We have a truly lively group here including A. Andeskie, E. Bausher, A. Delisle, L. Eichenlaub, C. Findlay, B. Gaschot, J. Knapp, W. Martin, J. Pilweski, and M. Reed.

Lastly, I owe thanks to my family: to my father for encouraging me to pursue engaging and emotionally sustaining career paths, to my mother for her kindness and eternal support (as well as access to a washing machine), and to my siblings - Timmy and Kate - who both exhibit strength and fortitude of character in ways that I often lack. They are both remarkable people, but show it in very different ways. Recently we all gathered to celebrate my sister's wedding (hey Craig!). Perhaps because it is so rare, I've come to appreciate opportunities to spend time with my family more and more throughout graduate school. It was particularly lovely to celebrate such a happy occasion together.

Thank you, folks. Hopefully being associated with me and this document isn't too embarrassing for you all…. It might be….

To my niece and nephew:
Ashby Cole Frier and Quinn Andrew Frier.

If you grow up and decide you want to go camping in Alaska, let me know. I'm the uncle for that.

TABLE OF CONTENTS

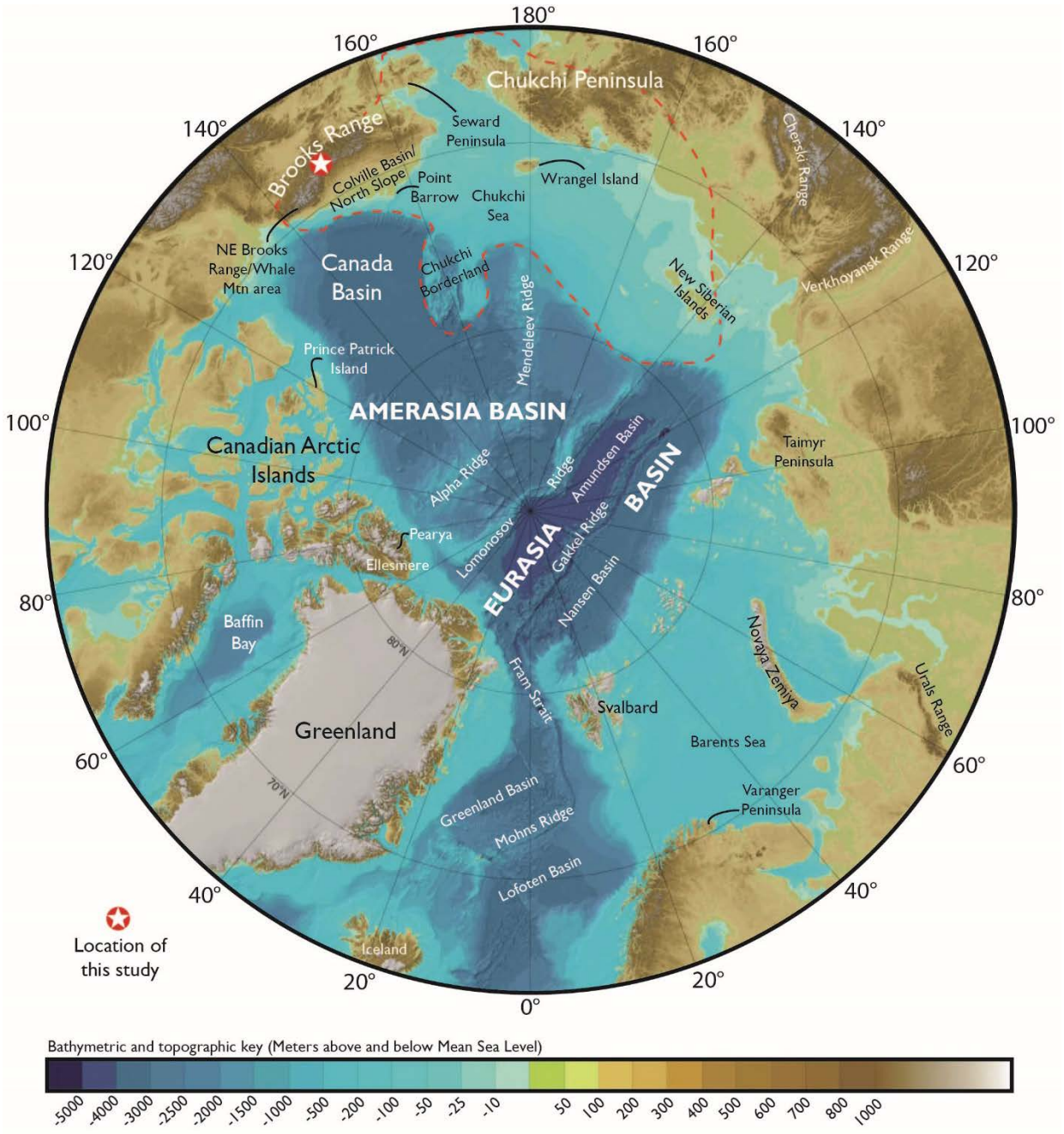

Figure 1: Polar-view index map of the region north of the Arctic Circle showing topography and bathymetry of various physiographic regions (after Jakobsson et al., 2012, Pease et al., 2014). The dashed red line marks the approximate bounds of the Arctic Alaska - Chukotka microplate. The white star outlined in red marks the location of fieldwork for this study.

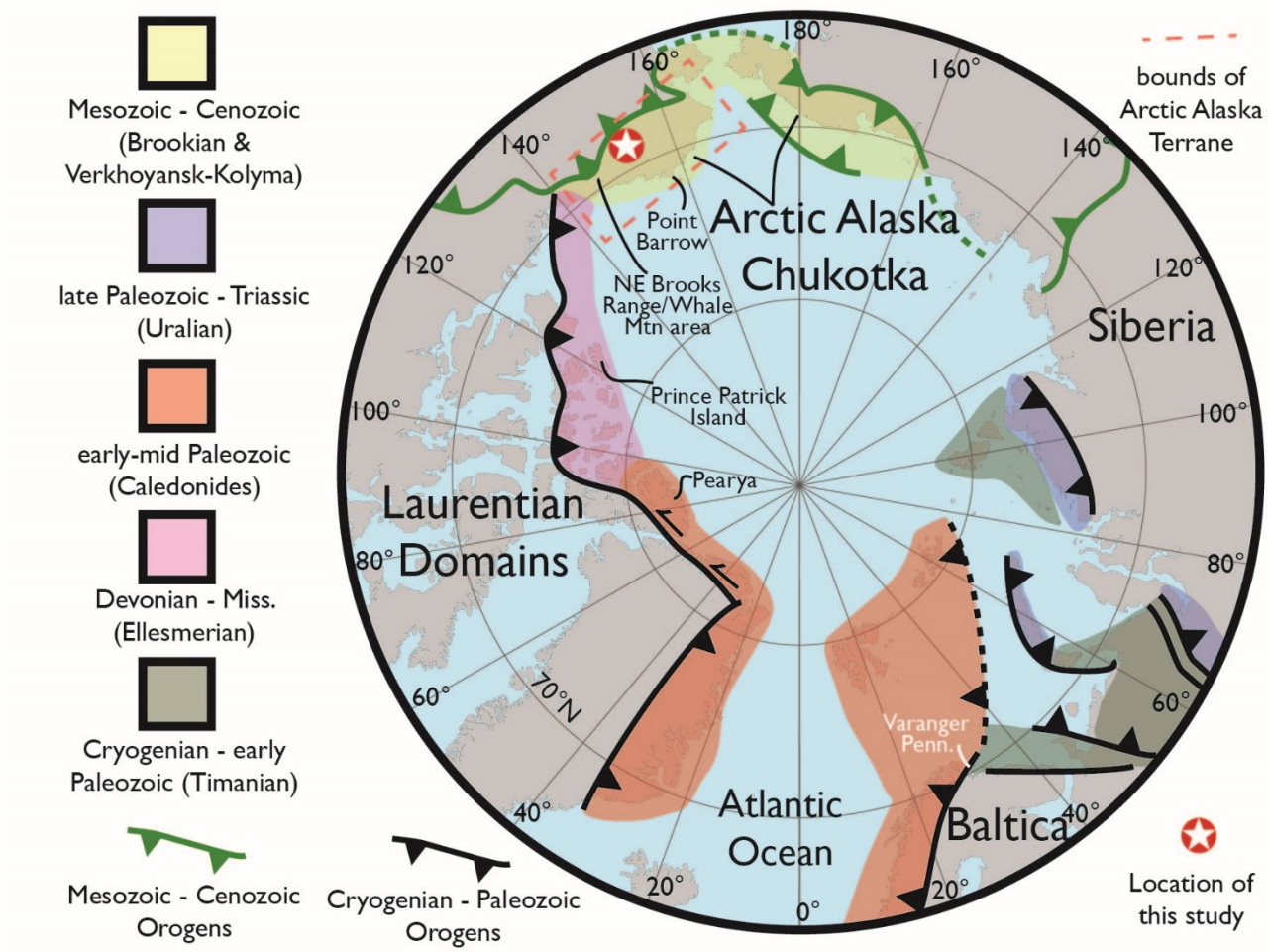

Figure 2: Simplified polar-view map showing the distribution of Proterozoic and Paleozoic orogens in the Arctic region. Modified from Colpron and Nelson (2011) and Strauss et al. (2013).

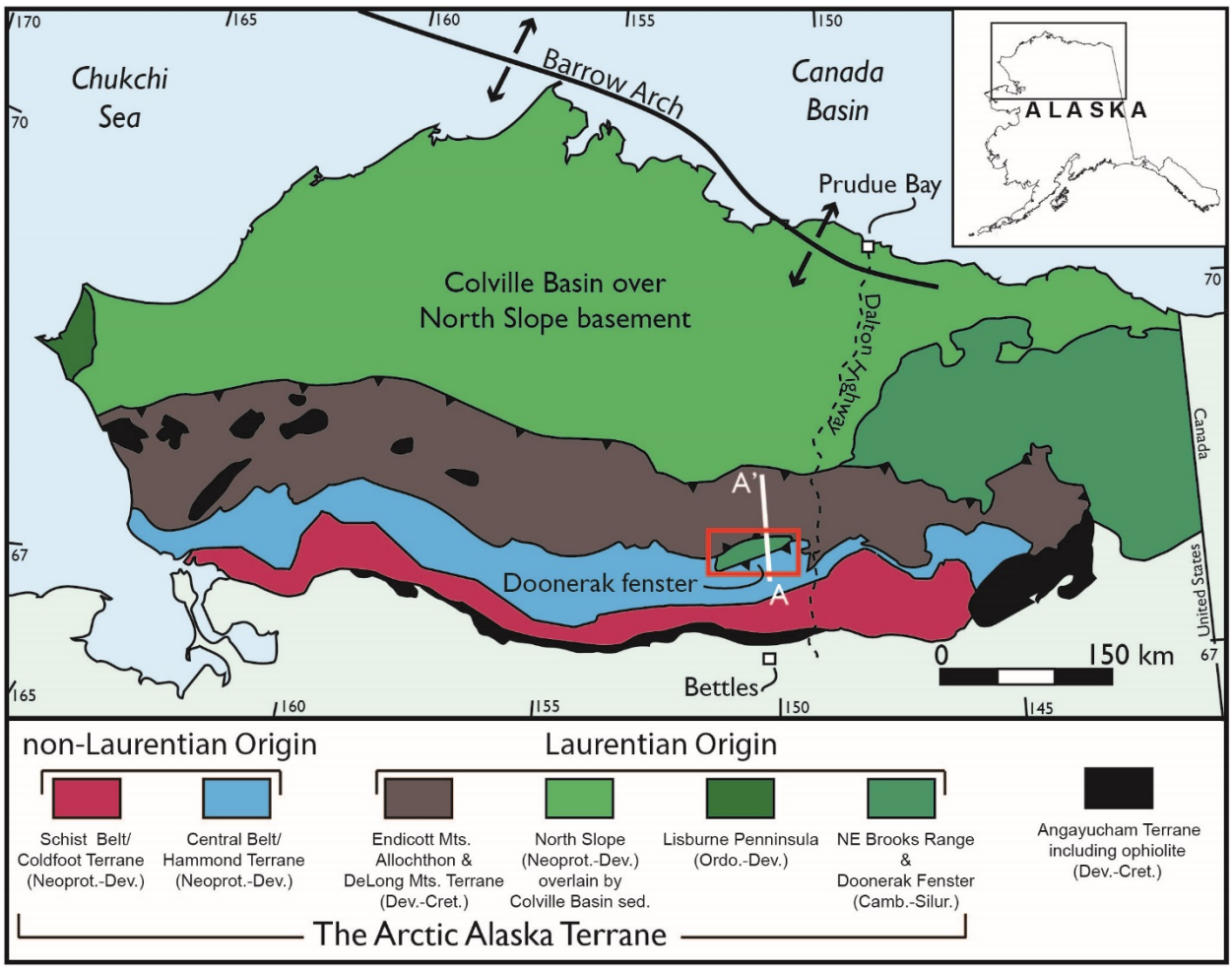

Figure 3: Simplified terrane map of Arctic Alaska colored to show regions of Laurentian and non-Laurentian origin (modified from Moore et al., 1994). Red box marks the location of the Doonerak fenster in the central Brooks Range, which is expanded in Figure 6. Line A-A' corresponds to the cross section in Figure 7.

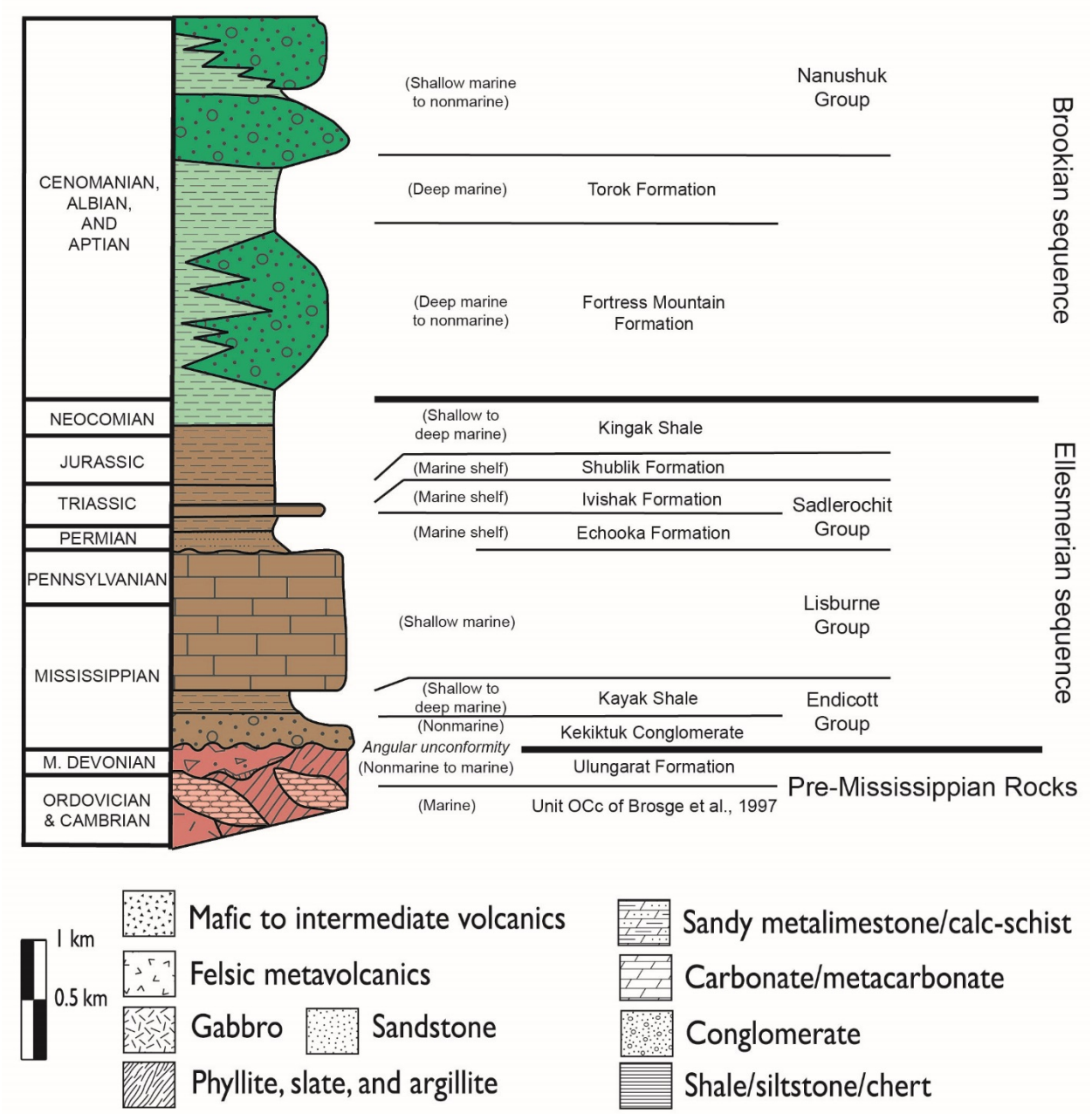

Figure 4: Generalized stratigraphic column of the North Slope portion of the Arctic Alaska terrane (pre-Mississippian rocks and Ellesmerian sequence) and the overlying terrigenous clastics of the Colville Basin fill (Brookian sequence). Column based on the southern portions of the North Slope, located ~ 100 km north east of the study area. Adapted from Moore et al., (1997).

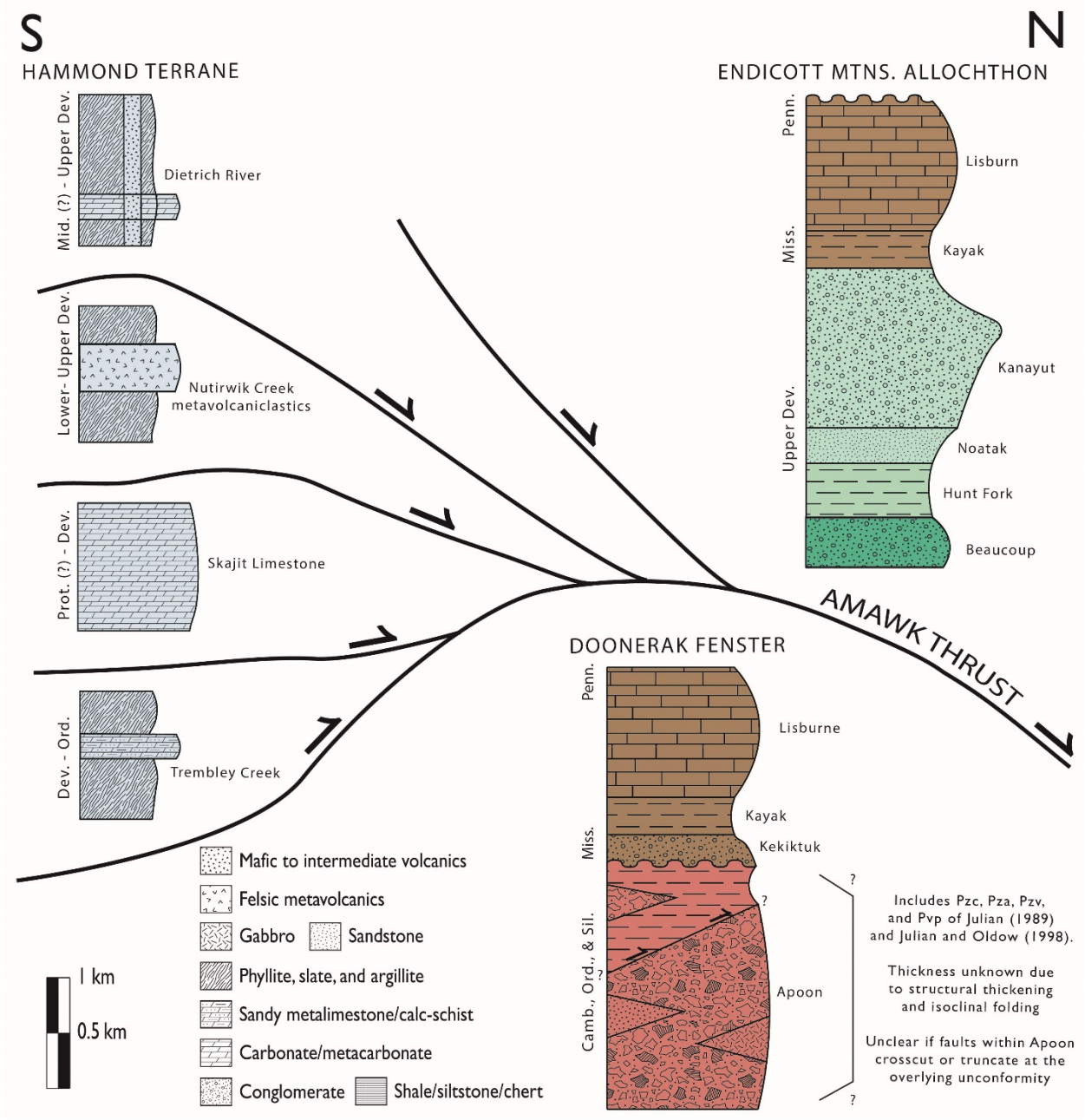

Figure 5: Relative structural positions and stratigraphic relationships of the Hammond subterrane, Endicott Mountains allochthon, and Doonerak fenster in the central Brooks Range. Adapted from Moore et al., (1997) with nomenclature from Julian (1989), Julian and Oldow (1998) and Moore et al., (1997).

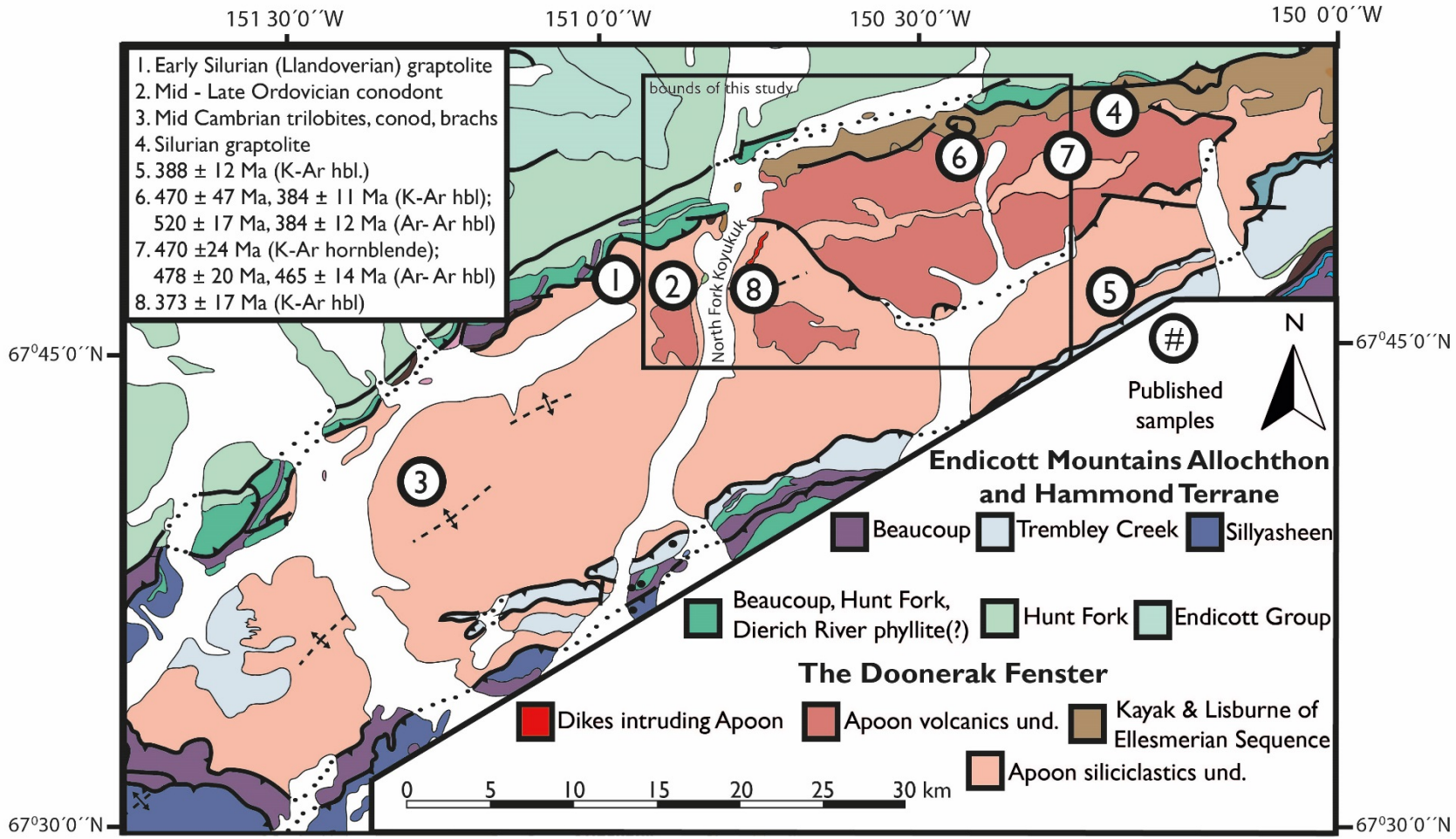

Figure 6: Simplified geologic map of the Doonerak fenster in the central Brooks Range after Dillon et al., (1986) and Strauss et al., (2017). Numbers represent samples from previous studies with age constraints from Dutro et al., (1976); Dutro et al., (1984); Julian and Oldow (1998); and Repetski et al., (1987). Numbers correspond to inset key. Box marks the approximate location of Figure 8.

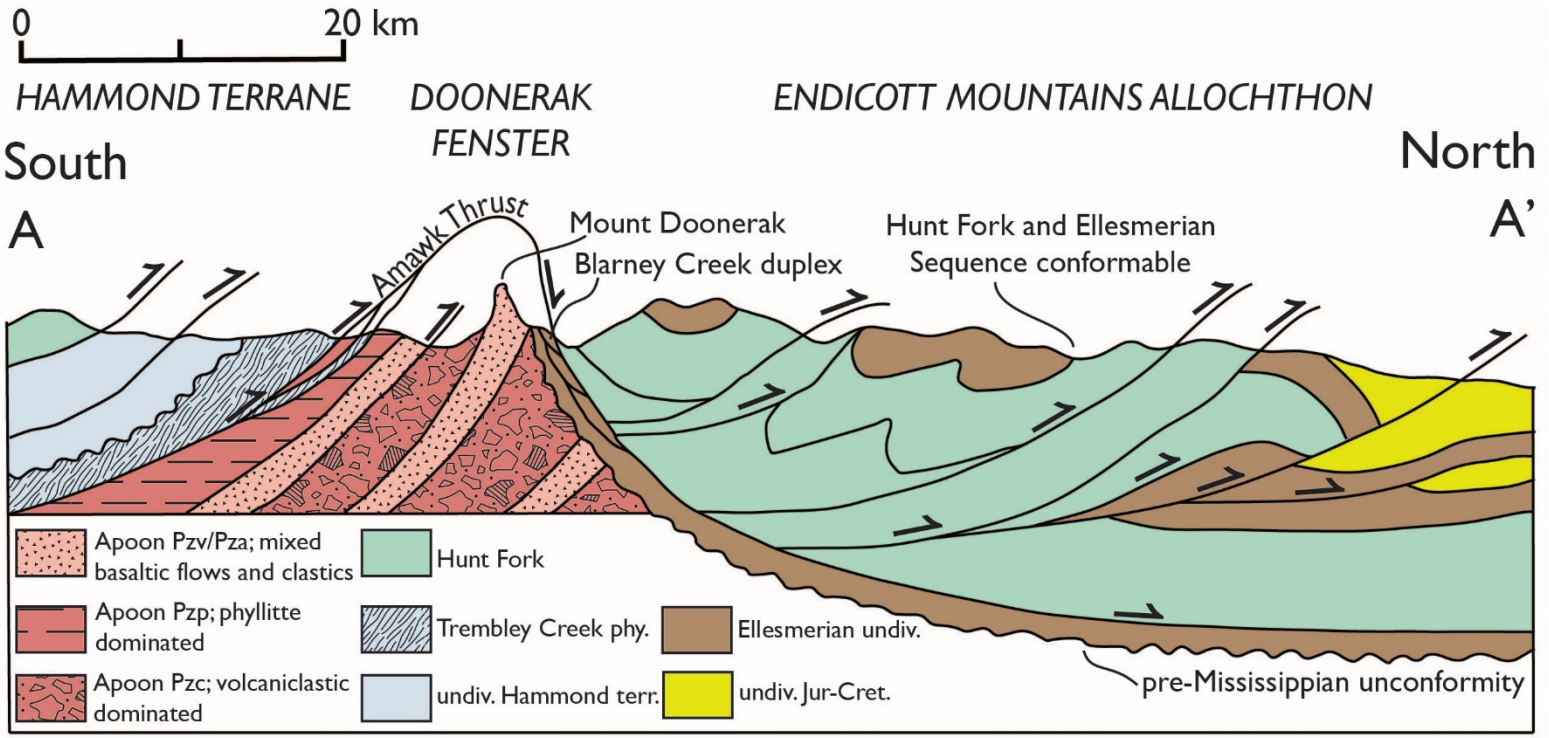

Figure 7: Schematic cross section (~ 2X vertical exaggeration) of the central Brooks Range illustrating the structural window at the Doonerak fenster modified after Dutro et al., (1976), Dillon et al., (1986), Mull et al., (1987), Oldow et al., (1987), Adams et al., (1997), Moore et al., (1997), and Julian and Oldow (1998). Cross section corresponds to the approximate location of line A-A' in Figure 3.

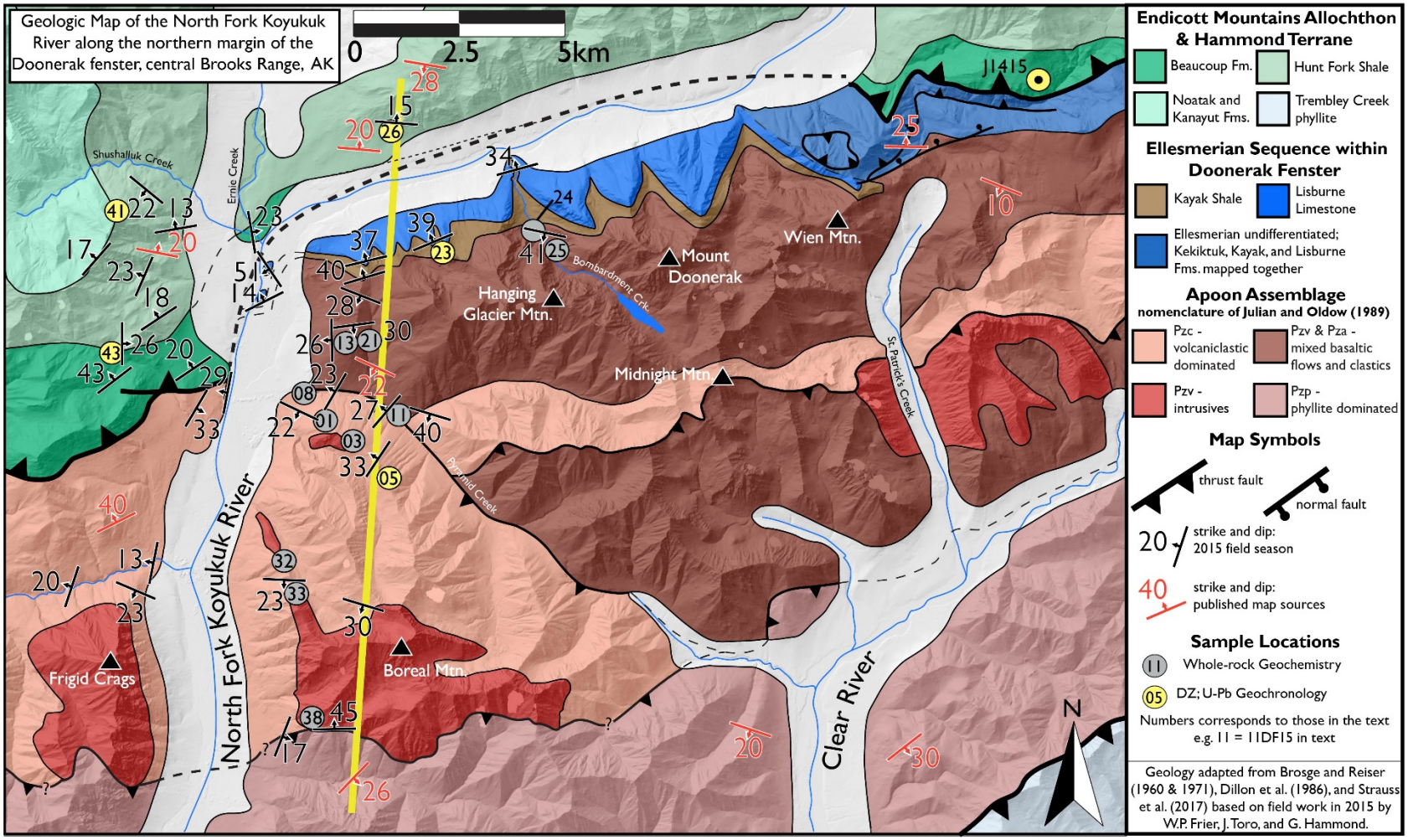

Figure 8: Simplified geologic map of the Doonerak fenster in the central Brooks Range showing structural data and sample locations. Structural data reflect the average of multiple strike and dip measurements taken in the field at that location. Yellow circles mark the location of samples collected for detrital zircon geochronology. Gray circles mark the location of samples collected for whole rock volcanic geochemistry. The northeast portion of this map (near sample J1415) is based on field mapping by J. Strauss in 2013, published in Strauss et al., (2017). All other field data comes from field work by W.P. Frier, J. Toro, and G. Hammond in 2015 and was supplemented by aerial and satellite imagery. The bold yellow line corresponds to Figure 9.

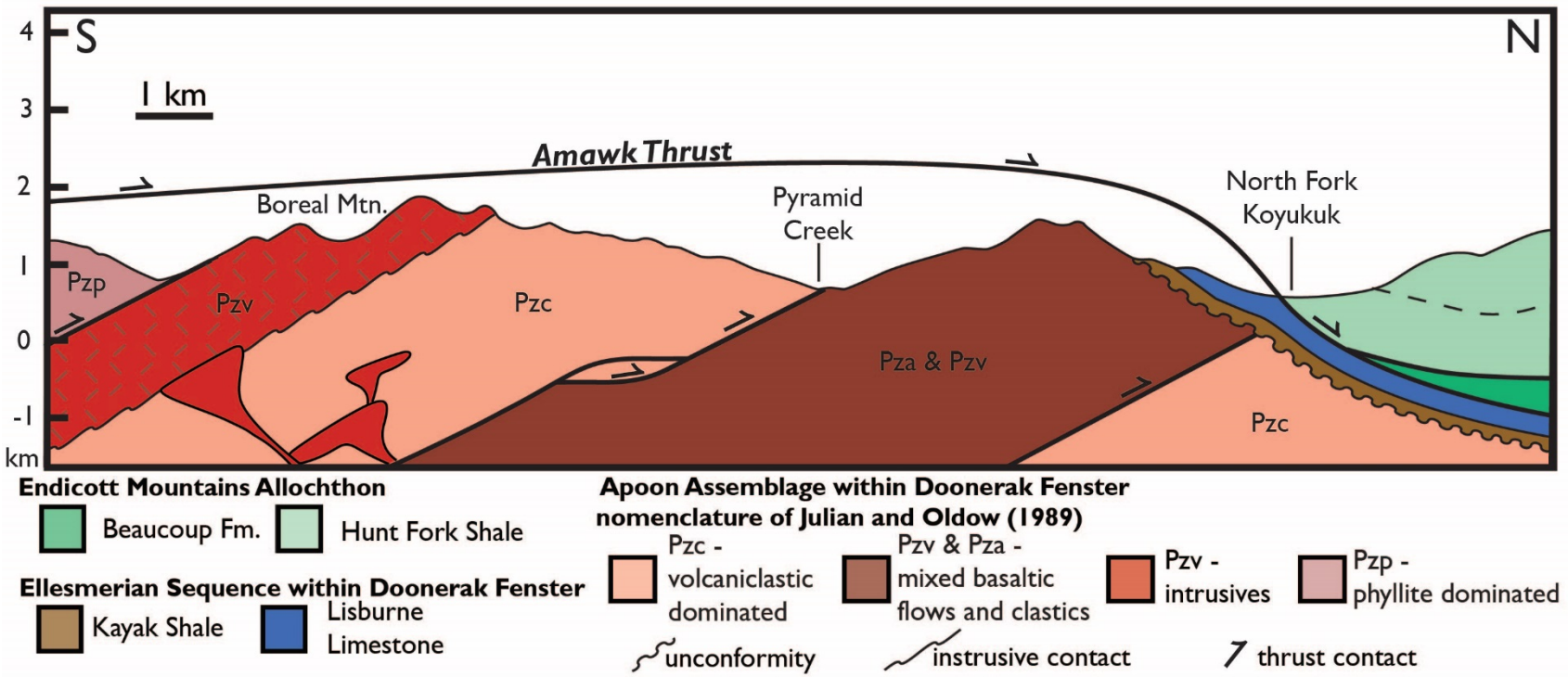

Figure 9: Schematic cross-section through the northern Doonerak fenster and southern Endicott Mountains Allochthon based on the map in Figure 8. Cross section corresponds to the bold yellow line in Figure 8. Notice the Ellesmerian Sequence unconformably atop the Apoon Assemblage and dipping beneath the Endicott Mountains Allochthon.

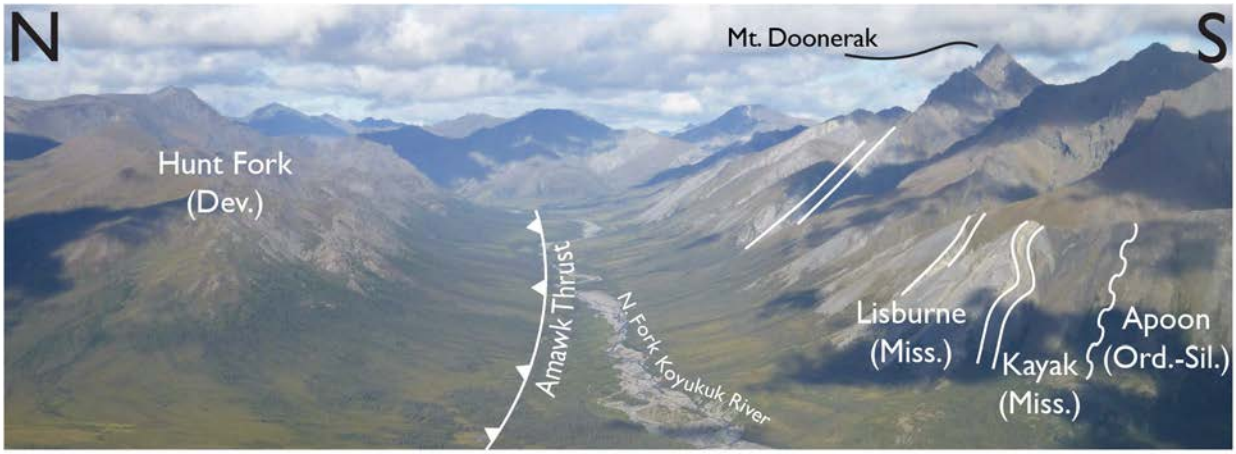

Figure 10: Field photo looking east along the North Fork of the Koyukuk River in the central Brooks Range. To the North (left) side of the image are of rocks of the Endicott Mountains allochthon, the Hunt Fork Shale. To the South (right) side of the image are rocks of the Lisburne Limestone, Kayak Shale (Ellesmerian sequence) and Apoon assemblage (pre-Mississippian basement) of the Doonerak fenster.

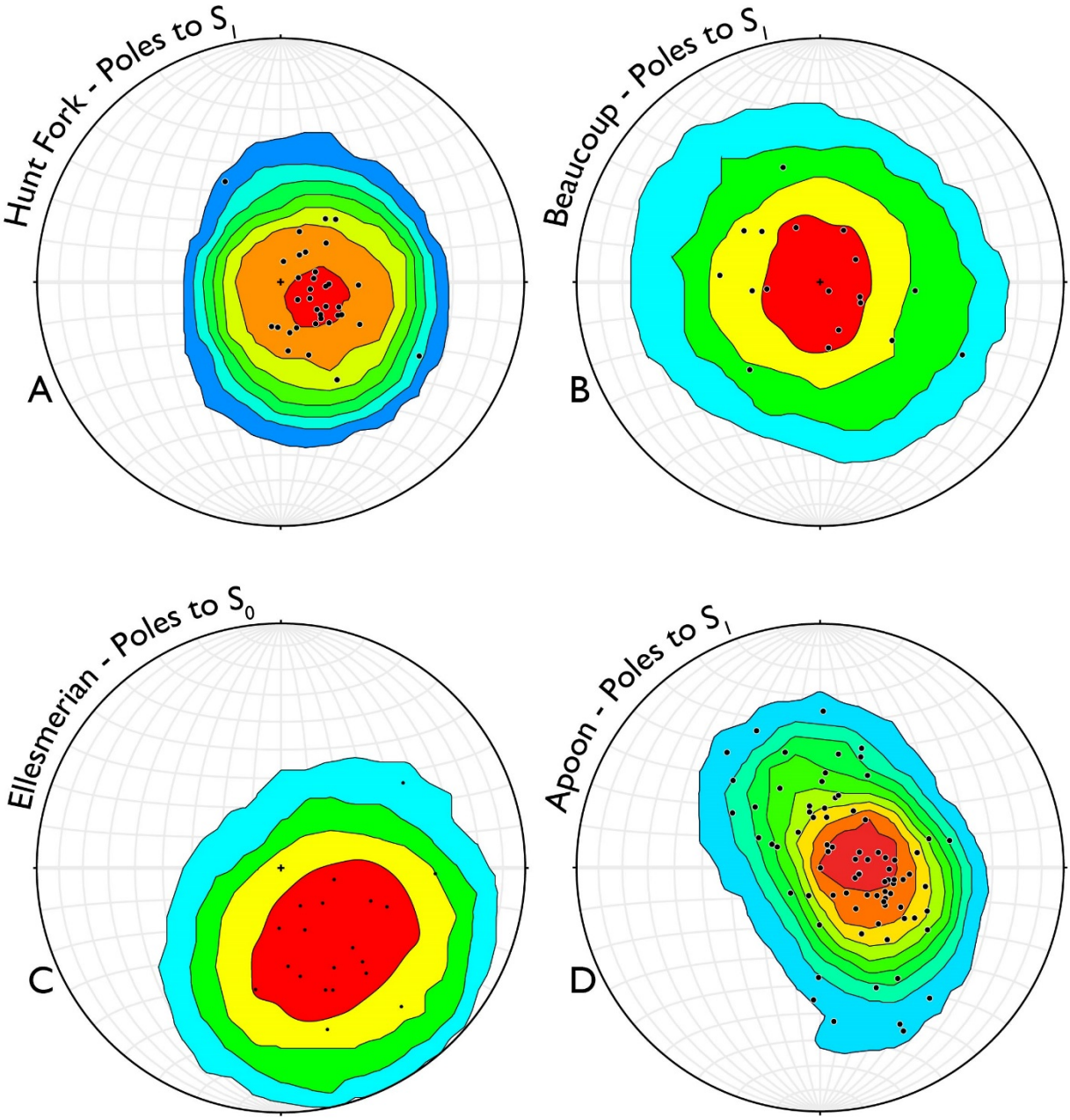

Figure 11: Contoured stereonets showing poles to dominant foliation (S_1) observed during the 2015 field season and organized based on lithostratigraphic association. In most cases the primary surface corresponds to dominate cleavage (S_1); however bedding (S_0) was evident within the Ellesmerian sequence consistently and periodically differentiated from cleavage in other formations.

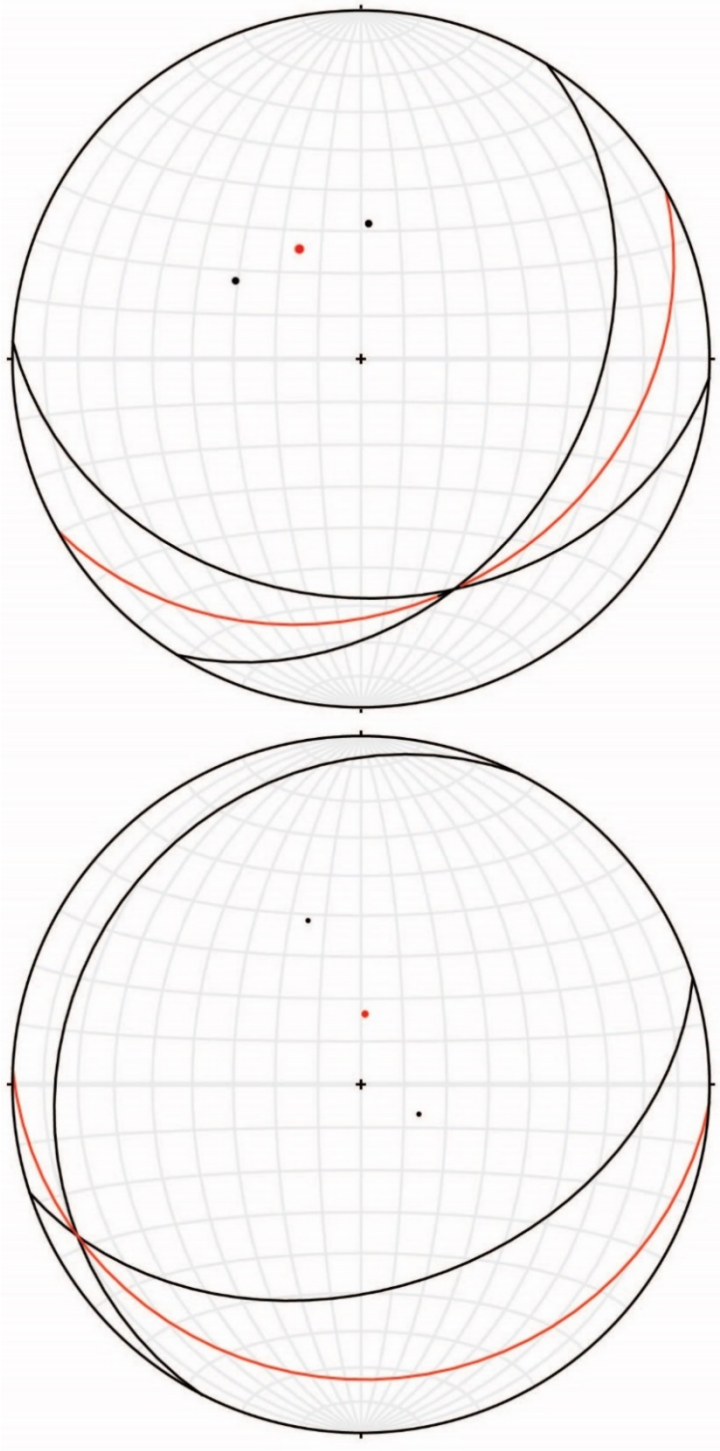

Figure 12: Great circles and their associated poles of bedding around folds observed within the Beaucoup formation, west of the North Fork Koyukuk River in 2015 (shown in black). The inferred fold axes are shown in red with their associated poles (also in red). The attitude of these folds is consistent with the dominant regional trend of Brookian folds.

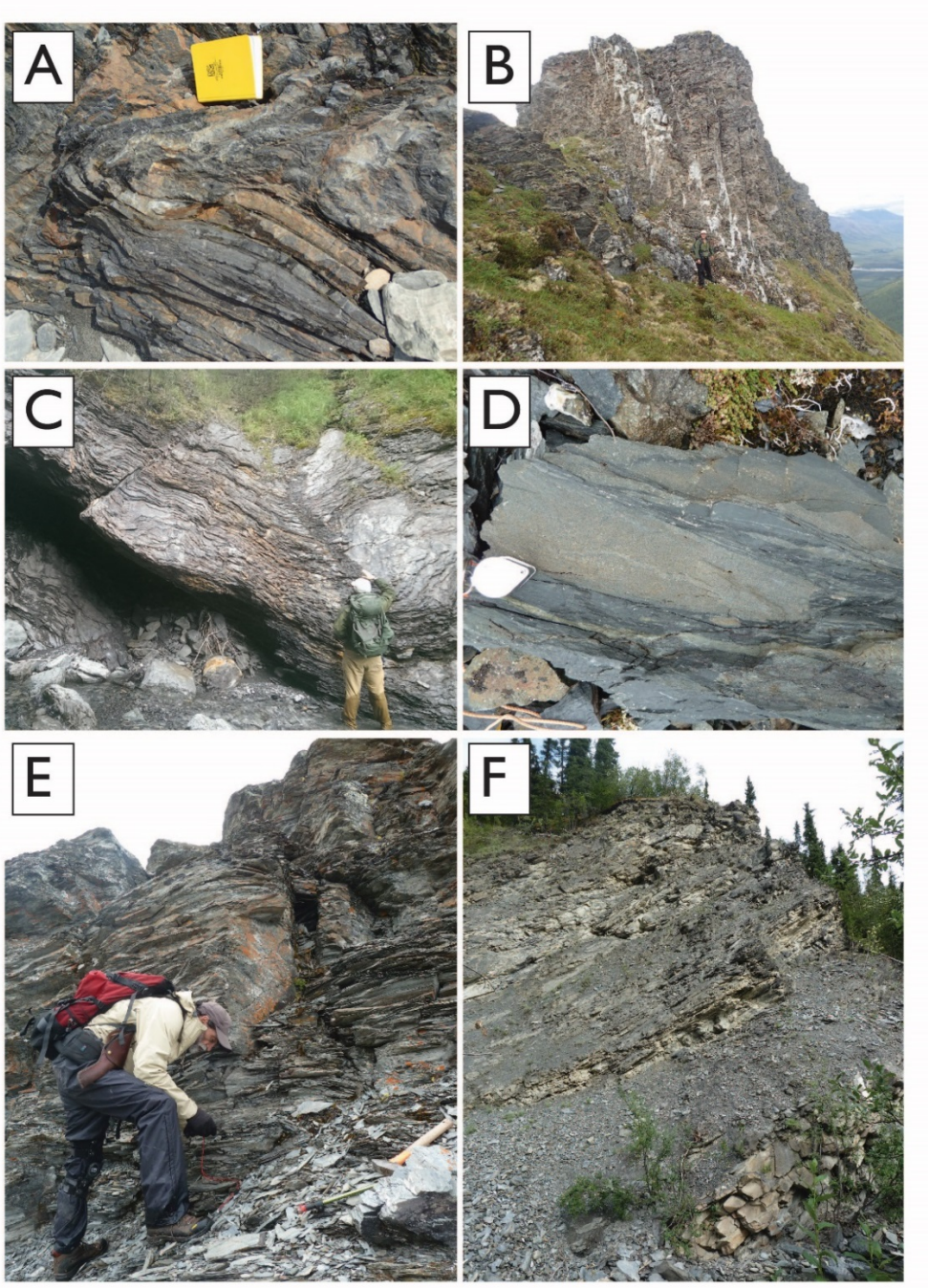

Figure 13: Field photos from clastic/volcaniclastic portions of the Apoon assemblage, Pzc. A - outcrop of recumbent isoclinal folds within slate and lithic sandstone along Pyramid Creek. Field book pictured is 19 cm x 12 cm. B - En echelon vein array atop ridge south of Pyramid Creek, defining a small fault zone between slates and tuffs within the Apoon assemblage. Person pictured is ~ 1.8 m tall. C - Broad gently plunging open folds within phyllites of the Apoon assemblage along Pyramid Creek. Person is ~ 1.8 m tall. D - Example of fine-to-medium grained lithic sandstone with intermediate slate from ridge south of Pyramid Creek. Hand lens is ~ 2 cm in length E & F - Typical variety among rocks of the Apoon assemblage. Range from fine grained thinly bedded slates and well foliated phyllites to thin-to-medium bedded lithic sandstone interbedded among slates.

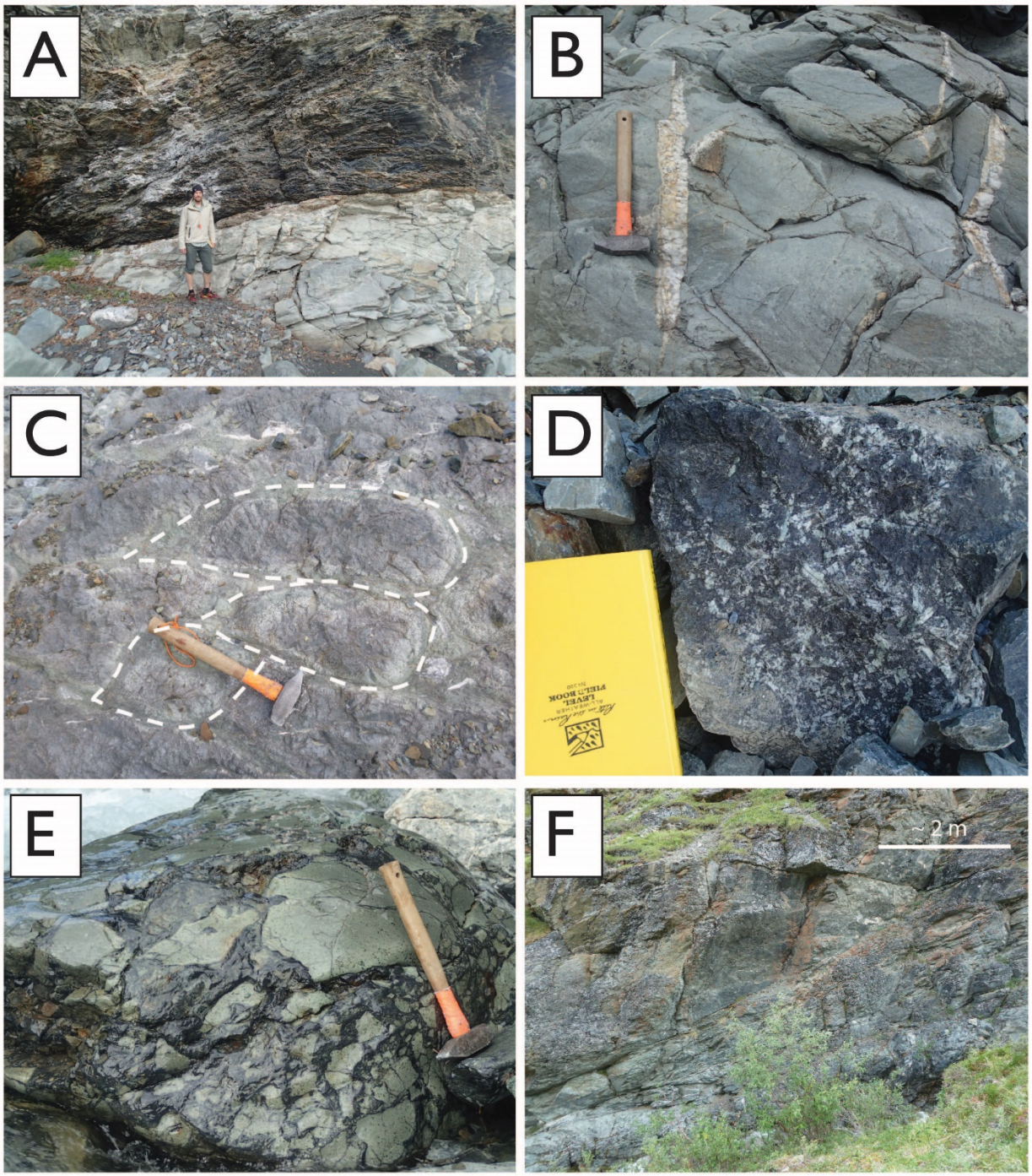

Figure 14: Field photos from volcanic/igneous portions of the Apoon assemblage. A & B - two images of the same outcrop along Pyramid Creek. Sill of andesite with crosscutting veins of quartz and calcite. Hammer pictured has a ~ 30 cm handle. Person pictured is ~ 1.8 m tall. C - aphanitic basalt pillows from Bombardment Creek. D - Porphyritic basaltic andesite from Boreal Mountain with large laths of plagioclase. E - Aphanitic greenstone found along Bombardment Creek (not in place) which likely formed as a basaltic flow top breccia. F - Fine grained basaltic greenstone north of Pyramid Creek with thoroughgoing brittle fractures.

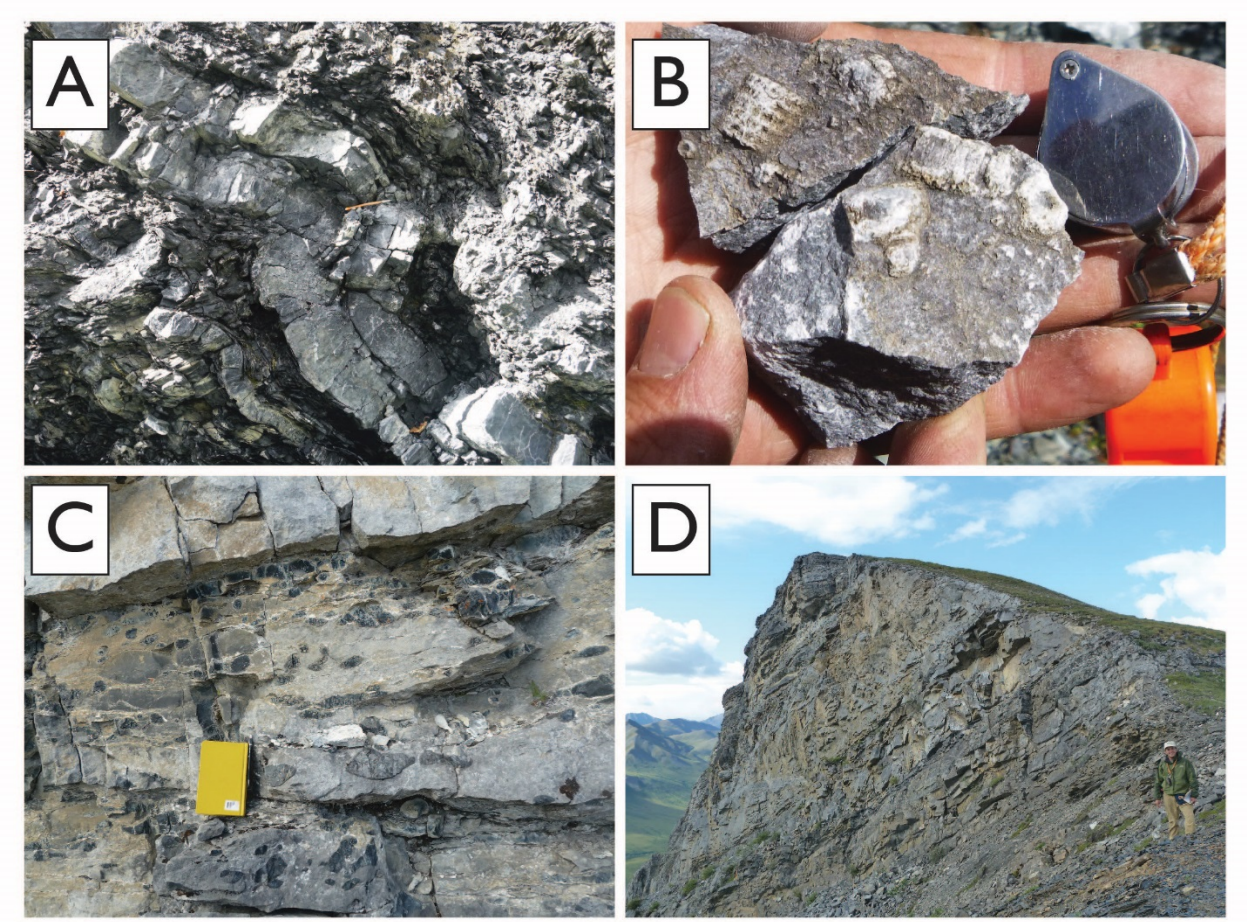

Figure 15: Field photos from the Ellesmerian Sequence within the Doonerak fenster. A - folded limestone and shale within the Kayak Shale along Bombardment Creek. Pencil for scale is ~ 11 cm in length. B - Crinoids within the Kayak Shale. Hand lens is ~ 2 cm in length. C - Nodular chert within thickly-bedded limestone of the Lisburne formation. Field book is ~19 cm long. D - Outcrop of thickly-bedded Lisburne Limestone south of the North Fork Koyukuk River in the northern portion of the field area. Person pictured (far right) is ~ 1.8 m tall.

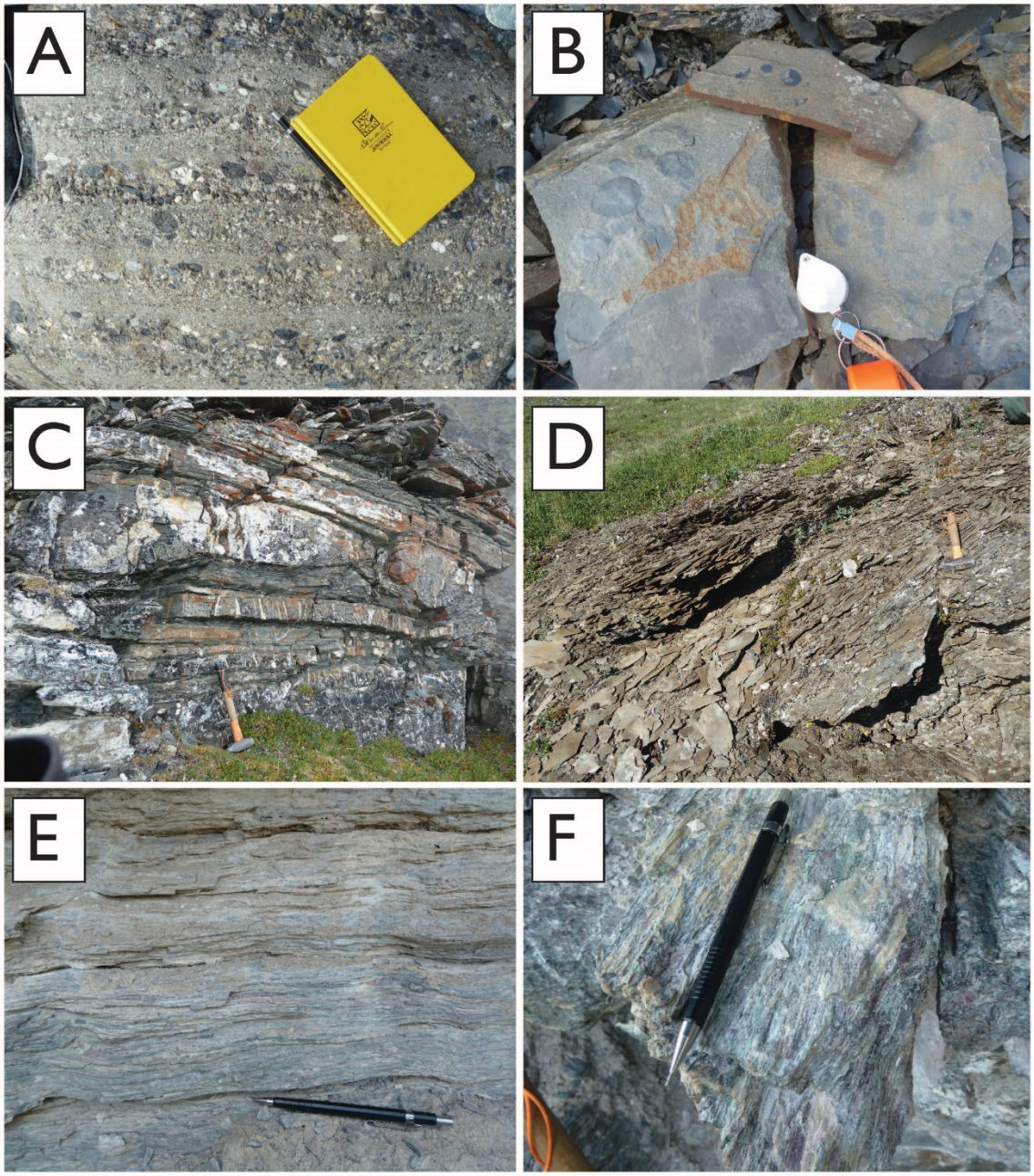

Figure 16: Field photos of other assorted formations. A - Kanayut Conglomerate: example of poorly-sorted quartz and chert pebble conglomerate. B - Hand samples of fine grained lithic sandstone found along the gradational transition from Hunt Fork Shale to Noatak Sandstone, stratigraphically below the Kanayut Conglomerate, northwest portion of map area.. C & D - Hunt Fork Shale - Examples of thin-to-medium bedded outcrop with small calcite filled veins and thinly-bedded, highly-foliated and fissile variety. E & F – Highly-foliated and sheared green-to-purple quartz and chert pebble conglomerate of the Beaucoup formation found just north of the North Fork Koyukuk River. Both photos are from the same outcrop.

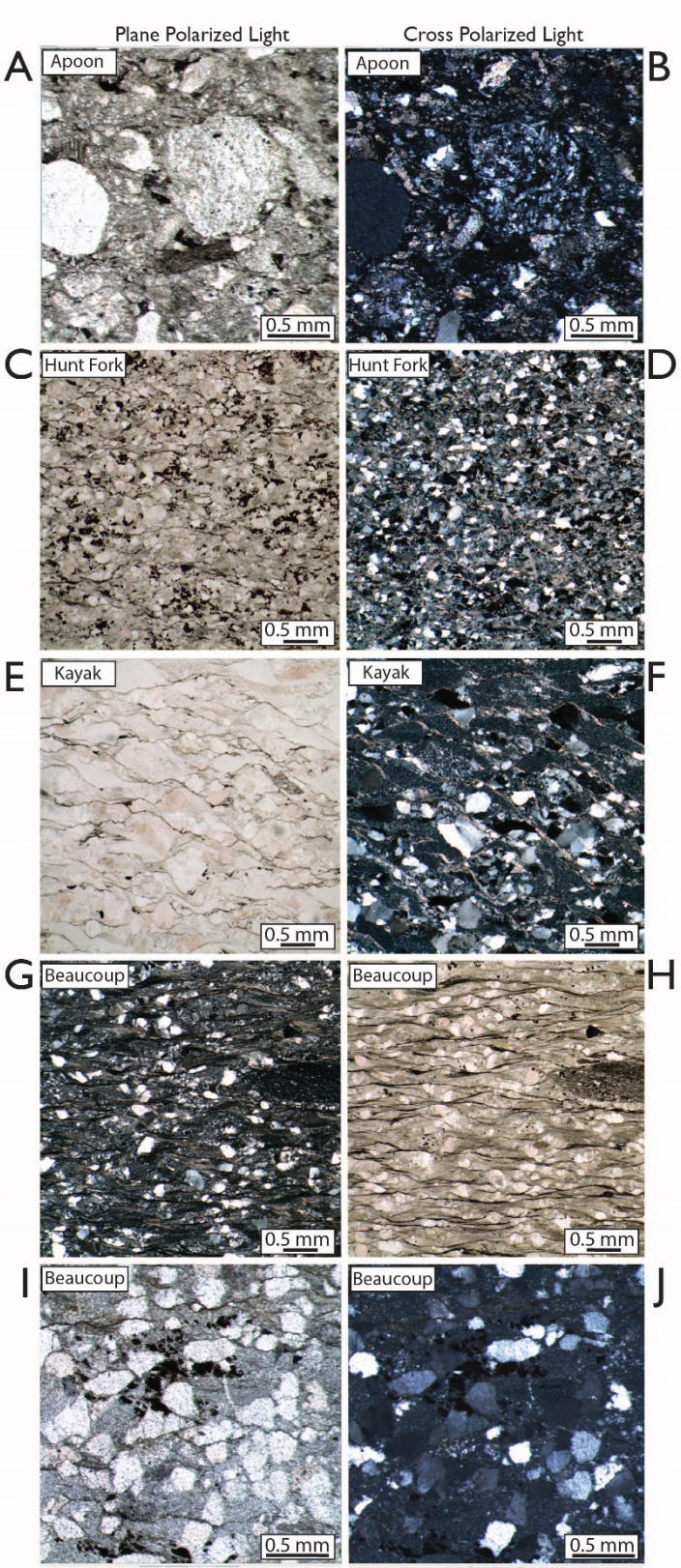

Figure 17: Thin section micrographs of various formations analyzed for detrital zircon geochronology in this study.

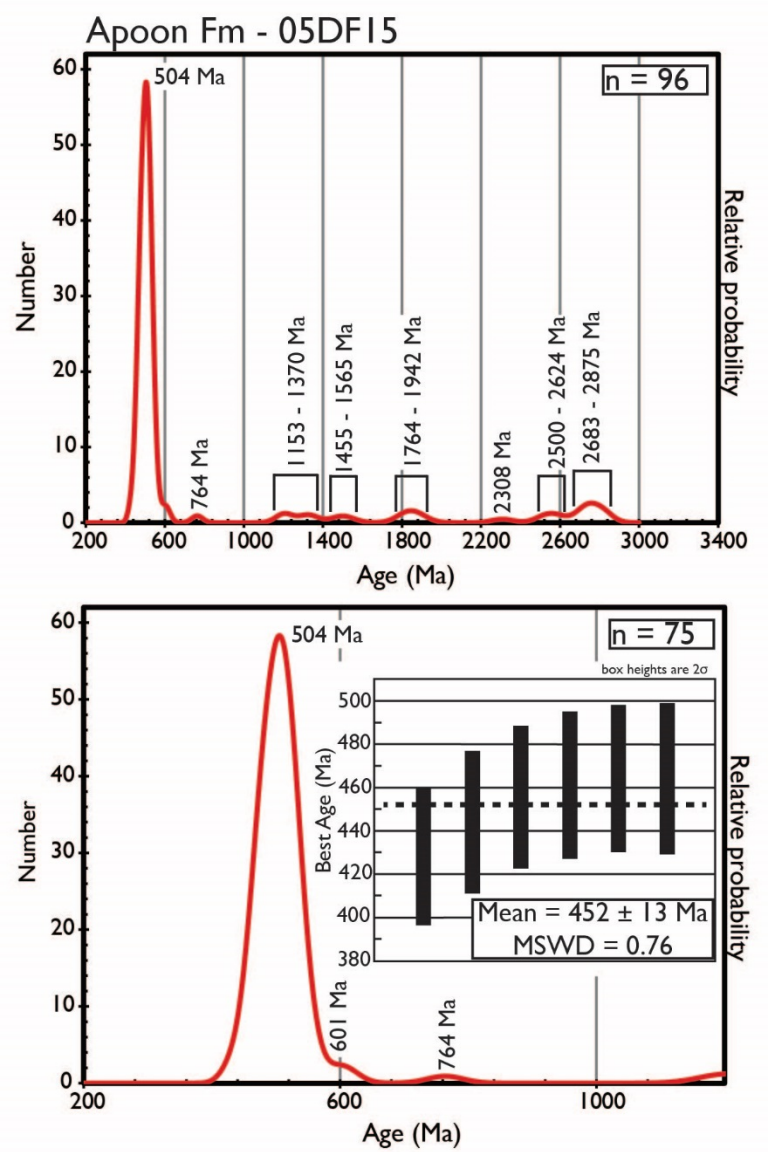

Figure 18: Probability density plot and max depositional age estimation generated from detrital zircon geochronology for sample 05DF15 - Apoon assemblage. See Figure 9 - marked as 05 - for sample location on a map. The top panel shows the entire range of the probability density plot. The lower panel shows a probability density plot generated from only the youngest grains, younger than 1200 Ma. Dominate age groupings are labeled. Box heights in the max depositional age figure represent the 2 σ error on the analysis of that grain. The mean of the youngest population and its associated error is provided in the inset box.

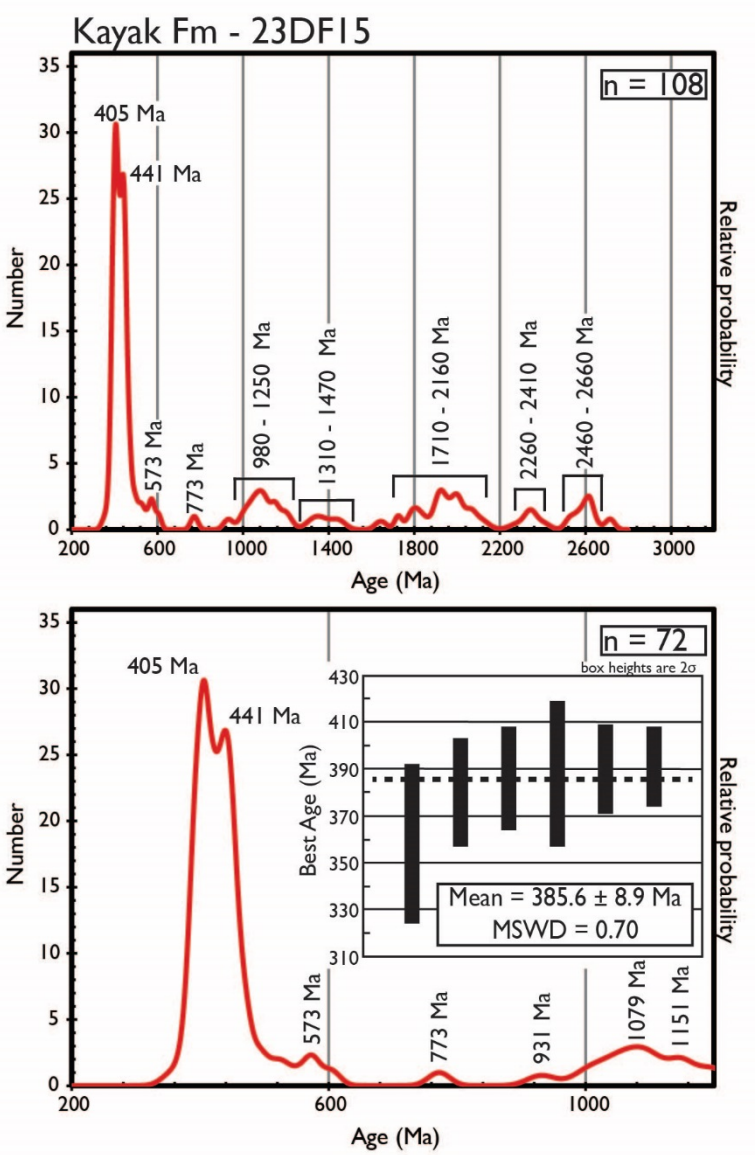

Figure 19: Probability density plot and max depositional age estimation generated from detrital zircon geochronology for sample 23DF15 - Kayak formation. See Figure 9 - marked as 23 - for sample location on a map. The top panel shows the entire range of the probability density plot. The lower panel shows a probability density plot generated from only the youngest grains - younger than 1200 Ma. Dominate age groupings are labeled. Box heights in the max depositional age figure represent the 2 σ error on the analysis of that grain. The mean of the youngest population and its associated error is provided in the inset box.

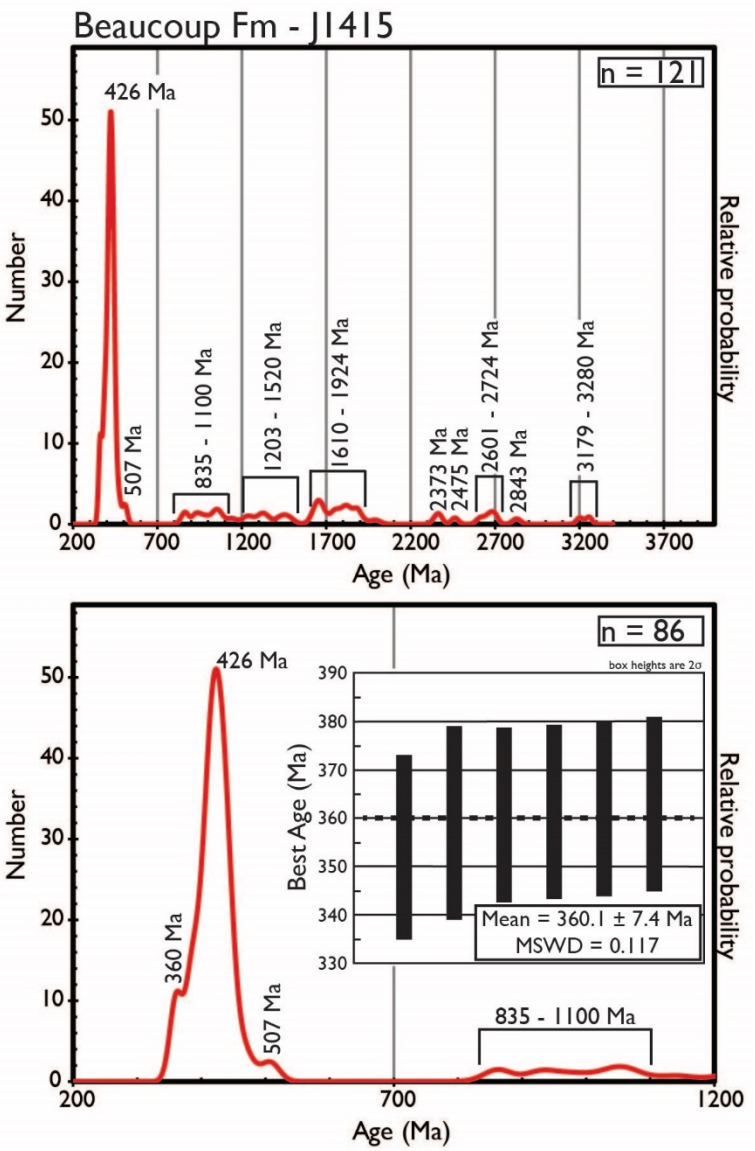

Figure 20: Probability density plot and max depositional age estimation generated from detrital zircon geochronology for sample J1415 - Beaucoup formation. See Figure 9 for sample location on a map. The top panel shows the entire range of the probability density plot. The lower panel shows a probability density plot generated from only the youngest grains - younger than 1200 Ma. Dominate age groupings are labeled. Box heights in the max depositional age figure represent the 2 σ error on the analysis of that grain. The mean of the youngest population and its associated error is provided in the inset box.

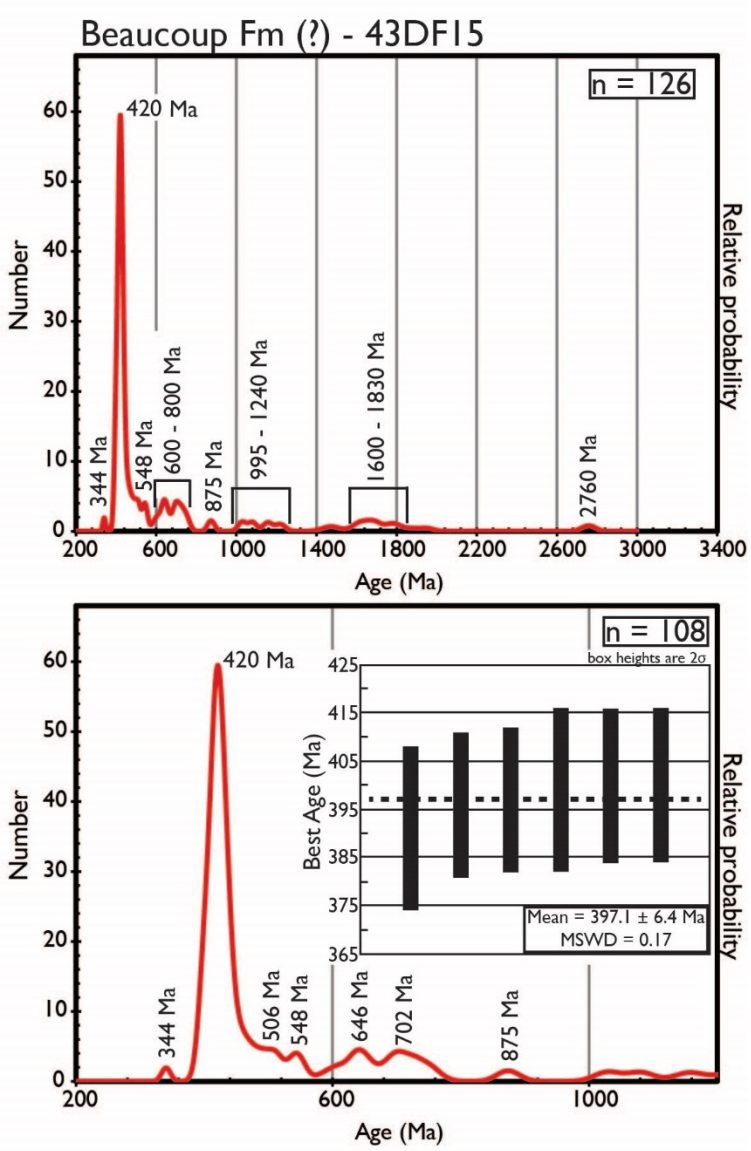

Figure 21: Probability density plot and max depositional age estimation generated from detrital zircon geochronology for sample 43DF15 - Beaucoup formation. See Figure 9 - marked as 43 - for sample location on a map. The top panel shows the entire range of the probability density plot. The lower panel shows a probability density plot generated from only the youngest grains - younger than 1200 Ma. Dominate age groupings are labeled. Box heights in the max depositional age figure represent the 2 σ error on the analysis of that grain. The mean of the youngest population and its associated error is provided in the inset box.

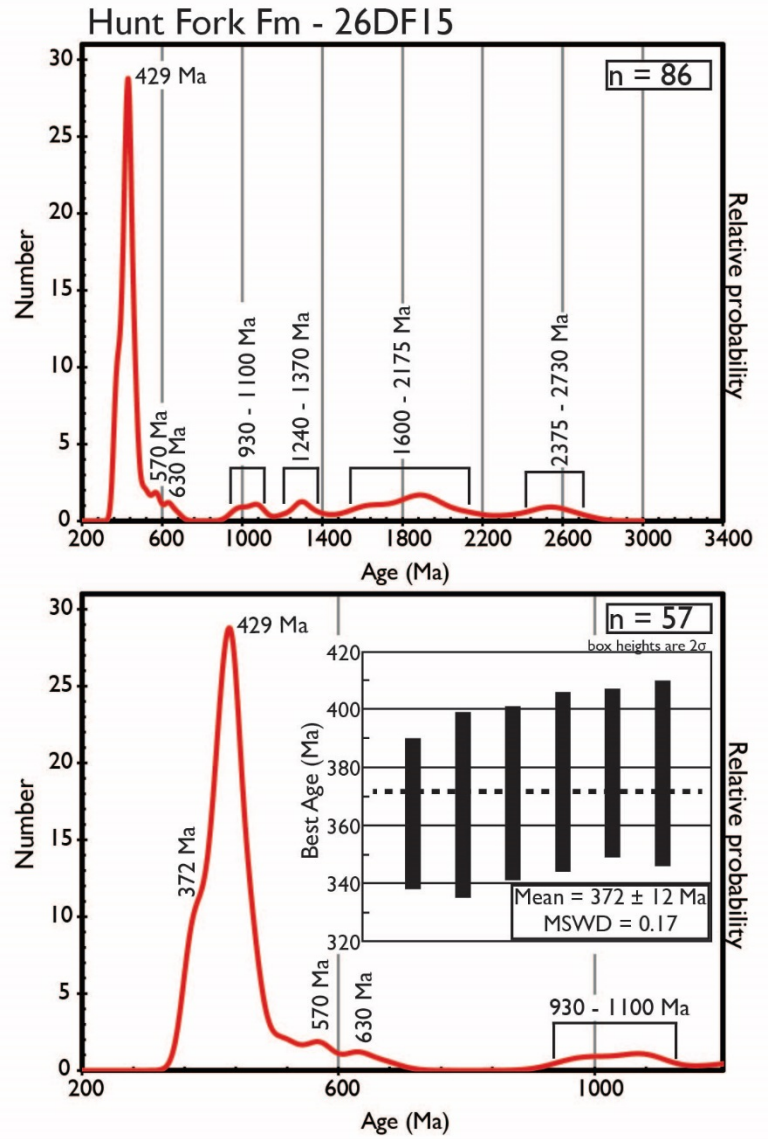

Figure 22: Probability density plot and max depositional age estimation generated from detrital zircon geochronology for sample 26DF15 - Hunt Fork (?) formation. See Figure 9 for sample location on a map. The top panel shows the entire range of the probability density plot. The lower panel shows a probability density plot generated from only the youngest grains - younger than 1200 Ma. Dominate age groupings are labeled. Box heights in the max depositional age figure represent the 2 σ error on the analysis of that grain. The mean of the youngest population and its associated error is provided in the inset box.

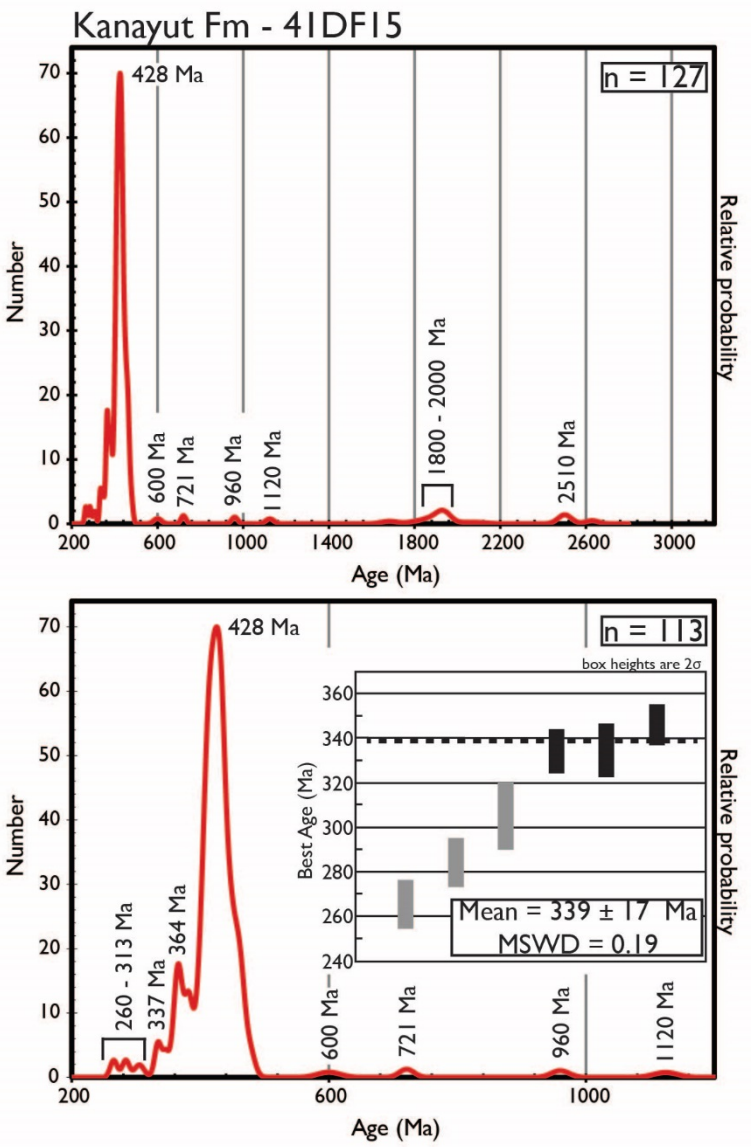

Figure 23: Probability density plot and max depositional age estimation generated from detrital zircon geochronology for sample 41DF15 - Kanayut formation. See Figure 9 for sample location on a map. The top panel shows the entire range of the probability density plot. The lower panel shows a probability density plot generated from only the youngest grains - younger than 1200 Ma. Dominate age groupings are labeled. Box heights in the max depositional age figure represent the 2 σ error on the analysis of that grain. The mean of the youngest population and its associated error is provided in the inset box.

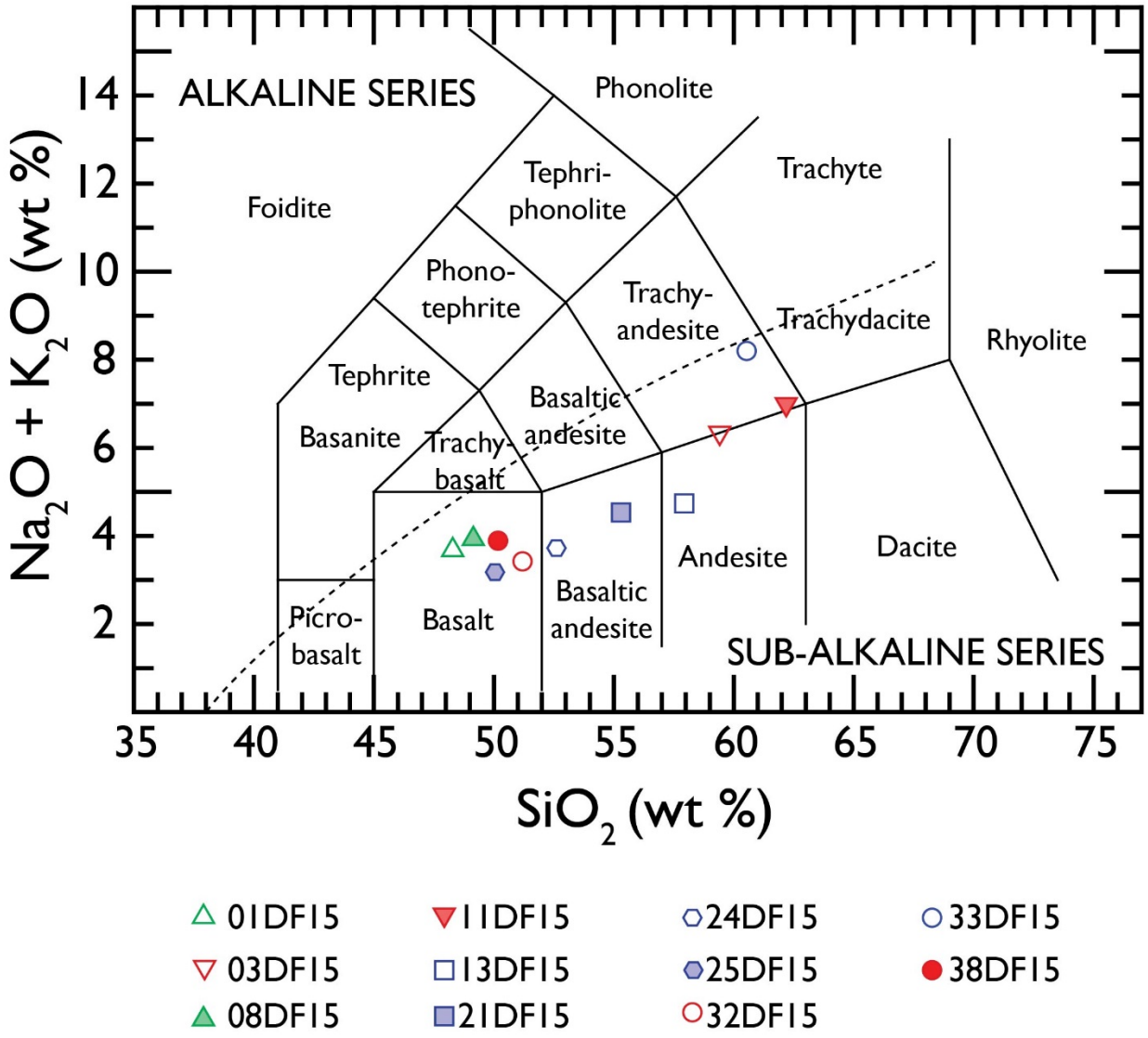

Figure 24: Total alkali ($Na_2O + K_2O$ in wt %) – silica (SiO_2 in wt %) diagram with fields after Le Maitre et al. (2002). Symbols used in this plot are used in all subsequent figures. Note that the Apoon rocks from this study all plot as subalkaline rocks and can be categorized as basalts, basaltic-andesites, andesites, and trachy-andesites. All samples are normalized to 100% anhydrous; raw geochemical data are presented in Supplemental Materials section.

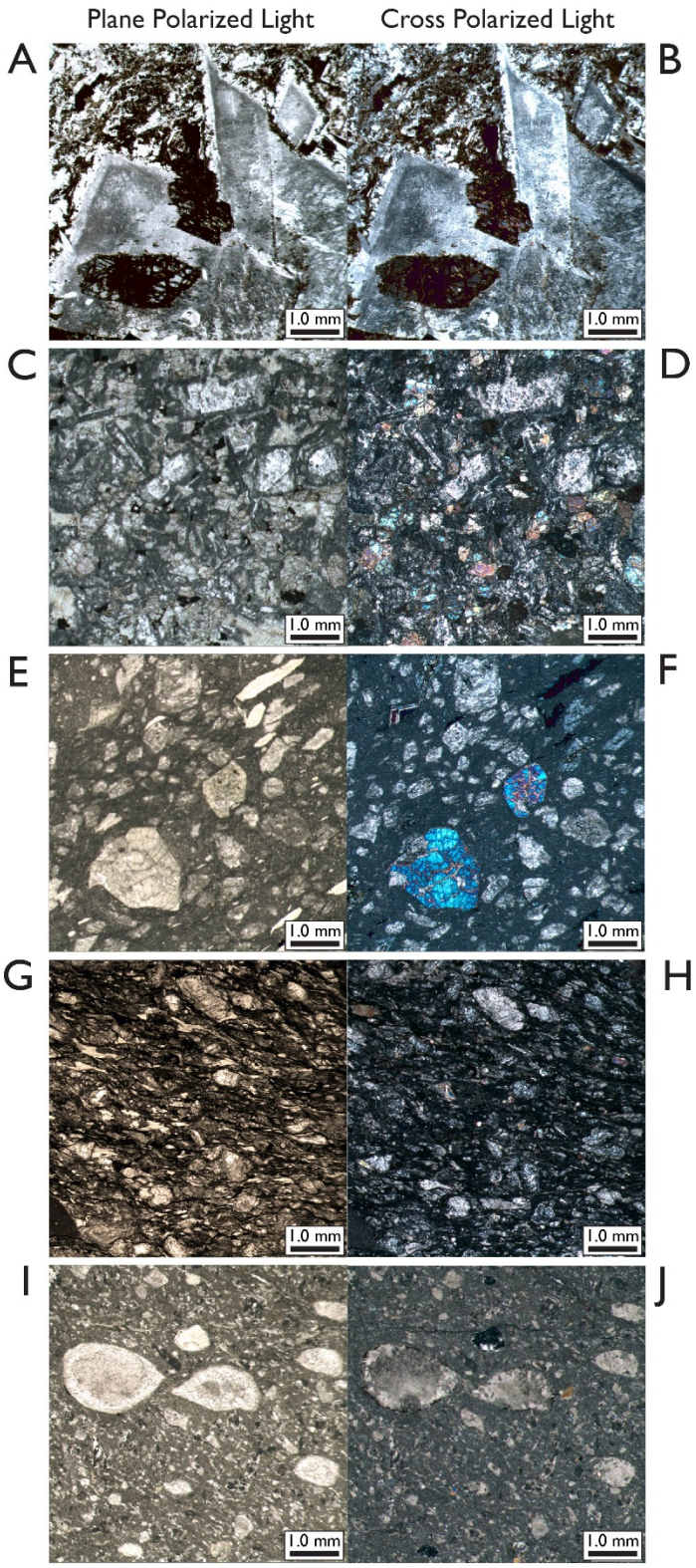

Figure 25: Representative thin section photomicrographs from igneous rocks within the Apoon assemblage demonstrating the textural and compositional variety of the Apoon assemblage's igneous portions.

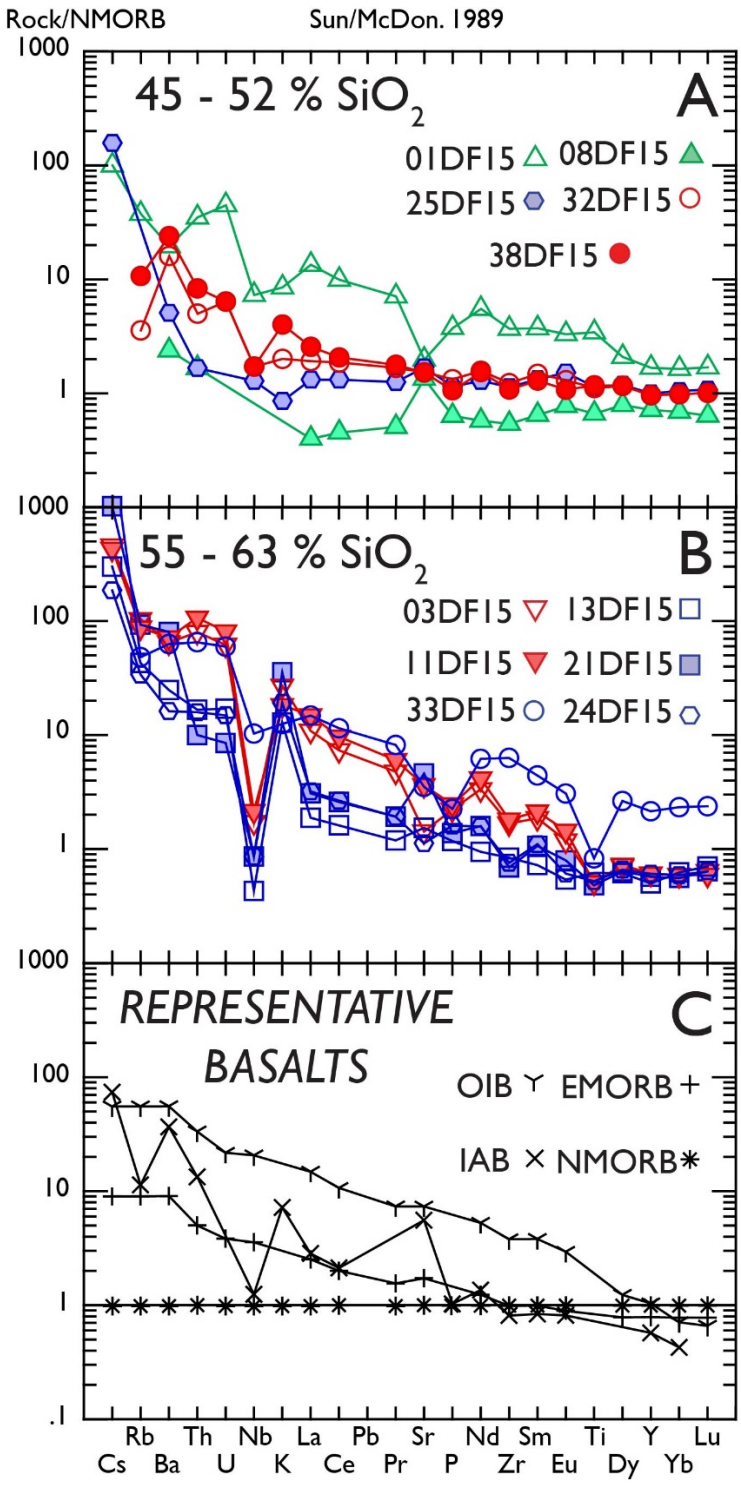

Figure 26: Trace element variation diagrams for eleven samples from the Apoon assemblage. All samples are normalized to the composition of a normal mid-ocean ridge basalt (NMORB) based on Sun and McDonnough (1989). The bottom frame plots representative basalt types from particular tectonic settings from Sun and McDonnough (1989) and Nye and Reid (1986). EMORB - Enriched Mid-Ocean Ridge Basalt; IAB - Island Arc Basalts; NMORB - Normal Mid-Ocean Ridge Basalt; OIB - Ocean Island Basalts.

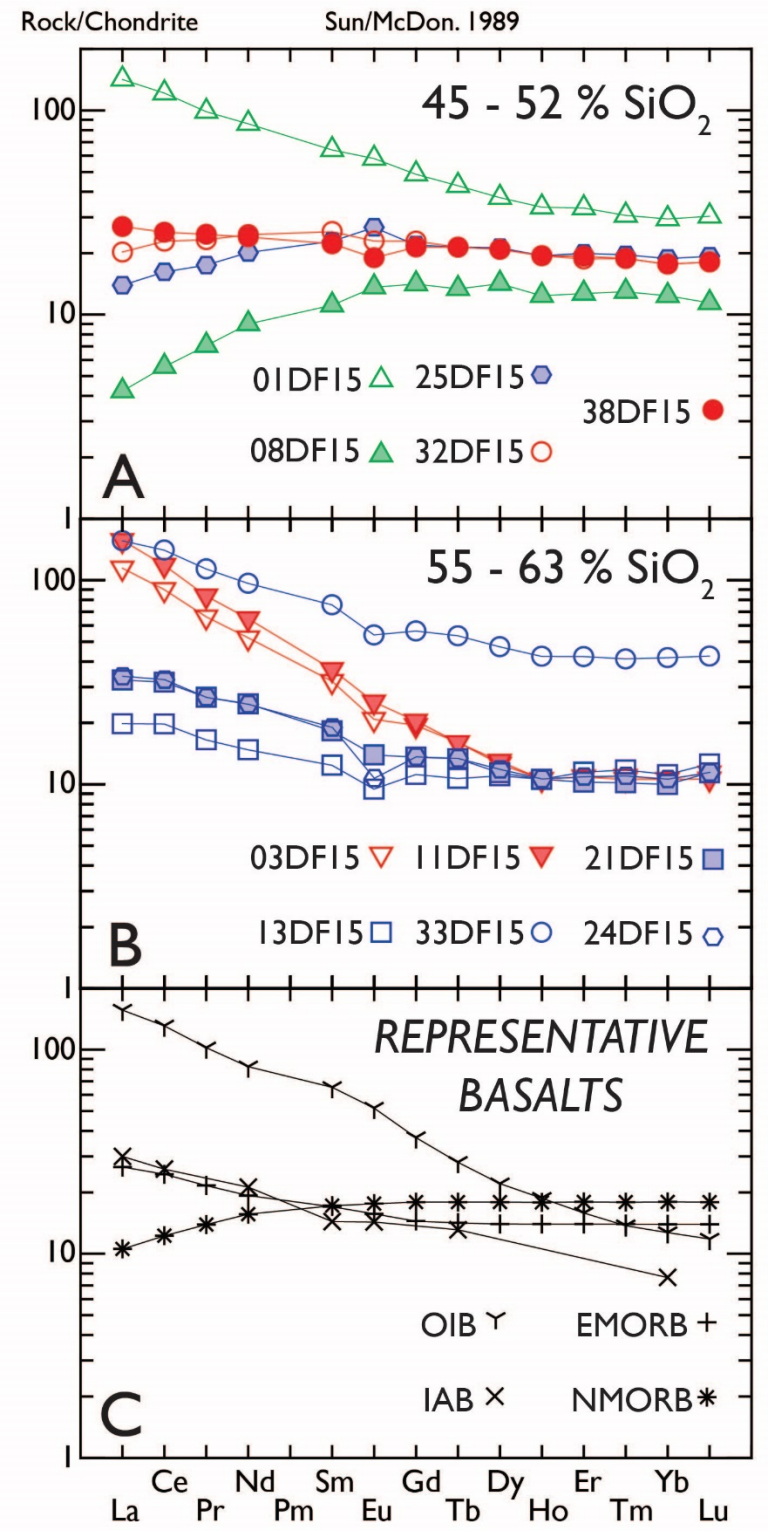

Figure 27: Chondrite-normalized trace element variation diagrams of the Apoon assemblage volcanic rocks (after Sun and McDonnough, 1989). The bottom frame plots representative basalt types from particular tectonic settings from Sun and McDonnough (1989) and Nye and Reid (1986). EMORB - Enriched Mid-Ocean Ridge Basalt; IAB - Island Arc Basalts; NMORB - Normal Mid-Ocean Ridge Basalt; OIB - Ocean Island Basalts.

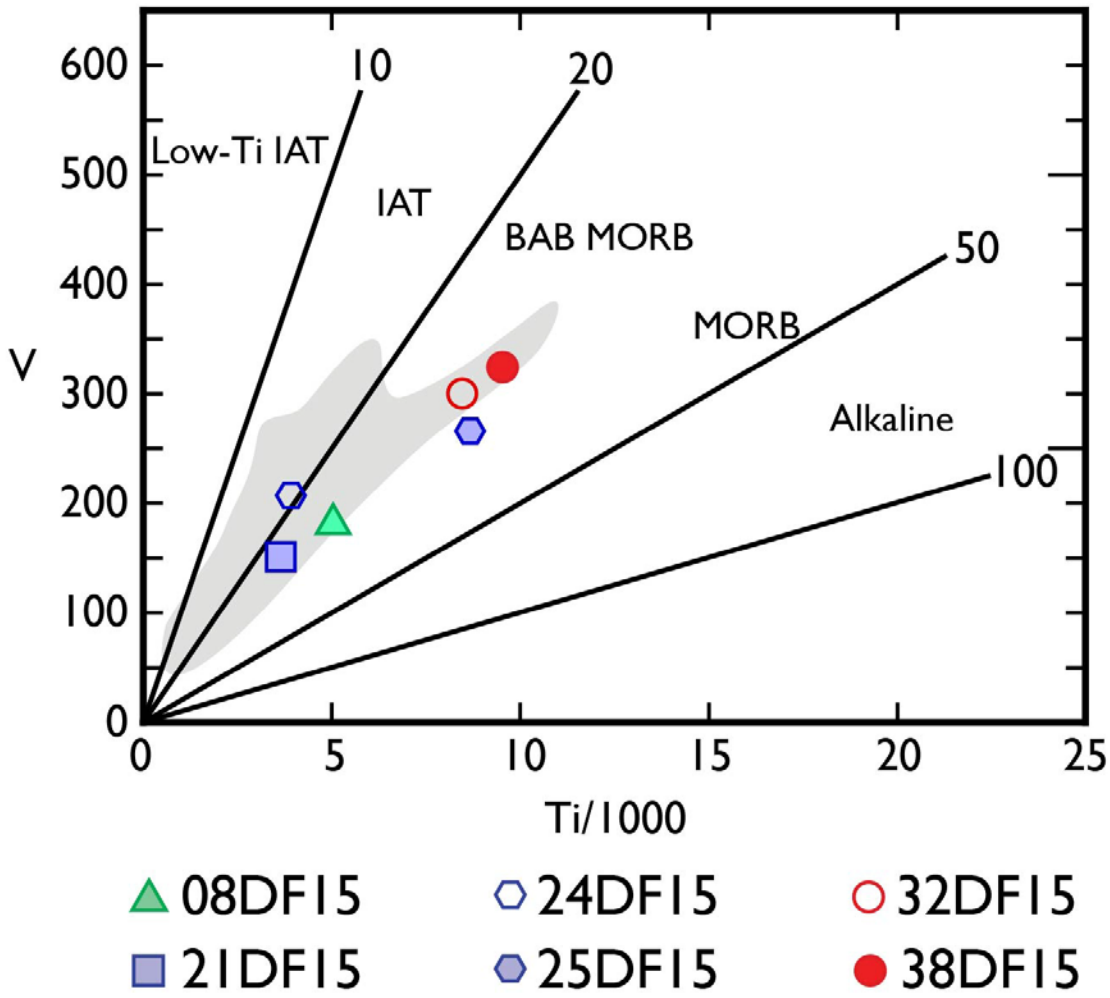

Figure 28: Ti - V tectonic discrimination diagram after Shervais (1982). The gray field marks the compositional range of samples from the Apoon assemblage from previous studies (Julian 1989; Julian and Oldow, 1998). The proportion of Ti:V is here used as a proxy for the oxygen activity within a magma during eruption and related to potential tectonic environments. BAB MORB - Back Arc Basin Mid-Ocean Ridge Basalt; IAT - Island Arc Tholeiitic; MORB - Mid-Ocean Ridge Basalt. Only those samples that classified as basalts and basaltic-andesite (i.e. <57 wt % SiO_2) were included in this plot (Shervais, 1982).

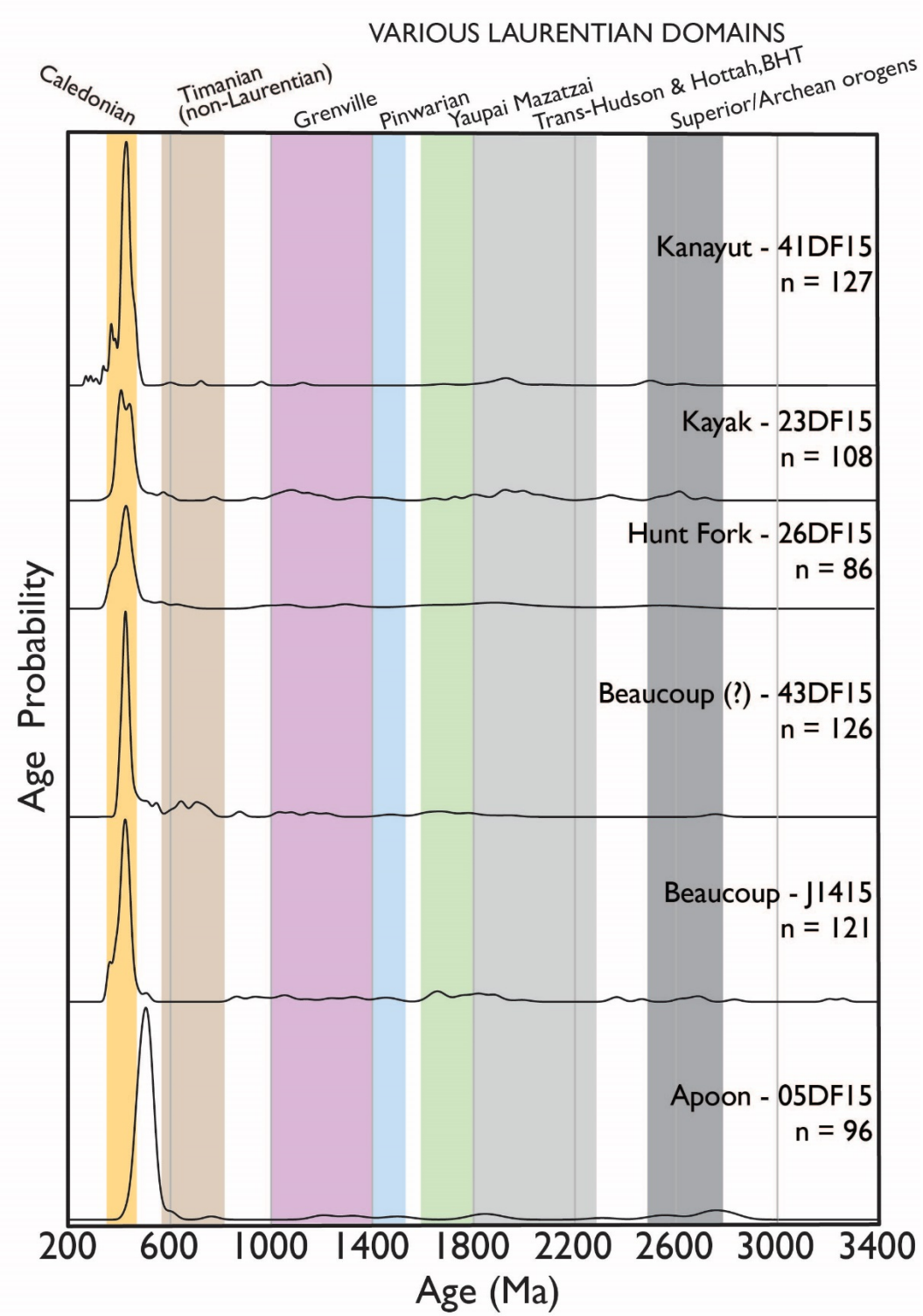

Figure 29: Stacked probability density plots from all samples within this study. Sample names and the number of grains in each analysis are given at the right side of the figure. The vertical colored bars represent the age of various orogenic episodes with affected rocks of the circum-Arctic.

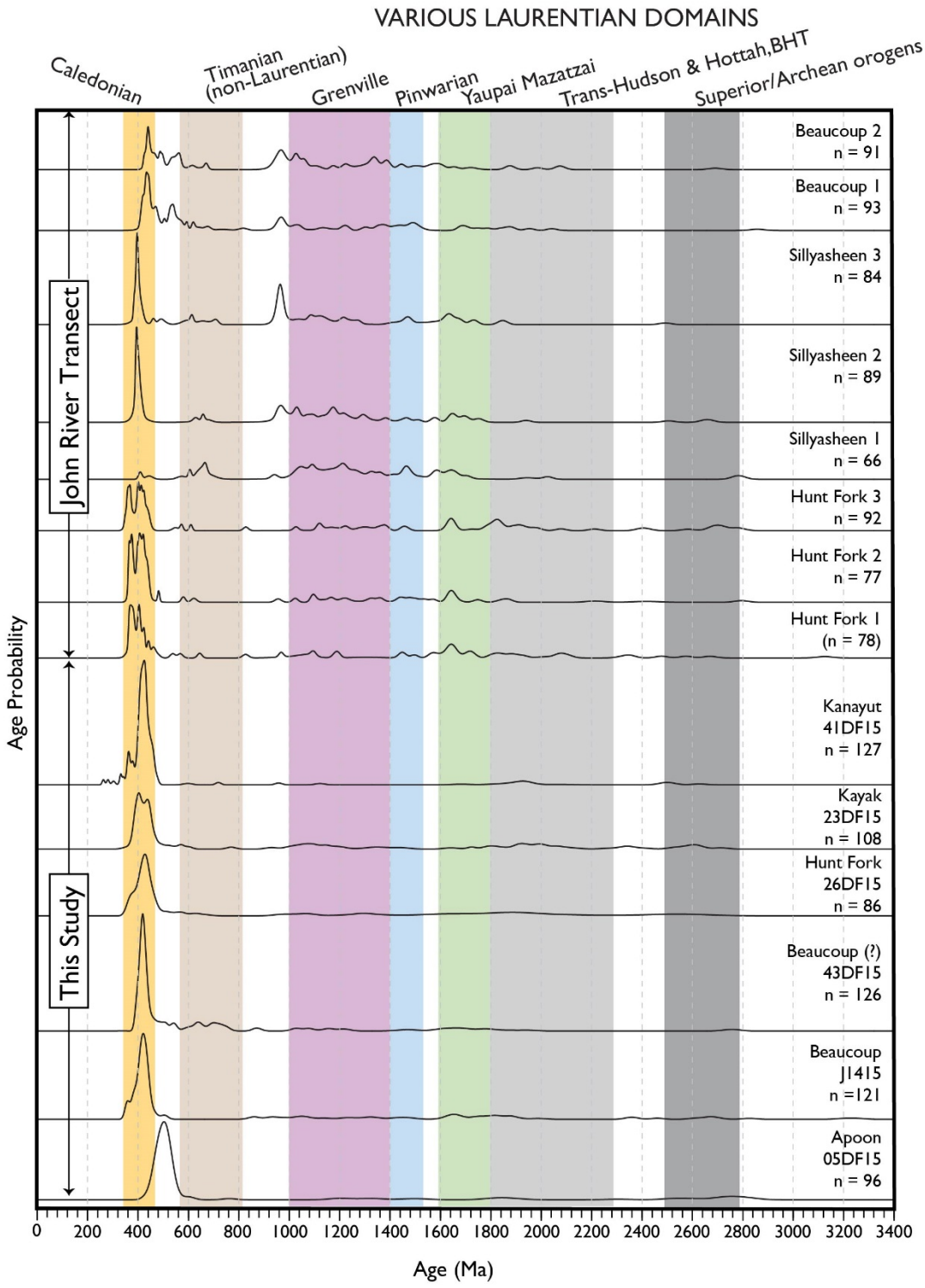

Figure 30: Stacked probability density plots from all samples within this study (lower portion of figure) and those from the John River transect of the central Brooks Range (west of Doonerak) by Miller, Pease, and Hoiland (unpublished data; upper portion of figure). Sample names and the number of grains in each analysis are given at the right side of the figure. The vertical colored bars represent the age of various orogenic episodes which may have contributed detritus to rocks of the circum-Arctic.

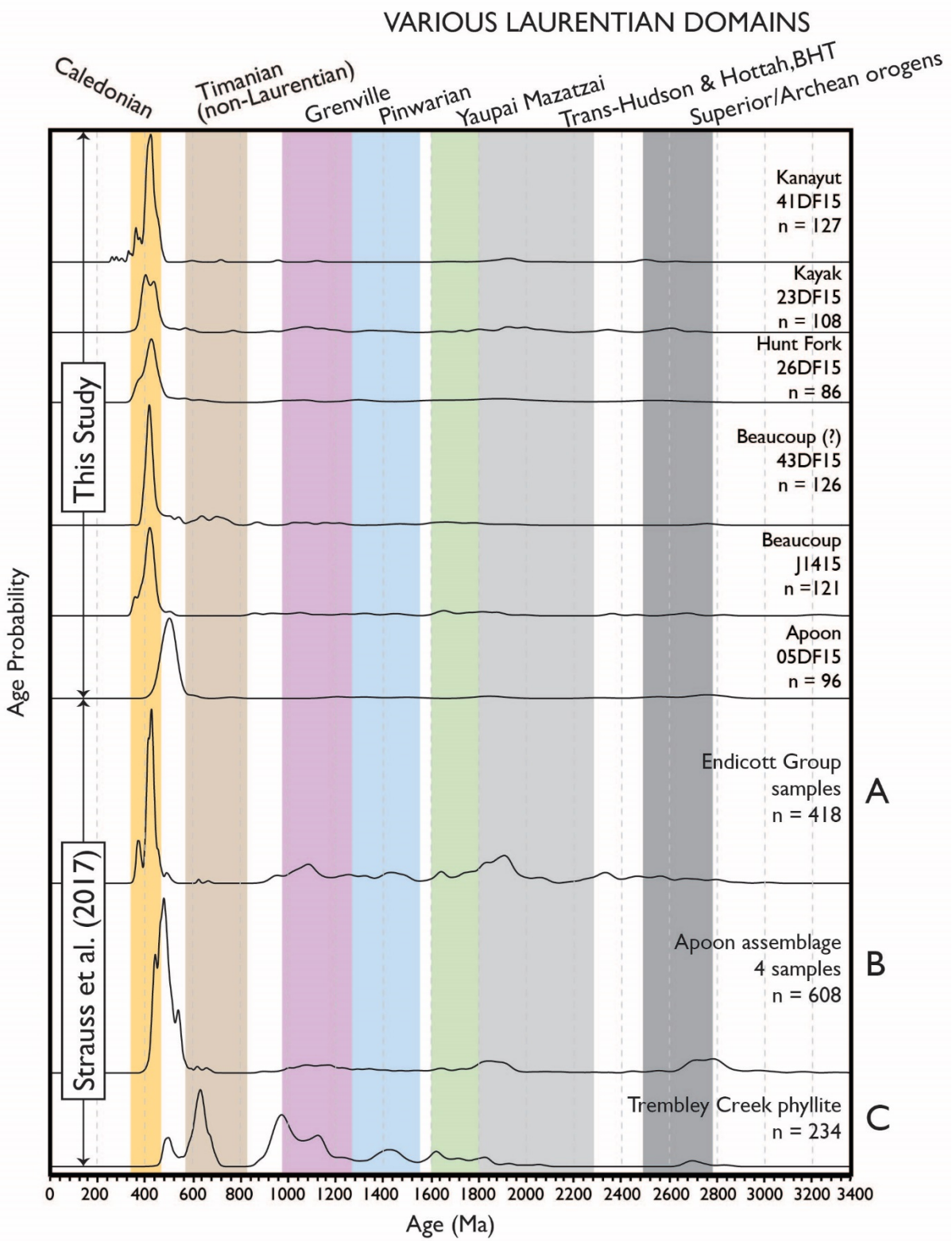

Figure 31: Stacked probability density plots from all samples within this study and those from Strauss et al. (2017). The curves from Strauss et al. (2017) provide the accumulated probability density plots from multiple samples from the same formations

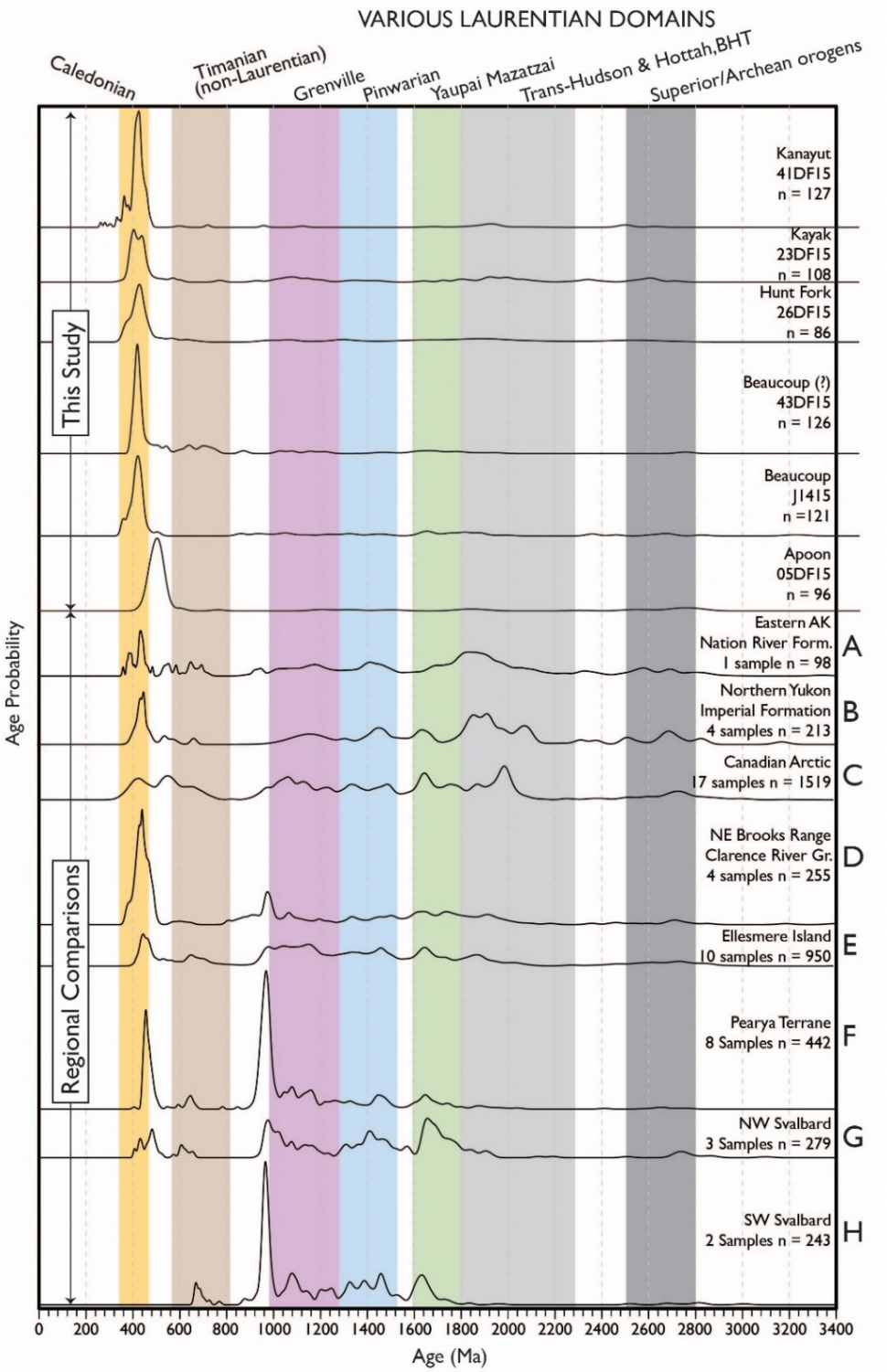

Figure 32: Stacked probability density plots from all samples within this study alongside those from a suite of regional published sources: (A) Ellesmerian clastic wedge of east-central Alaska (Gehrels and Pecha, 2014), (B) Ellesmerian clastic wedge in the Yukon (Beranek et al., 2010), (C) Ellesmerian clastic wedge in the Canadian Arctic Islands (Anfinson et al., 2012), (D) Clarence River Group of the northeast Brooks Range (Johnson et al., 2016), (E) Ellesmerian Island (Beranek et al., 2015), (F) Pearya terrane (Hadlari et al., 2014); (G) northwestern Svalbard (Petterson et al., 2010); and (H) Southwestern Svalbard (Gasser and Andersen, 2013).

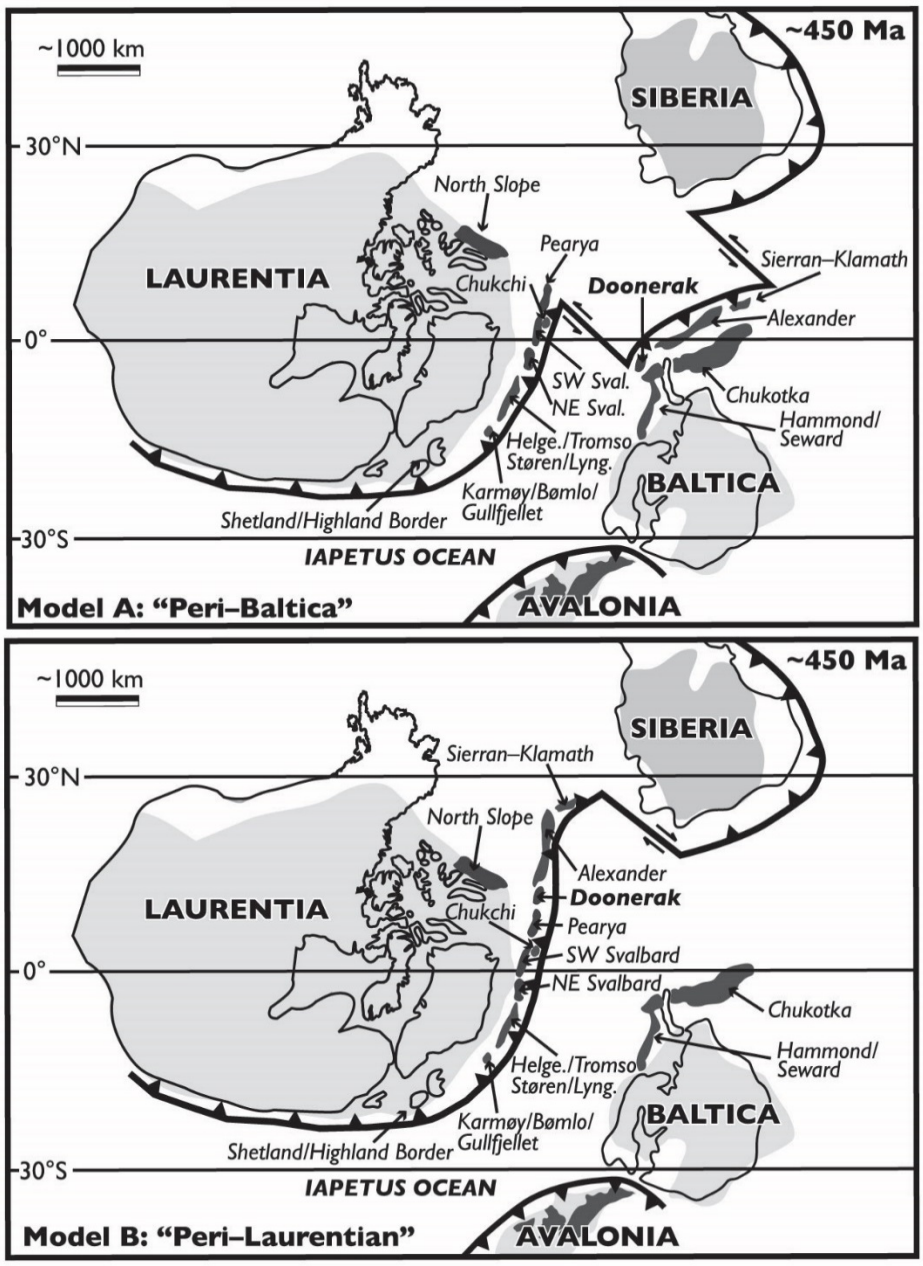

Figure 33: Schematic paleogeographic reconstructions of pertinent circum-Arctic paleo-continents, terranes, and microcontinents in the Late Ordovician from Strauss et al. (2017). Latitudinal positions are based on Cocks and Torsvik (2005, 2007, 2011, and references therein). The bulk of the North Slope of Arctic Alaska is on the peri-Laurentian margin following Strauss et al. (2013), Cox et al. (2015), and Johnson et al. (2016). (A) Paleogeographic model restoring Doonerak to a position proximal to Baltica in the Late Ordovician, in a setting similar to the Alexand er terrane and exotic portions of the Arctic Alaska-Chukotka microplate. In this model, Doonerak sits along the convergent margin of Baltica and there must be subduction polarity reversal to place Baltica on the lower plate during Scandian contraction. (B) Paleogeographic model that restores Doonerak and other circum-Arctic terranes to the northern extent of the Taconic orogenic system, proximal to Laurentia. Subduction polarity reversal is required to accrete the Pearya terrane and Doonerak onto the NE margin of Laurentia.

1. INTRODUCTION

Regional tectonic and paleogeographic models of the circum-Arctic (Fig. 1) are some of the least well constrained in the world due to the regions remoteness and complex geologic relationships (e.g. Pease et al., 2011). Many tectonostratigraphic terranes of the Arctic are remnants of oceanic and continental crust from the margins of the Paleozoic Iapetus Ocean and have Siberian, Baltic, Laurentian, Gondwanan, and/or Panthalassan affinities (e.g. Trettin, 1987; Amato et al., 2009; Colpron and Nelson, 2009, 2011; Grove et al., 2008; Miller et al., 2011; Beranek et al., 2013a&b). The Phanerozoic accretionary history of Laurentia (proto-North America) potentially involves the translation of exotic terranes (e.g. Arctic Alaska, Farewell, Alexander, Klamath-Sierra, and Pearya) across the continent's northern margin from the Caledonian-Appalachian orogen to the North American Cordillera (e.g. Colpron and Nelson, 2011; Cocks and Torsvik, 2011; Miller et al., 2011; and many others). These regional relationships make the Arctic a critical location for understanding the growth and evolution of continental margins by accretionary and, potentially, large-scale strike slip tectonics.

The Arctic Alaska terrane, one such tectonostratigraphic package, includes the Brooks Range, North Slope and Seward Peninsula of northern Alaska (Fig. 1 and 2). The northeast Brooks Range and most of the North Slope portions of the Arctic Alaska terrane share characteristics (stratigraphy, fossil assemblages, detrital zircon populations) with Laurentia (Fig. 3; Johnson et al., 2016; Strauss et al., 2013; Cox et al., 2015; McClelland et al., 2015; Lane et al., 2015), while the southwestern portion of the terrane, including the Hammond subterrane, Coldfoot subterrane, and Seward Peninsula, has dominantly Baltic and Siberian affinities (Fig. 3; Kos'ko et al., 1993; Patrick and McClelland, 1995; Natal'in et al., 1999; Blodgett et al., 2002; Dumoulin et al., 2002; 2014; Amato et al., 2009, 2014; Miller et al., 2006, 2010, 2011; Till et al.,

2014a, 2014b; Akinin et al., 2015). These relationships suggest that a suture must exist between these different areas within Arctic Alaska, which records the amalgamation and formation of the Arctic Alaska terrane itself. Although recent efforts have attempted to better define these relationships (e.g. Strauss et al., 2017), our understanding of the timing and location of this suturing event within Arctic Alaska remains poorly constrained. The goal of this project is to constrain the nature of this boundary within Arctic Alaska through analysis of the Doonerak fenster, a strategic location which exposes structural basement of the Brooks Range between these regions of Laurentian and non-Laurentian origin.

For instance, most Arctic plate tectonic models restore the northern portion of the Arctic Alaska terrane near Point Barrow, AK to a conjugate margin near Prince Patrick Island in the Canadian Arctic by Mesozoic time (Fig. 1 and 2; e.g. Grantz et al., 2011; Lawver and Scotese, 1990; Houseknecht and Connors, 2016). This may have been achieved by way of ~60° rotation of Arctic Alaska around a Euler pole in the Mackenzie Delta during the Early Cretaceous (e.g. Gottlieb et al., 2014); however, one of several unresolved questions related to refining tectonic models of the Arctic concerns the position of the North Slope of Arctic Alaska from the Middle Ordovician to Late Devonian at the time of the Caledonian-Appalachian orogen (ca. 470-350 Ma; e.g. Gee, 1975; Roberts, 2003; McKerrow et al., 2000). Recent detrital geochronology of pre-Mississippian units from the Whale Mountain area in the northeast Brooks Range (Fig. 1) records a major shift in provenance and sediment dispersal that coincides temporally with the Caledonian orogeny and could be related to closure of the northern Iapetus Ocean (Johnson et al., 2016, 2013). The continuity of these relationships in the central Brooks Range is unknown.

The Doonerak fenster provides a window into the pre-Mississippian basement of the central Brooks Range, exposes rocks somewhat similar to those found in the Whale Mountain

area, and has long been enigmatic within the central Brooks Range (e.g. Dutro et al., 1976) because it provides unique exposure of mafic-to-intermediate volcanic rocks of largely unknown origin. Recent igneous and detrital geochronology and Lu-Hf isotopic data from zircon in the Doonerak fenster suggest that the Doonerak area could contain a magmatic arc complex, potentially related to the boundary between rocks of Laurentian and non-Laurentian affinity in Arctic Alaska (Strauss et al., 2017). In this context, the Doonerak fenster is critically important for understanding magmatism along the northern margin of Laurentia and closure of the Iapetus Ocean. Resolving the full tectonic context of the rocks within the Doonerak fenster could have broad implications on Neoproterozoic - Paleozoic plate reconstructions of the circum-Arctic (e.g. Dutro et al., 1973; Moore et al., 1994; Strauss et al., 2013). Herein, I present new detrital geochronologic data from the Doonerak area (from the fenster itself and the overlying allochthonous package) and whole-rock geochemistry from Doonerak's suite of igneous rocks. The objective this work is to provide evidence to help resolve the tectonic setting of the Doonerak fenster and related areas of the Arctic Alaska terrane during Caledonian-Appalachian orogenesis and to further define the position and nature of the boundary between Laurentian and non-Laurentian rocks in Arctic Alaska.

2. THE ARCTIC LITHOSPHERE

2.1 The Arctic Oceanic Realm

The Arctic Ocean includes two distinct oceanic basins, the Eurasia and Amerasia Basins (Fig. 1), and is surrounded by continental landmasses that share many characteristics, such as floral and faunal assemblages, detrital zircon populations, and deformation histories (e.g. Pease

et al., 2014, 2011; Miller et al., 2010). However, the tectonic evolution that led to these relationships and to the modern configuration of these landmasses is poorly understood. The younger of these ocean basins, the Eurasia basin, formed by seafloor spreading along the northern portion of the modern Atlantic/Arctic spreading center, the Gakkel Ridge, during Cenozoic time. This spreading center marks the modern boundary between the North American and Eurasian lithospheric plates in the Arctic (Engen et al., 2003; Karasik, 1968; Kristoffersen, 1990; Savostin and Karasik, 1981; Vogt et al., 1979).

The Eurasia basin contains well-mapped magnetic anomalies, which indicate that spreading began in the Cenozoic (c. 58 Ma - magnetic chron A25) between the Lomonosov Ridge and the Barents-Kara continental margin (Brozena et al., 2003; Glebovsky et al., 2006; Grants et al., 2011; Karasik, 1968, 1974; Kristoffersen, 1990; Vogt et al., 1979). Rates of seafloor spreading along the Gakkel Ridge are among the slowest in the world (Cook et al., 1986; Glebovsky et al., 2006; Karasic, 1974; Vogt et al., 1979). Very slow spreading may have contributed to the great variability in topography of the basin as a product of interplay between variable magmatism and crustal production with extension of the crust itself (Louden et al., 1996; Mutter and Karson, 1992; Small and Sandwell, 1992).

The Lomonosov Ridge (Fig. 1) is a poorly understood fragment of Eurasian continental crust that extends from northern Greenland toward the Siberian continental shelf, bisecting the Arctic Ocean (Brozena et al., 2003; Glebovsky et al., 2006; Grantz et al., 2001; Jokat et al., 1992; Karasik, 1968, 1974; Kristoffersen, 1990; Vogt et al., 1979). The Amerasia Basin lies to the west of the Lomonosov Ridge (Fig. 1) and is surrounded by the Canadian Arctic Islands, northern Alaska, and the Chukotka peninsula of northern Russia. It is larger than the Eurasia Basin and highly heterogeneous. The pre-Amerasia Basin configuration of the Arctic's

landmasses and the processes by which the basin opened are both unclear. The Amerasia Basin consists of several different physiographic regions, including the Canada Basin.

The Canada Basin is the most pertinent portion of the Amerasia Basin in terms of this study. It is bordered to the north by the Alpha-Mendeleev ridge province, to the west by the Chukchi Borderland, to the southeast by the Canadian Arctic Islands (Ellesmerian Fold Belt), and to the southwest by the continental margin of Arctic Alaska (Fig. 1). The Canada Basin is enigmatic; there is no consensus as to the nature of its crust or the mechanisms by which it opened (e.g. Lawver and Scotese, 1990). Saltus et al. (2011) used magnetic data to conclude that the basin is underlain by crust that is not typical of oceanic lithosphere; however, gravity data (Laxon and McAdoo, 1994, 1998) and regional seismic lines (Dinkelman et al., 2008; Helwig et al., 2011) suggest the existence of an extinct spreading center. Despite a lack of direct dating of basement material, most models for the opening of the Canada Basin assume that sea-floor spreading occurred during the Cretaceous on the basis of stratigraphic similarities along the basin's margins (e.g. Lawver and Scotese, 1990; Grantz et al., 2011a; Mosher et al., 2012; Spencer et al., 2011; Lane, 1997).

2.2 The Arctic Continental Realm

One method to understand the evolution of the Arctic Ocean is to better define the linkages between the different tectonostratigraphic terranes of its surrounding landmasses. Many of the Arctic's landmasses include tectonostratigraphic terranes derived from oceanic and continental crust from the margins of the Iapetus Ocean. These include terranes of Siberian, Baltic, Laurentian, Gondwanan and Panthalassan affinities (e.g. Trettin, 1987; Amato et al.,

2009; Colpron and Nelson, 2009, 2011; Grove et al., 2008; Miller et al., 2011; Beranek et al., 2013). The Arctic Alaska - Chukotka Microcontinent (AACM) is one such tectonostratigraphic package. The AACM includes the Brooks Range, North Slope, and Seward Peninsula of Alaska, the Chukotka Peninsula, Wrangel Island, and New Siberian Islands of Russia, and the continental shelves surrounding the Bering, Beaufort, and Chukchi seas (Fig. 1 & 2; e.g. Miller et al., 2006). The southern terminus of the AACM is marked by the Angayucham suture in Alaska (e.g. Moore et al., 1994) and the South Anyui suture zone in Russia (e.g. Seslavinskiy, 1979; Sokolov et al., 2002), where belts of ophiolites record oceanic closure that occurred as terranes of southern Alaska and Siberia collided with the AACM (Moore et al., 1994; Pease et al., 2014; Nokleberg et al., 2000; Zonenshain and Napatov, 1989). The geology of the AACM preserves evidence of a long-lived multiphase accretionary history. Because of its location at the edge of the Canada Basin, the AACM also provides critical piercing points for developing Mesozoic reconstructions of the Arctic and opening of the Arctic Ocean (e.g. Miller et al., 2006). The AACM has important paleogeographic links with various circum-Arctic paleocontinents (Dumoulin et al., 2002, 2014; Blodgett et al., 2002; Amato et al., 2009, 2014; Macdonald et al., 2009; Cocks and Torsvik, 2011; Strauss et al., 2013; Cox et al., 2015); however, much of the older history has been overprinted by the relatively young Jurassic-Cretaceous orogenesis which formed the Brooks Range (Brookian orogeny) in Alaska (Moore et al., 1994 and references therein) and the Verkhoyansk-Kolyma and Chukotka orogenic belts in Russia (Fig. 2; e.g. Oxman, 2003 and references therein). These orogenic belts incorporated crust which had previously been affected by older circum-Arctic orogenic episodes (Fig. 2; section 3.4).

The Arctic Alaska terrane, the Alaskan portion of the AACM (Fig. 3), is internally complex, which complicates attempts to restore its paleogeography. The northeast Brooks Range

and North Slope portions of the Arctic Alaska terrane have stratigraphy, fossil assemblages, and detrital zircon populations that indicate a Laurentian (North American) origin (Johnson et al., 2016; Strauss et al., 2013; Cox et al., 2015; McClelland et al., 2015; Lane et al., 2015). Conversely, the Hammond and Coldfoot subterranes, to the southwest, have dominantly Baltic and Siberian affinities (Fig. 3; Kos'ko et al., 1993; Patrick and McClelland, 1996; Natal'in et al., 1999; Blodgett et al., 2002; Dumoulin et al., 2002; 2014; Amato et al., 2009, 2014; Miller et al., 2006, 2010, 2011; Till et al., 2014a, 2014b; Akinin et al., 2015). This implies that there must be a boundary between these different areas within Arctic Alaska. A presumably Paleozoic suture, which records the amalgamation and formation of the Arctic Alaska terrane, must lie between these crustal blocks separating Laurentian and non-Laurentian portions of the Arctic Alaska terrane. We do not know the precise timing or mechanism by which Arctic Alaska amalgamated; however, Ordovician-Silurian potentially arc-related rocks of the Doonerak fenster in the central Brooks Range could be related to that internal suture within Arctic Alaska (Mull, 1982; Moore et al., 1997; Grantz et al., 1991; Dumoulin et al., 2000; Strauss et al., 2013, 2017). As such, Doonerak is an important locale for understanding amalgamation of the Arctic Alaska terrane, Paleozoic magmatism, and the closure of the northern Iapetus Ocean.

2.3 Relationships between Arctic landmasses

Several models for the opening of the Canada Basin attempt to reconstruct the relationships between the Arctic's landmasses by placing portions of the North Slope in a position against the Canadian Arctic Margin in pre-Mesozoic time (e.g. Lawver and Scotese, 1990; Lawver et al., 2002; Miller et al., 2006; Colpron and Nelson, 2009; Macdonald et al.,

2009). These models all agree that parts of the Arctic Alaska terrane and Canadian Arctic Islands were previously contiguous because they share similar paleontological, detrital zircon, and stratigraphic relationships, but the models differ in the precise mechanisms by which Arctic Alaska achieved its modern position. Determining the precise pre-Canada Basin positions and relationships of these landmasses has direct bearing on developing viable paleogeographic reconstructions and models for basin opening. Defining the mechanisms by which Laurentian and non-Laurentian portions of Arctic Alaska amalgamated and simply defining the location of that boundary with more precision are needed to inform these models. This study provides new geochemical and geochronological data from border between Laurentian and non-Laurentian regions of Arctic Alaska in order to constrain these relationships.

One widely accepted model for the opening of the Canada Basin involves the clockwise rotation (~60-70°) of the AACM, including Arctic Alaska terrane, away from the Canadian Arctic Islands about a pole of rotation located in the Mackenzie Delta (e.g. Grantz et al., 2011; Lawver et al., 2002). This assumes that exotic terranes of Chukotka, Alaska, and the Canadian Arctic arrived against the Laurentian margin as the northern Iapetus Ocean closed, before any Mesozoic rifting (e.g. Lawver et al., 2002). The simple rotational model predicts opening of the Canada Basin as a consequence of this rotation, between the Canadian Arctic and Arctic Alaska; however, it fails to explain the overlap of the Siberian continental shelf and Canadian Arctic Islands (~600 km of overlap) implied by this restoration (Lane, 1997).

Miller et al. (2006) used a more complex combination of rifting and strike-slip displacement to rectify the overlap generated in the simple rotation model. This model allows portions of Arctic Alaska and Chukotka to behave as non-coherent, independent masses with different tectonic and depositional histories. Miller et al., (2006) use detrital zircon data from

Triassic sandstones of Siberia, Chukotka, northern Alaska, and northern Canada to suggest that Chukotka and the East Siberian Shelf were in a different pre-rift paleogeographic position than Arctic Alaska. During the Triassic, Chukotka and the East Siberian Shelf must have been in a position to receive detritus from the Siberian craton, while Arctic Alaska was receiving detritus from the northern margin of Laurentia near the Canadian margin (Miller et al., 2006).

The Paleozoic geographic position of these same landmasses is more unclear. Stratigraphic similarities between the Seward Peninsula (western AK), Chukotka Peninsula, and portions of the Brooks Range are suggestive of unified deposition in the Lower Paleozoic (Natal'in et al., 1999). Fossil evidence suggests a Siberian affinity for parts of Arctic Alaska and Chukotka in the mid-Paleozoic (Blodgett et al., 2002; Dumoulin et al., 2002) and that Arctic Alaska and Siberia shared faunal assemblages by the Early Ordovician (Dumoulin and Harris, 1994; Dumoulin et al., 2002). These data suggest that portions of Arctic Alaska may have rifted from Siberia in the Devonian or that they had Cambrian to Devonian ties to northeastern Baltica (e.g. Blodgett et al., 2002). Amato et al., (2009) used U-Pb zircon geochronology from igneous and detrital rocks, along with Nd isotopic data from basement rock of the Seward Peninsula to point to an origin exotic to western Laurentia. They also developed a pre-Canada Basin Mesozoic reconstruction in which the Brooks Range, Seward Peninsula, and North Slope are near the Canadian Arctic Islands from the Mississippian to the Jurassic.

2.4 Relation to research goals

In order to constrain its paleogeography, we need to better understand the internal complexity within Arctic Alaska and define the boundary between rocks of Laurentian and non-

Laurentian origin. Defining this boundary would provide greater constraints on Paleozoic-Mesozoic reconstructions and allow future studies to better evaluate the mechanisms and timing of that amalgamation. This study focuses on the Doonerak fenster, a strategic location in the central Brooks Range, which is one of the best candidates for identifying the Paleozoic suture that must exist between the Laurentian and non-Laurentian portions of Arctic Alaska. Thus, the overarching goal of this research is to provide evidence for the Paleozoic tectonic setting of the rocks exposed within the Doonerak fenster and to better understand their relationship to the allochthonous rocks which overlie the fenster within the Brookian fold thrust belt. To that end, the goals of this work are 1) determine the age and provenance of the metasedimentary rocks within the Doonerak area, both interior and exterior to the fenster and 2) characterize the geochemical affinities of the volcanic rocks exposed in the fenster that may be related to this presumed Paleozoic suture. The combination of these efforts will place tighter constraints on the Paleozoic suture and various paleogeographic models outlined above. We test the hypothesis that the Doonerak fenster preserves the remnant of an island arc complex and marks the location of the suture between Laurentia and Siberian portions of Arctic Alaska. The data presented herein complements recent publications focused on the northeastern Brooks Range and Doonerak fenster by Johnson et al. (2016) and Strauss et al. (2017) respectively.

3. THE DOONERAK FENSTER - LOCATION AND GEOLOGIC SETTING

3.1 Terranes and Subterranes - Context within Arctic Alaska

Broadly, northernmost Alaska contains two lithostratigraphic terranes: the Arctic Alaska terrane and Angayucham terrane (Fig. 3; Moore et al., 1994; Silberling et al., 1994). Both occupy

portions of the Brookian orogen. The Brooks Range is the 1000 km long E-W trending north-vergent fold-thrust belt that extends across northern Alaska and into the Yukon of Canada (e.g. Mull, 1982; Oldow et al., 1987a; Grantz et al., 1991; Moore et al., 1994).

The Angayucham terrane is the structurally highest nappe associated with the Brooks Range and contains mostly mafic and ultramafic rocks with minor pelagic rocks of Devonian to Jurassic age (Fig. 3; Roeder and Mull, 1978; Moore et al., 1994). Spatial relationships, stratigraphic associations, and geochemical trends from Angayucham's igneous rocks suggest that the terrane is an internally complex package of obducted oceanic crust which was transported northward and accreted onto the southern Arctic Alaska terrane during Jurassic to Cretaceous orogenesis (e.g. Roeder and Mull, 1978; Barker et al., 1988; Pallister and Budahn, 1989). The Arctic Alaska terrane is more extensive and underlies the Colville basin and Brooks Range (e.g. Mull, 1982; Moore et al., 1994). It can be divided into six subterranes or allochthons on the basis of stratigraphy, facies, metamorphic grade, and structural position (Fig. 3; e.g. Moore et al., 1994; Mull, 1982; Jones et al., 1987; Mayfield et al., 1988). From north to south (i.e. foreland to hinterland), these are the North Slope, Endicott Mountains, De Long Mountains, Hammond, Coldfoot, and Slate Creek subterranes. Variations in the nomenclature of the Brooks Range complicate understanding of the region in general (e.g. Karl and Mull, 1993). A belt nomenclature related to the metamorphic grade of these packages is also used to describe northern Alaska (Fig. 3). These nomenclatures are nearly equivalent, but the subterrane nomenclature will be used throughout this document.

The North Slope, the structurally lowest of Arctic Alaska's subterranes, includes rocks of the northeastern Brooks Range, Lisburne Hills, Barrow arch, and Colville basin subsurface (Fig. 3). In the Colville basin subsurface, these rocks are not extensively deformed by post-

Mississippian orogenesis, but in the northeastern Brooks Range the same units show considerable deformation by Cretaceous to Cenozoic contraction. The outcrop of North Slope units south of the Endicott Mountains, in the Doonerak fenster, indicates that the other subterranes within the Brooks Range are structurally emplaced above rocks that are related to the North Slope's basement (Fig. 3).

In some areas across the Brooks Range, the Endicott Mountains allochthon is structurally overlain by De Long Mountains subterrane. Both are imbricated packages of Paleozoic to Mesozoic rocks, but they differ in specific stratigraphic relations. The Hammond subterrane (Fig. 3), south of the Endicott Mountains and Doonerak fenster, includes most of the Proterozoic and lower Paleozoic sedimentary units found in the Endicott Mountains of the central Brooks Range; however, the Hammond subterrane includes ductile deformation structures and greenschist to blueschist facies mineralogy with only sporadic relict primary igneous and sedimentary textures (e.g. Moore et al., 1994). The Coldfoot and Slate Creek subterranes of the southern Brooks Range contain metamorphosed rocks of the Brookian hinterland. The Coldfoot subterrane contains blueschist and greenschist facies schist, calc-schist, marble, and metavolcanic rocks. The Slate Creek subterrane is mostly composed of phyllite and lesser metasandstone of Devonian age. The Colville basin, Koyukuk basin, and Beaufort Sea shelf flank the perimeter of the Arctic Alaska terrane and are post-tectonic basins, which have experienced only minor shortening from the Cretaceous to Cenozoic (Tailleur and Brosgé, 1970; Patton et al., 1994; Moore et al., 1994).

The various subterranes of Arctic Alaska can also be divided into two broad categories based on their paleogeographic relationships: those of Laurentian and non-Laurentian origin (Fig. 3). Several previous workers suggested a Laurentian origin for the North Slope and

northeastern Brooks Range portions of the Arctic Alaska terrane (e.g. Dutro et al., 1972; Moore et al., 1994, 2011; Lane, 2007; Johnson et al., 2016; Strauss et al., 2013, 2017), but others argue for an exotic origin on the basis of paleobiogeographic affinities of fossil assemblages and geochronologic constraints from the southwestern portion of Arctic Alaska (Dumoulin et al., 2002; Blodgett et al., 2002; Miller et al., 2006, 2010, 2011; Amato et al., 2009). It is important to define the boundary between these paleogeographically distinct regions in order to develop models for the Paleozoic tectonic evolution of the Arctic. The pre-Mesozoic origin of Arctic Alaska's subterranes and their relationships to Laurentia are also vitally important because they have direct bearing on developing constraints on kinematic models for the Jurassic-Cretaceous opening of the Amerasia Basin (e.g. Grantz and May, 1983) and on the development of hydrocarbon resources along the Arctic's continental shelves. The development of reliable piercing points for such Mesozoic tectonic reconstructions rests on constraining the relationships between the crustal fragments of the Arctic Alaska - Chukotka microcontinent.

3.2 Pertinent Stratigraphy

The Endicott Group unconformably overlies the lower Paleozoic volcanic and volcaniclastic rocks in the North Slope subsurface and within the Doonerak fenster. It consists of the Upper Devonian-to-Lower Mississippian Kekiktuk Conglomerate and the Lower Mississippian Kayak Shale (Fig. 4 & 5; Armstrong et al., 1976). The Kekiktuk Conglomerate is a terrigenous clastic succession which rests above a regional sub-Mississippian unconformity in the North Slope subsurface and northeast Brooks Range. Regionally, it ranges from many hundreds of meters thick in the North Slope subsurface (Melvin, 1993; Miller, 1991) to a

relatively thin and discontinuous unit in the northeast Brooks Range (Le Pain et al., 1994). The position of the Kekiktuk Conglomerate above the regional unconformity, its diversity of interpreted lithofacies and paleoenvironments, widespread distribution, and relationship to overlying marginal to shallow marine shales is suggestive of deposition along a progressively subsiding passive continental margin (e.g. Le Pain et al., 1994). The regional sub-Mississippian unconformity could reflect a transition from contractional tectonics below to extension and thermally controlled passive margin subsidence above (e.g. Le Pain, 1994, Anderson and Wallace, 1991; Moore et al., 1992; Anderson, 1993); therefore, the Kekiktuk Conglomerate (broadly correlative to the Kanayut Conglomerate of the Endicott Group within the Endicott Mountains allochthon; Fig. 5) is the basal terrigenous clastic portion of a larger continental margin succession - the Ellesmerian sequence (LePain et al., 1994; Moore et al., 1992).

En masse, the Endicott Group of the northeast Brooks Range is a transgressive succession (Brosgé et al., 1962; Armstrong, 1974; Armstrong and Bird, 1974; Nilsen, 1981). This succession is marked by the transition from the fluvial to marginal marine depositional settings of the Kekiktuk Conglomerate into the marginal marine to shallow marine lithofacies of the Kayak Shale. The unconformity at the base of the Kekiktuk is significant because it potentially marks cessation of the Devonian Romanzof (or Ellesmerian) orogeny, with dominantly contractional tectonics below and extension followed by thermal subsidence above (Churkin, 1969, 1975; Brosgé et al., 1962; Reed, 1968; Dutro, 1970; Sable, 1977; Oldow et al., 1987a&b; Moore et al., 1994; Lane, 2007; LePain, 1994). However, in the Endicott Mountains Allochthon (EMA), the sub-Mississippian unconformity is absent and Devonian age strata pass conformably up section into the Carboniferous (Fig. 5). The thick Upper Devonian to Carboniferous clastic package of the Endicott Mountains Allochthon (including the Devonian Beaucoup Formation,

Hunt Fork Shale, and Noatak Sandstone) is also considered to be part of the Endicott Group (Fig. 5), although within the Endicott Mountains allochthon the conglomeratic unit below the Kayak Shale is referred to as the Kanayut Conglomerate rather than the Kekiktuk Conglomerate. The Kanayut also reflects a transgressive-regressive-transgressive clastic wedge succession that formed as major fluvial-deltaic depocenters migrated along the Late Devonian to Early Carboniferous basin margin (Moore and Nilsen, 1984; Moore et al., 1992). The rocks of the Endicott Mountains allochthon (and the higher grade rocks of the Hammond subterrane; Fig. 3) were transported northward and emplaced into a structural position above the rocks of the Doonerak fenster during the Brookian orogen (Fig. 3, 5, and 7; e.g. Moore et al., 1997).

These regional relationships of Middle Devonian to Lower Carboniferous rocks in the Brooks Range characterize the early rift and drift phases in the evolution of a passive margin (Anderson and Wallace, 1991; Anderson et al., 1992; Moore et al., 1992; Anderson, 1993). The presence of the sub-Mississippian unconformity above the Apoon volcanics within the Doonerak fenster is similar to what is seen in the northeast Brooks Range and North Slope subsurface; however, the unconformity is absent in the overlying Endicott Mountains allochthon (EMA). This is one line of evidence used to suggest that the rocks interior to the Doonerak fenster are in fact structural "basement" to the Brookian fold-thrust belt, despite the fact that they only achieve greenschist metamorphic grade (e.g. Moore et al., 1994). The absence of the unconformity and generally thicker and more complete stratigraphic succession in the Endicott Mountains allochthon suggests that these rocks were deposited in a more basinal position relative to their coeval equivalents in the northeast Brooks Range and Doonerak fenster. The rocks of the Endicott Mountains mark the allochthonous portion of the Brookian orogen and should be restored to a position south of the Doonerak fenster. Understanding the provenance of the

Endicott Mountains rocks north of Doonerak would shed light on sediment pathways and variation in the Devonian section across the Brooks Range, prior to emplacement of those rocks above the Doonerak antiform.

3.3 Overview of orogenic events in northern Alaska and the Arctic

The Phanerozoic orogenic events of northern Alaska have historically been assigned to two major episodes, the Ellesmerian and Brookian (see review by Moore et al., 1994). Ellesmerian deformation affected units below the regionally recognizable sub-Mississippian unconformity in the North Slope subsurface and northeast Brooks Range (described in previous section) but its full extent is not well known. Lerand (1973) expanded the Ellesmerian orogeny to include all early Paleozoic deformation along the Arctic Ocean margin on the basis of presumably coeval sub-Mississippian structures in northern Alaska and the Canadian Arctic Islands. However, other work suggests that the deformation in the northeast Brooks Range is pre-Middle Devonian and therefore older than the Ellesmerian structures of the Canadian Arctic (e.g. Anderson et al., 1994). The pre-Middle Devonian deformation of the northeast Brooks Range is now treated as a distinct, yet related, orogenic event, the Romanzof Orogeny (Lane, 2007). Romanzof deformation was likely localized along the northwest margin of Laurentia and could be related to the Early-Middle Devonian accretion of the Whale Mountain allochthon onto the Laurentian margin (Johnson et al., 2016; Lane, 2007). The continuity of Romanzof vs. Ellesmerian structures elsewhere in Arctic Alaska is not well known, nor are the effects of this orogenic episode on sediment dispersal among other regions of Arctic Alaska containing early-mid Paleozoic stratigraphy.

The Brookian orogeny, the younger orogenic system of northern Alaska, formed the dominant east-west trending, north-vergent fold thrust system of the Brooks Range and occurred in two major phases (Gottschalk and Snee, 1998; Moore et al., 1994). Metamorphism of the southern Brooks Range and emplacement of far traveled thrust sheets in the northern Brooks Range occurred during the first Brookian phase in Middle Jurassic to Early Cretaceous time (Mull, 1982; Mayfield et al., 1988; Dillon 1989). The second Brookian phase formed structures in several deformational episodes affecting mid-Cretaceous and younger strata and occurred as a protracted series of deformational events. The uplift of the Doonerak antiform is attributed to this second phase (e.g. Moore et al., 1994; O'Sullivan et al., 1998). In the North Slope and Beaufort Sea, deformed Neogene and Quaternary units indicate that deformation continued into the recent geologic past (Grantz and May, 1983, Grantz et al., 1990).

Brookian deformation was also synchronous with regional metamorphism between 170 - 54 Ma, concentrated around 110 Ma (Turner et al., 1979), and contributed to the progressive uplift of the Brooks Range itself. Estimates of uplift from the Doonerak fenster in the central Brooks Range indicate ~8-12 km of denudation since ~70-65 Ma (O'Sullivan et al., 1998). Apatite fission-tracks suggest a minimum of ~4-6 km of denudation since the late Oligocene (O'Sullivan et al., 1998). Similarities between the Doonerak antiform and antiforms of the northeast Brooks Range and similarly rapid rates of denudation and uplift could indicate that the Doonerak antiform formed as the result of a deformational and uplift episode that affected both regions in the Oligocene (O'Sullivan et al., 1998).

Other regional orogenic episodes (Fig. 2) which may have contributed detritus to rocks pertinent to this study include the Caledonian orogeny of Greenland, Scandinavia, and the northernmost Atlantic and the Timanian orogeny of northernmost Europe (Baltica) and Russia.

Younger regional episodes, such as the Uralian orogeny of northern Baltica, which formed the Ural Mountains, the modern boundary between Europe and Asia, are generally too recent to have contributed detritus to rocks at Doonerak, but certainly may have overprinted portions of the Timanian fold thrust belt in northern Europe.

The Caledonian orogeny is the northern equivalent of the trans-Appalachian orogenic episodes associated with the closure of the Iapetus Ocean. It can be subdivided into numerous phases involving arc-arc and arc-continent collisions from Cambrian to Devonian time involving Laurentian, Baltican, and Avalonian crust (e.g. McKerrow et al., 2000). Early Caledonian phases are recorded in both Scandinavia and the United Kingdom and range from 550 - 500 Ma (e.g. Ramsay and Sturt, 1976; Sturt et al., 1978); however, the major collision between Laurentia and Baltica occurred from the Late Silurian to Early Devonian and is often referred to as the Scandian phase, which involved rapid subduction and the emplacement of plutonic igneous rocks between 490 - 390 Ma, with peak development around ~ 420 Ma (e.g. Gee, 1975; Roberts, 2003; McKerrow et al., 2000). The Ellesmerian and Romanzof structures and deformation along the Canadian and Alaskan margins may be related to the Caledonian orogen. Some paleogeographic models of the Arctic predict that terranes of Caledonian origin were transported along the Laurentian Arctic Margin in a strike-slip manner (Colpron and Nelson, 2009, 2011). These Caledonian terranes might have then been incorporated into the Ellesmerian and/or Romanzof orogenic episodes and could have provided pathways for sediment to move from the Caledonian realm toward Arctic Alaska.

The Timanian orogeny is a Neoproterozoic contractional event recorded in rocks of northern and eastern Baltica, spanning about 3000 km from the Ural Mountains of Kazakhstan to the Varanger Peninsula of northern Norway (Fig. 2; e.g. Gee and Pease, 2004 and references

therein). Timing of the Timanian orogen spans 800 - 550 Ma with igneous zircon from northeastern Baltica dated to ~555 Ma, ~620 Ma, and ~670 Ma by Gee et al., (1995). Remizov and Pease (2004) also defined Neoproterozoic cooling ages from a zircon bearing gabbro-norite, in concert with the ages from Gee et al., (1995). Major element, trace (including rare earth) element, and isotope (Rb-Sr and Sm-Nd) geochemistry from the basement of the Pechora Basin (NW Russia) indicate that at least portions of the Timanian system are related to a juvenile island arc, indicating that subduction related arc magmatism occurred along northeastern Baltica in the Neoproterozoic (Dovzhikova et al., 2004). In northernmost Norway, on the Varanger Peninsula, rocks of the Timanides are juxtaposed against those derived from the Caledonian orogen, indicating that a suture exists between Timanian and Caledonian rocks in the Arctic (Fig. 2; e.g. Gee and Pease, 2004). The Timanides and Caledonides are both important in the context of this study because we recognize Timanian and Caledonian age detritus in Alaskan rocks of the central Brooks Range (section 4).

3.4 The Doonerak fenster: location and basic relationships

The Doonerak fenster is a NE-SW trending doubly plunging antiform that exposes deep structural levels of the Brooks Range (Fig. 3, 5, 6, & 7; Dutro et al., 1976; Mull et al., 1987; Oldow et al., 1984). The fenster lies in the central part of the Brookian orogen below the basal detachment of the Endicott Mountains allochthon, the Amawk Thrust. The Endicott Mountains allochthon is a package of imbricated thrust sheets composed of Upper Devonian to Triassic siliciclastic and carbonate rocks, which are juxtaposed above Doonerak as a foreland dipping duplex (Fig. 6 & 7; e.g. Dutro et al., 1976, 1984a; Moore et al., 1994).

The polydeformed metamorphic core of the Brooks Range lies to the south of the Doonerak fenster, while the mildly deformed foreland thrust belt lies to its north (Fig. 7; e.g. Moore et al., 1994, 2015). Within this larger framework, the Doonerak area lies between the hinterland and foreland portions of the Brookian orogen (Fig. 3). Although the rocks at the core of the Doonerak fenster are Lower-to-Mid Paleozoic in age (Apoon Assemblage, Kekiktuk Conglomerate, Kayak Shale, Lisburne Limestone) and are overlain by allochthonous rocks also of Paleozoic age (Beaucoup Formation, Hunt Fork Shale, ect.) these two packages were not juxtaposed against each other until the Jurassic-Cretaceous Brookian orogeny. The modern antiform could have formed as recently as the Oligocene based on denudation and uplift calculated from apatite fission track data collected within the Doonerak fenster (O'Sullivan et al., 1998).

In the North Slope subsurface and northeastern Brooks Range portions of Arctic Alaska deformed lower Paleozoic and Proterozoic basement rocks similar to the Franklinian Sequence (e.g. Lerand, 1973; Carter and Laufeld, 1975) are separated from the overlying Ellesmerian Sequence by a regionally recognizable angular unconformity (Lerand, 1973; Grantz and May, 1983). In the northeast Brooks Range, the pre-Mississippian unconformity separates the Middle Devonian Ulungarat Formation from the Kekiktuk Conglomerate of the Ellesmerian Sequence (Fig. 4). Regionally, the pre-Mississippian unconformity likely formed following cessation of the Devonian Ellesmerian (or Romanzof) orogeny (Churkin, 1969, 1975; Brosgé et al., 1962; Reed, 1968; Dutro, 1970; Sable, 1977; Oldow et al., 1987a&b; Moore et al., 1994; Lane, 2007). The lower Paleozoic volcanic and volcaniclastic rocks in the interior of the Doonerak fenster, in the central Brooks Range, are known as the Apoon assemblage (next section) and are also interpreted as structural basement of the Brookian fold-thrust belt despite their modest

metamorphic grade (Fig. 5 and 7; Dutro et al., 1976, 1984a&b; Armstrong et al., 1976; Dillon et al., 1986; Mull, 1982; Mull et al., 1987; Oldow et al., 1987). The basement of the North Slope subsurface and northeast Brooks Range are both different than the rocks of the Apoon assemblage, but all three are overlain by an unconformity which separates basement rocks from the Ellesmerian Sequence of passive margin siliciclastics and carbonates (Moore et al., 1994 and references therein).

3.5 The Apoon Assemblage - Lower Paleozoic volcanic rocks

The Apoon assemblage of the Doonerak fenster consists of the lower Paleozoic "basement" rocks below the Amawk Thrust (Fig. 5 & 7), including volcanic and volcaniclastic rocks. The assemblage is subdivided into four poorly constrained lithologic units (Fig. 6 and 7): (1) a ~500 m thick unit dominated by volcanic rocks including basaltic lava and lapilli tuff mixed with pyroclastic breccia and rare phyllites - Pza , (2) a 1500 m thick mixed clastic unit of meta-argillite, phyllite, and siltstone interbedded with coarser lithologies of volcanic lithic sandstone, pebbly mudstone, and conglomerate - Pzc, (3) a highly variable ~400 m thick volcaniclastic unit containing basaltic lava flows, interbedded tuff, and litharenite with rare phyllite and argillite - Pzv, and (4) a ~3000 m thick mixed slate and phyllitic unit with occasional carbonates and thin isolated lenses of aphanitic greenstone - Pzp (Julian, 1989; Julian and Oldow, 1998). All of the Apoon rocks are strongly deformed and have experienced low grade metamorphism. The true stratigraphic thickness of the Apoon assemblage is very poorly constrained due to significant isoclinal folding and structural thickening - thicknesses above are approximate structural thicknesses based on mapping in the northeastern part of the fenster (Julian and Oldow, 1998).

Until recently, geochronologic constraints on the age of the Apoon assemblage were limited to six hornblende K-Ar and $^{40}Ar/^{39}Ar$ cooling ages from dikes and sills that range from ~520 - 373 Ma and exist in two primary groupings at ~380 Ma and ~470 Ma (Fig. 6; Dutro et al., 1976). Significantly, Strauss et al. (2017) conducted U-Pb SHRIMP-RG and Lu-Hf isotopic analysis on igneous zircon from a leucogabbro found in the Pzv section of the Apoon assemblage. This analysis yielded a $^{206}Pb/^{238}U$ age of 462 ± 8 Ma, in agreement with the ~470 Ma ages from hornblende by Dutro et al. (1976). Detrital zircons from the Apoon assemblage analyzed using LA-ICPMS methods yielded age groups of ca. 490 - 420, 540 - 520, 1250 - 960, 1500 - 1380, 1945 - 1750, and 2830 - 2650 Ma, with Lu - Hf data from the ~490 - 420 population indicative of juvenile crust and a distinct lack of crustal assimilation during presumed Ordovician-Silurian arc magmatism (Strauss et al., 2017).

A few sporadically located paleontological collections (Fig. 6; locations 1 - 4) also provide constraints on the age of the Apoon assemblage: (1) Middle Ordovician conodonts from siliceous volcaniclastics, probably of Pzv and Lower Silurian (Llandoverian) graptolites and conodonts presumably from Pzc identified by Repetski et al. (1987), (2) Silurian graptolites from Pzc near Amawk Mountain identified by Moore and Churkin (1984), and (3) early-middle Cambrian trilobites of Siberian affinity as well as proto-conodonts, hyolithids, and acrotretid brachiopods identified by Moore et al. (1984), probably from Pzp (Figure 3; also see Supplementary Materials section for a summary of age constraints). The ages and structural relationships between different subunits within the Apoon assemblage are not well defined and could benefit from detailed stratigraphic analysis. The oldest of Doonerak's fossils, early Cambrian trilobites of Siberian affinity, occur exclusively in the western portions of the fenster

(Moore et al., 1984), but the effects of structural thickening and the full suite of lithologies present in not well known.

Limited geochemical data from igneous rocks of the Apoon assemblage indicate compositions consistent with a magmatic arc complex and show similarities to the chemistry of volcanic rocks in the northeastern Brooks Range (Julian and Oldow, 1998; Moore et al., 1997; Moore, 1987). Despite some alteration, analyses from Pza and Pzv both show compositional overlap between major and trace element geochemical fields associated with calc-alkaline basalts, island-arc thoeliites, and mid-ocean ridge basalts (MORBs; Julian and Oldow, 1998; Moore, 1987; Julian 1989; Moore et al., 1997). These previous geochemical arguments by Julian and Oldow (1998) provide a good starting point for assessing the tectonic setting of the Apoon assemblage. Previous studies only considered a handful of trace element ratios and did not incorporate rare earth element trends or a sufficient diversity of trace elements, which are resistant to alteration by hydrothermal and metamorphic processes (Julian and Oldow, 1998; Moore et al., 1997; Moore, 1987). The detailed structure within the fenster and age relationships between these different igneous rocks are currently only known at a general level, which prevents determining if the variability within the geochemistry of these samples is the product of a genetically related series of melts or multiple distinct magma series.

Several important geologic features coexist within the Doonerak fenster: (1) Siberian fossils in the westernmost part of the fenster with (2) stratigraphic relationships indicative of Laurentian origin in the eastern part of the fenster – the sub-Mississippian unconformity overlain by the Ellesmerian Sequence as seen in the North Slope subsurface and (3) the presence of a wide range of potentially arc-related Early Paleozoic volcanic rocks within the Apoon assemblage. These data suggest that the Apoon assemblage of the Doonerak fenster could

represent an early Paleozoic magmatic arc succession based on limited lithological, geochemical, geochronological, and paleontological data, but its tectonic setting and full significance relative to the regional context of Arctic Alaska is unclear (Dutro et al., 1976; Moore, 1987; Julian, 1989; Julian and Oldow, 1998; Strauss et al., 2017). Previous workers have shown that the Doonerak area is a structural window (fenster) which exposes deep levels of the Brooks Range and that the Apoon assemblage is unlike other exposures in the central Brooks Range (e.g. Dutro et al., 1979; Moore et al., 1994; Moore et al., 1997). Limited geochemical data are inconclusive, but suggest that the Apoon assemblage may have formed in a subduction zone (Julian and Oldow, 1998; Moore et al., 1997). As such, the Doonerak fenster may delineate the boundary/suture between Laurentian and non-Laurentian rocks in Arctic Alaska, but more data is needed to address this hypothesis. Basic structural relationships, the general diversity of various map units, the textural and compositional diversity of the Apoon volcanics, and the provenance of various siliciclastic units all remain poorly constrained and are addressed in this study.

4. METHODS

4.1 Methodological goals

The goal of this study is to provide evidence which can be used to determine the tectonic setting of the Apoon assemblage of the Doonerak fenster and to better understand the relationship of the units exposed in Doonerak fenster to the rocks structurally emplaced above it, the Endicott Mountains allochthon. In order to do so, we constrained the age and provenance of detrital rocks from both above and below the basal detachment of the Endicott Mountains allochthon, the Amawk thrust, using U-Pb detrital zircon geochronology applied to the Apoon

assemblage, Ellesmerian Sequence and Endicott Group. Whole rock major and trace element geochemistry are used to define the tectonic setting in which the Apoon assemblage formed.

Fieldwork was conducted along the North Fork Koyukuk River, a throughgoing stream which passes through both the Endicott Mountains and the Doonerak Fenster. Fieldwork focused on an area which is approximately 17 km x 8.5 km centered on the North Fork Koyukuk River within the Gates of the Arctic National Park (Fig. 8). The following sections present data primarily focused on six sandstone samples collected for detrital zircon analysis and eleven igneous samples collected for geochemical analysis. The Supplementary Materials section of this document contains a table with a full list of all samples collected, basic descriptions and collection locations.

4.2 U-Pb Detrital Zircon Geochronology

U-Pb detrital zircon geochronology is a common tool for understanding the provenance and depositional age of sedimentary rocks (e.g. Dickinson and Gehrels, 2003; DeGraaf-Surpless et al., 2002; see review by Gehrels, 2014). Because zircon is mechanically and chemically resistant to breakdown it is commonly incorporated as a minor constituent in clastic sedimentary rocks. Dating zircons from a sedimentary rock provides information about that rock's depositional age and provenance. This can be achieved by comparing the ages calculated from detrital zircon within the rock in question to the ages of potential source regions that may have contributed primary igneous or metamorphic zircon grains as detritus. The U-Pb method is capable of capitalizing on three separate, yet related, radioactive geochronometers ($^{238}U \rightarrow {}^{206}Pb$, $t_{1/2}$ ~ 4.47 Ga; $^{235}U \rightarrow {}^{207}Pb$, $t_{1/2}$ ~ 0.70 Ga; $^{233}Th \rightarrow {}^{208}Pb$, $t_{1/2}$ ~14.01 Ga; Jaffey et al., 1971).

There are several analytical methods for measuring the abundance of various U, Th, and Pb isotopes within a zircon grain. Laser ablation-inductively coupled plasma-mass spectrometry (LA-ICP-MS) is commonly used to analyze large suites of zircon grains from sedimentary rocks because it is rapid, cost effective, and maintains precision and accuracy of 1-2% (e.g. Gehrels, 2014; Košler et al., 2013). This method uses a laser beam to ablate zircon material from a polished sample of zircon grains, extracted from the rock in question. The ablated material is fed into a stream of gas which flows into a mass spectrometer, where isotope analysis is conducted (e.g. Fryer et al., 1993; Košler et al., 2001; Košler and Sylvester, 2003). Zircon grains of a precisely known age (calculated by ID-TIMS) are used as standards and are periodically analyzed alongside unknown grains from the rock of interest in order to correct for downhole fractionation. $^{206}Pb/^{238}U$ ratios can be affected by fractionation during sample ablation. This periodic analysis of standard and unknown grains is referred to as standard-sample bracketing (e.g. review by Gehrels, 2014). Isotope ratios can then be used to calculate an age for each ablated zircon from the rock in question. The analyzed zircon grains are treated as a representative sample of the total population of detrital zircons within the rock of interest. Ideally, approximately one hundred to three hundred unknow zircon grains should be analyzed from each sample to allow for robust statistical treatment; however, it is common to report analyses with as few as 80 successful ages (e.g. review by Gehrels, 2014).

Six samples of sandstone from the vicinity of the Doonerak fenster in the central Brooks Range (both from the fenster itself and the overlying allochthonous package) were analyzed for U-Pb detrital zircon geochronology by LA-ICP-MS at the University of South Carolina's Center for Elemental Mass Spectrometry (CEMS). Each sample consisted of approximately 0.5 - 1.0 kg of rock collected from single beds. The coarsest fractions were

targeted because they have a greater likelihood of containing abundant usable zircon. Care was taken to avoid veins, weathering rinds and other potential sources of alteration or contamination. Processing of the raw data generated by the mass spectrometer during LA-ICP-MS analysis was conducted using the *UPbGeochronology3* data reduction scheme of the Iolite v.3 software suite (Paton et al., 2010) within the IgorPro data and computation package. Individual ages were then filtered based on the concordance, $^{206}Pb/^{207}Pb$ and $^{206}Pb/^{238}U$ ratios, total U and Th concentrations, and the degree of uncertainty in the resulting calculated ages. Concordance refers to the level of agreement between the $^{207}Pb/^{235}U$ and $^{206}Pb/^{238}U$ ages calculated from a single grain. A concordance filter of 85% and a reverse concordance filter of 105% was used as the acceptable cutoff, typical of detrital applications (e.g. Gehrels, 2014). The Sri Lanka (SL) zircon standard was used as the primary reference material for all analyses presented in this study (TIMS age = 563.5 ± 2.3 Ma, 2σ; 518 ppm U, 68 ppm Th, $^{206}Pb/^{204}Pb$ = 18000; Gehrels et al., 2008). The zircon standard 91500 (ID-TIMS age = 1065 ± 5 Ma; Wiedenbeck et al., 1995) was used as the secondary reference material. For consistency and comparability all ages reported are based on the reduction scheme using SL as the primary reference material. During analysis, both reference materials were analyzed following ablation of every five unknowns.

The resulting filtered data is presented herein as normalized age-probability density plots which were created using the program *IsoPlot v.3*. Individual sample information, full geochronologic data tables, procedures for sample collection, preparation, interpretation, U-Pb concordia diagrams (Wetherill, 1956), and accompanying descriptions for each sample are provided in the Supplementary Materials section of this document. The entire U-Pb data collection and processing procedure was conducted under the advisement of Dr. David Barbeau from the University of South Carolina.

4.3 Whole Rock Volcanic Geochemistry

Magmas contain distinctive trace element compositions which can be used to differentiate between basalts erupted from different tectonic settings (e.g. Pearce, 1983). More specifically, the characteristic enrichments and depletions of trace elements within these magmas can be used to provide clues to identify the source and processes responsible for magma formation. For instance, enrichment in large ion lithophile elements (LILEs; e.g. Cs, Rb, K, Ba, Pb, Sr, Th) and depletion of high field strength elements (HFSEs; e.g. Nb, Zr, Ti, Ta, P) in arc basalts are the result of metasomatic processes between the subducting lithospheric slab and the overlying mantle wedge and are highly indicative are arc-related tectonic settings (e.g. Tatsumi, 2005). Similarly, the systematic chemical behavior of rare earth elements (REEs) makes them a highly effective tool for determining the tectonic setting in which mafic to intermediate igneous rocks may have formed and the various petrogenic and alteration processes that may have affected them (e.g. Hanson, 1980; Pearce and Cann, 1973; Winchester and Floyd, 1977; Bacon et al., 1997; and many others). REE cations systematically decrease in size with increasing atomic number (from La to Lu) the distribution coefficients and partitioning behavior of REEs, a product of charge and size of an ion relative to crystal lattice sites, also vary systematically (e.g. Blundy and Wood, 1994; Hanson, 1980; Davidson et al., 2013). As such, petrogenetic processes (i.e. partial melting, fractional crystallization, melt mixing) affect REE patterns based on systematically variable properties dictated by variations in ionic radius and the abundance of particular mineral phases capable of incorporating REEs into their structure.

Eleven samples of igneous rock from the Apoon Assemblage of the Doonerak fenster were analyzed for whole rock major, trace, and REE geochemical abundances. Samples were

prepared and powered in the rock preparation laboratory at West Virginia University using standard practices and analyzed by a professional commercial laboratory (Activation Laboratories, Ontario, CA - Analysis type: Whole Rock Analysis + ICP 4 Lithoresearch QUANT). Care was taken to avoid weathering rinds and obviously altered rock surfaces. All samples were treated with an aggressive fusion technique and then digested in an acid solution, which is required to totally dissolve the entire sample and adequately assess major oxides, refractory minerals, REEs, and other high field strength elements. Analysis was conducted by ICP-OES and ICP-MS. A full table of results, detection limits, and individual sample descriptions is provided in the Supplementary Materials section of this document.

This work expands on that of Moore (1987), who compared the Apoon volcanics to volcanic rocks of the northeast Brooks Range, and Julian and Oldow (1998), who suggested that the lithogeochemistry of rocks in the northeastern part of the Doonerak fenster was indicative of a magmatic arc complex along an active continental margin. Several of the basalt discrimination diagrams used by Julian and Oldow (1998) are presented alongside the new data from this study in order to allow for direct comparison. Neither previous study considered the full suite of trace and REE trends presented herein. The new REE data presented in this study is also presented alongside representative data from global databases to aid in the comparison of geochemical trends. The N-MORB, E-MORB, OIB, and depleted mantle chemistry of Sun and McDonough (1989), Salters and Stracke (2004), and McDonough and Sun (1995) respectively is provided to aid in comparison and qualitatively compare different source regions. Focus is given to variation (spider) diagrams of trace and REEs because rocks of the Apoon assemblage have experienced hydrothermal and/or low grade metamorphic conditions, which complicate the interpretation of trends based on major elements or those based on other fluid mobile elements. Trace elements,

particularly REEs, are relatively immobile under hydrothermal and low grade metamorphic conditions, making them a more reliable means to assess these particular rocks (e.g. McLennan, 1989). The primary goal of these geochemical analyses is to define the likely tectonic setting in which the Apoon rocks formed.

5. RESULTS

5.1 Field Relationships, sample collection, and lithologic characteristics

Figure 8 provides an updated geologic map of the area containing the locations of samples analyzed for whole rock geochemistry and detrital zircon geochronology. Note that most samples and field data come from an area which is approximately 17 km x 8.5 km and focused around the North Fork Koyukuk River; however, one sample (J1415) was provided by J. Strauss northeast of all the other samples. The field relationships mapped in direct proximity to that sample come from their observations and mapping (see Strauss et al., 2017). The nomenclature on this map generally follows that of Julian and Oldow (1998) and Strauss et al. (2017). Some contacts and structures are inferred from aerial and satellite imagery. Some contacts are projected onto this map from the east where Strauss et al. (2017) conducted field work.

One of the most important field relationships observed during the 2015 field season along the North Fork of the Koyukuk River was confirmation of the presence of the sub-Mississippian unconformity between rocks of the Ellesmerian Sequence and rocks of the Apoon assemblage within the Doonerak fenster (below the Amawk thrust). Along the North Fork of the Koyukuk River east of its confluence with Ernie Creek the river's flow direction changes from E-W to N-S. Just upstream of that bend in the river, rocks of the Lisburne Limestone are easily visible at

the field scale as a dip slope on the south side of the river valley. Figure 10 provides an annotated field photo with a view to the east along this strategic portion of the North Fork of the Koyukuk River. To the north (left) side of the image, rocks of the Devonian Hunt Fork formation (Endicott Mountains allochthon) are exposed among rolling tan-gray hills. This is the approximate location of sample 26DF15, which was collected for detrital zircon geochronology (next section). The south (right) side of the image shows the Ellesmerian Sequence, including the Lisburne Limestone and Kayak Shale (Doonerak Fenster), and the Ordovician to Silurian age rocks of the Apoon assemblage. This is the approximate location of sample 23DF15 (Kayak fm), which was also collected for detrital zircon analysis (next section). At this location, the Kayak Shale sits unconformably atop the Apoon assemblage. Elsewhere within the fenster, the Kekiktuk Conglomerate, stratigraphically below the Kayak Shale (see Fig. 4 & 5), is described as resting in direct unconformable contact with the Apoon assemblage (e.g. Dutro et al., 1976; Julian, 1989; Strauss et al., 2017). This implies some variation along strike of this important contact. That variability has not been acknowledged previously and is different from what is observed in the northeast Brooks Range and North Slope subsurface. The abrupt craggy edifices making resistant peaks to the right (south) side of the image are composed of the Apoon igneous rocks (Fig. 10).

Stereographic projections of poles to the dominant foliation, S_1, of various outcrops are provided in Figure 11 (A - D), which is organized based on lithology. Interior to the fenster, rocks of the Kayak Shale and Lisburne Limestone (Ellesmerian Sequence in Fig. 11 - C) have poles to bedding, S_0, that indicate planes which dip consistently to the north and northwest; however the underlying rocks of the Apoon assemblage do not follow the same orientation (Fig. 11 - D). The attitude of the Apoon units is significantly more variable. Immediately south of the

sub-Mississippian unconformity, the Apoon units dip to the south opposite those of the Ellesmerian Sequence. Yet, in close proximity the same units strike north-south and dip to the west (see Fig. 8). The relationship and angle between cleavage and bedding (where both were identified) did not remain consistent throughout the area, being near parallel to each other in some places and at a steep angle to each other in others, indicating that the primary bedding planes are folded. Rocks of the Hunt Fork Formation (northern portions of Fig. 8) generally dip to the west and northwest with rare southward dipping structures (Fig. 11 - A). The underlying Beaucoup Formation, which occupies the hanging wall of the Amawk Thrust, contains chaotically organized fabrics (Fig. 11 - B), but generally mimic the orientation of the overlying Hunt Fork Shale.

Some structural features observed in the field exist below the scale of the map in Figure 8 and are not immediately apparent from the aggregated structural data (Fig. 11 A - D). Specifically, two upright, open outcrop scale anticlines were observed along the west side of the North Fork Koyukuk River, north of Frigid Crags and south of Shushalch Creek, near sample location 43 in Figure 8. Both folds were observed within the Beaucoup Formation in the hanging wall of the Amawk thrust, about 2.5 km from each other (Fig. 12). It was clear that these two anticlines deformed bedding because the lithologies at their centers differed from those at their edges. The axial planes of each of these folds strike approximately east-west or northeast-southwest (Fig. 12) and dip to the south or southeast, broadly similar to Brookian deformational trends regionally.

The Apoon assemblage contains a diversity of complex structures and lithologies that are easily recognized at the outcrop scale. There are multiple field examples of the internal complexity of the Apoon assemblage, both lithologically and structurally (Fig. 13). Small folds

deforming bedding in multiple orientations, folds superimposed over a preexisting cleavage, and various brittle structures (i.e. small faults and joints) suggest that the Apoon Assemblage experienced multiple episodes of deformation, some of which likely predate that observed within the Endicott Mountains allochthon (the Brookian structures). Along Pyramid Creek (Fig. 8), small scale (0.5 m wide) isoclinally folded beds of sandstone are exposed on the ground along a pavement outcrop (Fig. 13 - A). These small folds bend gray slate and 3 - 10 cm thick sandy beds. They have approximately vertical axial planes parallel to the dominant cleavage, angular hinges, and are crosscut by occasional northwest dipping dolomitic veins. This is markedly different from the broad, nearly upright, open folds seen further up the Pyramid creek drainage (Fig. 13 - C). This other set includes folds that deform a pre-existing foliation within units of mostly slate. The folds are approximately 2 - 10 m wide with rounded hinges and a gentle plunge to the northwest (Fig. 13 - C). South of Pyramid Creek (Fig. 8) an en echelon array of veins define a small normal fault zone separating tuff from slate within the Apoon assemblage (Fig. 13 - B). The clastic portions of the Apoon assemblage (Fig. 13 - D, E, and F) are widely variable lithologiocally and include slates, tuffs, sandstones, and phyllites.

The volcanic/igneous rocks of the Apoon assemblage show a wide variety of textures and field relationships (Fig. 14 A - F). Some clearly intrusive contacts were observed along Pyramid Creek (Fig. 14 - A and B) where sills of andesite, crosscut by veins of quartz and calcite, intruded the gray slates and sandstones of the Apoon clastics (Pzc). South along Boreal Mountain, a large igneous edifice deflects the surrounding phyllitic rocks and contains basaltic-andesite with large laths of plagioclase visible to the unaided eye (Fig. 14 - D). In contrast, the region north of Pyramid Creek is dominated by fine grained basaltic greenstone and only minor slates and clastics (Fig. 14 - F). Along Bombardment Creek, basaltic pillows form a massive (15

- 20 m tall) cliff (Fig. 14 - C). The same area contains out-of-place blocks of brecciated greenstone, which resembles a flow top igneous breccia (Fig. 14 - E).

The downstream portions of Bombardment Creek transect the Ellesmerian Sequence and expose gently folded limestone beds among the Kayak Shale and massive beautifully folded gray Lisburne Limestone high above the creek (Fig. 15). Rare crinoids were observed within the Kayak Shale (Fig. 15 - B). North of Pyramid Creek, along strike of Bombardment Creek, the Lisburne Limestone forms a massive slope south of the North Fork Koyukuk River and exposed bone gray micritic limestone with large black chert nodules (Fig. 15 - C and D).

In the northernmost part of the map area (Fig. 8), the Devonian Hunt Fork Shale outcrops among rolling tan-gray hills north of the North Fork Koyukuk River (Fig. 16). In this area the Hunt Fork dips consistently to the north and northwest; however older published maps suggest that its attitude changes to southeastward dipping strata just north of this study area (Fig 8; Dillon et al., 1986). At the outcrop scale, the Hunt Fork contains tan to brown-black shale and slate interbedded with brown fine grained sandstone and quartzite as well as rare lenses of brown limestone (Fig. 16 - C and D). To the west of the confluence between Ernie Creek and the North Fork Koyukuk River and to south of Shushalluk Creek, the Hunt Fork passes conformably up section into the Noatak Sandstone and Kanayut Conglomerate (Fig. 16 -A and B). The Noatak Sandstone was poorly expressed within a mostly covered interval; however the overlying Kanayut Conglomerate was present as a massive quartz-chert pebble conglomerate within interbedded sandstones (Fig 16 - A). Aerial and satellite imagery was used to supplement field observations and produce the contact relationship seen in Figure 8. This is the approximate location of sample 41DF15 (Kanayut Conglomerate), which was collected for detrital zircon analysis (next section).

The following section contains observations and data from samples collected for detrital geochronology and whole rock major and trace element geochemistry. These data are presented within Figures 17 - 22. All analyzed sample information is presented within the supplementary materials along with information on other samples collected, but not analyzed, during this study. This document focus on samples used for detrital zircon geochronology (six samples) and whole rock volcanic geochemistry (eleven samples), other samples (45 in total) are appropriate for other analyses. These may include assessment of deformational fabrics, Ar-Ar dating of detrital and potentially authigenic white mica along cleavage planes, and laser raman spectroscopy of carbonaceous material (forthcoming thesis by Greg Hammond will address estimates of maximum paleotemperature based on this technique). All samples could benefit from more detailed petrographic analysis, as this was only conducted on a preliminary basis for most samples in the course of the current project.

5.2 Detrital Zircon Geochronology

Six clastic samples (Figs. 8) were collected from the vicinity of the North Fork Koyukuk River in the Gates of the Arctic National Park, AK for laser ablation analysis and detrital zircon geochronology. Samples presented here are organized based on their sampling locations and respective formations. For instance, samples 05DF15 and 23DF15 (Fig. 8) represent the Apoon Assemblage and Kayak Formation respectively. These two samples come from the interior of the Doonerak fenster, definitively below the Amawk thrust. Samples 43DF15 and J1415 (Fig. 8) represent the Beaucoup Formation and come from the complicated northern margin of the fenster, where field relationships and contacts are difficult to decipher and there may be complication by faulted slivers of Apoon, EMA, and/or Hammond Terrane rocks. Samples

41DF15 and 26DF15 (Fig. 8) represent the Hunt Fork Shale and Kanayut Conglomerate respectively and come from the Endicott Mountains allochthon, north of and definitively above the Amawk thrust. The following sections contain details regarding the detrital zircon geochronology of the samples outlined above. All geochronologic data presented in Figures 18-23 and Figures 29-32 contain U-Pb analyses that have met the necessary filtering conditions outlined in the methods section based on concordance and abundance of various U, Th, and Pb isotopes and isotope ratios (e.g. Gehrels, 2014; more details provided in the Supplemental Materials section).

Fenster Interior: Apoon Assemblage and Kayak Shale

Sample 05DF15 is an impure lithic sandstone collected from the Apoon assemblage along a ridge south of Pyramid Creek and to the east of the North Fork Koyukuk River (Fig. 8; 67.861869 N, -150.787034 W). In hand sample and thin section it is poorly sorted and contains subrounded grains of quartz and K-feldspar, masses of microcrystalline quartz, minor chert fragments, and angular volcanic lithic fragments with clasts reaching an approximate maximum size of 0.6 mm (Fig. 17 - A and B). Detrital zircon spectra from 05DF15 (Fig. 18) are based on 96 successful zircon analyses. The maximum depositional age for 05DF15, calculated as a weighted mean of the six youngest zircon grains that fall within error of each other, is 452 ± 13 Ma (MSWD = 0.76). Probability density plots from sample 05DF15 (Fig. 18) show a dominant unimodal peak centered on 504 Ma. Other minor detrital populations are present at 601, 764, 1153 - 1370, 1455 - 1565, 1764 - 1942, 2308, 2500 - 2624, and 2683 - 2875 Ma.

Sample 23DF15 is a sandstone of the Ellesmerian sequence (Kayak Fm.), which was collected from the south side of the North Fork Koyukuk River between its confluence with Ernie Creek and Bombardment Creek (Fig. 8; 67.907896 N, -150.752165 W). It is a moderately sorted sandstone (Fig. 17 - E and F) containing subrounded to angular monocrystalline and polycrystalline quartz grains, with some grains showing undulose, or wavy, extinction within a fine dark matrix. It also sporadically contains throughgoing bands of mica which appear to define cleavage planes and extend along the boundary of some grains (Fig. 17 - F). Detrital spectra from 23DF15 (Fig. 19) are based on 108 successful zircon analyses. The maximum depositional age for 23DF15, calculated as a weighted mean of the six youngest zircon grains that fall within error of each other, is 385.6 ± 8.9 Ma (MSWD = 0.70). Probability density plots from sample 23DF15 (Fig. 19) show a dominant polymodal peak centered on 405 and 441 Ma. Other detrital populations are present at 573, 773, 931, 980 - 1250, 1310 - 1470, 1710 - 2160, 2260 - 2410, and 2460 - 2660 Ma.

Fenster Margin: Beaucoup Formation

Sample J1415 is a lithic/conglomeratic sandstone of the Beaucoup Formation, which was collected from an area approximately 10 miles east of the other samples. It was collected by J. Strauss from the east side of the North Fork Koyukuk River, north of the headwaters of Saint Patrick's Creek (Fig. 8; 67.938861 N, -150.427833 W). In hand sample, J1415 contained stretched grains of chert and quartz within a noticeable pervasive fabric. In thin section it contains many small thoroughgoing fractures and veins among subrounded clasts of quartz, plagioclase, with rare mica and opaques (Fig. 17 - I and J). Detrital zircon spectra from J1415

(Fig. 20) are based on 121 successful zircon analyses. The maximum depositional age for J1415, calculated as a weighted mean of the six youngest zircon grains that fall within error of each other, is 360.1 ± 7.4 Ma (MSWD = 0.117). Probability density plots from sample J1415 (Fig. 20) show a dominant unimodal peak centered around 426 Ma. Other detrital populations are present at 360, 507, 835 - 1000, 1203 - 1520, 1610 - 1924, 2373, 2475, 2601 - 2724, 2843, and 3179 - 3280 Ma.

Sample 43DF15 (Fig. 17 - G and H) is a slightly sheared lithic sandstone probably of the Beaucoup Formation (see discussion section), which was collected from the west banks of the North Fork Koyukuk River, south of the confluence with Ernie Creek (Fig. 8; 67.889526 N, -150.935793 W). This unit was mapped as part of the Hunt Fork formation in the field by Dillon et al., (1986) and rests near the Beaucoup - Hunt Fork contact, as drawn in this study. 43DF15 is a fine grained sandstone containing subrounded clasts of quartz and feldspar (Fig. 17 - G and H). It also contains obvious thoroughgoing bands of mica, partitioned onto cleavage planes. The sample was not collected oriented spatially, but grains appear to have rotated slightly within this pervasive banded framework, indicating some component of shear. Detrital zircon spectra from 43DF15 (Fig. 21) are based on 126 successful zircon analyses. The maximum depositional age for 43DF15, calculated as a weighted mean of the six youngest zircon grains that fall within error of each other, is 397.1 ± 6.4 Ma (MSWD = 0.17). A single anomalously young grain (340.4 ± 14 Ma) was not included in this calculation because it does not fall within error of the other youngest grains. Despite careful steps taken to avoid contamination, it is possible that this single grain is exotic to this sample. Therefore, no interpretations were made based on the age of this single grain. It is presented here and within the data tables because there was no impartial means by which to exclude it based on concordance, isotope ratios, or isotope abundances. Probability

density plots from sample 43DF15 show a dominant unimodal peak centered around 420 Ma. Other detrital populations are present at 506, 548, 646, 702, 875, 995-1240, 1600-1830, and 2760 Ma.

Endicott Mountains Allochthon: Hunt Fork and Kanayut Formations

Sample 26DF15 (Fig. 17 - C and D) is a sandstone of the Hunt Fork formation, which was collected from the north side of the North Fork Koyukuk River between its confluence with Ernie Creek and Bombardment Creek (Fig. 8; 67.933120 N, -150.778276 W). Sample 26DF15 was collected from a sandy fraction interbedded among the tan-gray shales/slates of the Hunt Fork. It is a fine grained sandstone containing rounded and subrounded grains of quartz, potassium feldspar, plagioclase, and opaques (Fig. 17 - C and D). Detrital zircon spectra from 26DF15 (Fig. 22) are based on 86 successful zircon analyses. The maximum depositional age for 26DF15, calculated as a weighted mean of the six youngest zircon grains that fall within error of each other, is 372 ± 12 Ma (MSWD = 0.17; Fig. 22). Probability density plots from sample 26DF15 (Fig. 21) show a dominant unimodal peak centered on 429 Ma. Other detrital populations are present at 372, 570, 630, 930 - 1100, 1240 - 1370, 1600 - 2175, and 2375 - 2730 Ma.

Sample 41DF15 is a lithic/conglomeratic sandstone of the Kanayut Formation, which was collected upslope of Shusaluk Creek, to the northwest of the confluence between Ernie Creek and the North Fork Koyukuk River (Fig. 8; 67.918660 N, -150.929762 W). In the field it was collected from a large 10 m x 10 m bounder near the top of the slope. This was done because the

terrain became impassible, but large in place blocks of Kanayut were visible just upslope from where this sample was collected. It is a quartz and chert pebble rich conglomerate with some potassium feldspar and well-rounded clasts held within a sandy matrix (Fig. 16 - A). Detrital spectra from 41DF15 (Fig. 23) are based on 127 successful zircon analyses. The maximum depositional age for 41DF15, calculated as a weighted mean of the three youngest zircon grains that fall within error of each other, is 339 ± 17 Ma (MSWD = 0.19). Three anomalously young grains (shaded gray in Fig. 23) which did not fall within error of each other were not included in calculation of the maximum depositional age (265.2 ± 11 Ma, 283.9 ± 11 Ma, 305 ± 15 Ma). Probability density plots from sample 41DF15 (Fig. 23) show a dominant unimodal peak centered around 428 Ma. Other detrital populations are present at 339, 364, 600, 721, 960, 1120, 1800 - 2000, and 2510 Ma.

5.3 Whole Rock Volcanic Geochemistry

The geochemical trends of volcanic rocks can be used to provide information on the tectonic setting in which they formed (e.g. Pearce, 1983; Tatsumi, 2005). Eleven igneous rock samples from the Apoon assemblage were analyzed for major, trace, and rare-earth element (REE) compositions. The geochemical data presented here is the first to include REE abundances from the Apoon assemblage and complements the work of Julian and Oldow (1998).

Major element data from are shown in the Supplemental Materials section. Data reports from Activation Laboratories (Ontario, CA) are included as well as the loss on ignition (LOI), the volatile abundance driven off during sample fusion. All of the major element abundances were recalculated to 100% without volatiles (H_2O or CO_2) for all pertinent figures and calculations. This was done so that all major element plots compare samples on the same

anhydrous basis, but the raw data is given in the Supplementary Materials section. Not all samples from this study have geochemical compositions that are suitable for use in all of the geochemical plots (i.e. basalt discrimination diagrams were only applied to samples with suitable major element compositions). The samples that contained SiO_2 (wt %) and CaO + MgO (wt %) abundances which prevent them from being classified as basalts or basaltic-andesites by the system of Pearce and Cann (1973) were not included in the basalt discrimination diagrams, but they were included in trace and rare-earth element variation diagrams. These high silica samples include 03DF15 (59.32% SiO_2 norm.), 11DF15 (62.16% SiO_2 norm.), 13DF15 (57.91% SiO_2 norm.), and 33DF15 (60.51% SiO_2 norm.). Among these, sample 33DF15 was distinct due to its ophitic to subophitic texture in thin section and large laths of plagioclase, as such this sample could not be classified as a basalt. Because all samples have experienced hydrothermal alteration and low grade regional metamorphism, emphasis is given to trace and rare-earth element geochemical trends, which are typically less susceptible to alteration than the major elements. As such, fluid-mobile elements (e.g. LILE) are used with precaution.

For comparison, representative basalt samples are presented alongside geochemical analyses in all trace and REE geochemical plots. These include island arc basalts (IABs; Sun and McDonough, 1989), normal and enriched mid ocean ridge basalts (NMORBs and EMORBs; Sun and McDonough, 1989), and ocean island basalts (OIBs; Nye and Reid, 1984).

Basic Classification - Major Elements and Thin Sections

Figure 24 is a total alkali - silica diagram, comparing the abundance of SiO_2 (wt %) and CaO + MgO (wt %) after Le Maitre et al., (2002). The dotted line represents the boundary

between alkaline and subalkaline compositions. The fields marked by solid lines denote IUGS classification of volcanic rock type based on the comparison of these major elements. In general, the Apoon Assemblage contains a diverse suite of igneous rock compositions, spanning ~45 to 64 wt% SiO_2 (Fig. 24). All of the collected samples (n = 11) from the Apoon Assemblage are classified as subalkaline basalts, basaltic-andesites, and andesites. Although two samples plot within the trachy-andesite field, they are still classified as subalkaline.

The five low SiO_2 samples (e.g. ~45-52 wt% SiO_2; 01DF15, 08DF15, 25DF15, 32DF15, and 38DF15) are plotted together (Fig. 26A and 27A). Similarly, the moderate-to-high silica samples (e.g. ~55- 63 wt% SiO_2; 03DF15, 11DF15, 13DF15, 21DF15, 24DF15, and 33DF15), are grouped together in the subsequent variation diagrams (Fig. 26B and 27B). Comparing these classifications to the spatial distribution of these samples (Fig. 8), highlights no discernable trends related to location within the fenster. South of Pyramid Creek sporadic dikes and sills crosscut clastics, including lithic sandstones and phyllites. In areas north of Pyramid Creek, the clastics are less abundant and massive outcrops of flows and pillows are found along Bombardment Creek. These textural and lithologic variations are visible sample-to-sample but the range of major element compositions observed does not follow any discernible spatial or lithologic pattern.

The igneous rock samples of the Apoon assemblage show wide variability in their textures and mineralogical character, ranging from ophitic/subophitic (Fig. 25 - A and B) to glassy and mildly vesicular (Fig. 25 - G, H, I and J). A mild pock-marked, texture was found on some plagioclase laths within sample 33DF15 (Fig. 25 - A and B) is not concentrated on the edge of grains and appears to muddle grain interiors, possibly as a result of some process during crystallization (trapping fluids or gasses). The thin sections also provide some corroborating

evidence of hydrothermal alteration. Many samples (e.g. 38DF15 and 01DF15) showed partial to extensive replacement of plagioclase feldspar by carbonate. Birefringent carbonate was ubiquitous across multiple samples, an example of which is visible in Figure 25 C and D. The birefringent carbonate and replacement of plagioclase is direct evidence for the alteration of primary mineral phases and suggests that some geochemical trends, especially major element trends, may have been affected by secondary alteration. Because many of the Apoon Assemblage rocks show evidence of hydrothermal alteration, fluid-mobile elements (e.g. LILE) are used with caution. However, these elements, along with other fluid-immobile trace elements (HFSE and REE) are evaluated in the next section. Greater emphasis is placed on the HFSE and REE elements. These are viewed alongside the fluid-mobile elements (LILE) for completeness and to better characterize geochemical trends within the collected rocks.

Variation/Spider Diagrams - Trace and Rare Earth Element Trends

Figure 26 (Trace element; NMORB normalized) and Figure 27 (REE; chondrite normalized) are variation diagrams for the Apoon Assemblage whole rock geochemical samples, based on the normalization and plotting scheme of Sun and McDonough (1989). Each of these figures (Fig. 26 and 27) separates the five low SiO_2 samples (A - top frame) from the moderate to high SiO_2 samples (B -middle frame) and provides normal mid-ocean ridge basalt (NMORB), enriched mid-ocean ridge basalt (EMORB), ocean island basalt (OIB), and island arc basalt (IAB) chemistries (Sun and McDonough, 1989; Nye and Reid, 1986) for comparison (C - bottom frame). The raw geochemical data used to generate these variation diagrams is provided in the Supplementary Materials section of this document.

Rock/NMORB

The horizontal axes of Figure 26, the NMORB-normalized trace element variation diagram, lists a series of trace elements organized based on their compatibility within common mineral structures (compatibility increasing to the right). The low SiO_2 samples (01DF15, 08DF15, 25DF15, 32DF15, and 38DF15; Fig 26 A) show a range of chemical trends, but all show enrichment among large ion lithophile elements (LILEs - e.g. Cs, Rb, Ba, Th) with values ranging from 30 to 110 times the concentration found in a NMORB. Some low SiO_2 samples show depletion among the high field strength elements (HFSEs - e.g. Nb, P, Zr, Ti) particularly samples 01DF15, 32DF15, and 38DF15.

The high SiO_2 samples (Fig. 26 B) show some similar trends. All six high SiO_2 samples (~55- 63 wt% SiO_2) display a negative Nb anomaly, meaning the concentration of Nb is less than would be expected from the values of adjacent trace elements on the plot. This is accompanied by depletion among other HFSEs (Ti and Zr) in samples 03DF15, 11DF15, and 33DF15. The negative Nb anomaly is particularly prevalent in samples 03DF15, 11DF15, 13DF15, 21DF15, and 24DF15. Depletion of Rb, Nb, P, and Zr all occur within the IAB representative sample. Among the most compatible trace elements (Y, Yb, Lu), all eleven samples show nearly flat trace element patterns, similar to the patterns of NMORBs and EMORBS.

The NMORB-normalized chemistry of rocks from the Apoon assemblage show similarities to the patterns observed within island arc basalts (IABs) and mid-ocean ridge basalts (MORBs). Specifically, the high-silica Apoon Assemblage samples contains LILE enrichments and HFSE depletions similar to IAB patterns world-wide (Fig. 26; e.g 03DF15, 11DF15,

13DF15, 21DF15, 33DF15, 25DF15). Similarly, some of the low-silica Apoon samples display similarities to MORB trends (Fig. 26; e.g. 01DF15, 08DF15, 25DF15, 32DF15, 38DF15). These are characterized by flat-lying patterns in compatible trace elements in MORB-normalized plots (e.g. Nd, Sm, Eu, Dy, Yb, Lu). No samples showed significant similarity to OIB patterns on NMORB-normalized trace element plots.

Rock/Chondrite

Chondrite-normalized rare earth element (REEs) variation diagrams are a special subset of trace element variation diagrams which capitalize on the unique behavior of the Lanthanide series of elements (La -Lu). Because the Lanthanides systematically decrease in atomic radius with increasing atomic number (La → Lu), their partition coefficients and partitioning behavior in igneous systems also vary systematically. Similar to Figure 26, low SiO_2 samples are plotted in the top frame (Fig. 27 A) and followed by the high SiO_2 samples (Fig. 27 B) and representative basalt samples (the same used previously; Fig. 27 C). All composition are normalized to the composition of a normal chondritic meteorite based on the values of Sun and McDonough (1989). Light rare earth elements (LREEs) refers to La, Ce, Pr, Nd. Middle rare earth elements (MREEs) refers to Sm, Eu, Gd, Tb, Dy, and Ho. Heavy rare earth elements (HREEs) refers to Er, Tm, Tb, and Lu.

The chondrite normalized REE variation diagrams from the Apoon assemblage show a wide range of patterns. In general, the low SiO_2 samples display an array of LREE enrichments. Specifically, sample 01DF15 shows a clear enrichment in LREE abundances, while sample 08DF15 shows a dramatically lower LREE abundances. The other low SiO2 samples (e.g

25DF15, 32DF15, and 38F15) have relatively flat REE patterns with LREE to HREE (right side of Fig. 27) abundances approximately 20-30x chondrite. For example, sample 38DF15 shows near parity among the REEs, meaning the abundance of each REE is similar to the others when normalized to chondritic compositions generating a relatively flat pattern. Its pattern most closely resembles that of the EMORB, which has very mild enrichment among LREEs and approximant parity across the MREEs and HREEs.

The high SiO_2 samples all show enrichment of the LREEs relative to the MREEs and HREEs. The LREEs in these samples range from ~20 to ~110 times the amount expected in chondritic meteorites. All high SiO_2 samples show flat patterns among the HREEs, similar to the patterns of both NMORBs and EMORBs. Five samples show anomalously low concentrations of Eu as compared to its adjacent REEs (38DF15, 33DF15, 24DF15, and 13DF15), a feature commonly attributed to the fractionation of plagioclase (see Section 6; discussion). Two samples (03DF15, 11DF15) show LREE and MREE patterns which resemble the composition of OIBs, but they have considerably different HREE patterns compared to OIB. One difference is the slight positive Eu anomaly within the OIB sample, which is noticeably different from the minor negative Eu anomaly within 03DF15 and 11DF15. These samples show similarities to both OIBs and highly LREE enriched IABs. Three samples (13DF15, 21DF15, and 24DF15) show LREE and MREE patterns which most closely resemble the chemistry of IABs.

Ti - V ratios

The Ti-V diagram of Shervais (1982) capitalizes on variation in the behavior of Ti and V as a product of differences in their partition coefficients. Because V is found in both reduced (V

3+) and oxidized states (V 4+, and V 5+) within magmas and Ti is not (only exists as Ti 4+), the proportion of V:Ti can serve as a proxy for the oxygen activity and fractional crystallization processes, which took place in a magma at the time of eruption. Shervais (1982) related this to the tectonic environment of eruption. Because Ti and V are generally immobile under hydrothermal alteration and intermediate metamorphic conditions, this method allows determination of tectonic setting from ancient rocks.

Figure 28 shows the Ti - V diagram of Shervais (1982) with data from the Apoon assemblage superimposed. The gray area marks the field of data from Julian and Oldow (1998) for comparison. Samples from this study plot within the island arc tholeiite and back arc basin MORB fields, and show considerable compositional overlap with the data from Julian and Oldow (1998). Only those samples which classified as basalts and basaltic andesites were included in this figure because the complexities of more highly evolved magmas can affect the proportion of Ti and V by other means (as per Shervais, 1982).

6. DISCUSSION

6.1 Field Relations and Overview

The Apoon assemblage has been tentatively related to a volcanic arc setting for four decades based on sparse and incomplete data (Dutro et al., 1976; Mull et al., 1987; Julian, 1989; Julian and Oldow, 1998). The relative inaccessibility and complicated field relationships within the Doonerak fenster have prevented conclusive determination of the tectonic setting in which the Apoon assemblage formed. Only small portions of the fenster have been studied in any

appreciable detail and its stratigraphic and structural architecture is complex and difficult to decipher. One goal of this research was to provide evidence to help constrain the setting in which the Apoon assemblage formed and test the possibility that rocks exposed in the Doonerak fenster are the remnant of an island arc complex, which could be related to the suture between Laurentian and non-Laurentian portions of Arctic Alaska. We also aimed to better understand the provenance of the Apoon assemblage and Ellesmerian Sequence within the fenster relative to the rocks of the Endicott Mountains allochthon and Hammond subterrane, which structurally overlie the fenster within the Brooks Range. The data presented in section 5 provides new insight into the origins of these sequences and, when placed in the context of other recent regional studies, corroborates the interpretation that the Apoon assemblage is the remnant of an island arc complex. The new data also highlights significant outstanding issues concerning the structure and stratigraphy of the Apoon assemblage and some regional relationships.

The updated geologic map and cross section of the North Fork Koyukuk River along the northern margin of the Doonerak fenster in the central Brooks Range (Fig. 5, 8 and 9) make several alterations from previous interpretations. Some notable changes include (1) treatment of the Apoon igneous sequence, Pzv, as two different units - Pzv intrusives and Pzv flows, which are mapped collectively with Pza in keeping with Strauss et al. (2017), (2) the extension of Pzp, the Apoon phyllitic unit, to the east along strike of where it was mapped by Strauss et al. (2017) in the southernmost portions of the map area, (3) the presence of an inferred thrust fault in the southern region to accommodate juxtaposition of Pzp against Pzv intrusives and Pzc, the Apoon clastics, (4) the grouping of several small discontinuous map units of Brosge and Reiser (1960, 1971) and Dillon et al., (1986) into the Beaucoup Formation along the northern margin of the fenster in the hanging wall of the Awawk thrust, (5) the differentiation of the Kayak and

Lisburne Formations along the southern banks of the North Fork Koyukuk, and (6) extension of the Hunt Fork - Endicott Group contact south of Shushalluk Creek in the northwest portion of the map area based on recognition of the Noatak and Kanayuk formations in that location.

Data from six samples of sandstone analyzed for detrital zircon geochronology from the vicinity of the North Fork Koyukuk River in the Gates of the Arctic National Park are summarized in Figure 29. Placing this data into context requires consideration of potential source regions, which may have contributed primary igneous and metamorphic zircon grains as detritus and potential sources of recycled detrital grains. Detrital spectra from particular regional map units allows for comparison to data from the same formations elsewhere and comparison to regionally associated units from elsewhere in the circum-Arctic. Unpublished detrital geochronologic data from elsewhere in the central Brooks Range was provided by E. L. Miller (Stanford) and V. Pease (U. of Stockholm) for comparison to relatively proximal portions of the Brooks Range (Fig. 30). These data come from the John River, an area also within the Gates of the Arctic National Park, but about 50 km west of the North Fork Koyukuk River. The John River transect samples include some of the same stratigraphy, the Beaucoup and Hunt Fork formations, but come from the Endicott Mountains allochthon and Hammond subterrane and also contain the Sillyasheen formation of the Hammond subterrane. Other detrital zircon data from the Apoon assemblage, Ellesmerian Sequence, and Trembly Creek phyllite (Fig. 31) allow for direct comparison of map units in the vicinity of the North Fork Koyukuk, within the Doonerak fenster from Strauss et al. (2017). These provide the most direct comparison to associated strata from within and near the Doonerak fenster. Lastly, a suite of detrital spectra from elsewhere in the Arctic (Fig. 32; NE Brooks Range, Canadian Arctic, and Svalbard) allow for comparison of regional trends in provenance.

6.2 The Beaucoup and Hunt Fork Formations: Hanging wall of the Awawk Thrust

The Beaucoup Formation and Hunt Fork Shale are widespread Late Devonian units of conglomerate, shale, slate, sandstone, and siltstone that are ubiquitous across much of the Brooks Range (e.g. Tailleur et al., 1967; Dutro et al., 1979; Moore et al., 1994). Their heterogeneity in terms of lithostratigraphy and provenance, although recognized, is poorly defined. Along the northern margin of the Doonerak fenster near the North Fork Koyukuk River, discontinuous units of sandstone, sheared green-purple conglomerate, wacke, shale, and slate have been assigned to both of these units by previous mappers (Dillon et al., 1986; Brosge and Reiser, 1961 and 1971). Herein, we define the contact where the fissile gray-tan shales/slates of the Hunt Fork become the dominant lithology (Fig. 8). This ascribes the complicated package of interbedded and folded conglomerates, wacke and sandstones to the Beaucoup Formation. What is herein defined as the Beaucoup also includes the well-foliated, sheared green-purple quartz and chert pebble conglomerate found near the confluence of the North Fork Koyukuk River and Ernie Creek (Fig. 8 and 16; previous section).

Some previous workers have also suggested that these units along the northern margin of the Doonerak fenster might fit better into formations of the Hammond Terrane particularly the Trembley Creek phyllite, which is recognized along the southern margin of the fenster (Strauss et al., 2017) and could have continuity to its northern side; however that assertion is not well borne out in the new data. Samples 43DF15 and J1415 both come from this complicated border zone in the hanging wall of the Amawk thrust. Sample J1415 is a sheared green-purple conglomerate definitively from the Beaucoup Formation; however, 43DF15 was a dark lithic

sandstone found in close proximity to the thinly bedded brown slates of the Hunt Fork Shale. In the field 43DF15 could arguably be assigned to either the Hunt Fork or the Beaucoup although it is most similar to the Beaucoup Formation. This ambiguity complicates interpretation of its unique detrital zircon spectrum (Fig. 31 and 21), which bears similarities to the other Beaucoup sample (J1415) and the Hunt Fork sample (26DF15); however, it is largely dissimilar to the Trembley Creek phyllite (Fig. 5) sample from Strauss et al. (2017), which completely lacks the otherwise prominent 440 Ma centered population in the other samples and has a greater abundance of 800 - 550 Ma zircons and other Precambrian populations.

Comparing these detrital zircon spectra highlights several similarities and differences between various formations. In regard to the calculated maximum depositional ages, none of these three formations produce anomalously young maximum depositional ages; however, it is curious that the youngest detritus within 26DF15 (Hunt Fork; Fig 22) is actually older than the youngest detritus within J1415 (Beaucoup; Fig. 20) because the Beaucoup is stratigraphically below the Hunt Fork (see Fig. 5). Both produce Late Devonian maximum depositional ages which fall within error of each other and are in concert with the stratigraphic age of both these formations. The fact that their maximum depositional ages fall within error of each other, prevents any major claims based solely on this; however, sample 43DF15 generates a maximum depositional age of 397.1 ± 6.4 Ma (Early Devonian) and therefore has a distinct detrital signature, and could be older than both J1415 and 26DF15. It is important to state explicitly that this does not necessarily mean 43DF15 is Early Devonian in depositional age, just that the youngest detrital zircon it contains are Early Devonian. It could still have been deposited in the Late Devonian, consistent with the Beaucoup stratigraphic age. 43DF15 also contains a minor

peak at 506 Ma, similar to one seen within J1415 (Beaucoup Formation), which is the same age as the dominant unimodal peak within sample 05DF15 (Apoon assemblage).

When considered relative to the Hunt Fork, Sillyasheen, and Beaucoup Formations of the John River transect (Fig. 30), sample 43DF15 bears similarities to all three, but more closely resembles the Beaucoup Formation than the Hunk Fork Shale based on the position of its prominent Caledonian population and the presence of some 800 – 550 Ma (Timanian) zircons. Ultimately the detrital spectra and lithologic characteristics of 43DF15 are more similar to the Beaucoup Formation, and it is therefore included within the Beaucoup Formation rather than the Hunt Fork Shale.

It is important to note another significant aspect of 43DF15, which makes it similar to the Trembley Creek phyllite in some respects. Figure 31 compares the samples of this study to those from Strauss et al. (2017). Strauss et al. (2017) analyzed one sample from the Trembley Creek phyllite of the Hammond subterrane from the southern margin of the Doonerak fenster. Interestingly, this sample contained a prominent population centered on 504 Ma, the exact same age as the major population found in 05DF15 (Apoon Assemblage). The Trembley Creek phyllite sample also contains a significant population centered on 635 Ma, a Timanian age, and accessory populations consistent with various Proterozoic detritus common to Laurentian rocks. Notice that sample 43DF15 contains a distinct population of 550 - 800 Ma zircon, which is also present within the Trembley Creek phyllite and is rare among other samples (Fig. 31; some rare grains of this age are present within the Endicott Group of this study and of Strauss et al., 2017). Detrital spectra of that age could be the result of detritus from the Timanian orogen of northern Baltica (see Fig. 2). This indicates that both 43DF15 (Beaucoup) and the Trembley Creek phyllite likely received some portion of their detritus from the Timanian orogen.

That said, the dominant population within 43DF15, a Caledonian age peak centered on 420 Ma, contains the vast majority of zircon from that sample. The complete lack of this population within the Trembley Creek phyllite indicates that these cannot possibly be from the same formation. While they may both contain some Timanian detritus, they are not from the same formation. The detrital zircon spectrum of sample 43DF15 is most similar to the Beaucoup Formation (see section 6.3 and 7 for more on the relationship to the Trembley Creek sample and the Timanian orogeny).

6.3 The Apoon Assemblage and the Endicott Group

Sample 05DF15 was collected from the volcaniclastic portion of the Apoon assemblage (Pzc of Julian and Oldow, 1998) south of Pyramid Creek and contains a dominantly unimodal detrital zircon spectrum (Fig. 18). A prominent peak centered on 504 Ma (Cambrian) contains ~75% of the zircon analyzed from this sample. The youngest grains from 05DF15 generate a maximum depositional age of 452 ± 13 Ma (Ordovician). Detrital populations of this same age appear as minor constituents in several other samples, J1415 and 43DF15, potentially indicating that minor amounts of Apoon detritus were recycled into the Beaucoup Formation or that the Beaucoup Formation received some portion of its detritus from the same regions as the Apoon itself.

Several interesting characteristics emerge when 05DF15 (Apoon; Fig 18) is compared to the detrital samples of Strauss et al. (2017) (Fig. 31). First, none of the Apoon samples from their study contain the same unimodal population (504 Ma centered population). Instead, their samples contain prominent peaks centered on ~440 Ma, ~ 475 Ma, ~483 Ma, or ~493 Ma. Their

aggregated Apoon Assemblage spectrum (Fig. 31 - B) has a prominent peak centered on ~480 Ma, noticeably younger than 05DF15's major population at 504 Ma. The samples they collected from the Apoon Assemblage Pzc unit, approximately along strike 05DF15, contain the same minor accessory peaks as 05DF15; however, they lack the 504 Ma population and instead contain younger (Ordovician-Silurian) major populations. One sample contained major populations both younger and older than that observed in 05DF15 (475 Ma and 540 Ma), but it still lacked detritus similar in age to the 504 Ma peak. Within the Apoon Assemblage phyllitic unit, Pzp, they recorded two samples. One contained a 440 Ma population and a complete lack of other detritus. The second contained a dominant population centered on 493 Ma (~80% of the sample) with minor populations at 570 Ma and 429 Ma.

When 05DF15 is considered in conjunction with all the samples from Strauss et al. (2017), the nomenclature of Julian and Oldow (1998) is brought into question. While their subdivisions of the Apoon assemblage are useful inasmuch as they provide helpful lithostratigraphic divisions of the broader succession, they cannot be clearly defined in terms of their age relationships. Julian and Oldow (1998) acknowledged that these units could overlap in age, but this results in the grouping of units in the field, which vary in age by up to 50 my and potentially over simplifies complex relationships. Despite their shortcomings, these subdivisions remain the most useful and practical subdivisions of the Apoon assemblage currently available and Figure 8 carries this nomenclature into the north-central portion of the fenster, in keeping with Strauss et al. (2017) to the east. This study only analyzed the detrital spectrum from one Apoon sample, 05DF15. Strauss et al. (2017) analyzed only five. The spectra of 05DF15 is markedly different from any of those five samples. This highlights the significant shortcomings in our current divisions of the Apoon assemblage. The full diversity of Apoon clastics has not

been sufficiently described. Future work should focus on analyzing a broader suite of Apoon siliciclastics to better define the range of ages present and to provide more useful subdivisions. As it currently stands, multiple non-age-equivalent map units are likely grouped together, misrepresenting the complexities of the Apoon Assemblage in both structure and stratigraphy.

Finally, apart from a greater abundance of Grenville and other Proterozoic detritus, the Endicott Group spectra of Strauss et al. (2017) are very similar to the Kayak and Kanayut curves from samples 23DF15 and 41DF15 respectively (Fig. 31 - A). Strauss et al. (2017) only sampled the Endicott Group within the Doonerak fenster. The similarity to sample 41DF15, which comes from the Endicott Group (Kanayut Formation) of the Endicott Mountains allochthon, implies that by the time these units were deposited (Mississippian) the Endicott Group of the Doonerak fenster and the Endicott Group of the Endicott Mountains allochthon were receiving detritus from similar areas. Recall that the rocks of the Endicott Mountains allochthon did not achieve their current structural position, in fault contact above the rocks of the Doonerak fenster, until the Mesozoic Brookian orogeny. Therefore, by Mississippian time rocks of the Endicott Mountains allochthon and those unconformably atop the Apoon assemblage were likely being deposited in the same broad system, prior to emplacement of the Endicott Mountains allochthon.

6.4 Circum-Arctic Comparisons and Paleotectonic Setting of the Apoon Assemblage

Understanding the similarities and differences between the detrital zircon spectra of rocks of the Doonerak fenster relative to other rocks in the Brooks Range is important for correlation of widely distributed map units. It does little, however, to help elucidate connections to other regions of the circum Arctic, which is necessary to inform paleogeographic models. Figure 33

illustrates two possible paleogeographic reconstructions of circum-Arctic terranes during the late Ordovician (~450 Ma), at the approximate time of deposition of the Apoon siliciclastics (sample 05DF15 maximum depositional age 452 ± 13 Ma). Two lines of evidence from this study can be used to evaluate such models and potentially help discriminate between them: (1) the comparison of detrital spectra to regional sediment sources and (2) the use of the whole rock geochemical data to help determine the paleotectonic setting in which the Apoon assemblage formed.

Limited evidence has been used to suggest that the Apoon assemblage formed in an arc setting for several decades (see section 3), but the data was inconclusive and did not provide exclusive determination of the Apoon's paleotectonic setting (e.g. Julian and Oldow, 1998). The new whole rock geochemical data herein provides an independent line of evidence to help determine the tectonic setting in which the Apoon Assemblage volcanics formed and can be compared to previous work to either corroborate or refute the assertion that the package formed as part of an island arc. Recall that at least some of the Apoon igneous rocks were dated to between 520 ± 17 Ma and 373 ± 17 Ma by K-Ar and Ar-Ar analysis of hornblende in mafic dikes crosscutting the Pzc unit (Dutro et al., 1976), therefore the reconstructions of Figure 33 represent a time when the Apoon volcanic units were still likely forming. Therefore the geochemistry of these volcanic units can be used to assess the validity of these paleogeographic reconstructions.

Trace element geochemistry is only useful for determining the tectonic environment in which a rock formed if we make some assumptions about the geological processes which control the distribution of trace elements in different tectonic settings. Some such processes are well understood and their effects on trace element distribution in magmas is well defined; however, the inherently incomplete nature of our understanding of chemical behavior of magmas

introduces uncertainty into deciphering the geological processes capable of generating any given trace element distribution. That said, several fundamental processes must be considered to determine which trace elements and trace element ratios provide the most reliable information about the environment in which an igneous rock formed. All rocks exposed to hydrothermal and metamorphic conditions have experienced some amount of element mobility. As such, high field strength elements (HFSEs), such as, Zr, Hf, Ti, Nb, Ta, and P (Pearce, 1983) which are immobile up to moderate metamorphic conditions are more reliable than their low field strength counterparts. Other elements are also commonly immobile (Co, Ni, V and Cr), but the degree of mobility of all elements is complicated by particular mineral phases capable of incorporating them and various fluid controls (Humphries, 1984). A special case of element mobility occurs in subduction zones, where dehydration of the subducted oceanic slab causes metasomatic reactions which mobilize some elements (Sr, K, Rb, Ba, Th, Ce, P, and Sm) which may be immobile under other conditions (Pearce, 1983; Tatsumi, 2005). This affects the composition of both the magma expelled from arc volcanoes, derived from the overlying mantle wedge, and the residual components of the slab. In terms of this study, which provides relatively little complementary evidence to understand how particular volcanic rocks are related to each other in the field, it is difficult to know if different samples are part of the same cogenetic suite or if they come from different sources entirely. Regardless, we must consider the affect any petrological process would have on the trace element distribution of both a partial melt and a residual solid.

The major element geochemistry of all rocks analyzed from the Apoon assemblage characterize them as part of the sub-alkaline series and define them as various basalts, basaltic-andesites, andesites, and minor trachyandesites based on their proportions of silica to total alkalis (SiO_2 to Na_2O+K_2O) after Le Maitre et al. (2002). While this simple classification helps

illustrate the range of rock types present, it does not help assign them to a particular tectonic environment, because basalts and andesites are common to multiple tectonic settings.

The NMORB normalized trace element diagrams (Fig. 26) highlight enrichment in highly incompatible trace elements, especially in the samples with the greatest abundance of SiO_2. Large ion lithophile elements (LILEs; e.g. Cs, Rb, Ba, Th) are enriched to between 50 and 1000 times the composition of a NMORB in the high SiO_2 samples. Those same elements are enriched, but to a lesser extent, in the low SiO_2 samples. Nearly all samples show depletion among HFSEs (e.g. Nb, P, Zr, and Ti), especially in Nb. Such depletion in HFSEs is characteristic of magmas from arc settings because HFSEs can be left within the down-going slab as other trace elements are liberated during dehydration and incorporated into the overlying mantle wedge, ultimately being incorporated into the magma of arc volcanoes (e.g. Tatsumi, 2005). Conversely, the patterns of the most compatible trace elements (e.g. Y, Yb, Lu) are similar to normal and enriched MORBs across all samples (flat lying patterns to the right side of Fig. 26).

On the whole, the Apoon Assemblage volcanic rocks cover a wide range of REE geochemical trends, even among samples with similar SiO_2 abundances, which classify as the same rock type based on their total alkali-silica compositions (Fig. 24). Samples 01DF15 and 08DF15 both classify as basalts based on their total alkali-silica abundances and come from relatively proximal locations within the field area south of Pyramid Creek (Fig. 8). Despite these similarities, these samples (01DF15 and 08DF15) have entirely different REE patterns (Fig. 27 - A). 08DF15 is depleted in the LREEs relative to the MREEs and HREEs, while 01DF15 is enriched in the LREEs relative to the MREEs and HREEs. These two samples are indistinguishable in terms of their textures, basic minerology, and major element compositions,

so these REE differences cannot be explained as a product of differences in rock type. Such variation in REE trends among otherwise similar rocks could be explained by small degrees of partial melting, which would preferentially liberate LREEs into the melt phase. Ultimately this could result in the residue and the melt phase forming two different rocks with mirrored REE patterns, as seen in 01DF15 and 08DF15. That said, because there is no age constraint on either of these samples and their field relationships are ambiguous it is not possible to determine if these two samples are in fact genetically related. The same geochemical trends could result from the melting of two different initial sources.

The high SiO2 samples (Fig. 27 - B) are all highly enriched in LREEs (03DF15, 11DF15, and 33DF15) relative to the MREEs and HREEs, ranging from 20 to 110 times the composition of a normal chondrite. Samples 03DF15 and 11DF15 (Fig. 27 - B) have geochemical trends and relative abundances of LREEs, MREEs, and HREEs that most closely resemble the ocean-island basalt (OIB) representative sample (Fig. 27 - C). Other high SiO_2 samples demonstrate some direct similarities to island arc volcanic rocks (IAB representative basalt in Fig. 27 - C) especially among the LREEs and MREEs in samples 13DF15, 21DF15, and 24DF15 (Fig. 27 - B).

Eight of the eleven samples also show a negative Eu anomaly - depletion of Eu relative to its adjacent REEs (Sm and Gd). Europium anomalies are controlled by the precipitation of feldspars from the melt because divalent Eu is easily incorporated into plagioclase, whereas other REEs (trivalent) are incompatible within the structure of feldspars. A melt can attain a negative Eu anomaly, as seen in many Apoon igneous samples, by the removal of feldspar by fractional crystallization or by the partial melting of a rock in which feldspar, laden with Eu, is retained in the source. At least one sample (25DF15) has a positive (rather than a negative) Eu anomaly,

which could result from the exact opposite scenario, if that sample were derived from a rock with abundant feldspar laden with Eu. As before, without age constraints and better defined field relationships it is not possible to confidently know if these samples are genetically related, but it is at least conceivable that 25DF15 (positive Eu anomaly) represents the residue from which the other samples (with negative Eu anomalies) might have been derived by partial melting. This further highlights the great range in REE geochemical trends found within igneous rocks of the Apoon Assemblage and suggests that the tectonic setting in which these rocks formed must be capable of producing a sufficiently wide range of geochemical trends. As a general rule, volcanic arcs and subduction zones are more capable of producing such a wide range in trace and REE trends than other tectonic settings (e.g. Bacon et al., 1997; Tatsumi, 2005).

Another high SiO_2 sample, 33DF15 (Fig. 27 - B), is also best explained through formation in an arc setting. Although 33DF15 has an overall higher REE pattern, meaning all REE occur in greater abundances than in the other samples, this could be explained by very small partial melts or considerable amounts of fractional crystallization. The overall shape of 33DF15's REE pattern is still consistent with that of the island arc basalt (IAB; Fig. 27 - C) representative sample, potentially indicating a wet and oxidized setting where plagioclase is not strongly crystallized (small Eu anomaly).

The depletions in high field strength elements (HFSEs) observed within the NMORB normalized diagram also suggests formation within an island arc setting. HFSEs are often retained within particular mineral structures and often not incorporated into the overlying mantel wedge along subductions zones, leading to a relative lack of some HFSEs in the magma of arc volcanoes as compared to the abundance of other trace elements. Niobium (Nb) is particularly useful in this regard because its abundance is not often controlled by the presence of any

particular mineral phase that might preferentially incorporate it, so if Nb is depleted relative to other trace elements it is best explained by formation in a subduction zone related tectonic setting, where Nb can be sequestered within the down going slab. Highly prevalent negative Nb anomalies occur within eight of the eleven samples analyzed from the Apoon Assemblage, further suggesting formation within an island arc tectonic setting.

Placing this information into context alongside the Ti:V ratios of the Apoon samples (Fig. 28) begins to highlight the strong likelihood that the igneous portions of the Apoon assemblage are likely derived from a subduction-related tectonic setting. Fig. 28 suggests formation within either an arc setting or a mixed back arc basin setting based on the proportion of Ti:V within these rocks, which occurs as a result of the oxygen activity and fractional crystallization processes within a magma chamber (Shervais, 1982). This in conjunction with the trace and REE data, further corroborates the formation of the Apoon in an arc setting.

It remains difficult to differentiate between the potential of either an island arc or a continental arc based on these chemical trends alone; however, the clean unimodal detrital zircon populations from Apoon Assemblage sample 05DF15 indicates that most detritus was contributed from a proximal source and that only a minor proportion came from some continental margin. This supports the idea that these rocks formed, at least initially, in a relatively isolated paleogeographic setting, which is more consistent with an island arc rather than a continental one. Additionally, some features within the Apoon rocks indicate subaqueous extrusion of magma during their formation (pillow basalts along Bombardment Creek; Fig. 15). This potential arc system could have been influenced by dry asthenosphere magmas, which could help form the MORB like geochemical trends, or by the subduction of non-typical oceanic crust (e.g. an ocean island or seamount), which could result in some of the ocean-island basalt like

geochemical trends. Those complexities cannot be determined from this data alone, but the diversity among the trace and rare earth elements seen within the Apoon assemblage is best explained by its formation within an island arc setting.

Other geochemical and isotopic evidence corroborates an island arc interpretation for the oridin of the Apoon Assemblage. Strauss et al. (2017) conducted U-Pb analysis on a set of igneous zircon from a leucogabbro within the Apoon assemblage in order to corroborate previous dating of the volcanic units (Fig. 6). The age Strauss et al. (2017) found fell within the range of previously published ages (462 ± 8 Ma; Ordovician); however they also conducted Hf isotopic analysis on the zircon grains and calculated highly positive ε Hf values (ε Hf = + 13), which suggest a distinct lack of crustal assimilation and corroborate the idea of these rocks having formed in an island arc setting. This strongly suggests that the rocks of the Apoon Assemblage had limited crustal influence, at least from ancient continental crust. Additionally, they found similar ε Hf values within their Ordovician age detrital populations from the Apoon Pzc unit. Again, this suggests that these clastics were receiving detritus from a highly juvenile source. Collectively, this data and the geochemical data presented herein indicate conclusively that the Apoon assemblage formed as part of an island arc complex, which could have persisted for tens of millions of years based on the range of depositional ages found from the Apoon assemblage, but more data is needed to fully address that.

We have demonstrated that sample 05DF15 contains a prominent unimodal detrital zircon population centered on 504 Ma (Cambrian; Fig. 29) and has a maximum depositional age of 452 ± 13 Ma (Ordovician). Strauss et al. (2017) demonstrated that detrital spectra from other samples of the Apoon assemblage contain prominent youngest peaks centered on ~ 475 Ma, 478, 483, 429, and 440 Ma (Fig. 31). This alone indicates that the Apoon assemblage was deposited

within a long lived depocenter, which must have persisted for 40 - 50 my. Apoon samples from Strauss et al. (2017) contain diagnostic accessory peaks (980 - 1200 Ma; 1300 -1500 Ma, 1600 - 1800 Ma, 2600 - 2800 Ma) that are suggestive of detritus from the Laurentian margin (Grenville, Pinwarian, Superior craton, ect.).

Additionally, a sample of the overlying Kayak Formation (23DF15) from this study and the Endicott Group of Strauss et al. (2017) contain prominent Caledonian age peaks centered on ~ 420 Ma (Fig. 31). Recall that sample 43DF15 (max depositional age 397.1 ± 6.4 Ma), which was assigned to the Beaucoup Formation, contains a prominent unimodal Caledonian age peak and significant amounts of Timanian age detritus (Fig. 21). This means that between the time of deposition of the youngest Apoon sample known (~ 420 Ma max depositional age; J1427 of Strauss et al. (2017)) and deposition of sample 43DF15 sedimentary provenance changed in several ways. There was an increase in the amount of Timanian detritus and the appearance of Caledonian age spectra all alongside typical Laurenitan spectra (Grenville, ect.). This change in provenance occurred between the deposition of these units; however, because the Beaucoup sample (43DF15) could have been transported a great distance during Brookian thrusting it is difficult to know how to fit this into a paleogeographic context.

Elsewhere in the Arctic, along the Varanger Peninsula (Fig. 1 and 2) of the northern Baltic states, Caledonian and Timaninan rocks are sutured together (e.g. Gee and Pease, 2004 and references therein). The coexistence of Timanian and Caledonian age detritus within 43DF15 (Beaucoup Formation), indicates that there may be continuity of this suture on the Alaskan side of the Arctic.

Caledonian age (Laurentian side) and Timanian age (Russian side) detritus is similarly ubiquitous across much, though not all, of the circum-Arctic and allows for comparison to the

units from this study (Fig. 33). Zircon between ~ 990 - 820 Ma from the Clarence River Group of the NE Brooks Range (Johnson et al., 2016) are mostly absent from samples collected along the North Fork of the Koyukuk River except for minimal sporadic grains. Tentative links between rocks of Doonerak and those of the northeast Brooks Range have been discussed for several decades (e.g. Moore, 1987; Moore et al., 1994; 1997) because broadly coeval mafic volcanic rocks of the Whale Mountain area (Fig. 1 and 2) have similar chemistry to those at Doonerak (Moore, 1987) and are similarly enigmatic. Zircon of this ~990 - 820 Ma range are not common however, and are thought to be related to the collapse of the Grenville orogen, related to rocks in the Central Gneiss Belt of Ontario, CA (Ketchum et al., 1998), the East Greenland Caledonides (Kalsbeek et al., 2000; Watt et al., 2000), the Canadian Arctic and Svalbard. The presence of these in the northeast Brooks Range and general lack of them in the Apoon samples (and others) at Doonerak suggests differences in the sediment pathways between Doonerak and the Whale Mountain area (Fig. 1 and 2).

Early Neoproterozoic (1000 – 541 Ma) magmatic rocks have also contributed detritus to the peri-Laurentian terranes of the Canadian Arctic and Greenland, including Pearya (e.g. Trettin, 1987) and Svalbard (e.g. Gee et al., 1995; Johnansson et al., 2004, 2005). Connections between Pearya, Svalbard and possibly the northeast Brooks Range are apparent (Fig 33), but the same cannot be said for the Apoon assemblage rocks of Doonerak. The prominent peak of the Apoon sample (05DF15) is slightly older than those associated with most other locales and generally lacks the accessory peaks which draw links to Svalbard, Pearya, and the Clements Markham Belt of Ellesmere Island (Canadian Arctic) (See Fig 1. for locations). This implies that while 05DF15 was being deposited (452 ± 13 Ma) there were only limited similarities in the sediment pathways between these landmasses. That said 05DF15 does contain some older

accessory peaks which link it to the Laurentian margin to some degree. Yet, the age of 05DF15's major peak (504 Ma) is rare among Laurentian rocks. Regarding the paleogeographic implications, there is admittedly limited data to support or refute either model proposed in Figure 33; however, the general dissimilarities between the detrital spectra of the Apoon as compared to those of Pearya, Ellesmere Island, northwest Svalbard, and southwest Svalbard more closely support Model A "Peri-Baltica" over Model B "Peri-Laurentian."

The unimodal Apoon sample from this study (05DF15) suggests that a geographically isolated island arc existed during the Cambrian and generated significant amounts of detritus, which was deposited to form some of the older Apoon siliciclastics. The increasing proportion of Laurentian affinity detritus within younger Apoon samples from Strauss et al. (2017; Fig. 31) indicates that this arc progressively approached the continental margin of Laurentia. All of the Devonian and Mississippian age rocks from this study (Beaucoup Fm., Hunt Fork Shale, Kayak Shale, Kanayut Conglomerate) contain prominent, generally unimodal, Caledonian age peaks within their detrital zircon spectra, which is evidence for an accretionary event. Some samples from this study, including the younger Mississippian age rocks (Kayak Shale, Kanayut Conglomerate), contain both Caledonian and Timanian detritus (both sides of the orogen) and likely reflect a post accretionary overlap assemblage. The Trembley Creek phyllite sample of Strauss et al. (2017) mostly lacks the Caledonian age peak, which could be explained by derivation from the passive margin side of this orogen.

7. CONCLUSIONS

This study aimed to provide evidence which would place the Doonerak fenster into greater context. One goal was to determine the tectonic setting in which the Apoon assemblage

of the Doonerak fenster formed. Whole rock volcanic geochemistry, including trace and rare earth elements, was applied to igneous rocks of the Apoon assemblage and provides clear evidence for formation within a subduction zone related tectonic setting, likely an island arc. Another goal of this study was to constrain the sedimentological links between rocks of the Doonerak fenster and the Endicott Mountains allochton. Detrital zircon geochronology was applied to the Apoon Assemblage and Kayak Formation within the Doonerak fenster and to the Endicott Group of the Endicott Mountains allochthon. These data highlighted a major change in provenance from the Apoon assemblage (05DF15) to the overlying Carboniferous rocks of the Ellesmerian Sequence and showed the coexistence of detritus from the Caledonian (Laurentian) and Timanian (Baltican) orogens. Together these data help constrain the origins of the Apoon assemblage and highlight the Doonerak fenster as a probable location for the boundary between Laurentian and non-Laurentian rocks within Arctic Alaska. Several new conclusions (below) can be drawn from these data:

- The Apoon assemblage likely formed along a subduction zone as part of an island arc complex. HFSE depletions and enrichment among LREEs and MREEs suggest formation along an island arc. Although there is a considerable amount of geochemical variability within the Apoon Assemblage, many of the analyzed rocks contain chemistries similar to patterns observed within IAB and MORB world-wide. An arc interpretation is also supported by the Hf isotopic data of Strauss et al. (2017).
- Caledonian age detritus was the dominant source of clastic material for all units except the Apoon assemblage, suggesting that the Doonerak arc initially formed in a different and relatively isolated paleogeographic setting, fed by a proximal arc. The near complete

lack of detritus from other sources (i.e. minimal presence of zircon from other populations; general lack of Grenville and other Laurentian sources) within 05DF15 indicates it formed in this isolated setting, where most detritus feeding 05DF15 was proximal. This change in provenance among the overlying units is evidence for an accretionary event which occurred between the time of deposition for sample 05DF15 (Apoon; 452 ± 13 Ma) and the other clastic samples of this study, all of which contain ~ 420 Ma centered populations (Caledonian detritus).

- The Apoon volcaniclastics were deposited in a long lived (50 my +) depocenter based on the range of depositional ages from the Apoon assemblage.
- Portions of the Apoon assemblage received detritus from similar source regions as the Beaucoup Formation and Trembley Creek phyllite, both of which contain a 504 Ma peak, identical to the dominant peak in the Apoon assemblage. The Cambrian detritus of the Endicott Mountains allochthon and Hammond subterrane could be recycled from the Apoon Assemblage.
- Similarities between the detrital spectra of the Endicott Group interior and exterior to the fenster indicate shared provenance for the Endicott Mountains allochthon and Doonerak regions by Mississippian time.
- The presence of Timanian age detritus (800 – 550 Ma; Baltican) alongside Caledonia detritus (~ 420 Ma; Laurentian) in some samples (e.g. 43DF15) indicates the juxtaposition of Timanian (Baltican) and Caledonian (Laurentian) source regions in Arctic Alaska by late Devonian to Mississippian time. This likely represents a post accretionary assemblage, deposited after the amalgamation Laurentian and non-Laurentian terranes.

- Cumulative detrital zircon spectra indicate significant dissimilarities between rocks of the Apoon assemblage and those of the Canadian Arctic and Svalbard during deposition of sample 05DF15 (Apoon), further supporting the idea that this sample was deposited in an isolated paleogeographic setting (Max Depositional Age = 452 ± 13 Ma).
- Based on the data presented here, the Apoon Assemblage likely initially formed in an isolated island arc setting. This arc progressively approached and eventually docked onto the northwest margin of Laurentian in the early Paleozoic, juxtaposing Laurentian and non-Laurentian terranes within Arctic Alaska. Accretion was complete by late Devonian-to-Mississippian time leading to post assembly overlap assemblages containing both Caledonian (Laurentian) and Timanian (Baltican) age detritus, which reflect both sides of the orogen.

REFERENCES

Akinin, V.V., Gottlieb, E.S., Miller, E.L., Polsunenkov, G.O., Stolbov, N.M., and Sobolev, N.N., 2015, Age and composition of basement beneath the De Long archipelago, Arctic Russia, based on zircon U-Pb geochronology and O-Hf isotopic systematics from crustal xenoliths in basalts of Zhokhov Island: Arktos, v. 1. p. 9

Amato, J.M., Toro, J., Miller, E.L., Gehrels, G.E., Farmer, G.L., Gottlieb, E.S., and Till, A.B., 2009, Late Proterozoic–Paleozoic evolution of the Arctic Alaska–Chukotka terrane based on U-Pb igneous and detrital zircon ages: Implications for Neoproterozoic paleogeographic reconstructions: Geological Society of America Bulletin, v. 121, p. 1219-1235.

Amato, J.M., Aleinikoff, J.N., Akinin, V.V., McClelland, W.C., and Toro, J., 2014, Age, chemistry, and correlations of Neoproterozoic –Devonian igneous rocks of the Arctic Alaska–Chukotka terrane: An overview with new U-Pb ages, in Dumoulin, J.A., and Till, A.B., eds., Reconstruction of a Late Proterozoic to Devonian Continental Margin Sequence, Northern Alaska: Its Paleogeographic Significance and Contained Base-Metal Sulfide Deposits: Geological Society of America Special Paper, v. 506, p. 29–57, doi: 10.1130/2014.2506(02).

Anderson, A.V., Wallace, W.K., and Mull, C.G., 1994, Depositional record of a major tectonic transition in northern Alaska: Middle Devonian to Mississippian rift-basin margin deposits, upper Kongakut River region, eastern Brooks Range, Alaska, *in* Thurston, D.K., and Fujita, K., eds., 1992 Proceedings of the International Conference on Arctic Margins: Anchorage, Alaska, U.S. Department of the Interior, Minerals Management Service, p. 71–76.

Anderson, A.V., and Wallace, W.K., 1991, Middle Devonian to Early Mississippian stratigraphic record of the formation of a passive continental margin in northeastern Alaska: Geological Society of America Abstracts with Programs, v.23. No. 5, p. 436.

Armstrong, A.K., Mamet, B.L., Brosgé, W.P., and Reiser, H.N., 1976, Carboniferous section and unconformity at Mount Doonerak, Brooks Range, northern Alaska: American Association of Petroleum Geologists, v. 60, p. 962–972.

Bacon, C. R., Bruggman, P. E., Christiansen, R. L., Clynne, M. A., Donnelly-Nolan, J. M., & Hildret, W., 1997. Primitive magmas at five Cascades volcanic fields: Melts from hot, heterogeneous sub-arc mantle. Canadian Mineralogist, v. 35, p. 397-424.

Barker, F., Jones, D. L., Budahn, J. R., and Coney, P. J., 1988. Ocean plateau-seamount origin of basaltic rocks, Angayuchaln terrane, central Alaska, J. Geol., v. 96, p. 368-374.

Beranek, L.P., van Staal, C.R., McClelland, W.C., Israel, S.A., and Mihalynuk, M.G., 2013a, Baltican crustal provenance for Cambrian–Ordovician sandstones of the northern Alexander terrane, Saint Elias Mountains, northwestern Canada: The Journal of Geology, v. 120, p. 293–314.

Beranek, L.P., van Staal, C.R., McClelland, W.C., Israel, S.A., and Mihalynuk, M.G., 2013b, Detrital zircon Hf isotopic compositions indicate a northern Caledonian connection for the Alexander terrane: Lithosphere, v. 5, no. 2, p. 163–168.

Blodgett, R.B., Rohr, D.M., and Boucot, A.J., 2002, Paleozoic links among some Alaskan accreted terranes and Siberia based on megafossils, *in* Miller, E.L., Grantz, A., and Klemperer, S.L., eds., Tectonic evolution of the Bering Shelf–Chukchi Sea–Arctic Margin and Adjacent Landmasses: Geological Society of America Special Paper 360, p. 273-290.

Blundy, J., & Wood, B. 1994. Prediction of crystal-melt partition coefficients from elastic moduli. Nature, v. 372 no. 6505, p. 452-454.

Brosgé, W.P. and Reiser, H.N., 1971, Preliminary bedrock geologic map, Wiseman and eastern Survey Pass Quadrangles, Alaska: U.S. Geological Survey Open-File Map 71-56, scale 1:250,000.

Brosgé, W.P., Dutro, J.T., Jr., Mangus, M.D., and Reiser, H.N., 1962, Paleozoic sequence in eastern Brooks Range, Alaska: American Association of Petroleum Geologists Bulletin, v. 46, p. 174-198.

Brozena, J.M., Childers, V.A., Lawver, L.A., Gahagan, L.M., Forsberg, R., Faleide, J.I., Eldholm, O., 2003. New aerogeophysical study of the Eurasia Basin and Lomonosov Ridge: implications for basin development. Geology 31, 825–828.

Carter, C., and Laufeld, S., 1975, Ordovician and Silurian fossils in well cores from North Slope of Alaska: American Association of Petroleum Geologists Bulletin, v. 59, p. 457-464.

Churkin, M., Jr., 1975, Basement rocks of Barrow Arch, Alaska, and circum-Arctic Paleozoic mobile belts: American Association of Petroleum Geologists, v. 59, no. 3, p. 451–456.

Churkin, M., Jr., Whitney, J.W., and Rogers, J.F., 1985, The North American–Siberian connection, a mosaic of craton fragments in a matrix of oceanic terranes, in Howell, D.G., ed., Tectonostratigraphic Terranes of the Circum-Pacific Region, Earth Science Series 1: Houston, Texas, Circum–Pacific Council for Energy and Mineral Resources, p. 79–84.

Cocks, L.R.M., and Torsvik, T.H., 2011, The Palaeozoic geography of Laurentia and western Laurussia: A stable craton with mobile margins: Earth Science Reviews, v. 106, p. 1–51.

Cook, D.B., Fujita, K., McMullen, C.A., 1986. Present-day plate interactions in Northeast Asia: North American, Eurasian, and Okhotsk plates. J. Geodyn. 6, 33–51.

Cook, F.A., Coflin, K.C., Lane, L.S., Dietrich, J.R., Dixon, 1987. Structure of the southeast margin of the Beaufort–Mackenzie basin, Arctic Canada, from crustal seismicreflection data. Geology 15, 931–935.

Colpron, M., and Nelson, J.L., 2009, A Palaeozoic Northwest Passage: incursion of Caledonian, Baltican and Siberian terranes into eastern Panthalassa, and the early evolution of the North American Cordillera: Geological Society of London, Special Publications, v 318, p. 273–307.

Colpron, M., and Nelson, J.L., 2011, A Paleozoic Northwest Passage and the Timanian, Caledonian, and Uralian connections to some exotic terranes in the North American Cordillera, in, Spencer, A.M., Embry, A.F., Gautier, D.L., Stoupakova, A.V., and Sorensen, K., eds., Arctic Petroleum Geology, Geological Society of London Memoir 35, p. 463-484.

Cox, G.M., Strauss, J.V., Halverson, G.P., Schmitz, M.A., McClelland, W.C., Stevenson, R.S., and Macdonald, F.A., 2015, Kikiktat volcanics of Arctic Alaska–Melting of harzburgitic mantle associated with the Franklin large igneous province: Lithosphere, v. 7, no. 3, p. 275–295.

Davidson, J., Turner, S., and Plank, T., 2013. Dy/Dy*: Variations arising from mantle sources and petrogenetic processes. Journal of Petrology v. 54, no. 3, p. 525-537.

Dillon, J.T., 1989, Structure and stratigraphy of the southern Brooks Range and northern Koyukuk Basin near the Dalton Highway, in Mull, C.G., and Adams, K.E., Dalton Highway, Yukon River to Prudhoe Bay, Alaska: Bedrock Geology of the Eastern Koyukuk Basin, Central Brooks Range, and East-Central Arctic Slope, Alaska Division of Geological and Geophysical Surveys, Guidebook 7, v. 2, p. 157–187.

DeGraaff-Surpless, K., Graham, S. A., Wooden, J. L., & McWilliams, M. O., 2002. Detrital zircon provenance analysis of the Great Valley Group, California: Evolution of an arc-forearc system. Geological Society of America Bulletin, 114(12), 1564-1580.

Dickinson, W. R., & Gehrels, G. E., 2003. U–Pb ages of detrital zircons from Permian and Jurassic eolian sandstones of the Colorado Plateau, USA: paleogeographic implications. Sedimentary Geology, 163(1), 29-66.

Dillon, J.T., Brosgé, W.P., and Dutro, J.T., Jr., 1986, Generalized geologic map of the Wiseman quadrangle, Alaska: U.S. Geological Survey Open-File Report 86-219, scale 1:250,000.

Dinkelman, M.G., Kumar, N., Helwig, J., Emmet, P., Granath, J., 2008. Highlights of petroleum and crustal framework of the Beaufort–Mackenzie Basin: key results from BeaufortSPAN(TM) East Phases I and II surveys. Can. Soc. Explor. Geophys. Rec. 35, 22–25.

Dovzhikova, E., Pease, V., and Remizov, D., 2004., Neoproterozoic island are magmatism beneath the Pechora Basin, NW Russia, GFF, 126:4, 353-362, DOI: 10.1080/11035890401264353

Dumoulin, J.A., Harris, A.G., Bradley, D.C., and de Freitas, T.A., 2000, Facies patterns and conodont biogeography in Arctic Alaska and the Canadian Arctic Islands: Evidence against juxtaposition of these areas during Early Paleozoic time: Polarforschung, v. 68, p. 257–266.

Dumoulin, J.A., Harris, A.G., Gagiev, M., Bradley, D.C., and Repetski, J.E., 2002, Lithostratigraphic, conodont, and other faunal links between lower Paleozoic strata in northern and central Alaska

and northeastern Russia, in Miller, E.L., Grantz, A., and Klemperer, S.L., eds., Tectonic evolution of the Bering Shelf–Chukchi Sea–Arctic Margin and Adjacent Landmasses: Geological Society of America Special Paper 360, p. 291-312.

Dumoulin, J.A., Harris, A.G., and Repetski, J.E., 2014, Carbonate rocks of the Seward Peninsula, in Dumoulin, J.A., and Till, A.B., eds., Reconstruction of a Late Proterozoic to Devonian Continental Margin Sequence, Northern Alaska: Its Paleogeographic Significance and Contained Base-Metal Sulfide Deposits: Geological Society of America Special Paper 506.

Dutro, J.T., Jr., Brosgé W.P., Lanphere, M.A., and Reiser, H.N., 1976, Geologic significance of Doonerak structural high, central Brooks Range, Alaska: American Association of Petroleum Geologists Bulletin, v. 60, p. 952-961.

Dutro, J.T., Jr., Palmer, A.R., Repetski, J.E., and Brosgé W.P., 1984a, The Doonerak anticlinorium revisited, in Coonrad, W.L., and Elliot, R.L., eds., The U.S. Geological Survey in Alaska – Accomplishments during 1981: U.S. Geological Survey Circular 868, p. 17-19.

Dutro, J.T., Jr., Palmer, A.R., Repetski, J.E., and Brosgé W.P., 1984b, Middle Cambrian fossils from the Doonerak anticlinorium, central Brooks Range, Alaska: Journal of Paleontology, v. 58, p. 1364-1371.

Engen, Ø., Eldholm, O., Bungum, H., 2003. The Arctic plate boundary. J. Geophys. Res. B 108 (2). http://dx.doi.org/10.1029/2002JB001809 (ETG 5-1–5-17).

Floyd, P. A., and Winchester, J. A., 1978. Identification and discrimination of altered and metamorphosed volcanic rocks using immobile elements. Chemical Geology v. 21, no. 3, p. 291-306.

Fryer BJ, Jackson SE, Longerich HP. 1993. The application of laser ablation microprobe–inductively coupled plasma mass spectrometry (LAM-ICPMS) to in situ (U)-Pb geochronology. Chem. Geol. 109:1–8

Gee, D. G., 1975. A tectonic model for the central part of the Scandinavian Caledonides. American Journal of Science, v. 275A, p. 468-515.

Gee, D. G., & Pease, V., 2004. The Neoproterozoic Timanide Orogen of eastern Baltica: introduction. In Gee, D. G. & Pease, V. (eds) 2004. The Neoproterozoic Timanide Orogen of Eastern Baltica. Geological Society, London, Memoirs, 30, 1-3. 0435-4052/04/$15

Gee, D., Johansson, Å., Ohta, Y., and Tebenkov, A., 1995, Grenvillian basement and a major unconformity within the Caledonides of Nordaustlandet, Svalbard: Precambrian Research, v. 70, no. 3–4, p. 215–234, doi:10.1016/0301-9268(94)00041-O.

Gehrels, G. 2014. Detrital zircon U-Pb geochronology applied to tectonics. Annu. Rev. Earth Planet. Sci. 2014. 42:127–49 doi: 10.1146/annurev-earth-050212-124012

Gehrels, G.E., Valencia, V., Ruiz, J., 2008, Enhanced precision, accuracy, efficiency, and spatial resolution of U-Pb ages by laser ablation–multicollector–inductively coupled plasma–mass spectrometry: Geochemistry, Geophysics, Geosystems, v. 9, Q03017, doi:10.1029/2007GC001805.

Glebovsky, V.Yu., Kaminsky, V.D., Minakov, A.N., Merkur'ev, S.A., Childers, V.A., Brozena, J. M., 2006. Formation of the Eurasia Basin in the Arctic Ocean as inferred from geohistorical analysis of the anomalous magnetic field. Geotectonics v.40 no.4, p. 263–281.

Gottlieb, E.S., Meisling, K.E., Miller, E.L., and Mull, C.G., 2014, Closing the Canada Basin: Detrital zircon geochronology relationships between the North Slope of Arctic Alaska and the Franklinian mobile belt of Arctic Canada: Geosphere, v. 10, no. 6, p. 1-19.

Gottschalk, R.R. and Snee, L.W., 1998. Tectonothermal evolution of metamorphic rocks in the south-central Brooks Range, Alaska: Constraints from 40Ar/39Ar geochronology. Geological Society of America Special Papers, 324, p.225-251.

Grantz, A., Moore, T.E., and Roeske, S.M., 1991, Continent-ocean transect A-3: Gulf of Alaska to Arctic Ocean: Geological Society of America Centennial Continent/Ocean Transect 15, 72 p., 3 sheets, scale 1:500 000.

Grantz, A., Pease, V.L., Willard, D.A., Phillips, R.L., Clark, D.L., 2001. Bedrock cores from 898 North: implications for the geologic framework and Neogene paleoceanography of Lomonosov Ridge and a tie to the Barents shelf. Geol. Soc. Am. Bull. 113, 1272–1281.

Grantz, A., Hart, P., May, S.D., Coastal, W.R., 2004. Seismic reflection and refraction data acquired in Canada Basin, Northwind Ridge, and Northwind Basin, Arctic Ocean in 1988, 1992 and 1993. US Geological Survey, Reston, VA, Open-file Reports, 2004-1243 (World Wide Web Address http://pubs.usgs.gov/of/2004/1243/).

Grantz, A., May, S., Hart, P., 1990. Geology of the Arctic continental margin of Alaska. Geol. North Am. 50, p. 257-288.

Grantz, A., Dinter, D.A., and Culotta, R.C., 1987, Structure of the continental shelf north of the Arctic National Wildlife Refuge, in Bird, K.J., and Magoon, L.B., eds., Petroleum geology of the northern part of the Arctic National Wildlife Refuge, northeastern Alaska: U.S. Geological Survey Bulletin v. 1778, p. 271-276.

Grantz, A., and May, S. D.,1983. Rifting history and structural development of the continental margin north of Alaska. Studies in continental margin geology: AAPG Memoir, v. 34, p. 77-100.

Grantz, A., Hart, P., Childers, V., 2011a. Geology and tectonic development of the Amerasia and Canada Basins, Arctic Ocean. In: Spencer, A.M., Embry, A.F., Gautier, D.L., Stoupakova, A.V., Sørensen, K. (Eds.), Arctic Petroleum Geology. Geological Society (London) Memoirs, 35, pp. 771–799.

Grantz, A., Scott, R.A., Drachev, S.S., Moore, T.E., Valin, Z.C., 2011b. Sedimentary successions of the Arctic Region (58–64° to 90°N) that may be prospective for hydrocarbons. In: Spencer, A.M., Embry, A.F., Gautier, D.L., Stoupakova, A.V., Sørensen, K. (Eds.), Arctic Petroleum Geology. Geological Society (London) Memoirs, 35, pp. 17–37.

Grove, M., Gehrels, G.E., Cotkin, S.J., Wright, J.E., and Zou, H., 2008, Non-Laurentian cratonal provenance of Late Ordovician eastern Klamath blueschists and a link to the Alexander terrane, in Wright, J.E., and Shervais, J.W., eds., Ophiolites, arcs and batholiths: A tribute to Cliff Hopson: Geological Society of America Special Paper 438, p. 223–250.

Hadlari, T., Davis, W.J., Dewing, K., 2014. A peri-cratonic model for Pearya Terrane as an extension of the Franklinian margin of Laurentia, Canadian Arctic. Geol. Soc. Am. Bull. 126 (1–2), 182–200

Hanson, G. N., 1980. Rare earth elements in petrogenetic studies of igneous systems. Annual Review of Earth and Planetary Sciences v. 8, no. 1, p.371-406.

Hawkesworth, C. J., Gallagher, K., Hergt, J. M., McDermott, F., 1993, Mantle and slab contributions in arc magmas. Annual Review of Earth and Planetary Sciences, 21(1), p. 175-204.

Helwig, J., Kumar, N., Emmet, P., Dinkelman, M.G., 2011. Regional seismic interpretation of crustal framework, Canadian Arctic passive margin, Beaufort Sea, with comments on petroleum potential. In: Spencer, A.M., Embry, A.F., Gautier, D.L., Stoupakova, A.V., Sørensen, K. (Eds.), Arctic Petroleum Geology. Geological Society (London) Memoirs, 35, pp. 527–543.

Houseknecht, D.W., and Connors, C.D., 2016, Pre-Mississippian tectonic affinity across the Canada Basin–Arctic margins of Alaska and Canada: Geology, v. 44, n. 7, p. 507-510.

Humphries, S.E., 1984, The mobility of the rare earth elements in the crust. In: Henderson, P. (ed.), Rare earth element geochemistry. Elsevier, Amsterdam, p. 315-341

Jaffey AH, Flynn KF, Glendenin LE, Bentley WC, Essling AM. 1971. Precision measurement of half-lives and specific activities of ^{235}U and ^{238}U. Phys. Rev. C4:1889–906

Johansson, Å., Larionov, A.N., Gee, D.G., Ohta, Y., Teben'kov, A.M., and Sadelin, S., 2004, Grenvillian and Caledonian tectonomagmatic activity in northeasternmost Svalbard, *in* Gee, D.G., and Pease, V., eds., The Neoproterozoic Timanide Orogen of Eastern Baltica: Geological Society of London Memoir 30, p. 207–232.

Johansson, Å., Gee, D., Larionov, A., Ohta, Y., and Tebenkov, A., 2005, Grenvillian and Caledonian evolution of eastern Svalbard—A tale of two orogenies: Terra Nova, v. 17, p. 317 325, doi:10.1111/j.1365-3121.2005.00616.x.

Johnson, B.G., Strauss, J.V., Toro, J., Benowitz, J.A., and Ward, W.P., *in review*, Geochronological constraints from synorogenic detritus and early Paleozoic accretionary tectonics in the NE Brooks Range: *Lithosphere*, v. 8, no.6; p. 649-667.

Jokat, W., Uenzelmann-Neben, G., Kristoffersen, Y., Rasmussen, T.M., 1992. Lomonosov Ridge — a double-sided continental margin. Geology 20, 887–890.

Jones, D. L., Bounday-Sanders, S., Murray, R. L , Howell, D. G., and Wiley, T. J., 1987. Tectonic contacts of miogeoclinal strata in east-central Alaska: American Association of Petroleum Geologists Abstracts with Programs, V. 7J, p. 573.

Jones, P. B., 1982, Mesozoic rifting in the western Arctic ocean basin and its relationship to Pacific seafloor spreading, in Embry, A. F., and Balkwill, H. R., eds., Arctic geology and geophysics; Proceedings of the Third International Symposium on Arctic Geology: Canadian Society of Petroleum Geologists Memoir 8, p. 83- 99.

Julian, F.E., 1989, Structure and stratigraphy of lower Paleozoic rocks, Doonerak Window, central Brooks Range, Alaska (Ph.D. Thesis): Houston, Texas, Rice University, 127 p.

Julian, F.E., and Oldow, J.S., 1998, Structure and lithology of the lower Paleozoic Apoon Assemblage, eastern Doonerak Window, central Brooks Range, Alaska, *in* Oldow, J.S., and Ave Lallemant, H.G., eds., Architecture of the central Brooks Range fold and thrust belt, Arctic Alaska: Geological Society of America Special Paper 324, p. 65-80.

Karasik, A.M., 1968. Magnetic Anomalies of the Gakkel Ridge and the origin of the Eurasia Subbasin of the Arctic Ocean. Geofizicheskie metody razvedki i Arktike 5, 8–19 (in Russian).

Karasik, A.M., 1974. The Eurasia Basin of the Arctic Ocean from the Point of View of Plate Tectonics: Problems in Geology of Polar Regions of the Earth. NauchnoIsseledovateliskiy Institut Geologii, Leningrad, (in Russian).

Kos'ko, M.K., Cecile, M.P., Harrison, J.C., Banelin, V.G., Khandoshko, N.V., and Lopatin, B.G., 1993, Geology of Wrangel Island, between Chukchi and East Siberian seas, northeastern Russia: Geological Survey of Canada Bulletin, v. 461, 101 p.

Košler J, Sylvester PJ. 2003. Present trends and the future of zircon in U-Pb geochronology: laser ablation ˇ ICPMS. See Hanchar & Hoskin 2003, pp. 243–75

Košler J, Fonneland H, Sylvester P, Tubrett M, Pedersen R-B. 2002. U-Pb dating of detrital zircons for sediment provenance studies—a comparison of laser ablation ICPMS and SIMS techniques. Chem. Geol. 182: 605–18

Košler J, Tubrett M, Sylvester P. 2001. Application of laser ablation ICPMS to U-Th-Pb dating of monazite. Geostand. Newsl. 25: 375–86

Košler J, Sláma J, Belousova E, Corfu F, Gehrels GE, et al. 2013. U-Pb detrital zircon analysis—results of inter-laboratory comparison. Geostand. Geoanal. Res. 37: 243–59

Kristoffersen, Y., 1990. Eurasia Basin. In: Grantz, A., Johnson, G.L., Sweeney, J.F. (Eds.), The Arctic Ocean region. The Geology of North America, L. Geological Society of America, Boulder, CO, pp. 365–378.

Lane, L.S., 1997. Canada Basin, Arctic Ocean: evidence against a rotational origin. Tectonics 5, 252–276.

Lane, L.S., 2007, Devonian–Carboniferous paleogeography and orogenesis, northern Yukon and adjacent Arctic Alaska: Canadian Journal of Earth Sciences, v. 44, p. 679-694.

Lane, L.S., Gehrels, G.E., and Layer, P.W., 2015, Provenance and paleogeography of the Neruokpuk Formation, northwest Laurentia: An integrated synthesis: Geological Society of America Bulletin.

Lawver, L.A., and Scotese, C.R., 1990, A review of tectonic models for the evolution of the Canadian Basin, in Grantz, A., et al., eds., The Arctic Ocean region: Boulder, Colorado, Geological Society of America, Geology of North America, v. L, p. 593–618.

Laxon, S., McAdoo, D., 1994. Arctic Ocean gravity field derived from ERS-1 satellite altimetry. Science 265, 621–624.

Laxon, S.W., McAdoo, D.C., 1998. Satellites provide new insights into Polar geophysics. EOS Trans. 79 (69), 72–73.

Le Bas, M. J., 1986. A chemical classification of volcanic rocks based on the total alkali-silica diagram. Journal of Petrology, 27, 745-750.

Le Maitre, R. W., Streckeisen, A., Zanettin, B., Le Bas, M. J., Bonin, B., Bateman, P, & Lameyre, J., 2002. Igneous Rocks: A Classification and Glossary of Terms: Recommendations of the International Union of Geological Sciences, Subcommission on the Systematics of Igneous Rocks. Cambridge University Press, Cambridge

LePain, D.L., Crowder, R.K., and Wallace, W. K., 1994, Early Carboniferous transgression on a passive continental margin: deposition of the Kekiktuk conglomerate, northeastern Brooks Range, Alaska. AAPG Bulletin, v. 78, no. 5, p. 679-699.

Lerand, M., 1973, Beaufort Sea, in McCrossam, R.G., ed., The Future Petroleum Provinces of Canada —Their Geology and Potential: Canadian Society of Petroleum Geology Memoir 1, p. 315–386.

Louden, K., Osler, J., Srivastava, S., Keen, C., 1996. Formation of oceanic crust at slow spreading rates: new constraints from an extinct spreading center in the Labrador Sea. Geology 24, 771–774.

Macdonald, F.A., McClelland, W.C., Schrag, D.P., and Macdonald, W.P., 2009, Neoproterozoic glaciation on a carbonate platform margin in Arctic Alaska and the origin of the North Slope subterrane: Geological Society of America Bulletin, v. 121, p. 448-473.

Mayfield, C. F., Tailleur, I. L., and Ellersieck, I., 1988, Stratigraphy, structure, and palinspastic synthesis of the western Brooks Range, northwestern Alaska, in Geology and Exploration of the National Petroleum Reserve in Alaska, 1974 to 1982, edited by G. Gryc, U.S. Geol. Surv. Prof. Paper, 1399, p.143-186.

McClelland, W.C., Colpron, M., Piepjohn, K., von Gosen, W., Ward, W., and Strauss, J.V., 2015, Preliminary detrital zircon geochronology of the Neruokpuk Formation in the Barn Mountains, Yukon: *in* Yukon Exploration and Geology, K.E. MacFarlane, M.G. Nordling, and P.J. Sack (eds.), Yukon Geological Survey, p. 123–143.

McDonough, W.F. and Sun, S.S., 1995. The composition of the Earth. Chemical geology, v. 120 no. 3-4, p.223-253.

McKerrow, W. S., Mac Niocaill, C., & Dewey, J. F., 2000. The Caledonian orogeny redefined. Journal of the Geological Society, v. 157 no. 6, p. 1149-1154.

McLennan, S.L., 1989, Rare Earth Elements in Sedimentary Rocks: influence of Provenance and Sedimentary Processes in Lipin, B.R. and McKay G.A., eds., Geochemistry and Mineralogy of Rare Earth Elements, Reviews in Mineralogy, vol. 21, pgs. 169-200.

Miller, E.L., Toro, J., Gehrels, G., Amato, J.M., Prokopiev, A., Tuchkova, M.I., Akinin, V.V., Dumitru, T.A., Moore, T.E., and Cecile, M.P., 2006, New insights into Arctic paleogeography and tectonics from U-Pb detrital zircon geochronology: Tectonics, v. 25, TC3013, 19 p.

Miller, E., Gehrels, G., Pease, V., and Sokolov, S., 2010, Stratigraphy and U-Pb detrital zircon geochronology of Wrangel Island, Russia: Implications for Arctic paleogeography: AAPG bulletin, v. 94, no. 5, p. 665.

Miller, E.L., Kuznetsov, N., Soboleva, A., Udoratina, O., Grove, M.J., and Gehrels, G., 2011, Baltica in the Cordillera?: Geology, v. 39, no. 8, p. 791–794, doi: 10.1130/G31910.1.

Moore, T.E., 1987, Geochemical and tectonic setting of some volcanic rocks of the Franklinian assemblage, central and eastern Brooks Range, *in* Tailleur, I.L. and Weimer, P., eds., Alaskan North Slope Geology: Bakersfield, California, Society of Economic Paleontologists and Mineralogists, Pacific Section, and Alaska Geological Society, Book 50, p. 691-710.

Moore, T.E. and Churkin, M., Jr., 1984, Ordovician and Silurian graptolite discoveries from the Neruokpuk Formation (sensu lato), northeastern and central Brooks Range, Alaska: Paleozoic Geology of Alaska and Northwestern Canada Newsletter, no. 1, p. 21-23.

Moore, T.E., Wallace, W.K., Bird, K.J., Karl, S.M., Mull, C.G., and Dillon, J.T., 1994, Geology of northern Alaska, *in* Plafker, G., and Berg, H.C., eds., The Geology of Alaska: Boulder, Colorado, Geological Society of America, The Geology of North America, v. G-1, p. 49-140.

Moore, T.E., Wallace, W.K., Mull, C.G., Adams, K.E., Plafker, G., and Nokleberg, W.J., 1997, Crustal implications of bedrock geology along the Trans-Alaska Crustal Transect (TACT) in the Brooks Range, northern Alaska: Journal of Geophysical Research, v. 102, no. B9, p. 20645-20684.

Moore, T.E., Potter, C.J., and O'Sullivan, P.B., 2007, Detrital zircon U-Pb analysis of pre-Mississippian metasedimentary basement strata, North Slope, Alaska: Evidence of a Caledonian connection: Geological Society of America Abstracts with Programs, v. 39, no. 6, p. 488.

Moore, T.E., O'Sullivan, P.B., Potter, C.J., and Donelick, R.A., 2015, Provenance and detrital zircon geochronologic evolution of lower Brookian foreland basin deposits of the western Brooks Range, Alaska, and implications for early Brookian tectonism: Geosphere, v. 11, no. 1, p. 93–122.

Mosher, D.C., Shimeld, J., Hutchinson, D., Chian, D., Lebedova-Ivanova, Jackson, R., 2012. Canada Basin revealed. Arctic Technology Conference Proceedings, OTC 23797 (11 pp.).

Mull, C.G., 1982, The tectonic evolution and structural style of the Brooks Range, Alaska: An illustrated summary, in Powers, R.B., ed., Geological Studies of the Cordilleran Thrust Belt, Volume 1: Denver, Colorado, Rocky Mountain Association of Geologists, p. 1-45.

Mull, C.G., Adams, K.E., and Dillon, J.T., 1987a, Stratigraphy and structure of the Doonerak fenster and Endicott Mountains allochthon, central Brooks Range, Alaska, in Tailleur, I., and Weimer, P., eds., Alaskan North Slope Geology: Bakersfield, California, Society of Economic Paleontologists and Mineralogists (SEPM), Pacific Section, and Alaska Geological Society, Book 50, p. 663-679.

Mutter, J.C., Karson, J.A., 1992. Structural processes at slow-spreading ridges. Science 257, 627–634.

Nakamura, N. 1974. Determination of REE, Ba, Fe, Mg, Na and K in carbonaceous and ordinary chondrites. Geochimica et Cosmochimica Acta v38, p. 757-775.

Natal'in, B.A., Amato, J.M., Toro, J., and Wright, J.E., 1999, Paleozoic rocks of northern Chukotka Peninsula, Russian Far East: Implications for the tectonics of the Arctic region: Tectonics, v. 18, p. 977–1003.

Nokleberg, W.J., Parfenov, L.M., Monger, J.W., Norton, I.O., Chanďuk, A.I., Stone, D.B., Scotese, C.R., Scholl, D.W., Fujita, K., 2000. Phanerozoic Tectonic Evolution of the Circum-North Pacific. US Department of the Interior, US Geological Survey.

Oldow, J.S., Avé Lallemant, H.G., Julian, F.E., and Seidensticker, C.M., 1984, The Doonerak window duplex: regional implications: Geological Society of America Abstracts with Programs, v. 16, p. 326.

Oldow, J.S., Avé Lallemant, H.G., Julian, F.E., and Seidensticker, C.M., 1987a, Balanced cross sections through the central Brooks Range and North Slope, Arctic Alaska: American Assoication of Petroleum Geologists Special Publication, v. 19, 19 p., 8 plates.

Oldow, J.S., Avé Lallemant, H.G., Julian, F.E., and Seidensticker, C.M., 1987b, Ellesmerian(?) and Brookian deformation in the Franklin Mountains, northeastern Brooks Range, Alaska, and its bearing on the origin of the Canada Basin: Geology, v. 15, p. 37-41.

O'Sullivan, P.B., Moore, T.E. and Murphy, J.M., 1998. Tertiary uplift of the Mt. Doonerak antiform, central Brooks Range, Alaska: Apatite fission-track evidence from the Trans-Alaska Crustal Transect, in Architecture of the Central Brooks Range Fold and Thrust Belt, Arctic Alaska, edited by Oldow, J., and Avé Lallement, H., p.179.

Oxman, V. S., 2003. Tectonic evolution of the Mesozoic Verkhoyansk–Kolyma belt (NE Asia). Tectonophysics, 365(1), 45-76.

Pallister, J.S., Budahn, J.R. and Murchey, B.L., 1989. Pillow basalts of the Angayucham terrane: Oceanic plateau and island crust accreted to the Brooks Range. Journal of Geophysical Research: Solid Earth, 94, p.15901-15923.

Paton, C., Hellstrom, J., Paul, B., Woodhead, J., & Hergt, J. 2011. Iolite: Freeware for the visualisation and processing of mass spectrometric data. Journal of Analytical Atomic Spectrometry, v. 26, p. 2508-2518.

Patton, W.W., Jr., Box, S. E., and Grybeck, D. J., 1994, Ophiolites and other mafic-ultramalic complexes in Alaska, in Plafker, G., and Berg, H. C., eds., The Geology of Alaska: Boulder, Colorado, Geological Society of America, The Geology of North America, v. G-1, p. 671-686.

Patrick, B.E., and McClelland, W.C., 1995, Late Proterozoic granitic magmatism on Seward Peninsula and a Barentian origin for Arctic Alaska–Chukotka: Geology, v. 23, p. 81-84.

Pearce, J.A., 1983. Role of the sub-continental lithosphere in magma genesis at active continental margins. In Hawksworth, C.J. and Norry, M. J. (eds.), Continental basalts and mantle xenoliths. Shiva, Nantwich, p. 230-249

Pearce, J.A., and Cann, J., 1973. Tectonic setting of basic volcanic rocks determined using trace element analysis. Earth Planet. Sci. Lett., v. 19, p. 290-300.

Pease, V., 2011, Eurasian orogens and Arctic tectonics: an overview, in Spencer, A.M., Embry, A.F., Gautier, D.L., Stoupakova, A.V., and Sorensen, K., eds., Arctic Petroleum Geology: Geological Society, London, Memoir 35, p. 311-324.

Pease, V., Drachev, S., Stephenson, R., & Zhang, X., 2014. Arctic lithosphere—A review. Tectonophysics, v. 628, p. 1-25.

Pease, V., Dovzhikova, E., Beliakova, L., & Gee, D. G., 2004. Late Neoproterozoic granitoid magmatism in the basement to the Pechora Basin, NW Russia: geochemical constraints indicate westward subduction beneath NE Baltica. *Geological Society, London, Memoir 30, p* 75-85.

Ramsay, D. M. & Sturt, B. A., 1976, The syn-metamorphic emplacement of the Magerøy Nappe. Norsk Geologisk Tidsskrift, Vol. 56, pp. 291-307.

Reed, B. L., 1968, Geology of the Lake Peters area, northeastern Brooks Range, Alaska: U.S. Geological Survey Bulletin, v. 1236, p. 1–132.

Remizov, D., and Pease, V., 2004. The Dzela complex, Polar Urals, Russia: a Neoproterozoic island arc in The Neoproterozoic Timanide Orogen of eastern Baltica (eds.) Gee, D. G., and Pease, V., Geological Society of London, Memoir 30, p. 107 – 123.

Repetski, J.E., Carter, C., Harris, A.G., and Dutro, J.T. Jr., 1987, Ordovician and Silurian fossils from the Doonerak anticlinorium, central Brooks Range, Alaska, in Hamilton, T.D., and Galloway, J.P., eds., Geologic studies in Alaska by the U.S. Geological Survey during 1986: U.S. Geological Survey Circular 998, p. 40-42.

Roberts, D., 2003. The Scandinavian Caledonides: event chronology, palaeogeographic settings and likely modern analogues. Tectonophysics, v. 365 no. 1, p. 283-299.

Roberts, D and Olovyanishnikov, V., 2004, Structural and tectonic development of the Timanide orogen in The Neoproterozoic Timanide Orogen of eastern Baltica (eds.) Gee, D. G., and Pease, V., Geological Society of London, Memoir 30, p. 47 – 57.

Roeder, D., and Mull, C. G., 1978., Tectonics of Brooks Range ophiolites, Alaska, AAPG Bull., v. 62, p. 1696-1702.

Sable, E.G., 1977, Geology of the western Romanzof Mountains, Brooks Range, northeastern Alaska: U.S. Geological Survey Professional Paper 897, 84 p. Saleeby, J.B., 1983, Accretionary tectonics of the North American Cordillera: Annual Review of Earth and Planetary Sciences, v. 11, p. 45–73, doi:10.1146/annurev.ea.11.050183 .000401.

Salters, V. J. M. & Stracke, A. 2004. Composition of the depleted mantle. Geochemistry, Geophysics, Geosystems 5, doi:10.1029/ 2003GC000,597

Saltus, R.W., Miller, E.M., Gaina, C., Brown, P.J., 2011. Regional magnetic domains of the circum-Arctic — a framework for geodynamic interpretation. In: Spencer, A.M., Embry, A.F., Gautier, D.L., Stoupakova, A.V., Sørensen, K. (Eds.), Arctic Petroleum Geology. Geological Society (London) Memoirs, 35, pp. 49–60.

Savostin, L.A., Karasik, A.M., 1981. Recent plate tectonics of the Arctic basin and of northeastern Asia. Tectonophysics 74, 111–145.

Shervais, J. W., 1982. Ti-V plots and the petrogenesis of modern and ophiolitic lavas. Earth and planetary science letters, v. 59, no. 1, p. 101-118.

Silberling, N.L., Jones, D.L., Monger, J.W.H., Coney, P.J., Berg, H.C. and Plafker, G., 1994. Lithotectonic terrane map of Alaska and adjacent parts of Canada, *in* Plafker, G., and Berg, H.C.,

eds., The Geology of Alaska: Boulder, Colorado, Geological Society of America, The Geology of North America, v. G-1, 1 sheet, 1:250000.

Small, C., Sandwell, D.T., 1992. An analysis of ridge axis gravity roughness and spreading rate. J. Geophys. Res. Solid Earth 97, 3235–3245 (1978–2012).

Spencer, A.M., Embry, A.F., Gautier, D.L., Stoupakova, A.V., Sørensen, K., 2011. An overview of the petroleum geology of the Arctic. In: Spencer, A.M., Embry, A.F., Gautier, D.L., Stoupakova, A.V., Sørensen, K. (Eds.), Arctic Petroleum Geology. Geological Society (London) Memoirs, 35, pp. 1–15.

Strauss, J.V., Macdonald, F.A., Taylor, J.F., Repetski, J.E., and McClelland, W.C., 2013, Laurentian origin for the North Slope of Alaska: Implications for the tectonic evolution of the Arctic: Lithosphere, v. 5, no. 5, p. 477–482.

Strauss, J. V., Hoiland, C. W., Ward, W. P., Johnson, B. G., Nelson, L. L., & McClelland, W. C., 2017, Orogen transplant: Taconic–Caledonian arc magmatism in the central Brooks Range of Alaska. Geological Society of America Bulletin, 129 (5-6), p. 649-676.

Sturt, B. A., Pringle, I. R., & Ramsay, D. M., 1978. The Finnmarkian phase of the Caledonian orogeny. Journal of the Geological Society, 135(6), 597-610.

Sun, S.S., and McDonough, W.F., 1989, Chemical and isotopic systematics of oceanic basalts: implications for mantle composition and processes, *in* Saunders, A.D. and Norry, M.J., eds., Magmatism in Ocean Basins: Geological Society of London Special Publication No. 42, p. 313–345.

Tailleur, l. L .. and Brosgé, W. P., 1970, Tectonic history of northern Alaska. In Adkison, W. L., and Brosgé, M. M., eds., Proceedings, Geological seminar on the North Slope of Alaska: Los Angeles, American Association of Petroleum Geologists Pacific Section Meeting, p. El- E20.

Tatsumi, Y., The subduction factory: How it operates in the evolving Earth. GSA Today: v. 15, no. 7, p. 4-10 doi: 10:1130/1052-5173(2005)015<4:TSFHIO>2.0.CO;2

Till, A.B., Dumoulin, J.A., Harris, A.G., Moore, T.E., Bleick, H., and Siwiec, B., 2008, Bedrock geologic map of the southern Brooks Range, Alaska, and accompanying conodont data: U.S. Geological Survey Open-File Report 2008–1149, 88 p., 2 sheets.

Till, A.B., Amato, J.M., Aleinikoff, J.N., and Bleick, H.A., 2014a, U-Pb detrital zircon geochronology as evidence for the origin of the Nome Complex, northern Alaska, and implications for regional and trans-Arctic correlations, *in* Dumoulin, J.A., and Till, A.B., eds., Reconstruction of a Late Proterozoic to Devonian Continental Margin Sequence, Northern Alaska: Its Paleogeographic Significance and Contained Base-Metal Sulfide Deposits: Geological Society of America Special Paper 506, p. 111–131.

Till, A.B., Dumoulin, J.A., Ayuso, R.A., Aleinikoff, J.N., Amato, J.M., Slack, J.F., and Shanks, W.C.P., III, 2014b, Reconstruction of an early Paleozoic continental margin basin on the nature

of protoliths in the Nome Complex, Seward Peninsula, Alaska, *in* Dumoulin, J.A., and Till, A.B., eds., Reconstruction of a Late Proterozoic to Devonian Continental Margin Sequence, Northern Alaska: Its Paleogeographic Significance and Contained Base-Metal Sulfide Deposits: Geological Society of America Special Paper 506.

Trettin, H.P., 1987, Pearya: A composite terrane with Caledonian affinities in northern Ellesmere Island: Canadian Journal of Earth Sciences, v. 24, p. 224–245.

Trettin H.P., 1998, Pre-Carboniferous geology of the northern part of the Arctic islands, Chapter 4: Geology of Pearya: Geological Survey Canada Bulletin, v. 425, pp. 108–192.

Turner, D. L., Forbes, R. B., and Dillon, J. T., 1979, K-Ar geochrooometry of the southwestern Brooks Range, Alaska: Canadian Journal of Earth Sciences, v. 16. p. 1789- 1804.

Vogt, P.R., Taylor, P.T., Kovacs, L.C., Johnson, G.L., 1979. Detailed aeromagnetic investigation of the Arctic Basin. J. Geophys. Res. Solid Earth 84, 1071–1089.

Vogt, P., Jung, W., Jakobsson, M., Mayer, L., Williamson, M., 2006. The Alpha Mendeleev Magmatic Province, Arctic Ocean: a new synthesis. EOS Trans. Am. Geophys. Union 87, 36.

Wiedenbeck, M. A. P. C., Alle, P., Corfu, F., Griffin, W. L., Meier, M., Oberli, F. V., & Spiegel, W. 1995. Three natural zircon standards for U-Th-Pb, Lu-Hf, trace element and REE analyses. Geostandards and Geoanalytical Research, 19(1), p. 1-23.

Winchester, J. A., and Floyd, P. A., 1977. Geochemical discrimination of different magma series and their differentiation products using immobile elements. Chemical geology v. 20, p.325-343.

Zonenshain, L.P., Natapov, L.M., 1989. Tectonic history of the Arctic Region from the Ordovician through the Cretaceous. In: Herman, Y. (Ed.), The Arctic Seas: Climatology, Oceanography, Geology and Biology. Van Nostrand Reinhold, New York, pp. 829–862.

SUPPLEMENTARY MATERIALS \ APPENDIX

NOTE ON THE NOMENCLATURE OF SAMPLE DESCRIPTIONS/NAMES

Reconnaissance scale mapping of the Wiseman Quadrangle by Dillon et al. (1986) and Brosge and Reiser (1960 & 1971) are the most current and comprehensive geological maps in the vicinity of the Doonerak fenster in the central Brooks Range. Some detailed mapping and stratigraphic studies were conducted in the eastern part of the fenster by Julian (1989) and Strauss et al., (2017). Additional regional work by Mull et al. (1987) and Moore (1987) add further complexity to the nomenclature of major rock units making the comparison of results increasingly difficult. For these reasons and to increase comparability, I utilized on the mapping and unit descriptions of the most recent published work from Doonerak - Strauss et al. (2017). This nomenclature recycles the nomenclature of Julian (1989) and Julian and Oldow (1998) for the lower Paleozoic volcanic rocks of the Doonerak fenster (Apoon assemblage) but otherwise generally remains consistent with Dillon et al., (1986). Even so, it is important to acknowledge the difficulty of defining precise unit boundaries in an area of poorly constrained stratigraphic relations. The samples from this study can be generally divided into those from the Endicott Mountains allochthon (above the Amawk thrust), those from the Doonerak fenster but above the regionally recognizable pre-Mississippian unconformity (Ellesmerian Sequence), and those from the Doonerak fenster and below the major unconformity (Apoon assemblage). The sample summary table (below) includes the sample locations and types of analysis pertaining to the various samples. It also shows samples available for potential future analysis.

NOTE ON DETRITAL ZIRCON SAMPLE PREPARATION

Zircon-rich separates were acquired from whole rock samples by mechanical disaggregation and by density and magnetic differentiation of the resulting rock powders in the

rock preparation lab at West Virginia University. This procedure was adapted from the standardized protocol used by the Arizona LaserChron Center and other laser ablation labs (e.g. e.g. Gehrels, 2014).

Samples were disaggregated to < ~250 µm particle sizes using a jaw crusher (Bico Braun Chipmunk) and disc mill (Bico Braun UA Pulverizer). After each crushing or pulverizing step, all material finer than 250 µm was removed from further disaggregation via standard U.S. series sieves (No. 60 - opening .0098 in; 250 µm). Sieves were thoroughly cleaned before and after each sample using an air compressor, fine brush, and alcohol wash. Each sieve was visually inspected prior to use to ensure no foreign material was added to the separate.

The disaggregated rock powders were then separated based on their hydrodynamic characteristics (mainly density) using a shaking water table (MD Mineral Technologies MK2 Gemini). The most dense sample grains, those that entered the most distant three of seven receptacles attached to the water table, proceeded to further processing. Less dense material which entered the upper four receptacles was examined, dried, and archived when found to be absent of zircon.

The densest grains were then separated by their magnetic properties. First a hand magnet was used to remove highly magnetic material (mostly iron filings incorporated during crushing and pulverizing). Samples were then progressively separated according to magnetic susceptibility when exposed to an electromagnet within an L-1 Frantz isodynamic magnetic separator operating at a vertical angle of 15 degrees. Paramagnetic grains were removed from the sample in ~0.25 ampere increments up to ~1.5 amperes, and archived progressively. Nonmagnetic fractions at ~1.5 amperes were retained for further processing.

The nonmagnetic dense mineral fractions were then combined with a lithium polytungstate solution (LPT; density = 2.85 ± 0.02 g/mL) in a ~50 mL glass funnel fixed with a gasket and rotatable valve at the base. Each sample was agitated and allowed to settle for approximately 45 min within the LPT, until grains could be observed within distinct floating and sunken fractions with an intervening clear heavy liquid zone between them. The gasket at the base of the funnel was then briefly opened to allow the dense mineral fraction to fall into a second glass funnel fixed with filter paper. Dense separates were then washed repeatedly using deionized water, sonicated, and dried before proceeding to further processing. The lighter mineral fraction was similarly treated, washed repeatedly, inspected to confirm the absence of zircon, and archived.

The nonmagnetic mineral separates denser than LPT proceeded to further heavy liquid processing. The densest grains from previous steps were combined with a methylene iodide solution (MEI; density = 3.3 ± 0.02 g/mL) in glass constriction tubes, inserted into test tubes following the procedure of Dumitru and Stockli (1998). Grains were left to settle within the MEI filled constriction tubes for ~ 1 hour. Lighter grains were removed by inserting a needle into the opening of the constriction tube and removing the constriction tube with forceps. The lighter grains were then transferred to filter paper, washed repeatedly with acetone, transferred to a vile and archived. The denser mineral fraction was then transferred to a separate funnel with filter paper, repeatedly washed with acetone, sonicated, washed again, and dried in a low temperature oven. The final dense zircon-rich mineral separate was inspected to assess the proportion of zircon. Those samples found to contain significant amounts of pyrite progressed to further processing. Those samples found to be sufficiently zircon-rich without significant amounts of other dense nonmagnetic mineral grains progressed to sample mounting.

Pyrite rich samples were placed within glass beakers, warmed over a hot plate and agitated with a magnetic stirrer while submerged in a 20% nitric acid solution in order to dissolve the pyrite (~25 min). Samples were then washed repeatedly, sonicated, dried and transferred to a new vial. The final zircon rich mineral separate progressed to sample mounting steps.

To avoid the biases related to the selection of individual grains, each sample's resulting zircon-rich separate was simply poured onto double-sided tape attached to a hard glass tile within the bounds of a 1" diameter Buehler circular ring form. Any un-adhered grains were then poured off to yield a representative mounted subset. Samples were again visually inspected to ensure that the resulting mounted aliquot was zircon-rich. Obvious grains of non-zircon high-density nonmagnetic minerals (e.g. pyrite, barite, apatite) were removed from the mount by hand using tweezers. Approximately 300 individual zircon grains were mounted in this manner for each sample.

Grain mounts were then constructed using Buehler Epo-Thin epoxy resin and hardener (Buehler #20-8142-016 & #20-8140-032). Epoxy resin was mixed with hardener at a ratio of 100:39 and poured over top the grains within the 1" diameter Buehler ring form and allowed to harden for 48 hours. Mounts were then removed from the glass tile and sanded using progressively finer wet sandpaper - standard 2500 grit paper followed by 9 micron and 5 micron film paper (Precision Surfaces PSI-1609-6 and PSI-1605-6). Sanding progressed until grains were polished between ⅓ - ½ way into the surface of most grains without removing the smallest grains. Mounts were inspected under the microscope between each sanding step. When found to be sufficiently well sanded, mounts were finally polished using a solution of 1 micron gamma

alumina Buehler micropolish B on a Buehler MINIMET auto-polisher, sonicated, dried, and stored in clean sample containers until LA-ICP-MS analysis.

NOTE ON LASER-ABLATION MASS-SPECTROMETRY

Detrital-zircon U-Pb geochronologic analysis was performed at the University of South Carolina's Center for Elemental Mass Spectrometry (CEMS) by laser-ablation high-resolution single-collector inductively coupled plasma mass-spectrometry (LA-HR-SC-ICP-MS) in 2 different sample runs during December of 2015 (23DF15 & 26DF15) and May of 2016 (05DF15, 41DF15, 43DF15 & J1415).

Grain ablation was conducted using a PhotonMachines Analyte G2 193 nm (deep ultraviolet) ArF exciplex laser operating with a 25 μm diameter spot aimed at the center of individual sample zircons, "unknowns," and reference zircons "standards." Reference zircon standards come from natural zircons of well-constrained and known ages determined by U-Pb isotope dilution thermal ionizonation mass-spectrometry (ID-TIMS). All zircon grains were mounted in 1" polished epoxy resin-filled ring forms and contained within a nine-hole stage held within a HelEx sample cell. Unknown zircons were randomly selected, shot by the laser and ablated in batches of five unknown grains each. Natural reference "standard" zircons were analyzed after each set of five unknown grains. The method of sequentially shooting five unknowns followed by standards is referred to as the "standard-unknown bracketing" approach and is used to correct for instrumental drift age-offset, and down-hole elemental fractionation as the laser ablates (e.g. Gehrels, 2014). Instrumental drift and down-hole fractionation both introduce uncertainties in age accuracy and precision (e.g. Gehrels, 2014) as compared to data

collected by ID-TIMS; however, this is offset by the larger datasets used it detrital provenance studies such as this one.

For the purposes is of this study the Sri Lanka (SL) zircon standard was used as the primary reference material (TIMS age = 563.5 ± 2.3 Ma, 2σ; 518 ppm U, 68 ppm Th, $^{206}Pb/^{204}Pb$ = 18000; Gehrels et al., 2008). The zircon standard 91500 (ID-TIMS age = 1065 ± 5 Ma; Wiedenbeck et al., 1995) was used as the secondary reference material. For consistency and comparability all ages reported are based on the reduction scheme using SL as the primary reference material. During analysis, both reference materials were ablated following ablation of every five unknowns.

Ablated material was transported in He carrier gas flowing from internal and external HelEx sample cell mass flow controllers toward the torch of the mass spectrometer. Entering the mass spectrometer, the carrier gas mixed with Ar sample gas in a mixing chamber before flowing into the dry plasma torch of the Thermo ELEMENT2 high resolution single collector mass spectrometer, where the ablatant passed through the plasma and was ionized. A portion of the ionized material then passed through the sample and skimmer cones into the vacuum of the mass spectrometer where it could be analysed and discriminated using the ELEMENT2's double-focusing magnetic sector field mass analyzer.

Before each analysis, the entire LA-HR-SC-ICP-MS system was manually adjusted to maximize signal and performance using the NIST 612 synthetic glass standard (Hollocher and Ruiz, 1995). Manual tuning included adjusting the torch position as well as sample and carrier gas flow rates while attempting to minimize oxide formation. Analysis of unknown and reference zircons involved the collection of signal intensity data for a set of masses (202, 204, 206, 207, 208, 232, and 238) using the ion counting feature of the ELEMENT2. The mass of 235 was

found by dividing the signal intensity of 238 by 137.88 (Nier, 1939 a&b; Nier et al., 1941). During analysis, laser ablation of “unknown” and “standard” zircons was preceded by 5 seconds of background data collection and followed by approximately 15 seconds for signal washout and data recording. In this manner, between 50 and 75 standard and unknown grains could be measured per hour, including time for periodic manual laser focusing and selection of spot locations.

NOTE ON DETRITAL ZIRCON DATA REDUCTION AND PROCESSING

Processing of the raw data generated by the mass spectrometer was conducted using the *UPbGeochronology3* data reduction scheme of the Iolite v.3 software package (Paton et al., 2010) within the IgorPro data and computation package.

Processing began with the import of individual .FIN2 files acquired from analysis of each unknown or reference zircon and its associated baseline and washout signals into the time-constrained reference frame of the IgorPro environment. Following data import, integration windows for baseline and ablatant signals were selected automatically by trimming 5 sec respectively from the start and end of each data file for baseline integrations, and 15 sec respectively from the start and end of each data file for ablation signals. In addition to removing the baseline signal for the ablatant signal, the latter data trimming removes any surface contamination incorporated into the mount surface during grinding, polishing and storage. Small offsets in analytical start times caused by operator error or computational delays in compiling prior analyses’ data occasionally yielded inaccurately auto-selected integration windows; the ablation of epoxy in insufficiently ground zircons and/or small zircons drilled through during standard ablation durations yielded similarly inappropriate windows. Adjustment of these windows was achieved by manual grain-by-grain data inspection, as was the elimination of

analyses of grains known not to be zircon (e.g., by very low U signals, etc.). In the case of the former, care was taken to ensure that the start time of each ablatant integration window was spatially equivalent to those of grains with auto-selected windows in order to optimize the accuracy of down-hole fraction correction models.

Following data import, selection, and inspection of integration windows, Iolite-based data reduction involved: (1) subtraction of background signals from an automatic (best-fit: see Paton et al. 2010) interpolation model; (2) determination of an appropriate downhole-fractionation correction model by separately stacking the $^{206}Pb/^{238}U$, $^{207}Pb/^{235}U$ and $^{208}Pb/^{232}Th$ downhole ratios for each of the primary reference zircon analyses, calculating best-fit exponential curves to those stacked datasets, and applying the resulting models to transform the isotopic ratios of analyzed 'unknown' zircons, ideally to optimize ratio steadiness; (3) estimation and correction of instrumental age-offsets and drift by comparison of determined (raw) and accepted (i.e., ID-TIMS) isotopic ratios of the primary reference zircon; and (4) calculation of final ages and values, including (a) propagated uncertainties determined from analyses of the primary reference zircon as pseudo-secondary standards, progressively removing them individually from the dataset, reprocessing the data, and calculating uncertainty, and (b) error correlations using the IgorPro StatsCorrelation function. See Paton et al. (2010) for further clarification and discussion of methods of Iolite data reduction of U-Pb zircon data.

LIST OF SUPPLEMENTAL DATA TABLES: PRESENTED ON SUBSEQUENT PAGES

Table 1: Sample Collection and Analyses Run

All Samples are stored with the Dept. of Geology and Geography at WVU

Sample Number	WPF Fieldbook	Collection	Northing	Easting	Elevation	Locale	Lithology	Thin Sectioned	DZ Sep	LA-ICPMS	Powdered	ActLabs
01DF15	PF002	7/19/2015	591604	7530431	3324	Pyramid Creek Area-S	basalt	Y			Y	Y
02DF15	PF004	7/19/2015	591957	7530138	3635	Pyramid Creek Area-S	ss					
03DF15	PF006	7/19/2015	592251	7529975	-	Pyramid Creek Area-S	metatuff	Y			Y	Y
04DF15	PF011	7/19/2015	593039	7529146	-	Pyramid Creek Area-S	metatuff	Y				
05DF15	PF012	7/19/2015	593047	7529129	-	Pyramid Creek Area-S	lithic ss	Y	Y	Y		
06DF15	PF014	7/19/2015	591784	7529758	-	Pyramid Creek Area-S	tuff	Y			Y	
07DF15	PF015	7/19/2015	590949	7530392	1901	Pyramid Creek Area-S	ss	Y				
08DF15	PF017	7/20/2015	591095	7531135	1712	Pyramid Creek Area-N	basalt	Y			Y	Y
09DF15	PF019	7/20/2015	591467	7531140	1828	Pyramid Creek Area-N	basalt	Y			Y	
10DF15	PF021	7/20/2015	592495	7531188	2105	Pyramid Creek Area-N	slate	Y				
11DF15	PF026	7/20/2015	593242	7530575	2069	Pyramid Creek Area-N	andesite	Y			Y	Y
12DF15	PF027	7/20/2015	593393	7530598	2100	Pyramid Creek Area-N	ss	Y				
13DF15	PF035	7/21/2015	592123	7532190	3632	Pyramid Creek Area-N	metabasalt	Y			Y	Y
14DF15	PF037	7/21/2015	592068	7532273	3584	Pyramid Creek Area-N	metabasalt					
15DF15	PF037	7/21/2015	592068	7532273	3584	Pyramid Creek Area-N	phyllite					
16DF15	PF039	7/21/2015	592286	7532571	3605	Pyramid Creek Area-N	andesite					
17DF15	PF040	7/21/2015	592291	7532648	3657	Pyramid Creek Area-N	andesite	Y			Y	
18DF15	PF043	7/21/2015	592452	7533689	3810	Pyramid Creek Area-N	slate					
19DF15	PF044	7/21/2015	592492	7533815	3768	Pyramid Creek Area-N	slate					
20DF15	PF052	7/21/2015	592672	7532630	-	Pyramid Creek Area-N	andesite	Y				
21DF15	PF054	7/21/2015	592618	7532385	-	Pyramid Creek Area-N	andesite	Y			Y	Y
22DF15	PF061	7/22/2015	594157	7534481	3839	S of the N. Fork - btw Ernie and Bomb.	ss	Y				
23DF15	PF062	7/22/2015	594326	7534310	4265	S of the N. Fork - btw Ernie and Bomb.	ss	Y	Y	Y		
24DF15	PF070	7/23/2015	596421	7534790	2407	Bomdardment Creek	andesite	Y			Y	Y
25DF15	PF072	7/23/2015	596874	7534364	2817	Bomdardment Creek	andesite	Y			Y	Y
26DF15	PF075	7/24/2015	593130	7537081	2481	N of the N Fork - btw Ernie and Bomb.	ss	Y	Y	Y		
27DF15	PF076	7/24/2015	593126	7537293	2797	N of the N Fork - btw Ernie and Bomb.	shale					
28DF15	PF084	7/25/2015	590112	7534985	1699	N Fork Koyukuk	slate	Y				
29DF15	PF085	7/25/2015	590064	7534806	1670	N Fork Koyukuk	conglomerate	Y				
30DF15	PF092	7/26/2015	587088	7526376	2983	Kachawara Creek	phyllite					
31DF15	PF093	7/26/2015	586761	7526449	2532	Kachawara Creek	andesite					
32DF15	PF104	7/27/2015	590601	7527188	3482	Boriel Mtn Area	basalt	Y			Y	Y
33DF15	PF107	7/27/2015	590899	7526653	3577	Boriel Mtn Area	tuff	Y			Y	Y
34DF15	PF108	7/27/2015	590952	7526601	3580	Boriel Mtn Area	phyllite	Y				
35DF15	PF114	7/29/2015	590915	7523411	3006	Boriel Mtn Area	tuff					
36DF15	PF115	7/29/2015	591057	7523464	3356	E of N Fork - N of Fishless	tuff	Y				
37DF15	PF116	7/29/2015	591167	7523404	3537	E of N Fork - N of Fishless	ss					
38DF15	PF119	7/29/2015	591309	7423635	3971	E of N Fork - N of Fishless	andesite	Y			Y	Y
39DF15	PF124	7/31/2015	588889	7535206	1823	Shusaluk Area	shale					
40DF15	PF128	7/31/2015	587871	7535347	3022	Shusaluk Area	ss	Y				
41DF15	PF133	7/31/2015	586836	7535250	4223	Shusaluk Area	ss		Y	Y		
42DF15	PF159	8/2/2015	586888	7532129	3592	Koyukuk	ss	Y	Y			
43DF15	PF160	8/2/2015	586692	7531995	3143	Koyukuk	lithic ss	Y	Y	Y		
44DF15	PF160	8/2/2015	586692	7531995	3143	Koyukuk	lithic ss	Y				
45DF15	PF166	8/2/2015	587552	7532070	2946	Koyukuk	wacke	Y				
46DF15	PF173	8/3/2015	588426	7531505	2301	Frigid Craggs	ss	Y				
47DF15	PF175	8/3/2015	588350	7531230	2425	Frigid Craggs	ss	Y				
J1409	Strauss	-	67 55'49.8"	150 28'15.0"	-	E side of Fenster, Justin	ss	Y	Y			
J1415	Strauss	-	67 56' 19.9"	150 25'40.2"	-	E side of Fenster, Justin	conglomerate	Y	Y	Y		
J1417	Strauss	-	67 56' 08.8"	150 26' 21.9"	-	E side of Fenster, Justin	ss	Y	Y-f			

Table 2: Raw Geochemical Data of Apoon Volcanic Rocks

Analyte	Unit	Det. Limit	Method	01DF15	03DF15	08DF15	11DF15	13DF15	21DF15	24DF15	25DF15	32DF15	33DF15	38DF15
Lat (N)	deg	-	-	67.874	67.869704	67.880471	67.87477	67.889606	67.891193	67.911505	67.907531	67.845244	67.840358	67.813177
Long(W)	deg	-	-	-150.820238	-150.805255	-150.831753	-150.781184	-150.806428	-150.794473	-150.701873	-150.691463	-150.846776	-150.840137	-150.832909
SiO2	%	0.01	FUS-ICP	46.34	54.77	46.36	58.41	54.77	50.47	51.42	48.44	49.38	57.62	48.48
Al2O3	%	0.01	FUS-ICP	15.46	16.11	15.97	15.85	16.67	15.5	12.8	13.61	14	15.82	16.18
Fe2O3(T)	%	0.01	FUS-ICP	17.46	5.12	9.01	5.3	10.83	8.2	5.63	10.85	10.3	7.97	10.61
MnO	%	0.001	FUS-ICP	0.22	0.135	0.147	0.122	0.125	0.154	0.135	0.171	0.19	0.111	0.183
MgO	%	0.01	FUS-ICP	4.3	4.56	9.05	2.75	5.35	7.4	5.35	8.52	6.79	0.93	5.93
CaO	%	0.01	FUS-ICP	4.03	4.92	9.26	4.1	1.45	9.87	12.77	10.67	11.03	3.72	9.95
Na2O	%	0.01	FUS-ICP	3.02	4.06	3.75	5.32	3.63	2.24	1.83	3.03	3.17	6.95	3.49
K2O	%	0.01	FUS-ICP	0.59	1.8	< 0.01	1.24	0.88	1.33	2.39	0.06	0.14	0.86	0.28
TiO2	%	0.001	FUS-ICP	4.177	0.602	0.794	0.606	0.742	0.635	0.566	1.401	1.362	1	1.441
P2O5	%	0.01	FUS-ICP	0.42	0.24	0.07	0.27	0.13	0.18	0.15	0.13	0.15	0.25	0.12
LOI	%		FUS-ICP	4.81	7.78	6.16	6.17	5.45	4.58	7.47	3.33	2.88	3.4	3.38
Total	%	0.01	FUS-ICP	100.8	100.1	100.6	100.1	100	100.6	100.5	100.2	99.37	98.62	100.1
Sc	ppm	1	FUS-ICP	39	21	33	11	33	40	19	39	42	10	38
Be	ppm	1	FUS-ICP	1	1	< 1	1	< 1	< 1	< 1	< 1	< 1	< 1	< 1
V	ppm	5	FUS-ICP	386	151	181	101	236	207	151	266	300	14	321
Ba	ppm	2	FUS-ICP	123	407	15	451	156	102	505	32	101	396	151
Sr	ppm	2	FUS-ICP	178	128	121	326	138	101	413	152	138	316	137
Y	ppm	1	FUS-ICP	47	17	20	17	14	17	16	28	27	60	27
Zr	ppm	2	FUS-ICP	273	124	40	134	62	56	51	84	91	466	80
Cr	ppm	20	FUS-MS	60	110	230	40	70	260	140	360	120	30	100
Co	ppm	1	FUS-MS	44	21	42	13	29	33	16	45	34	7	34
Ni	ppm	20	FUS-MS	40	40	130	20	40	100	70	190	50	< 20	60
Cu	ppm	10	FUS-MS	20	50	80	< 10	60	60	30	80	20	< 10	120
Zn	ppm	30	FUS-MS	130	60	60	60	90	60	50	70	60	80	100
Ga	ppm	1	FUS-MS	24	14	12	13	15	12	9	12	14	21	15
Ge	ppm	1	FUS-MS	3	2	1	2	1	2	1	2	2	2	2
As	ppm	5	FUS-MS	13	< 5	< 5	< 5	8	< 5	< 5	< 5	< 5	< 5	< 5
Rb	ppm	2	FUS-MS	21	58	< 2	49	24	19	52	< 2	2	27	6
Nb	ppm	1	FUS-MS	17	4	< 1	5	1	2	2	3	4	24	4
Mo	ppm	2	FUS-MS	< 2	< 2	< 2	< 2	< 2	< 2	< 2	< 2	< 2	3	< 2
Ag	ppm	0.5	FUS-MS	0.8	< 0.5	< 0.5	< 0.5	< 0.5	< 0.5	< 0.5	< 0.5	< 0.5	1.3	< 0.5
In	ppm	0.2	FUS-MS	< 0.2	< 0.2	< 0.2	< 0.2	< 0.2	< 0.2	< 0.2	< 0.2	< 0.2	< 0.2	< 0.2
Sn	ppm	1	FUS-MS	1	1	< 1	< 1	< 1	2	5	1	1	4	< 1
Sb	ppm	0.5	FUS-MS	0.9	0.9	0.8	1.7	1.5	0.8	0.8	0.8	0.8	1	1.6
Cs	ppm	0.5	FUS-MS	0.7	3.2	< 0.5	3	2.1	1.3	7.1	1.1	< 0.5	23.1	< 0.5
La	ppm	0.1	FUS-MS	33.6	27.2	1	37.2	4.7	8	7.7	3.3	4.8	37	6.4
Ce	ppm	0.1	FUS-MS	74.4	55.1	3.4	72.5	12.1	19.9	19.4	9.9	14	86	15.5
Pr	ppm	0.05	FUS-MS	9.37	6.29	0.67	7.96	1.57	2.53	2.54	1.66	2.21	10.8	2.35
Nd	ppm	0.1	FUS-MS	40.2	24.4	4.2	30.3	6.9	11.5	11.6	9.4	11.5	45.1	11.2
Sm	ppm	0.1	FUS-MS	9.8	4.9	1.7	5.6	1.9	2.9	2.8	3.5	3.9	11.6	3.4
Eu	ppm	0.05	FUS-MS	3.37	1.21	0.79	1.47	0.55	0.62	0.81	1.55	1.33	3.13	1.1
Gd	ppm	0.1	FUS-MS	10	4	2.9	4.2	2.3	2.8	2.8	4.5	4.7	11.6	4.4
Tb	ppm	0.1	FUS-MS	1.6	0.6	0.5	0.6	0.4	0.5	0.5	0.8	0.8	2	0.8
Dy	ppm	0.1	FUS-MS	9.5	3.2	3.6	3.3	2.8	3	2.9	5.4	5.3	12	5.3
Ho	ppm	0.1	FUS-MS	1.9	0.6	0.7	0.6	0.6	0.6	0.6	1.1	1.1	2.4	1.1
Er	ppm	0.1	FUS-MS	5.5	1.8	2.1	1.8	1.9	1.8	1.7	3.3	3.1	7	3.2
Tm	ppm	0.05	FUS-MS	0.78	0.28	0.33	0.27	0.3	0.28	0.26	0.5	0.48	1.05	0.48
Yb	ppm	0.1	FUS-MS	5	1.8	2.1	1.8	1.9	1.8	1.7	3.2	3	7.1	3
Lu	ppm	0.01	FUS-MS	0.77	0.29	0.29	0.27	0.32	0.29	0.29	0.49	0.46	1.08	0.46
Hf	ppm	0.2	FUS-MS	6.1	2.9	1.2	3.1	1.7	1.5	1.3	2.1	2.4	9.9	2
Ta	ppm	0.1	FUS-MS	1.3	0.3	< 0.1	0.4	0.1	0.2	0.1	0.2	0.3	1.8	0.3
W	ppm	1	FUS-MS	6	3	2	4	3	2	20	2	3	3	3
Tl	ppm	0.1	FUS-MS	0.1	0.3	< 0.1	0.3	< 0.1	< 0.1	0.2	< 0.1	< 0.1	0.2	< 0.1
Pb	ppm	5	FUS-MS	< 5	14	< 5	8	7	< 5	< 5	< 5	< 5	6	< 5
Bi	ppm	0.4	FUS-MS	< 0.4	< 0.4	< 0.4	< 0.4	< 0.4	< 0.4	< 0.4	< 0.4	< 0.4	< 0.4	< 0.4
Th	ppm	0.1	FUS-MS	4.2	9.6	0.2	12.8	2	1.9	1.2	0.2	0.6	7.8	1
U	ppm	0.1	FUS-MS	2.1	2.9	< 0.1	3.8	0.8	0.7	0.4	< 0.1	0.3	2.8	0.3

Table 3: Apoon Detrital Zircon U-Pb Data - 05DF15

						Isotope ratios					Apparent ages (Ma)									
Analysis	U (ppm)	U/Th	206Pb 207Pb	± 2 sigma	error corr.	207Pb 235U	± 2 sigma	206Pb 238U	± 2 sigma	error corr.	206Pb 238U	± (Ma)	207Pb 235U	± (Ma)	206Pb 207Pb	± (Ma)	Best age (Ma)	± (Ma)	Ef. Conc (%)	Use? (1-y; 0-n)
05DF15 n=99/120						use prop uncertainty														
X05DF_1	218	2.5	0.0562	0.0041	0.54619	0.625	0.068	0.08	0.0061	0.084761	496	37	492	42	430	160	496	37	100%	1
X05DF_3	521	3.05	0.0788	0.0047	0.18369	2.201	0.23	0.203	0.016	0.78183	1203	91	1179	72	1162	120	1203	91	104%	1
X05DF_4	143	3.05	0.0577	0.0064	0.18161	0.662	0.086	0.0866	0.0068	0.04327	535	40	512	49	440	200	535	40	100%	1
X05DF_8	568	3.56	0.0561	0.0037	-0.011555	0.68	0.073	0.0877	0.0067	0.56335	542	39	525	44	444	140	542	39	100%	1
X05DF_9	79.9	5.22	0.0601	0.007	0.42888	0.723	0.098	0.0895	0.0067	-0.14193	553	40	546	57	520	230	553	40	100%	1
X05DF_10	1100	2.93	0.0563	0.0036	-0.082742	0.695	0.075	0.0894	0.0067	0.67015	552	40	535	45	451	140	552	40	100%	1
X05DF_11	314	2.21	0.0574	0.0039	0.38337	0.677	0.072	0.0855	0.0065	0.40044	529	38	524	43	489	150	529	38	100%	1
X05DF_12	122.4	3.35	0.0557	0.0062	0.1574	0.661	0.092	0.0863	0.0067	-0.054047	534	40	509	51	320	170	534	40	100%	1
X05DF_15	2580	1.564	0.0584	0.0037	0.30674	0.547	0.058	0.0687	0.0054	0.67036	428	32	442	38	544	130	428	32	100%	1
X05DF_16	374	1.9	0.0605	0.0041	0.17541	0.695	0.076	0.0833	0.0066	0.59161	516	39	542	46	604	150	516	39	100%	1
X05DF_17	315	2.64	0.0588	0.0047	0.062434	0.691	0.077	0.0855	0.0066	0.14721	529	39	532	46	520	170	529	39	100%	1
X05DF_18	2143	0.904	0.0578	0.0034	0.019555	0.564	0.059	0.0714	0.0055	0.85475	444	33	454	38	526	120	444	33	100%	1
X05DF_19	1031	1.948	0.0569	0.0038	0.31585	0.666	0.071	0.085	0.0065	0.69767	526	38	521	47	482	150	526	38	100%	1
X05DF_20	844	2.9	0.0577	0.0036	0.67222	0.647	0.066	0.0809	0.0061	0.41393	501	37	506.3	41	512	130	501	37	100%	1
X05DF_21	218	2.73	0.0945	0.0059	0.26032	3.453	0.36	0.2659	0.02	0.57316	1519	100	1514	81	1510	120	1510	120	101%	1
X05DF_22	265	4	0.0579	0.0039	0.2389	0.65	0.071	0.0823	0.0065	0.59739	510	39	507	44	508	150	510	39	100%	1
X05DF_23	101.6	4.73	0.0649	0.0099	0.12313	0.72	0.13	0.0807	0.0062	-0.044847	500	37	540	66	610	260	500	37	100%	1
X05DF_24	1369	1.746	0.1071	0.0091	-0.41905	1.47	0.2	0.0985	0.0082	0.74441	605	48	904	77	1710	150	605	48	100%	1
X05DF_25	937	5.42	0.0581	0.0038	0.26367	0.603	0.065	0.0754	0.006	0.56238	469	36	478	41	520	140	469	36	100%	1
X05DF_26	192.6	4.41	0.0571	0.0042	0.042828	0.629	0.074	0.0795	0.0061	0.36697	493	36	493	45	490	180	493	36	100%	1
X05DF_27	965	1.493	0.1321	0.0087	-0.074195	1.767	0.19	0.098	0.0076	0.70511	602	45	1047	67	2117	110	602	45	100%	1
X05DF_28	213.7	2.65	0.0597	0.004	0.11123	0.657	0.071	0.0794	0.0058	0.023857	492.8	35	512	44	576	150	492.8	35	100%	1
X05DF_29	258.7	3.38	0.0609	0.0041	0.16106	0.615	0.065	0.0732	0.0055	0.28716	455.4	33	486	41	618	150	455.4	33	100%	1
X05DF_30	395.8	1.597	0.0572	0.0039	0.4395	0.587	0.062	0.0746	0.0057	0.3874	464	34	468	40	509	150	464	34	100%	1
X05DF_31	384	0.81	0.0567	0.0039	0.23213	0.617	0.066	0.0775	0.0059	0.31851	481	35	487	41	478	140	481	35	100%	1
X05DF_32	1101	3.21	0.0578	0.0041	0.10316	0.605	0.067	0.076	0.0059	0.47	472	35	480	42	557	160	472	35	100%	1
X05DF_33	249	4.07	0.0811	0.0051	-0.037712	2.297	0.25	0.2057	0.016	0.70775	1205	84	1214	78	1214	120	1205	84	99%	1
X05DF_34	226.9	3.17	0.0573	0.0045	0.12414	0.598	0.07	0.0783	0.0065	0.57642	486	39	474	44	490	180	486	39	100%	1
X05DF_35	2448	2.185	0.0621	0.004	0.33416	0.488	0.051	0.0571	0.0043	0.48943	358	26	403	35	666	140	358	26	100%	1
X05DF_36	180	1.004	0.0963	0.0067	-0.043524	3.09	0.35	0.2322	0.018	0.57894	1345	93	1425	85	1536	130	1345	93	88%	1
X05DF_37	1174	2.36	0.0591	0.0035	0.19594	0.598	0.063	0.0747	0.0058	0.8187	464	35	475	40	566	130	464	35	100%	1
X05DF_38	270	4.69	0.0581	0.0041	0.012217	0.608	0.066	0.0761	0.0056	0.31356	472.6	33	481	41	533	150	472.6	33	100%	1
X05DF_39	215.7	3.56	0.0552	0.0037	0.18643	0.608	0.068	0.0773	0.0058	0.51597	480	35	481	42	423	160	480	35	100%	1
X05DF_40	1145	4.15	0.095	0.014	-0.203	0.79	0.14	0.0602	0.0049	0.30567	377	30	582	79	1430	270	377	30	100%	1
X05DF_41	170	2.9	0.0571	0.0047	-0.028301	0.688	0.083	0.0856	0.0067	0.42015	529	40	528	49	480	180	529	40	100%	1
X05DF_42	125	3.1	0.1652	0.01	0.074969	11.25	1.2	0.484	0.039	0.778	2542	170	2538	100	2511	100	2511	100	101%	1
X05DF_43	656	3.11	0.0556	0.0035	0.31958	0.655	0.068	0.0858	0.0067	0.60995	531	40	514	39	451	140	531	40	100%	1
X05DF_44	52.2	2.59	0.1995	0.012	0.35044	15.75	1.7	0.568	0.044	0.67585	2910	170	2857	100	2816	100	2816	100	103%	1
X05DF_45	273	3.88	0.0589	0.0042	0.05498	0.639	0.071	0.0782	0.006	0.49245	485	36	500	43	538	160	485	36	100%	1
X05DF_46	1590	2.38	0.0618	0.0054	0.60517	0.715	0.081	0.0822	0.0063	-0.090198	509	38	546	48	660	200	509	38	100%	1
X05DF_47	154.4	3.5	0.0655	0.0066	-0.087726	0.67	0.085	0.0742	0.0057	0.17859	461	34	517	49	730	180	461	34	100%	1
X05DF_48	197	2.54	0.1746	0.011	0.40345	12.31	1.3	0.516	0.039	0.50169	2682	160	2626	96	2597	100	2597	100	103%	1
X05DF_49	383	3.08	0.0568	0.0038	0.1909	0.612	0.069	0.0764	0.0061	0.67757	475	37	483	43	502	130	475	37	100%	1
X05DF_50	184.5	2.76	0.0565	0.0045	0.035677	0.624	0.074	0.0811	0.0063	0.24033	503	37	490	46	450	170	503	37	100%	1
X05DF_52	333	2.73	0.0558	0.0039	0.016626	0.596	0.066	0.0779	0.0061	0.56116	483	36	473	42	441	160	483	36	100%	1
X05DF_53	936	1.765	0.0577	0.0036	0.3476	0.635	0.067	0.0804	0.0063	0.64806	499	37	498	42	506	140	499	37	100%	1
X05DF_54	1065	1.317	0.0576	0.0035	0.24654	0.644	0.067	0.0827	0.0064	0.6597	512	38	504	41	519	130	512	38	100%	1
X05DF_57	307	3.27	0.0556	0.0039	0.12606	0.624	0.066	0.0835	0.0064	0.40334	517	38	491	42	396	120	517	38	100%	1
X05DF_59	220.1	1.706	0.1162	0.007	0.32403	5.59	0.58	0.3532	0.026	0.66828	1949	130	1918	95	1895	110	1895	110	103%	1
X05DF_60	1490	11.02	0.0569	0.0036	0.40357	0.656	0.068	0.0832	0.0063	0.43375	515	37	511	42	498	140	515	37	100%	1
X05DF_61	319.6	3.1	0.1115	0.0066	0.42647	5.24	0.53	0.3355	0.025	0.5595	1864	120	1858	87	1820	110	1820	110	102%	1
X05DF_62	181	3.13	0.0931	0.0059	0.15807	3.51	0.37	0.2713	0.021	0.56721	1547	100	1526	82	1492	110	1492	110	104%	1
X05DF_63	375	2.02	0.0581	0.0037	0.13395	0.648	0.068	0.0826	0.0064	0.71012	511	38	515	51	524	140	511	38	100%	1
X05DF_64	376	4.46	0.0714	0.0047	0.46208	0.813	0.087	0.0833	0.0069	0.46292	516	41	603	49	956	140	516	41	100%	1
X05DF_65	129.3	1.358	0.1897	0.011	-0.0050268	13.48	1.4	0.5144	0.038	0.90512	2674	160	2711	97	2737	96	2737	96	98%	1
X05DF_66	363	2.18	0.0585	0.0041	0.15183	0.646	0.072	0.08	0.0062	0.44454	496	37	508	42	527	150	496	37	100%	1
X05DF_67	176.4	3.71	0.0611	0.0045	0.26641	0.673	0.075	0.0795	0.006	0.30201	493	36	521	45	610	160	493	36	100%	1
X05DF_69	480	2.93	0.0577	0.0038	0.66382	0.662	0.068	0.084	0.0064	0.051345	520	38	515.7	41	504	150	520	38	100%	1
X05DF_70	340	3.28	0.059	0.0039	0.11417	0.647	0.07	0.078	0.0059	0.58424	484	35	506	43	563	140	484	35	100%	1
X05DF_71	501	2.69	0.0566	0.0035	0.0116	0.642	0.068	0.0812	0.0061	0.56974	503	36	503	42	468	140	503	36	100%	1
X05DF_72	408	4.68	0.061	0.0041	0.18643	0.662	0.071	0.0805	0.0061	0.53895	499	37	515	43	639	140	499	37	100%	1
X05DF_73	293	3.13	0.0566	0.0038	0.082213	0.584	0.063	0.0753	0.0056	0.56144	467.9	34	466	40	475	150	467.9	34	100%	1
X05DF_74	239	4.03	0.0604	0.004	0.21131	0.655	0.07	0.0784	0.0062	0.66246	486	37	511	43	616	130	486	37	100%	1
X05DF_75	600	2.993	0.0572	0.0035	0.39511	0.664	0.068	0.0843	0.0064	0.40578	522	38	516.9	41	502	140	522	38	100%	1
X05DF_77	950	1.92	0.113	0.018	-0.53862	1.42	0.32	0.0844	0.0074	0.75106	522	44	850	110	1730	270	522	44	100%	1
X05DF_78	450	1.652	0.0648	0.0044	0.10699	0.781	0.085	0.0876	0.0067	0.45162	541	40	585	48	748	140	541	40	100%	1
X05DF_79	2600	2.97	0.096	0.027	-0.83775	0.89	0.37	0.0591	0.0057	0.93634	370	34	520	120	1120	340	370	34	100%	1
X05DF_80	401	2.148	0.0562	0.0034	0.46261	0.641	0.066	0.0824	0.0062	0.47775	510	37	502	41	452	140	510	37	100%	1
X05DF_82	1229	2.27	0.0564	0.0034	0.31311	0.65	0.067	0.0843	0.0062	0.30632	523.4	38	508	41	463	140	523.4	38	100%	1
X05DF_84	801	2.94	0.0606	0.0037	0.34006	0.669	0.07	0.0806	0.0061	0.45207	500	37	519	42	618	130	500	37	100%	1
X05DF_85	371	3.45	0.0573	0.0038	0.093973	0.616	0.068	0.0773	0.0059	0.34963	480	35	486	42	490	140	480	35	100%	1
X05DF_86	1078	1.901	0.0556	0.0035	0.209	0.587	0.061	0.0765	0.0058	0.44424	475	35	468	39	439	150	475	35	100%	1
X05DF_87	189.2	1.766	0.1877	0.012	0.40327	11.24	1.2	0.434	0.032	0.29835	2323	140	2540	97	2714	110	2714	110	86%	1
X05DF_89	583	2.43	0.0588	0.0037	0.10256	0.689	0.072	0.0829	0.0063	0.6319	513	37	532	43	549	140	513	37	100%	1
X05DF_90	178	2.287	0.0627	0.0051	0.0073879	0.706	0.08	0.085	0.0063	0.28836	525.6	37	545	50	650	170	525.6	37	100%	1
X05DF_91	225	1.061	0.0647	0.0043	0.068363	1.119	0.12	0.1252	0.0096	0.50889	764	57	764	57	764	150	764	57	100%	1
X05DF_92	1241	3.36	0.0599	0.0037	0.49314	0.691	0.071	0.0845	0.0063	0.34495	523	38	533	43	593	130	523	38	100%	1
X05DF_93	317	3.11	0.059	0.0039	0.24229	0.642	0.069	0.0782	0.0059	0.51458	485	35	505	41	567	140	485	35	100%	1
X05DF_94	553	1.873	0.0601	0.004	-0.22955	0.708	0.079	0.0839	0.0064	0.70757	519	38	542	46	605	130	519	38	100%	1
X05DF_95	246	4.03	0.0674	0.0045	0.38537	0.701	0.075	0.0758	0.006	0.4459	471	36	538	45	848	130	471	36	100%	1
X05DF_96	141.8	4.3	0.1971	0.013	0.29795	14.42	1.5	0.534	0.04	0.58148	2755	170	2775	100	2795	100	2795	100	99%	1
X05DF_98	887	2.69	0.0577	0.0039	0.47383	0.642	0.069	0.0816	0.0065	0.57521	505	39	503	42	529	150	505	39	100%	1
X05DF_99	247	4.5	0.0563	0.0038	0.36328	0.657	0.071	0.0834	0.0065	0.48734	516	39	511	44	459	160	516	39	100%	1
X05DF_100	141	2.62	0.1473	0.0092	0.24728	8.81	0.93	0.43	0.034	0.75518	2316	160	2315	98	2308	110	2308	110	100%	1
X05DF_101	212	2.34	0.1896	0.012	0.23567	14.55	1.6	0.559	0.044	0.64784	2857	180	2803	110	2731	110	2731	110	105%	1
X05DF_102	122.4	3.62	0.058	0.0047	0.0054992	0.665	0.08	0.0831	0.0063	0.27234	514	38	515	48	490	180	514	38	100%	1
X05DF_103	393	0.787	0.057	0.0036	0.071756	0.614	0.066	0.0808	0.0063	0.73028	501	38	488	40	479	140	501	38	100%	1
X05DF_104	95.5	1.414	0.1123	0.0068	0.019916	5.22	0.55	0.3372	0.025	0.68764	1872	120	1858	93	1841	120	1841	120	102%	1
X05DF_105	312	4.87	0.097	0.014	-0.52971	3	0.53	0.225	0.017	0.69951	1308	91	1371	110	1460	200	1308	91	90%	1
X05DF_106	68.1	2.031	0.19	0.011	0.48817	13.33	1.4	0.51	0.039	0.88808	2656	170	2700	99	2738	99	2738	99	97%	1
X05DF_107	49.6	0.582	0.1129	0.0071	0.2103	5.32	0.56	0.3402	0.026	0.5678	1895	130	1868	88	1838	120	1838	120	103%	1
X05DF_108	418	2.57	0.0562	0.0036	0.12466	0.657	0.07	0.0839	0.0064	0.49784	521	37	512	43	466	160	521	37	100%	1
X05DF_109	332	2.95	0.0574	0.0035	0.16184	0.642	0.067	0.0821	0.0062	0.68975	509	37	503	41	497	140	509	37	100%	1
X05DF_110	168.5	2.69	0.062	0.005	0.31473	0.696	0.08	0.0809	0.0062	0.12375	501	37	534	47	660	160	501	37	100%	1
X05DF_111	207	2.21	0.1699	0.01	0.33667	11.15	1.2	0.476	0.037	0.79034	2507	160	2539	93	2554	100	2554	100	98%	1

Table 3: Apoon Detrital Zircon U-Pb Data - 05DF15 cont.

X05DF_112	294	5.63	0.2005	0.013	-0.21267	12.88	1.4	0.463	0.036	0.79378	2450	160	2674	110	2824	100	2824	100	87%	1
X05DF_115	262.7	3.92	0.0562	0.0038	0.1763	0.638	0.069	0.0821	0.0061	0.22013	509	37	500	43	442	150	509	37	100%	1
X05DF_117	322	1.965	0.0602	0.0044	0.16562	0.701	0.077	0.0856	0.0063	0.2316	529.1	38	538	45	584	150	529.1	38	100%	1
X05DF_120	80.3	7.23	0.0636	0.0053	0.27645	0.685	0.078	0.0783	0.006	0.054685	486	36	528	47	680	180	486	36	100%	1
~~X05DF_2~~	~~157~~	~~3.01~~	~~0.0747~~	~~0.0053~~	~~-0.010611~~	~~2.19~~	~~0.25~~	~~0.2083~~	~~0.016~~	~~0.275~~	~~1220~~	~~83~~	~~1159~~	~~64~~	~~1038~~	~~150~~	~~1220~~	~~83~~	~~118%~~	~~0~~
~~X05DF_5~~	~~177.7~~	~~3.4~~	~~0.1127~~	~~0.0072~~	~~0.22339~~	~~5.87~~	~~0.62~~	~~0.3805~~	~~0.029~~	~~0.4806~~	~~2077~~	~~130~~	~~1952~~	~~92~~	~~1834~~	~~120~~	~~1834~~	~~120~~	~~113%~~	~~0~~
~~X05DF_6~~	~~17.06~~	~~0.1676~~	~~0.524~~	~~0.04~~	~~0.25477~~	~~14.03~~	~~1.6~~	~~0.1932~~	~~0.016~~	~~0.27952~~	~~1138~~	~~84~~	~~2743~~	~~100~~	~~4294~~	~~110~~	~~1138~~	~~84~~	~~27%~~	~~0~~
~~X05DF_7~~	~~507~~	~~4.4~~	~~0.079~~	~~0.0052~~	~~0.39615~~	~~2.503~~	~~0.26~~	~~0.2268~~	~~0.017~~	~~0.45532~~	~~1317~~	~~90~~	~~1270~~	~~77~~	~~1158~~	~~130~~	~~1317~~	~~90~~	~~114%~~	~~0~~
~~X05DF_13~~	~~88.1~~	~~1.204~~	~~0.1845~~	~~0.012~~	~~0.35426~~	~~14.56~~	~~1.6~~	~~0.577~~	~~0.046~~	~~0.74422~~	~~2950~~	~~180~~	~~2801~~	~~97~~	~~2704~~	~~100~~	~~2704~~	~~100~~	~~109%~~	~~0~~
~~X05DF_14~~	~~170.8~~	~~5.16~~	~~0.1886~~	~~0.012~~	~~0.50452~~	~~15.59~~	~~1.6~~	~~0.607~~	~~0.047~~	~~0.63589~~	~~3055~~	~~190~~	~~2854~~	~~100~~	~~2731~~	~~110~~	~~2731~~	~~110~~	~~112%~~	~~0~~
~~X05DF_51~~	~~35.2~~	~~0.317~~	~~0.827~~	~~0.052~~	~~-0.042138~~	~~398~~	~~48~~	~~3.53~~	~~0.33~~	~~0.90819~~	~~9670~~	~~470~~	~~6087~~	~~120~~	~~5023~~	~~120~~	~~5023~~	~~120~~	~~193%~~	~~0~~
~~X05DF_55~~	~~378~~	~~2.67~~	~~0.114~~	~~0.0071~~	~~0.053439~~	~~5.7~~	~~0.62~~	~~0.364~~	~~0.029~~	~~0.77183~~	~~1998~~	~~130~~	~~1926~~	~~93~~	~~1860~~	~~110~~	~~1860~~	~~110~~	~~107%~~	~~0~~
~~X05DF_56~~	~~18.9~~	~~1.16~~	~~0.1817~~	~~0.013~~	~~0.1374~~	~~16.47~~	~~1.9~~	~~0.662~~	~~0.054~~	~~0.2983~~	~~3270~~	~~210~~	~~2877~~	~~100~~	~~2631~~	~~81~~	~~2631~~	~~81~~	~~124%~~	~~0~~
~~X05DF_58~~	~~45.6~~	~~0.464~~	~~0.792~~	~~0.048~~	~~0.30194~~	~~76.7~~	~~8~~	~~0.703~~	~~0.055~~	~~0.75454~~	~~3426~~	~~210~~	~~4416~~	~~100~~	~~4944~~	~~110~~	~~4944~~	~~110~~	~~69%~~	~~0~~
~~X05DF_68~~	~~409~~	~~6.58~~	~~0.1159~~	~~0.0076~~	~~0.41626~~	~~6.01~~	~~0.64~~	~~0.374~~	~~0.029~~	~~0.43624~~	~~2055~~	~~130~~	~~1973~~	~~92~~	~~1894~~	~~120~~	~~1894~~	~~120~~	~~108%~~	~~0~~
~~X05DF_76~~	~~46.2~~	~~0.434~~	~~0.81~~	~~0.049~~	~~0.059552~~	~~65.4~~	~~8.6~~	~~0.588~~	~~0.065~~	~~0.96007~~	~~2950~~	~~270~~	~~4225~~	~~140~~	~~4985~~	~~110~~	~~4985~~	~~110~~	~~59%~~	~~0~~
~~X05DF_81~~	~~209.6~~	~~2.83~~	~~0.0738~~	~~0.0047~~	~~0.3315~~	~~1.958~~	~~0.2~~	~~0.1933~~	~~0.015~~	~~0.56434~~	~~1139~~	~~80~~	~~1099~~	~~70~~	~~1038~~	~~130~~	~~1139~~	~~80~~	~~110%~~	~~0~~
~~X05DF_83~~	~~35.8~~	~~0.384~~	~~0.809~~	~~0.049~~	~~0.24636~~	~~76.2~~	~~8~~	~~0.684~~	~~0.053~~	~~0.72601~~	~~3371~~	~~200~~	~~4409~~	~~110~~	~~4984~~	~~110~~	~~4984~~	~~110~~	~~68%~~	~~0~~
~~X05DF_88~~	~~221~~	~~2.24~~	~~0.0991~~	~~0.0066~~	~~0.42888~~	~~4.16~~	~~0.44~~	~~0.3058~~	~~0.023~~	~~0.29455~~	~~1719~~	~~120~~	~~1663~~	~~84~~	~~1594~~	~~120~~	~~1594~~	~~120~~	~~108%~~	~~0~~
~~X05DF_97~~	~~100~~	~~1.385~~	~~0.1873~~	~~0.012~~	~~0.4714~~	~~14.81~~	~~1.5~~	~~0.57~~	~~0.043~~	~~0.55466~~	~~2920~~	~~190~~	~~2801~~	~~97~~	~~2721~~	~~99~~	~~2721~~	~~99~~	~~107%~~	~~0~~
~~X05DF_113~~	~~258~~	~~3.56~~	~~0.1052~~	~~0.0063~~	~~0.19539~~	~~4.87~~	~~0.5~~	~~0.3366~~	~~0.025~~	~~0.68726~~	~~1869~~	~~120~~	~~1805~~	~~86~~	~~1714~~	~~110~~	~~1714~~	~~110~~	~~109%~~	~~0~~
~~X05DF_114~~	~~247~~	~~4.08~~	~~0.2149~~	~~0.013~~	~~0.14573~~	~~20.57~~	~~2.2~~	~~0.695~~	~~0.052~~	~~0.59729~~	~~3398~~	~~200~~	~~3115~~	~~100~~	~~2938~~	~~100~~	~~2938~~	~~100~~	~~116%~~	~~0~~
~~X05DF_116~~	~~204~~	~~2.79~~	~~0.0733~~	~~0.0046~~	~~0.1174~~	~~1.829~~	~~0.19~~	~~0.1817~~	~~0.014~~	~~0.6466~~	~~1076~~	~~75~~	~~1054~~	~~60~~	~~1013~~	~~130~~	~~1076~~	~~75~~	~~106%~~	~~0~~
~~X05DF_118~~	~~125~~	~~3.11~~	~~0.0761~~	~~0.0049~~	~~0.15388~~	~~2.207~~	~~0.23~~	~~0.2112~~	~~0.016~~	~~0.50344~~	~~1235~~	~~84~~	~~1181~~	~~73~~	~~1096~~	~~130~~	~~1235~~	~~84~~	~~113%~~	~~0~~
~~X05DF_119~~	~~119.3~~	~~2.417~~	~~0.0767~~	~~0.0049~~	~~0.35247~~	~~2.178~~	~~0.23~~	~~0.2071~~	~~0.016~~	~~0.60941~~	~~1213~~	~~86~~	~~1172~~	~~73~~	~~1104~~	~~120~~	~~1213~~	~~86~~	~~110%~~	~~0~~
~~X05DF_121~~	~~23.9~~	~~1.11~~	~~0.1873~~	~~0.012~~	~~0.22831~~	~~15.03~~	~~1.6~~	~~0.582~~	~~0.045~~	~~0.52084~~	~~2955~~	~~180~~	~~2812~~	~~100~~	~~2708~~	~~110~~	~~2708~~	~~110~~	~~109%~~	~~0~~

Table 4: Kayak Detrital Zircon U-Pb Data - 23DF15

						Isotope ratios					Apparent ages (Ma)									
Analysis	U (ppm)	U/Th	207Pb/206Pb	± 2 sigma	error corr.	207Pb/235U	± 2 sigma	206Pb/238U	± 2 sigma	error corr.	206Pb/238U	± (Ma)	207Pb/235U	± (Ma)	206Pb/207Pb	± (Ma)	Best age (Ma)	± (Ma)	Ef. Conc (%)	Use? (1-y; 0-n)
23DF15 n = 106/120						use prop uncertainty														
WPF23_2	278	5.38	0.0547	0.0029	0.11752	0.552	0.055	0.0719	0.006	0.81327	447	36	441	35	370	110	447	36	100%	1
WPF23_3	488	8.8	0.0881	0.005	-0.062781	2.96	0.27	0.243	0.018	0.76057	1395	90	1377	69	1370	110	1395	90	102%	1
WPF23_4	850	2.7	0.055	0.0024	0.013943	0.5	0.043	0.0698	0.0065	0.92761	434	39	409	28	392	94	434	39	100%	1
WPF23_5	247	6.21	0.0559	0.0023	-0.24825	0.555	0.054	0.0726	0.0053	0.81929	451	31	450	36	427	90	451	31	100%	1
WPF23_6	286	9.24	0.0557	0.0029	-0.014417	0.579	0.075	0.0735	0.0073	0.91746	456	44	454	45	460	110	456	44	100%	1
WPF23_7	791	2.2	0.0593	0.0041	0.09483	0.547	0.041	0.0647	0.0031	0.48952	404	19	440	27	540	150	404	19	100%	1
WPF23_8	126.9	6.28	0.1138	0.0065	0.25483	5.64	0.46	0.356	0.025	0.71841	1950	120	1911	73	1870	100	1870	100	104%	1
WPF23_9	245	5.9	0.0546	0.0026	0.14072	0.526	0.049	0.0717	0.0066	0.87889	445	39	424	31	410	100	445	39	100%	1
WPF23_11	374	1.93	0.055	0.003	-0.13475	0.565	0.068	0.0759	0.0059	0.85793	471	35	463	43	380	120	471	35	100%	1
WPF23_12	346	3.29	0.0603	0.0049	-0.059438	0.468	0.061	0.0572	0.0055	0.77176	358	34	382	41	540	170	358	34	100%	1
WPF23_15	217	7.64	0.0592	0.0029	0.062722	0.758	0.046	0.0934	0.0038	0.67053	575	23	570	26	560	100	575	23	100%	1
WPF23_17	103.4	3.45	0.0613	0.004	0.30351	0.781	0.062	0.0907	0.0052	0.56728	559	31	587	37	620	140	559	31	100%	1
WPF23_18	167	4.36	0.0721	0.0039	0.0061165	0.999	0.08	0.0982	0.0049	0.67178	603	29	696	39	950	110	603	29	100%	1
WPF23_19	205	3.72	0.1667	0.0044	-0.028546	10.99	0.84	0.474	0.034	0.93396	2480	150	2498	71	2525	45	2525	45	98%	1
WPF23_20	1130	7.49	0.0588	0.0022	0.035731	0.501	0.045	0.0621	0.0052	0.88413	388	31	419	32	539	83	388	31	100%	1
WPF23_21	160	3.22	0.0663	0.0045	-0.12129	0.606	0.059	0.0673	0.0049	0.71869	419	29	483	39	780	140	419	29	100%	1
WPF23_23	132.9	3.38	0.1181	0.004	-0.029973	5.63	0.47	0.34	0.025	0.9048	1880	120	1898	69	1938	65	1938	65	97%	1
WPF23_24	773	4.74	0.0598	0.0018	-0.12598	0.515	0.03	0.0624	0.0031	0.78246	390	19	420	20	586	65	390	19	100%	1
WPF23_25	415	3.21	0.0576	0.0018	0.018793	0.499	0.03	0.0633	0.0036	0.88596	396	21	413	21	510	70	396	21	100%	1
WPF23_26	71.2	2.87	0.1734	0.0053	0.01865	11.02	0.64	0.458	0.023	0.844	2440	100	2522	51	2600	51	2600	51	94%	1
WPF23_27	237	3.48	0.1876	0.005	-0.33523	10.07	0.64	0.386	0.019	0.90658	2098	87	2435	59	2715	43	2715	43	77%	1
WPF23_28	129.5	2.92	0.1175	0.003	0.13182	5.19	0.29	0.332	0.02	0.91303	1839	97	1860	52	1912	46	1912	46	96%	1
WPF23_29	211	3.72	0.0769	0.0021	-0.1829	1.96	0.17	0.178	0.012	0.93484	1065	68	1096	57	1111	54	1065	68	96%	1
WPF23_30	1250	7.68	0.0561	0.0016	0.031761	0.563	0.041	0.0725	0.0049	0.92742	450	29	455	27	457	60	450	29	100%	1
WPF23_31	161	4.42	0.0733	0.0031	0.39417	0.725	0.037	0.0721	0.0035	0.63363	448	21	555	21	1031	87	448	21	100%	1
WPF23_32	379	6.64	0.0569	0.0019	-0.12026	0.554	0.044	0.0707	0.005	0.90128	440	30	444	28	471	72	440	30	100%	1
WPF23_33	598	2.96	0.0553	0.0016	-0.049964	0.489	0.035	0.0618	0.0037	0.92662	386	22	406	25	424	62	386	22	100%	1
WPF23_34	172	2.63	0.055	0.0014	-0.098188	0.498	0.041	0.0656	0.005	0.93909	409	30	417	29	406	55	409	30	100%	1
WPF23_35	362	5.82	0.0561	0.0016	-0.25418	0.543	0.036	0.0699	0.0037	0.89322	435	22	442	24	455	62	435	22	100%	1
WPF23_36	247	9.71	0.0591	0.0021	0.16944	0.558	0.041	0.0703	0.0053	0.91272	438	32	453	28	581	75	438	32	100%	1
WPF23_37	437	2.76	0.0561	0.0011	0.046831	0.502	0.019	0.0651	0.002	0.85215	406	12	414	14	475	41	406	12	100%	1
WPF23_38	146	5.52	0.0852	0.0031	0.25716	2.16	0.13	0.186	0.012	0.83634	1099	66	1171	45	1306	71	1099	66	84%	1
WPF23_39	121.7	4.17	0.1489	0.0048	-0.0547	8.39	0.66	0.407	0.028	0.9246	2190	120	2265	70	2333	53	2333	53	94%	1
WPF23_40	587	5.53	0.0556	0.0017	-0.19942	0.531	0.042	0.067	0.0043	0.87931	418	26	429	28	439	72	418	26	100%	1
WPF23_41	308	3.53	0.0596	0.0016	0.067334	0.654	0.035	0.0794	0.004	0.89188	492	24	509	21	580	57	492	24	100%	1
WPF23_42	270	3.99	0.0562	0.0015	0.035954	0.544	0.031	0.0706	0.0038	0.90091	439	23	439	21	459	57	439	23	100%	1
WPF23_43	143.5	5.92	0.0545	0.0019	-0.0067047	0.518	0.039	0.0656	0.0037	0.87462	409	22	421	26	394	74	409	22	100%	1
WPF23_44	327	2.59	0.0552	0.0015	-0.12488	0.501	0.036	0.064	0.0037	0.89628	400	22	409	24	423	64	400	22	100%	1
WPF23_45	187	3.42	0.1193	0.0037	0.17025	5.59	0.37	0.343	0.022	0.88109	1890	110	1900	56	1945	54	1945	54	97%	1
WPF23_46	130	5.29	0.083	0.0028	-0.14302	2.06	0.18	0.18	0.014	0.9145	1061	75	1140	62	1267	67	1061	75	84%	1
WPF23_47	28.2	5.94	0.156	0.0062	-0.13835	8.21	0.68	0.384	0.03	0.90319	2110	140	2260	80	2399	65	2399	65	88%	1
WPF23_48	1016	4.96	0.0561	0.0018	-0.27065	0.534	0.041	0.0692	0.0042	0.92588	431	25	431	27	440	74	431	25	100%	1
WPF23_49	418	1.425	0.0561	0.0011	0.073764	0.571	0.025	0.0721	0.0031	0.85546	449	19	457	16	449	45	449	19	100%	1
WPF23_50	52.9	2.3	0.1174	0.0033	-0.12889	5.56	0.4	0.335	0.02	0.91196	1857	96	1902	63	1918	48	1918	48	97%	1
WPF23_51	470	2.9	0.0553	0.0018	-0.060392	0.508	0.039	0.0653	0.004	0.91488	407	24	414	26	422	73	407	24	100%	1
WPF23_52	136.6	5.18	0.057	0.0018	-0.16899	0.54	0.038	0.0698	0.0044	0.8912	434	27	436	25	478	70	434	27	100%	1
WPF23_53	262	11.4	0.1692	0.0042	-0.072693	11.48	0.86	0.487	0.029	0.9039	2550	130	2557	62	2564	48	2564	48	99%	1
WPF23_55	144.2	4.34	0.1124	0.0039	0.10245	3.53	0.24	0.23	0.015	0.86941	1330	75	1533	54	1826	62	1330	75	73%	1
WPF23_56	80	4.43	0.0768	0.0023	-0.21924	1.92	0.16	0.184	0.013	0.93903	1084	71	1086	55	1116	58	1084	71	97%	1
WPF23_57	14.6	7.67	0.176	0.0066	-0.2133	11.84	0.89	0.488	0.03	0.88317	2570	130	2569	72	2603	63	2603	63	99%	1
WPF23_58	363	2.38	0.0544	0.0019	0.022585	0.473	0.034	0.0638	0.0041	0.88685	398	25	395	24	370	77	398	25	100%	1
WPF23_59	245	2.81	0.1511	0.0044	-0.066076	9.11	0.69	0.437	0.03	0.9348	2320	130	2338	71	2350	49	2350	49	99%	1
WPF23_60	363	2.25	0.1232	0.0033	-0.10075	6.12	0.43	0.357	0.022	0.91511	1960	100	1977	61	2004	49	2004	49	98%	1
WPF23_61	231	9.91	0.0564	0.0017	-0.049415	0.537	0.041	0.0693	0.0048	0.90646	432	29	433	26	467	70	432	29	100%	1
WPF23_62	525	13.5	0.082	0.0021	-0.045941	2.26	0.14	0.203	0.012	0.91775	1191	64	1191	44	1239	50	1191	64	96%	1
WPF23_63	119	6.25	0.1298	0.0067	-0.086972	5.98	0.55	0.339	0.026	0.77295	1870	130	1945	80	2088	89	2088	89	90%	1
WPF23_64	143.1	8.4	0.0912	0.0029	-0.022755	3.11	0.22	0.245	0.016	0.88599	1407	83	1421	55	1450	63	1450	63	97%	1
WPF23_65	560	2.36	0.059	0.0012	-0.1002	0.535	0.024	0.067	0.0027	0.88616	418	17	437	17	570	46	418	17	100%	1
WPF23_66	883	2.57	0.0554	0.0013	-0.098796	0.497	0.027	0.0649	0.0031	0.91352	405	19	408	18	430	55	405	19	100%	1
WPF23_67	380	6.66	0.1128	0.0034	-0.094257	5.17	0.39	0.323	0.02	0.87193	1796	97	1828	63	1835	55	1835	55	98%	1
WPF23_68	436	2.19	0.0568	0.0017	0.19631	0.517	0.026	0.0672	0.0035	0.84736	419	21	425	17	481	65	419	21	100%	1
WPF23_69	154	5.69	0.179	0.0067	-0.10475	12.2	1	0.494	0.034	0.89216	2570	140	2606	77	2631	61	2631	61	98%	1
WPF23_70	802	8.54	0.1058	0.002	0.38317	4.5	0.15	0.309	0.011	0.86879	1732	53	1728	27	1725	34	1725	34	100%	1
WPF23_71	404	5.68	0.0577	0.0022	0.24474	0.554	0.031	0.0704	0.0032	0.76872	438	19	450	21	512	86	438	19	100%	1
WPF23_72	226	5.93	0.1179	0.0045	0.08548	5.7	0.47	0.354	0.028	0.8608	1940	130	1921	73	1935	68	1935	68	100%	1
WPF23_73	240	5.25	0.074	0.0021	-0.13646	1.75	0.14	0.174	0.012	0.92258	1030	65	1034	53	1031	58	1030	65	100%	1
WPF23_74	190.5	4.79	0.1462	0.0066	-0.08547	6.69	0.44	0.332	0.016	0.86196	1845	77	2058	55	2283	77	2283	77	81%	1
WPF23_75	265	11.15	0.0825	0.0027	0.36509	2.174	0.084	0.195	0.0065	0.6453	1148	35	1170	27	1268	63	1148	35	91%	1
WPF23_76	146	3.24	0.1314	0.0054	-0.0016871	6.31	0.57	0.353	0.028	0.91764	1940	130	1996	74	2111	74	2111	74	92%	1
WPF23_77	869	4.88	0.0553	0.0016	-0.053795	0.464	0.031	0.0609	0.0038	0.84958	380	23	385	22	412	65	380	23	100%	1
WPF23_78	268	6.31	0.0832	0.0036	0.37025	2.15	0.11	0.1862	0.0088	0.6398	1099	47	1165	37	1252	86	1099	47	88%	1
WPF23_79	290	1.91	0.0557	0.0016	-0.082156	0.483	0.028	0.0627	0.0029	0.87178	392	18	399	19	453	70	392	18	100%	1
WPF23_82	192	3.88	0.0549	0.002	0.18447	0.481	0.033	0.063	0.0037	0.8326	394	22	396	22	388	82	394	22	100%	1
WPF23_83	483	8.71	0.0898	0.0024	-0.0065011	2.52	0.21	0.196	0.014	0.92937	1153	74	1271	61	1414	53	1153	74	82%	1
WPF23_84	442	86	0.0731	0.0019	0.28975	1.53	0.071	0.1556	0.0079	0.87056	931	44	939	28	1018	49	931	44	91%	1
WPF23_85	467	23.6	0.0733	0.0021	0.083898	1.68	0.1	0.1684	0.0088	0.91193	1002	48	995	37	1012	59	1002	48	99%	1
WPF23_86	198	3.53	0.0607	0.002	-0.30522	0.585	0.045	0.0701	0.0044	0.90228	436	26	469	30	616	70	436	26	100%	1
WPF23_87	89.5	3.77	0.0571	0.0028	-0.10942	0.52	0.047	0.0651	0.0045	0.87627	406	27	426	32	480	110	406	27	100%	1
WPF23_88	190	5.66	0.1228	0.0037	-0.36395	5.91	0.43	0.353	0.02	0.93404	1943	94	1958	63	1988	55	1988	55	98%	1
WPF23_89	82.7	2.25	0.0625	0.0019	0.049178	0.646	0.029	0.0756	0.003	0.81313	470	18	508	19	680	65	470	18	100%	1
WPF23_90	731	2.7	0.0547	0.0013	-0.05556	0.503	0.03	0.0669	0.0037	0.91444	417	22	416	21	391	53	417	22	100%	1
WPF23_91	237	9.5	0.056	0.0014	0.12541	0.481	0.022	0.0625	0.0027	0.79981	391	17	401	14	467	56	391	17	100%	1
WPF23_92	238	4.85	0.0602	0.0029	0.16006	0.592	0.041	0.0736	0.0052	0.79802	457	31	476	28	640	100	457	31	100%	1
WPF23_93	476	1.93	0.0556	0.0017	-0.053796	0.494	0.033	0.0649	0.0038	0.86017	405	23	406	22	425	66	405	23	100%	1
WPF23_94	96.6	3.67	0.0765	0.0019	-0.26585	1.9	0.14	0.179	0.011	0.93786	1058	58	1086	51	1110	51	1058	58	95%	1
WPF23_95	505	1.62	0.0555	0.0011	-0.21528	0.492	0.033	0.064	0.0034	0.93056	399	20	404	22	425	46	399	20	100%	1
WPF23_96	190	2.81	0.0852	0.003	-0.10173	2.78	0.24	0.234	0.017	0.89907	1352	87	1343	63	1316	70	1352	87	103%	1
WPF23_97	520	4.28	0.1088	0.003	-0.018388	4.84	0.26	0.323	0.015	0.83991	1799	73	1790	46	1789	51	1789	51	101%	1
WPF23_98	21.8	2.53	0.1255	0.004	0.17816	4.56	0.3	0.257	0.015	0.8674	1470	75	1728	54	2026	57	2026	57	73%	1
WPF23_101	112.4	1.92	0.107	0.01	-0.28357	1.28	0.19	0.0827	0.0058	0.59041	512	34	796	66	1690	160	512	34	100%	1
WPF23_102	203	3.85	0.0559	0.0021	-0.11298	0.517	0.049	0.0662	0.0056	0.90937	413	34	418	32	428	84	413	34	100%	1
WPF23_104	265	3.21	0.1105	0.0032	0.0078495	5.07	0.36	0.325	0.02	0.88521	1809	97	1814	59	1800	53	1800	53	101%	1
WPF23_105	725	5.86	0.0568	0.0014	0.22666	0.685	0.041	0.0855	0.005	0.91005	528	30	527	24	475	54	528	30	100%	1
WPF23_107	137.3	3.8	0.0931	0.0026	0.42779	2.61	0.13	0.206	0.01	0.78504	1203	54	1303	35	1482	53	1203	54	81%	1
WPF23_108	114.7	0.998	0.0849	0.0029	0.12109	1.512	0.082	0.1273	0.0059	0.74435	772	34	930	33	1327	67	772	34	100%	1

Table 4: Kayak Detrital Zircon U-Pb Data - 23DF15 - cont.

WPF23_109	395	1.8	0.0619	0.0026	-0.014349	0.564	0.038	0.066	0.0036	0.81686	412	22	452	24	677	89	412	22	100%	1
WPF23_110	172	1.64	0.1281	0.0033	0.049426	6.79	0.49	0.387	0.026	0.92727	2100	120	2076	64	2065	45	2065	45	102%	1
WPF23_112	211	1.02	0.1231	0.0032	0.32761	5.18	0.29	0.308	0.019	0.91612	1726	92	1847	50	1995	46	1995	46	87%	1
WPF23_113	79.6	1.93	0.1016	0.003	0.023787	3.62	0.23	0.266	0.017	0.88148	1516	87	1562	54	1644	54	1644	54	92%	1
WPF23_114	81.6	5.87	0.0647	0.0032	0.017043	0.642	0.064	0.0713	0.0053	0.8591	443	32	497	39	750	100	443	32	100%	1
WPF23_115	729	4.06	0.0583	0.0021	0.29759	0.57	0.033	0.0711	0.004	0.81505	442	24	456	21	523	77	442	24	100%	1
WPF23_116	327	3.71	0.0554	0.0018	-0.094379	0.525	0.043	0.0686	0.0047	0.93477	427	28	425	28	436	73	427	28	100%	1
WPF23_117	969	5.06	0.0555	0.0018	0.33532	0.548	0.033	0.0709	0.0041	0.8234	441	25	442	22	435	68	441	25	100%	1
WPF23_118	543	3.05	0.0591	0.0019	-0.070981	0.596	0.034	0.0722	0.0031	0.82298	449	19	473	21	570	72	449	19	100%	1
WPF23_119	375	5.02	0.0558	0.0023	0.058222	0.495	0.04	0.0648	0.0047	0.871	404	28	405	26	422	87	404	28	100%	1
WPF23_120	212	3.19	0.1761	0.004	0.093173	11.58	0.47	0.476	0.017	0.80657	2507	74	2577	38	2619	36	2619	36	96%	1
WPF23_1	99	6.6	0.056	0.0034	-0.025753	0.529	0.069	0.0697	0.0078	0.93242	433	47	422	44	410	130	433	47	100%	0
WPF23_10	84	5.3	0.065	0.0064	0.12259	0.71	0.1	0.075	0.0098	0.82575	464	58	526	61	660	200	464	58	100%	0
WPF23_13	179	4.72	0.0541	0.0035	-0.081701	0.564	0.086	0.0718	0.0079	0.89551	446	47	442	52	390	120	446	47	100%	0
WPF23_14	390	2.55	0.0536	0.0026	-0.026477	0.536	0.059	0.075	0.0078	0.83533	464	47	430	38	340	110	464	47	100%	0
WPF23_16	51.3	3.33	0.0586	0.0035	0.1361	0.86	0.11	0.104	0.011	0.87914	633	65	628	59	510	130	633	65	100%	0
WPF23_22	146.4	3.06	0.0848	0.0023	0.26764	2.83	0.13	0.242	0.012	0.80758	1397	63	1364	33	1303	51	1397	63	107%	0
WPF23_54	470	13.9	0.0757	0.0016	0.32062	2.18	0.1	0.208	0.0099	0.89032	1216	52	1170	32	1082	43	1216	52	112%	0
WPF23_80	142	1.28	0.1187	0.0045	0.096592	3.21	0.25	0.194	0.014	0.85077	1141	76	1447	61	1927	68	1141	76	59%	0
WPF23_81	683	5.01	0.0719	0.0031	-0.11317	1.91	0.21	0.185	0.018	0.90793	1087	95	1061	73	978	88	1087	95	111%	0
WPF23_99	363	3.78	0.1068	0.0019	0.058491	5.13	0.34	0.347	0.022	0.94261	1910	100	1835	56	1741	33	1741	33	110%	0
WPF23_100	132	4.94	0.0677	0.0032	0.056896	0.78	0.11	0.082	0.01	0.9233	505	59	573	56	832	96	505	59	100%	0
WPF23_103	3.8	1.06	0.699	0.068	0.12622	46.6	8.5	0.47	0.09	0.913	2400	360	3790	180	4720	160	4720	160	51%	0
WPF23_106	105	2	0.1082	0.0045	0.063086	2.89	0.32	0.183	0.018	0.90861	1080	100	1363	86	1770	79	1080	100	61%	0
WPF23_111	3.66	4.24	0.737	0.081	0.19629	32.3	7.9	0.313	0.062	0.89387	1700	290	3390	210	4810	190	4810	190	35%	0

Table 5: Beaucoup Detrital Zircon U-Pb Data - J1415

						Isotope ratios					Apparent ages (Ma)								
Analysis	U (ppm)	U/Th	207Pb/206Pb	± 2 sigma	error corr.	207Pb/235U	± 2 sigma	206Pb/238U	± 2 sigma	error corr.	206Pb/238U	± (Ma)	207Pb/235U	± (Ma)	206Pb/207Pb	± (Ma)	Best age (Ma)	± (Ma)	Ef. Conc (%)	Use? (1-y; 0-n)
J1415 n=122/130						use prop uncertainty														
J1415_1	72	3.5	0.0565	0.0032	0.38571	0.545	0.039	0.0698	0.0036	0.080714	435	22	441	26	440	120	435	22	100%	1
J1415_2	112.8	1.66	0.1024	0.0031	0.41821	4.05	0.23	0.2876	0.015	0.52778	1635	77	1646	45	1661	57	1661	57	98%	1
J1415_5	40.8	3.73	0.0589	0.0055	-0.32006	0.577	0.075	0.0677	0.0034	0.54443	422	21	442	35	480	190	422	21	100%	1
J1415_6	66.2	1.611	0.0901	0.0025	0.37859	3.277	0.19	0.2606	0.013	0.4994	1492	68	1473	46	1421	54	1421	54	105%	1
J1415_7	62.9	1.746	0.1526	0.0036	0.481	9.59	0.54	0.4598	0.023	0.72667	2437	100	2397	53	2372	41	2372	41	103%	1
J1415_8	354	6.34	0.1085	0.003	0.56538	3.2	0.2	0.2125	0.012	0.79465	1241	65	1454	48	1769	50	1241	65	70%	1
J1415_9	57.8	3.04	0.1059	0.0036	0.05214	4.65	0.28	0.3164	0.016	0.5906	1771	78	1762	54	1740	63	1740	63	102%	1
J1415_10	184.4	1.831	0.1154	0.0025	0.1339	5.29	0.31	0.3275	0.016	0.79779	1832	82	1868	52	1884	39	1884	39	97%	1
J1415_11	199	6.3	0.086	0.0029	0.31651	2.074	0.13	0.1717	0.01	0.71156	1021	55	1138	42	1328	67	1021	55	77%	1
J1415_12	732	24.95	0.071	0.0016	0.31008	1.488	0.083	0.1537	0.0076	0.7351	921	43	927	33	961	44	921	43	96%	1
J1415_13	97.7	3.13	0.0608	0.0027	0.01643	0.555	0.04	0.0656	0.0037	0.47765	409	22	447	26	608	98	409	22	100%	1
J1415_14	189.8	3.74	0.0552	0.0025	0.12664	0.519	0.038	0.0665	0.0035	0.44293	417	22	423	25	412	100	417	22	100%	1
J1415_15	129.4	1.81	0.1072	0.0029	0.32878	4.79	0.3	0.316	0.018	0.80081	1776	93	1778	53	1747	49	1747	49	102%	1
J1415_16	134.4	3.11	0.0577	0.0029	0.24143	0.461	0.032	0.0577	0.0028	0.013317	362.9	18	384	22	490	110	362.9	18	100%	1
J1415_18	71	1.259	0.2612	0.0058	0.3017	22.8	1.3	0.636	0.032	0.77488	3170	130	3216	55	3257	37	3257	37	97%	1
J1415_19	269	2.166	0.0553	0.0023	0.21605	0.488	0.033	0.065	0.0036	0.49981	406	22	405	24	421	89	406	22	100%	1
J1415_20	60.4	2.75	0.0605	0.0053	0.21945	0.533	0.049	0.0655	0.0036	0.032799	413	21	431	32	540	170	413	21	100%	1
J1415_21	75.3	3.76	0.0555	0.0038	0.28817	0.533	0.042	0.0687	0.0034	0.036821	428.3	20	432	28	390	150	428.3	20	100%	1
J1415_23	149	4.43	0.0646	0.0034	0.27957	0.648	0.044	0.0727	0.0036	0.012998	452.6	22	506	27	750	120	452.6	22	100%	1
J1415_24	78.4	3.47	0.0563	0.0033	-0.067753	0.512	0.04	0.0667	0.0033	0.39232	416.5	20	418	27	430	120	416.5	20	100%	1
J1415_25	191.2	1.99	0.0574	0.0026	0.24538	0.531	0.035	0.0671	0.0034	0.30504	418	21	432	23	481	100	418	21	100%	1
J1415_26	156.5	3.6	0.0565	0.0026	0.17909	0.523	0.035	0.0667	0.0036	0.28076	416	21	426	23	446	98	416	21	100%	1
J1415_27	14.44	1.3	0.1118	0.0051	0.21986	4.88	0.37	0.313	0.02	0.44548	1753	96	1789	64	1828	75	1828	75	96%	1
J1415_28	88	3.11	0.1223	0.0042	0.18843	5.89	0.39	0.352	0.021	0.73452	1942	100	1962	54	1990	63	1990	63	98%	1
J1415_29	137.3	2.13	0.0613	0.0028	0.31992	0.654	0.046	0.077	0.005	0.53553	478	30	509	28	660	110	478	30	100%	1
J1415_30	353	3.35	0.0634	0.0029	-0.33999	0.587	0.042	0.0669	0.0035	0.56974	417	21	463	23	700	93	417	21	100%	1
J1415_31	194.7	1.686	0.273	0.019	-0.66193	3.17	0.34	0.0819	0.0046	0.84255	508	27	1436	84	3300	120	508	27	100%	1
J1415_32	379	1.335	0.0555	0.0017	0.35857	0.486	0.028	0.0643	0.0032	0.52238	401.9	19	403.6	19	422	68	401.9	19	100%	1
J1415_33	92.3	3.68	0.0677	0.0039	0.17738	0.655	0.052	0.0699	0.004	0.37306	435	24	509	32	820	130	435	24	100%	1
J1415_34	270.5	1.49	0.0849	0.0074	-0.70049	0.807	0.093	0.0699	0.0039	0.8538	435	24	593	49	1250	150	435	24	100%	1
J1415_35	188.4	3.46	0.161	0.004	-0.027124	9.55	0.65	0.429	0.025	0.91277	2295	110	2384	63	2462	42	2462	42	93%	1
J1415_36	80.9	3.89	0.1028	0.0032	0.31405	3.97	0.24	0.2821	0.014	0.56217	1601	73	1625	50	1676	60	1676	60	96%	1
J1415_37	227	2.31	0.0556	0.0016	0.18618	0.445	0.028	0.0577	0.003	0.63851	361.3	18	373	19	440	68	361.3	18	100%	1
J1415_38	308.6	1.519	0.0549	0.0018	0.19429	0.49	0.029	0.065	0.0033	0.59802	406	20	404.2	20	397	73	406	20	100%	1
J1415_39	220	2.19	0.0604	0.0021	0.05457	0.55	0.042	0.0676	0.0039	0.60287	422	24	447	26	604	78	422	24	100%	1
J1415_41	231	3.11	0.0566	0.0021	0.45287	0.534	0.034	0.0673	0.0035	0.26795	420	21	434	22	460	83	420	21	100%	1
J1415_42	58.5	5.25	0.054	0.0026	0.13161	0.541	0.04	0.0702	0.0037	0.45506	437	22	438	26	380	110	437	22	100%	1
J1415_43	84.5	3.55	0.0576	0.0039	0.13405	0.525	0.043	0.067	0.0037	0.22081	418	22	426	28	490	130	418	22	100%	1
J1415_44	116.4	3.72	0.0925	0.0031	0.34795	3.19	0.19	0.2472	0.013	0.50995	1423	65	1451	47	1488	62	1488	62	96%	1
J1415_45	220	13.03	0.0576	0.0026	-0.043323	0.481	0.033	0.061	0.0032	0.57158	382	19	398	23	508	95	382	19	100%	1
J1415_46	51.9	3.81	0.0609	0.0045	0.067535	0.559	0.053	0.0666	0.0036	0.47348	416	22	453	35	600	150	416	22	100%	1
J1415_47	803	1.58	0.0582	0.0022	0.018522	0.45	0.031	0.0565	0.0031	0.74319	354	19	379	23	552	74	354	19	100%	1
J1415_48	175.1	3.15	0.0602	0.0026	0.2043	0.56	0.038	0.0667	0.0037	0.47546	416	22	451	24	588	92	416	22	100%	1
J1415_49	85.4	6.02	0.0535	0.0029	0.075585	0.52	0.044	0.0691	0.004	0.42531	431	24	423	29	320	120	431	24	100%	1
J1415_50	48.1	0.942	0.0849	0.0063	0.30176	2.14	0.22	0.181	0.016	0.5458	1071	88	1157	71	1390	190	1071	88	77%	1
J1415_52	48.5	3.19	0.0566	0.0046	0.16652	0.541	0.054	0.0689	0.0037	0.16791	430	22	435	35	460	180	430	22	100%	1
J1415_53	122.1	3.08	0.0569	0.0034	-0.037339	0.545	0.041	0.0714	0.0036	0.43826	444	22	440	26	450	120	444	22	100%	1
J1415_54	203.6	4.25	0.0939	0.0028	0.26907	2.898	0.18	0.2259	0.014	0.80179	1311	71	1384	43	1499	56	1311	71	87%	1
J1415_55	197.7	1.598	0.0558	0.0021	0.22614	0.53	0.034	0.0684	0.0037	0.5185	426	22	431	22	428	82	426	22	100%	1
J1415_56	204	3.08	0.0556	0.0027	0.12264	0.545	0.037	0.0709	0.0039	0.36039	442	23	441	25	410	110	442	23	100%	1
J1415_57	35.4	0.733	0.809	0.023	0.1563	92	7.2	0.823	0.063	0.90458	3840	230	4597	79	4984	52	4984	52	77%	1
J1415_58	328	3.99	0.0796	0.0019	0.17461	2.128	0.13	0.194	0.0099	0.79912	1143	54	1155	43	1183	48	1143	54	97%	1
J1415_59	276	3.63	0.0556	0.002	0.47946	0.575	0.034	0.0749	0.0038	0.37282	466	23	460	22	435	77	466	23	100%	1
J1415_60	127.7	2.46	0.176	0.0047	-0.057889	11.81	0.73	0.483	0.025	0.74133	2539	110	2584	58	2611	46	2611	46	97%	1
J1415_61	188.1	2.26	0.091	0.011	-0.60092	0.89	0.14	0.069	0.0041	0.75489	430	25	624	74	1310	250	430	25	100%	1
J1415_62	87	4.93	0.1115	0.003	0.30415	5.08	0.31	0.334	0.019	0.67775	1854	89	1830	51	1820	49	1820	49	102%	1
J1415_63	90.2	1.594	0.1112	0.0036	0.33098	5.04	0.29	0.3305	0.016	0.43308	1840	79	1824	49	1810	59	1810	59	102%	1
J1415_64	37.9	3.12	0.0843	0.0038	0.28579	2.4	0.16	0.2097	0.012	0.53087	1226	66	1245	50	1326	78	1226	66	92%	1
J1415_65	76.7	1.718	0.1142	0.0035	0.23288	5	0.31	0.3134	0.017	0.634	1764	79	1816	52	1861	55	1861	55	95%	1
J1415_66	147	3.38	0.0535	0.0024	0.4362	0.507	0.031	0.069	0.0038	0.37766	430	23	416	21	328	97	430	23	100%	1
J1415_67	257	3.84	0.0596	0.0022	0.37719	0.479	0.029	0.0576	0.0029	0.38069	360.7	18	397	20	573	79	360.7	18	100%	1
J1415_68	133.2	3.3	0.2534	0.0064	0.23686	21.94	1.2	0.626	0.03	0.61917	3151	120	3184	57	3203	40	3203	40	98%	1
J1415_69	55.6	2.692	0.1022	0.0034	0.32566	4.13	0.25	0.2949	0.015	0.53529	1665	75	1662	51	1656	60	1656	60	101%	1
J1415_70	369	2.82	0.055	0.0019	0.40439	0.509	0.03	0.0675	0.0033	0.25662	421.1	20	417	20	410	76	421.1	20	100%	1
J1415_71	176.1	3.89	0.0534	0.0022	0.015476	0.464	0.035	0.0616	0.0032	0.29294	385.2	19	385	24	327	89	385.2	19	100%	1
J1415_73	73.8	2.38	0.1508	0.004	0.17943	9.11	0.54	0.442	0.022	0.82138	2360	98	2345	56	2350	46	2350	46	100%	1
J1415_74	269	1.61	0.0559	0.0021	0.35499	0.519	0.031	0.0691	0.0036	0.55702	431	21	426	23	430	84	431	21	100%	1
J1415_75	210	2.41	0.1014	0.0043	0.30483	4.11	0.27	0.292	0.017	0.54863	1650	82	1663	58	1647	74	1647	74	100%	1
J1415_76	59.5	1.703	0.1174	0.0035	0.31085	5.31	0.32	0.3276	0.017	0.71805	1835	78	1876	55	1909	54	1909	54	96%	1
J1415_77	141	2.82	0.0718	0.002	0.16807	1.632	0.099	0.1638	0.0083	0.6721	978	46	981	38	973	56	978	46	101%	1
J1415_78	294	2.97	0.0562	0.0026	0.56892	0.52	0.037	0.0689	0.0044	0.73464	429	27	424	24	434	100	429	27	100%	1
J1415_79	382	13.94	0.072	0.0024	-0.00095371	1.431	0.1	0.1428	0.0085	0.84889	860	48	898	43	983	69	860	48	87%	1
J1415_80	321	11.71	0.0697	0.0022	0.4653	1.502	0.087	0.1576	0.0081	0.51726	943	45	930	35	908	66	943	45	104%	1
J1415_81	109.7	1.74	0.066	0.0031	0.33968	0.56	0.039	0.0619	0.0032	0.31668	387.2	19	450	26	796	99	387.2	19	100%	1
J1415_82	106	7.26	0.0605	0.0033	0.10643	0.568	0.044	0.0679	0.0035	0.25662	424	21	454	28	610	110	424	21	100%	1
J1415_83	144	5.31	0.0556	0.0021	0.21941	0.536	0.034	0.0705	0.0036	0.36747	439	22	435	22	418	84	439	22	100%	1
J1415_84	155.6	4.37	0.0547	0.0021	0.45745	0.525	0.032	0.0694	0.0035	0.17576	433	21	428	21	383	84	433	21	100%	1
J1415_85	404	1.74	0.0549	0.0016	0.2313	0.525	0.033	0.0685	0.0036	0.60683	427	22	427	22	399	68	427	22	100%	1
J1415_86	361	2.141	0.0555	0.0016	0.0017513	0.503	0.033	0.0659	0.0034	0.65771	412.9	19	413	22	435	71	412.9	19	100%	1
J1415_87	634	1.108	0.054	0.0018	0.23777	0.454	0.028	0.0613	0.0034	0.66472	384	20	380	20	370	76	384	20	100%	1
J1415_88	115.8	2.98	0.0573	0.0029	0.31727	0.532	0.036	0.0689	0.0036	0.13833	430	21	432	24	480	110	430	21	100%	1
J1415_89	169.5	2.23	0.0582	0.0032	0.051687	0.525	0.042	0.066	0.0038	0.45319	412	23	426	28	530	110	412	23	100%	1
J1415_90	166.9	2.01	0.0565	0.0033	0.46686	0.492	0.035	0.0615	0.003	-0.051799	384.8	18	405	24	490	130	384.8	18	100%	1
J1415_91	335	1.496	0.0544	0.0019	0.36019	0.483	0.03	0.0642	0.0033	0.44001	401	20	399	21	389	81	401	20	100%	1
J1415_92	48.9	1.243	0.2009	0.0059	0.25233	14.21	0.86	0.516	0.026	0.57825	2681	110	2770	58	2828	49	2828	49	95%	1
J1415_93	116	2.49	0.1856	0.0047	0.35892	13.21	0.77	0.514	0.026	0.74179	2672	110	2697	52	2700	42	2700	42	99%	1
J1415_94	655	3.32	0.0588	0.0017	0.29837	0.532	0.03	0.0658	0.0032	0.31183	410.7	19	434.5	21	552	65	410.7	19	100%	1
J1415_95	316	6.8	0.1003	0.0032	0.58577	4.08	0.24	0.3	0.017	0.70244	1688	84	1649	48	1631	58	1631	58	103%	1
J1415_96	50	3.96	0.0583	0.0046	0.025507	0.672	0.071	0.082	0.0051	0.30937	508	30	515	42	520	160	508	30	100%	1
J1415_97	133.3	3.52	0.055	0.0027	0.26701	0.437	0.031	0.0573	0.0032	0.20551	359	20	370	20	390	110	359	20	100%	1
J1415_98	124.7	2.313	0.0562	0.0025	0.083663	0.489	0.034	0.0644	0.0034	0.45393	402	20	406	24	439	97	402	20	100%	1
J1415_99	176.1	1.7	0.0567	0.0022	0.077321	0.488	0.032	0.0632	0.0033	0.66598	395	20	406	23	502	80	395	20	100%	1
J1415_100	77.9	5.55	0.0924	0.0029	0.40819	2.917	0.17	0.2281	0.012	0.41916	1324	61	1388	46	1468	60	1324	61	90%	1
J1415_101	240.9	2.89	0.0558	0.0018	0.26953	0.437	0.026	0.0578	0.0029	0.37163	361.9	18	370	20	435	71	361.9	18	100%	1
J1415_102	144.8	1.918	0.0574	0.0026	-0.053466	0.503	0.036	0.0638	0.0035	0.50665	399	21	412	24	483	99	399	21	100%	1

Table 5: Beaucoup Detrital Zircon U-Pb Data - J1415 - cont.

J1415_103	69	4.83	0.0581	0.0041	0.21021	0.533	0.046	0.0676	0.0034	0.042175	421.4	20	431	30	480	140	421.4	20	100%	1
J1415_104	103.1	3.1	0.0586	0.0039	0.27985	0.564	0.043	0.0716	0.0036	0.15299	446	22	452	28	500	140	446	22	100%	1
J1415_105	550	2.53	0.0562	0.0018	0.38862	0.46	0.027	0.0601	0.0031	0.50579	376.4	19	383.7	19	463	68	376.4	19	100%	1
J1415_106	342.1	2.38	0.1089	0.0035	-0.026189	4.59	0.3	0.3054	0.015	0.66555	1717	76	1748	53	1774	57	1774	57	97%	1
J1415_107	291	1.171	0.0548	0.0024	0.20008	0.459	0.033	0.0616	0.0035	0.62408	385	21	383	23	438	100	385	21	100%	1
J1415_108	166	3.97	0.0766	0.0025	0.50171	1.876	0.11	0.1801	0.0095	0.60825	1067	52	1071	40	1100	64	1067	52	97%	1
J1415_109	203	3.74	0.0533	0.0024	0.4682	0.536	0.036	0.0716	0.004	0.39348	446	24	434	24	320	96	446	24	100%	1
J1415_110	59.8	4.78	0.0531	0.0031	0.1829	0.538	0.043	0.0707	0.0039	0.33752	440	23	435	29	300	120	440	23	100%	1
J1415_111	75	2.83	0.0775	0.0023	0.23147	1.909	0.12	0.1771	0.0088	0.51911	1051	48	1082	40	1126	59	1051	48	93%	1
J1415_113	452	1.385	0.0555	0.0017	0.41991	0.499	0.028	0.0653	0.0033	0.39604	408	20	411.1	19	421	67	408	20	100%	1
J1415_114	34.7	2.14	0.1825	0.006	0.27623	13.01	0.8	0.522	0.029	0.69256	2706	120	2682	60	2668	54	2668	54	101%	1
J1415_115	96.8	3.77	0.0714	0.0043	0.070408	0.702	0.061	0.0702	0.0037	0.45251	437	23	536	36	990	120	437	23	100%	1
J1415_116	103.1	1.684	0.1826	0.0063	0.39594	13.5	0.83	0.531	0.028	0.53021	2744	120	2711	58	2668	57	2668	57	103%	1
J1415_117	173	10.25	0.0568	0.0021	-0.11373	0.546	0.036	0.0698	0.0034	0.58268	435	21	442	24	479	85	435	21	100%	1
J1415_118	12.46	2.06	0.1122	0.0059	0.3481	5.08	0.35	0.3339	0.017	0.29388	1856	84	1825	59	1824	92	1824	92	102%	1
J1415_119	161.5	1.014	0.102	0.003	0.32089	4.09	0.24	0.2934	0.015	0.61924	1658	75	1655	46	1654	55	1654	55	100%	1
J1415_120	107.4	2.39	0.0573	0.0024	0.31989	0.524	0.034	0.0666	0.0034	0.43407	416	21	427	23	497	97	416	21	100%	1
J1415_121	128	4.86	0.099	0.018	-0.48413	1.1	0.24	0.075	0.0044	0.75284	466	26	706	100	1380	310	466	26	100%	1
J1415_122	94.5	4.99	0.0768	0.0029	0.23457	1.521	0.1	0.1434	0.0073	0.35015	864	41	945	37	1116	80	864	41	77%	1
J1415_123	341	3.87	0.0909	0.0024	0.43581	3.142	0.19	0.2509	0.014	0.70831	1442	70	1441	46	1457	55	1457	55	99%	1
J1415_124	89.4	3.1	0.0863	0.0029	0.14227	2.758	0.17	0.2308	0.013	0.59845	1345	69	1342	45	1347	62	1345	69	100%	1
J1415_125	127.3	3.87	0.0599	0.0032	0.32635	0.585	0.041	0.0706	0.0037	0.21075	440	22	466	27	590	120	440	22	100%	1
J1415_126	246	1.799	0.0598	0.0027	0.080516	0.543	0.04	0.0665	0.0035	0.45687	415	21	439	26	570	100	415	21	100%	1
J1415_127	142.8	3.84	0.059	0.0032	0.27245	0.555	0.039	0.068	0.0036	0.2167	424	22	447	25	560	130	424	22	100%	1
J1415_128	63.4	3.33	0.0627	0.0044	0.013803	0.595	0.057	0.07	0.0045	0.38588	436	27	470	36	640	140	436	27	100%	1
J1415_129	133.3	2.75	0.0583	0.0027	0.16085	0.513	0.036	0.063	0.0031	0.22112	393.5	19	419	24	540	110	393.5	19	100%	1
J1415_130	180	2.57	0.0555	0.0022	0.10493	0.547	0.04	0.0703	0.004	0.49122	438	24	441	26	414	88	438	24	100%	1
~~J1415_3~~	~~200~~	~~6~~	~~0.0864~~	~~0.0023~~	~~0.2194~~	~~2.989~~	~~0.18~~	~~0.2472~~	~~0.012~~	~~0.39865~~	~~1426~~	~~64~~	~~1402~~	~~45~~	~~1343~~	~~50~~	~~1343~~	~~50~~	~~106%~~	~~0~~
~~J1415_4~~	~~49.4~~	~~1.505~~	~~0.0824~~	~~0.0038~~	~~0.40875~~	~~2.812~~	~~0.16~~	~~0.245~~	~~0.013~~	~~0.41502~~	~~1412~~	~~65~~	~~1357~~	~~44~~	~~1257~~	~~63~~	~~1257~~	~~63~~	~~112%~~	~~0~~
~~J1415_17~~	~~3.13~~	~~0.654~~	~~0.666~~	~~0.026~~	~~0.14107~~	~~38.3~~	~~3.6~~	~~0.418~~	~~0.036~~	~~0.90556~~	~~2230~~	~~170~~	~~3727~~	~~83~~	~~4669~~	~~61~~	~~4669~~	~~61~~	~~48%~~	~~0~~
~~J1415_22~~	~~36.2~~	~~2.35~~	~~0.0828~~	~~0.0043~~	~~0.082318~~	~~1.619~~	~~0.12~~	~~0.144~~	~~0.0069~~	~~0.25488~~	~~867~~	~~39~~	~~973~~	~~46~~	~~1260~~	~~94~~	~~867~~	~~39~~	~~69%~~	~~0~~
~~J1415_40~~	~~551~~	~~3.89~~	~~0.0899~~	~~0.0026~~	~~0.24799~~	~~3.188~~	~~0.18~~	~~0.2605~~	~~0.013~~	~~0.55915~~	~~1492~~	~~67~~	~~1452~~	~~45~~	~~1416~~	~~55~~	~~1416~~	~~55~~	~~105%~~	~~0~~
~~J1415_51~~	~~38.8~~	~~1.047~~	~~0.768~~	~~0.02~~	~~0.15007~~	~~60.3~~	~~4.2~~	~~0.575~~	~~0.037~~	~~0.85451~~	~~2920~~	~~150~~	~~4171~~	~~70~~	~~4890~~	~~45~~	~~4890~~	~~45~~	~~60%~~	~~0~~
~~J1415_72~~	~~580~~	~~14.9~~	~~0.0706~~	~~0.002~~	~~0.18081~~	~~1.639~~	~~0.1~~	~~0.1698~~	~~0.0086~~	~~0.66167~~	~~1011~~	~~47~~	~~984~~	~~38~~	~~955~~	~~58~~	~~1011~~	~~47~~	~~106%~~	~~0~~
~~J1415_112~~	~~62.9~~	~~1.036~~	~~0.622~~	~~0.019~~	~~0.38444~~	~~16.9~~	~~0.99~~	~~0.1992~~	~~0.01~~	~~0.55564~~	~~1170~~	~~55~~	~~2931~~	~~53~~	~~4557~~	~~45~~	~~1170~~	~~55~~	~~26%~~	~~0~~

Table 6: Beaucoup Detrital Zircon U-Pb Data - 43DF15

						Isotope ratios					Apparent ages (Ma)									
Analysis	U (ppm)	U/Th	207Pb/206Pb	± 2 sigma	error corr.	207Pb/235U	± 2 sigma	206Pb/238U	± 2 sigma	error corr.	206Pb/238U	± (Ma)	207Pb/235U	± (Ma)	206Pb/207Pb	± (Ma)	Best age (Ma)	± (Ma)	Ef. Conc (%)	Use? (1-y; 0-n)
43DF15 n = 126/129						use prop uncertainty														
X43DF_1	567	1.8	0.0556	0.0019	0.40493	0.545	0.021	0.0703	0.0032	0.69944	438	19	441.3	14	450	66	438	19	100%	1
X43DF_2	59.9	2.203	0.1043	0.0046	0.19417	4.42	0.24	0.298	0.015	0.72149	1681	76	1709	44	1703	78	1703	78	99%	1
X43DF_3	93.5	3.11	0.0747	0.0026	0.2413	1.873	0.072	0.1818	0.0079	0.7048	1076	43	1070	25	1057	72	1076	43	102%	1
X43DF_4	421	1.988	0.061	0.0027	0.43028	0.567	0.023	0.0668	0.0029	0.4743	417	18	456	15	655	88	417	18	100%	1
X43DF_5	505	2.61	0.0607	0.0022	0.22811	0.545	0.021	0.0662	0.0028	0.71911	413	17	444	15	631	81	413	17	100%	1
X43DF_6	450	2.31	0.057	0.0022	0.41755	0.522	0.022	0.0665	0.0028	0.6106	415	17	426	14	492	85	415	17	100%	1
X43DF_7	237	3.04	0.0637	0.0023	0.075888	1.028	0.04	0.1188	0.0051	0.82181	724	30	717	20	735	80	724	30	100%	1
X43DF_8	264	2.51	0.0627	0.003	0.40074	0.575	0.025	0.0674	0.0027	0.28808	420.7	16	460	16	681	100	420.7	16	100%	1
X43DF_9	350	3.33	0.0565	0.0021	0.25866	0.506	0.019	0.0662	0.0028	0.68062	413	17	415.6	13	475	85	413	17	100%	1
X43DF_11	370	2.79	0.0563	0.0023	0.11363	0.526	0.024	0.068	0.0028	0.37509	424	17	429	16	454	89	424	17	100%	1
X43DF_12	167.3	2.01	0.0543	0.003	0.32063	0.514	0.024	0.0683	0.003	0.33027	426	18	421	16	360	120	426	18	100%	1
X43DF_13	174	2.5	0.0556	0.0024	0.4703	0.541	0.025	0.0696	0.0031	0.46244	434	19	439	16	436	100	434	19	100%	1
X43DF_14	295	3.34	0.0595	0.0026	-0.12059	0.573	0.033	0.0698	0.0031	0.65897	435	19	459	22	572	96	435	19	100%	1
X43DF_15	98.8	5.63	0.0739	0.0055	-0.0083702	0.835	0.067	0.0796	0.0037	0.46426	494	22	611	37	980	150	494	22	100%	1
X43DF_16	498	2.47	0.0566	0.0026	0.1315	0.546	0.025	0.0674	0.0027	0.34027	422	17	442	16	460	100	422	17	100%	1
X43DF_17	432	4.04	0.1097	0.0052	0.22669	4.5	0.25	0.291	0.014	0.67409	1646	71	1731	47	1793	81	1793	81	92%	1
X43DF_18	136	4.13	0.0634	0.0035	0.55395	0.739	0.035	0.083	0.0039	0.22112	514	23	564	21	714	110	514	23	100%	1
X43DF_19	98.1	3.28	0.0565	0.003	-0.19658	0.648	0.044	0.0811	0.0041	0.62882	503	25	505	27	448	110	503	25	100%	1
X43DF_20	943	3.66	0.0858	0.0052	-0.49389	0.925	0.073	0.0739	0.0035	0.76762	459	21	659	38	1320	120	459	21	100%	1
X43DF_21	50.3	5.42	0.0573	0.0037	0.038279	0.592	0.045	0.0724	0.0033	0.54063	451	20	469	29	470	140	451	20	100%	1
X43DF_22	250	5.19	0.0724	0.0029	0.053028	1.778	0.07	0.1737	0.0075	0.81506	1032	41	1036	25	1001	77	1032	41	103%	1
X43DF_23	280	3.15	0.1019	0.0038	-0.071653	4.17	0.18	0.2875	0.011	0.62409	1628	55	1664	35	1653	69	1653	69	98%	1
X43DF_24	1018	0.701	0.0543	0.002	0.56823	0.501	0.019	0.0652	0.0029	0.69546	407	18	412.1	13	378	83	407	18	100%	1
X43DF_25	619	2.19	0.0563	0.0022	0.057184	0.521	0.024	0.0672	0.0028	0.70595	419	17	425	16	455	86	419	17	100%	1
X43DF_26	166	2.97	0.0572	0.0024	0.057234	0.711	0.032	0.0887	0.0037	0.69003	548	22	545	19	513	92	548	22	100%	1
X43DF_27	394	2.96	0.0551	0.0022	0.65502	0.485	0.018	0.064	0.0027	0.51033	400	16	401.1	13	416	87	400	16	100%	1
X43DF_28	546	2.003	0.0618	0.0027	0.54866	0.546	0.022	0.0668	0.0035	0.62737	417	21	442	14	653	94	417	21	100%	1
X43DF_29	436	2.13	0.0613	0.0023	0.67499	0.518	0.018	0.0639	0.0028	0.43604	399	17	423.3	12	645	82	399	17	100%	1
X43DF_30	392	3.75	0.0557	0.0022	0.60844	0.508	0.019	0.0684	0.0027	0.49689	426.3	16	418.6	12	454	95	426.3	16	100%	1
X43DF_31	48.8	1.022	0.0646	0.0031	0.2692	1.022	0.053	0.1184	0.0054	0.5416	721	31	713	27	743	100	721	31	100%	1
X43DF_32	165.9	2.75	0.1935	0.0069	0.52783	13.4	0.48	0.51	0.021	0.62539	2653	87	2706	34	2775	55	2775	55	96%	1
X43DF_33	130.4	2.168	0.0585	0.0025	0.1727	0.532	0.023	0.0681	0.0025	0.45093	424.9	15	433	16	534	93	424.9	15	100%	1
X43DF_34	930	2.24	0.0595	0.0022	0.59151	0.554	0.027	0.0702	0.0043	0.90552	437	26	447	18	589	80	437	26	100%	1
X43DF_35	22.1	5.33	0.0601	0.0044	0.43409	0.625	0.041	0.077	0.0033	-0.063182	478	20	491	25	630	160	478	20	100%	1
X43DF_36	64.8	2.42	0.0568	0.0025	0.057413	0.491	0.025	0.0635	0.0025	0.48093	396.9	15	407	18	502	110	396.9	15	100%	1
X43DF_37	250.6	2.95	0.0652	0.0029	0.33922	0.832	0.039	0.0954	0.0045	0.54555	587	27	614	21	782	97	587	27	100%	1
X43DF_38	10.22	1.674	0.0798	0.0046	0.17835	2.17	0.12	0.1959	0.009	0.46328	1152	48	1189	41	1180	120	1152	48	98%	1
X43DF_39	85.8	2.96	0.0842	0.0029	0.068974	2.44	0.14	0.2076	0.011	0.91645	1214	61	1251	40	1294	67	1214	61	94%	1
X43DF_40	274	2.95	0.0549	0.0025	0.55498	0.498	0.02	0.0645	0.0028	0.37335	403	17	412	14	407	100	403	17	100%	1
X43DF_41	74.4	0.732	0.12	0.0044	0.26396	5.88	0.25	0.3571	0.015	0.65014	1967	71	1954	38	1952	66	1952	66	101%	1
X43DF_42	419	2.17	0.05524	0.0018	0.29708	0.522	0.018	0.0678	0.0026	0.73821	422.9	15	425.9	12	419	75	422.9	15	100%	1
X43DF_43	333	4.26	0.0589	0.0023	0.10309	0.851	0.041	0.1009	0.0047	0.7416	619	28	627	23	569	77	619	28	100%	1
X43DF_44	194	6.01	0.0573	0.0025	0.31679	0.701	0.039	0.0875	0.0044	0.55271	540	26	538	23	489	97	540	26	100%	1
X43DF_45	128.5	2.13	0.1099	0.0043	0.30491	5.11	0.22	0.335	0.015	0.68554	1859	71	1834	37	1792	71	1792	71	104%	1
X43DF_46	128.9	1.756	0.059	0.0033	0.3987	0.524	0.028	0.0625	0.0028	0.24124	391	17	427	18	542	120	391	17	100%	1
X43DF_47	171	1.202	0.0615	0.0056	-0.39465	0.591	0.057	0.0697	0.0036	0.62447	434	22	467	33	590	170	434	22	100%	1
X43DF_48	354	2.17	0.107	0.013	0.53177	1.44	0.16	0.0986	0.0041	-0.21087	606	24	900	67	1610	220	606	24	100%	1
X43DF_49	280.9	3.59	0.0775	0.0028	0.39649	2.098	0.076	0.1969	0.008	0.54595	1158	43	1147	25	1136	69	1158	43	102%	1
X43DF_50	103.7	1.556	0.561	0.022	0.25012	4.12	0.18	0.0542	0.0024	0.63138	340.4	14	1654	35	4404	57	340.4	14	100%	1
X43DF_51	370	2.171	0.0551	0.0022	0.18131	0.504	0.02	0.0678	0.0027	0.58304	422.8	16	415.8	13	418	91	422.8	16	100%	1
X43DF_52	207	1.64	0.0537	0.003	0.19653	0.511	0.031	0.0694	0.0032	0.38463	432	19	418	21	360	130	432	19	100%	1
X43DF_53	413	2.37	0.0708	0.0033	0.1682	0.656	0.03	0.0675	0.0028	0.44781	421	17	511	18	937	98	421	17	100%	1
X43DF_54	166.1	5.64	0.0762	0.0033	0.31508	1.829	0.078	0.1724	0.0073	0.39735	1025	40	1054	28	1101	81	1025	40	93%	1
X43DF_55	527	2.202	0.0537	0.0021	0.16516	0.514	0.023	0.0686	0.0029	0.59152	428	18	420	15	349	87	428	18	100%	1
X43DF_56	458	2.91	0.0566	0.0022	0.46356	0.51	0.022	0.065	0.003	0.67833	406	18	418	15	478	90	406	18	100%	1
X43DF_57	411	3.01	0.0555	0.0024	0.31595	0.525	0.023	0.0657	0.0027	0.47763	410	16	428	15	419	96	410	16	100%	1
X43DF_58	68.9	2.77	0.0753	0.0036	-0.043403	1.959	0.11	0.1832	0.0073	0.45056	1084	40	1097	36	1061	95	1084	40	102%	1
X43DF_59	368	1.266	0.0525	0.0021	0.3726	0.477	0.018	0.0645	0.0027	0.48677	403	16	395.4	12	297	91	403	16	100%	1
X43DF_60	204	2.278	0.0574	0.0026	0.33834	0.828	0.035	0.1031	0.0042	0.36043	633	25	612	20	505	100	633	25	100%	1
X43DF_61	267	1.05	0.0609	0.0031	0.29442	0.608	0.032	0.0698	0.0029	0.36768	435	18	481	20	634	100	435	18	100%	1
X43DF_62	65.7	2.49	0.0719	0.0038	0.17656	1.114	0.061	0.115	0.0046	0.46879	701	27	767	30	1009	110	701	27	100%	1
X43DF_63	159	2.155	0.0635	0.0026	0.2395	1.01	0.043	0.1147	0.0045	0.5848	700	26	708	22	724	84	700	26	100%	1
X43DF_64	454	2.73	0.0561	0.002	-0.035398	0.5	0.021	0.0664	0.0027	0.72827	414.2	16	412	14	453	78	414.2	16	100%	1
X43DF_65	181	1.357	0.0652	0.0037	-0.012663	0.587	0.031	0.067	0.0032	0.52124	418	19	468	20	754	120	418	19	100%	1
X43DF_66	97.1	1.73	0.0836	0.0086	0.01212	1.02	0.11	0.0886	0.0046	0.23981	547	27	702	52	1190	180	547	27	100%	1
X43DF_67	32.2	2.09	0.0658	0.0056	-0.094464	0.987	0.098	0.1059	0.0052	0.30971	653	29	688	48	730	170	653	29	100%	1
X43DF_68	162	1.876	0.0541	0.0026	0.38725	0.519	0.025	0.0694	0.0031	0.34234	432	18	426	16	359	110	432	18	100%	1
X43DF_69	294	1.941	0.0565	0.0023	0.035766	0.522	0.024	0.0669	0.0027	0.57351	417	16	426	16	462	89	417	16	100%	1
X43DF_70	475	2.38	0.059	0.0027	-0.094398	0.541	0.031	0.0668	0.0028	0.62547	417	17	438	20	566	100	417	17	100%	1
X43DF_71	141.1	2.1	0.152	0.016	-0.16127	1.54	0.18	0.0728	0.0032	0.41385	453	19	927	71	2320	170	453	19	100%	1
X43DF_72	112.3	0.866	0.0574	0.0039	0.082795	0.519	0.035	0.0652	0.0027	0.27236	407	16	422	23	470	140	407	16	100%	1
X43DF_73	369	2.54	0.062	0.0028	0.31999	0.575	0.026	0.0663	0.0026	0.46942	413.6	16	461	17	672	99	413.6	16	100%	1
X43DF_74	138	1.799	0.0561	0.0031	0.28151	0.52	0.029	0.0677	0.0029	0.37306	422	17	424	19	460	130	422	17	100%	1
X43DF_75	618	1.983	0.0538	0.002	0.034874	0.508	0.021	0.0697	0.0028	0.72551	434	17	419	15	353	85	434	17	100%	1
X43DF_77	118.7	2.33	0.1146	0.0044	0.35288	5.16	0.24	0.327	0.015	0.68927	1821	75	1847	38	1878	73	1878	73	97%	1
X43DF_78	224	1.504	0.0593	0.0023	-0.038936	0.555	0.027	0.0704	0.0028	0.71425	438	17	447	18	581	87	438	17	100%	1
X43DF_79	180	1.578	0.0559	0.0026	0.41459	0.53	0.027	0.0687	0.003	0.064063	428	18	430	18	436	100	428	18	100%	1
X43DF_80	173	5.63	0.0663	0.0032	0.69306	0.999	0.044	0.1128	0.005	0.48055	689	29	702	22	815	96	689	29	100%	1
X43DF_81	502	2.562	0.0534	0.002	0.29744	0.507	0.022	0.0684	0.0029	0.69493	426	17	416	15	349	80	426	17	100%	1
X43DF_82	600	2.19	0.0581	0.0034	0.27473	0.513	0.027	0.064	0.0026	0.05034	399.8	16	419	18	500	120	399.8	16	100%	1
X43DF_83	195	2.005	0.0572	0.0024	0.23937	0.537	0.025	0.0676	0.0027	0.46701	421	16	435	16	487	94	421	16	100%	1
X43DF_84	51.8	2.306	0.053	0.0032	0.23038	0.633	0.041	0.087	0.0046	0.19368	537	27	496	25	310	130	537	27	100%	1
X43DF_85	572	2.414	0.0541	0.0024	0.31701	0.501	0.021	0.0665	0.0027	0.46272	415.1	16	412	14	360	97	415.1	16	100%	1
X43DF_86	539	2.456	0.0531	0.0019	0.17539	0.497	0.02	0.0674	0.0026	0.64706	420.6	16	411.5	13	350	81	420.6	16	100%	1
X43DF_87	291	1.55	0.0529	0.0023	0.26161	0.47	0.023	0.0647	0.0029	0.64808	404	17	393	16	311	98	404	17	100%	1
X43DF_88	234	1.801	0.0923	0.0035	0.27045	3.33	0.14	0.2603	0.01	0.53192	1491	53	1491	33	1476	75	1476	75	101%	1
X43DF_89	207.3	1.71	0.1088	0.0098	-0.59604	1.11	0.13	0.0691	0.003	0.79287	431	18	731	49	1720	150	431	18	100%	1
X43DF_90	185	3.57	0.0668	0.003	0.29528	0.768	0.034	0.0826	0.0032	0.429	512	19	578	20	848	81	512	19	100%	1
X43DF_91	126	2.51	0.0624	0.0028	0.40529	1.095	0.055	0.124	0.0059	0.61635	758	35	749	27	689	99	758	35	100%	1
X43DF_92	461	2.23	0.0688	0.003	0.11426	0.673	0.029	0.0705	0.0031	0.57166	439	19	522	18	894	85	439	19	100%	1
X43DF_93	451	2.72	0.136	0.0056	-0.029775	1.39	0.065	0.075	0.0031	0.56552	468	18	882	28	2170	73	468	18	100%	1
X43DF_94	77	2.35	0.0704	0.0034	0.061149	1.389	0.075	0.1462	0.006	0.45646	880	34	887	29	922	97	880	34	95%	1
X43DF_95	59.8	3.49	0.0579	0.0041	0.23789	0.616	0.044	0.0771	0.0033	0.094663	479	20	485	27	520	160	479	20	100%	1
X43DF_96	340	3.76	0.0679	0.0026	0.53929	1.042	0.052	0.1171	0.0067	0.75756	713	38	723	26	861	79	713	38	100%	1
X43DF_97	144	4.83	0.1086	0.004	-0.12126	4.62	0.19	0.3185	0.012	0.67399	1782	59	1755	32	1771	67	1771	67	101%	1

Table 6: Beaucoup Detrital Zircon U-Pb Data - 43DF15 - cont.

X43DF_98	25.2	3.57	0.1004	0.0069	0.1572	3.64	0.27	0.2635	0.012	0.044218	1506	64	1548	53	1600	120	1600	120	94%	1
X43DF_99	79.7	2.55	0.103	0.0039	0.49403	4.27	0.16	0.3044	0.012	0.79899	1712	61	1685	31	1674	70	1674	70	102%	1
X43DF_100	198	1.396	0.15	0.013	-0.58691	1.49	0.13	0.0741	0.0033	0.75201	461	20	916	52	2300	130	461	20	100%	1
X43DF_101	233	2.6	0.148	0.011	-0.11691	1.48	0.16	0.0716	0.0046	0.7457	445	28	918	65	2330	130	445	28	100%	1
X43DF_102	528	2.45	0.0569	0.0025	0.51428	0.533	0.023	0.0668	0.0034	0.59315	417	20	433	15	474	93	417	20	100%	1
X43DF_103	333	19	0.0685	0.0032	0.4515	1.173	0.05	0.1206	0.0054	0.24816	734	31	787	23	883	96	734	31	100%	1
X43DF_105	25.2	1.224	0.084	0.0084	-0.10363	1.29	0.14	0.1045	0.0045	0.40971	641	26	827	60	1310	200	641	26	100%	1
X43DF_106	63.1	1.208	0.0993	0.0039	0.3011	4.02	0.16	0.2834	0.011	0.56565	1608	57	1640	33	1613	68	1613	68	100%	1
X43DF_107	568	2.68	0.0566	0.0021	0.1693	0.526	0.022	0.0667	0.0027	0.69762	416	17	429	15	487	83	416	17	100%	1
X43DF_108	346	2.52	0.0562	0.0022	0.12395	0.511	0.02	0.066	0.0027	0.61033	412	16	421	14	479	83	412	16	100%	1
X43DF_109	61.1	1.233	0.0992	0.0038	0.36452	3.676	0.14	0.2683	0.011	0.46243	1531	55	1568	29	1613	69	1613	69	95%	1
X43DF_110	237	1.622	0.0588	0.0028	0.39433	0.537	0.023	0.0672	0.0028	0.30978	419	17	436	15	574	100	419	17	100%	1
X43DF_111	569	2.499	0.0559	0.0023	0.3851	0.52	0.02	0.0675	0.0025	0.34929	420.9	15	426.3	14	450	95	420.9	15	100%	1
X43DF_112	137.6	3.6	0.1901	0.0067	0.53534	13.93	0.49	0.531	0.02	0.58369	2746	85	2743	33	2740	57	2740	57	100%	1
X43DF_113	124.1	1.041	0.0645	0.0031	0.24787	0.952	0.046	0.1069	0.0041	0.17309	655	24	682	22	740	100	655	24	100%	1
X43DF_114	56.4	2.9	0.0579	0.0037	0.0046471	0.558	0.035	0.0709	0.0031	0.39839	441	19	449	23	490	140	441	19	100%	1
X43DF_115	373	1.93	0.058	0.0026	0.1781	0.536	0.025	0.0675	0.003	0.71398	421	18	435	17	528	100	421	18	100%	1
X43DF_116	523	2.028	0.0572	0.0025	0.64209	0.541	0.021	0.0698	0.0028	0.49111	435.2	17	438.9	14	486	93	435.2	17	100%	1
X43DF_117	27.1	1.671	0.0977	0.01	-0.22915	1.51	0.17	0.1109	0.0047	0.50776	678	28	913	71	1510	210	678	28	100%	1
X43DF_118	513	1.97	0.0576	0.0024	0.21512	0.543	0.022	0.0685	0.003	0.5148	427	18	440	15	503	93	427	18	100%	1
X43DF_119	347	2.73	0.057	0.0023	0.081207	0.544	0.024	0.0688	0.0027	0.48171	429.1	16	440	16	498	84	429.1	16	100%	1
X43DF_120	261	2.074	0.062	0.0039	-0.25529	0.688	0.056	0.0794	0.0036	0.61519	493	21	527	32	640	120	493	21	100%	1
X43DF_121	82	4.98	0.0835	0.0037	0.55287	2.403	0.094	0.2087	0.0087	0.33991	1221	47	1246	30	1270	85	1221	47	96%	1
X43DF_122	32.8	2.56	0.0917	0.0044	0.37934	3.08	0.15	0.2461	0.01	0.40462	1418	53	1435	36	1460	89	1460	89	97%	1
X43DF_123	136	3.02	0.0621	0.0029	0.29793	1.054	0.054	0.1231	0.0054	0.51962	752	29	729	26	674	100	752	29	100%	1
X43DF_124	280	1.374	0.1037	0.0036	0.065203	4.31	0.16	0.3052	0.012	0.69543	1717	58	1694	32	1696	60	1696	60	101%	1
X43DF_125	505	2.87	0.0603	0.0023	0.20633	0.579	0.027	0.0686	0.0031	0.7415	428	19	463	17	606	82	428	19	100%	1
X43DF_126	497	2.32	0.0657	0.003	0.27516	0.61	0.028	0.0662	0.0029	0.47535	413	18	485	17	795	91	413	18	100%	1
X43DF_127	406	2.22	0.0612	0.0025	0.1281	0.889	0.04	0.1042	0.0043	0.68042	639	25	645	21	647	86	639	25	100%	1
X43DF_128	284.7	1.962	0.0601	0.003	-0.013885	0.537	0.029	0.0633	0.0025	0.50094	395.8	15	435	19	585	110	395.8	15	100%	1
X43DF_129	435	17.7	0.0722	0.0029	-0.13137	1.454	0.068	0.1442	0.0058	0.74185	868	33	909	28	984	82	868	33	88%	1
X43DF_10	252	11.09	0.0748	0.0026	0.48474	1.948	0.068	0.19	0.0068	0.63724	1121	37	1097	24	1059	70	1121	37	106%	0
X43DF_76	8.3	0.966	0.724	0.046	0.045731	26.1	2.2	0.27	0.019	0.68845	1539	97	3352	81	4789	110	4789	110	32%	0
X43DF_104	114	2.22	0.1267	0.0048	0.12093	7.24	0.29	0.405	0.018	0.76429	2192	85	2139	34	2048	66	2048	66	107%	0

Table 7: Kanayut Detrital Zircon U-Pb Data - 41DF15

						Isotope ratios						Apparent ages (Ma)							
Analysis	U (ppm)	U/Th	207Pb/206Pb	± 2 sigma	error corr.	207Pb/235U	± 2 sigma	206Pb/238U	± 2 sigma	error corr.	206Pb/238U	± (Ma)	207Pb/235U	± (Ma)	206Pb/207Pb	± (Ma)	Best age (Ma)	± (Ma)	Ef. Conc (%)	Use? (1-y; 0-n)
41DF15 n = 127/129						use prop uncertainty														
WPF41_1	233	233.0	0.0562	0.0022	0.31775	0.519	0.025	0.0664	0.0019	0.40494	414.2	11	423.8	17	451	88	414	11	100%	1
WPF41_3	537	537	0.06352	0.0019	0.056644	0.488	0.023	0.0551	0.0015	0.70821	345.9	9.1	402.9	16	730	71	345.9	9.1	100%	1
WPF41_4	63.6	63.6	0.0589	0.0041	0.043101	0.537	0.037	0.0671	0.0018	0.20769	418.9	11	429	24	520	140	418.9	11	100%	1
WPF41_5	57.2	57.2	0.0551	0.0033	0.21453	0.501	0.032	0.0664	0.002	0.12378	414.1	12	415	22	390	130	414.1	12	100%	1
WPF41_6	363	363	0.0559	0.0021	0.54338	0.504	0.025	0.0655	0.0022	0.5166	411	13	415.5	17	438	84	411	13	100%	1
WPF41_7	74.5	74.5	0.0579	0.0036	-0.015338	0.532	0.042	0.0653	0.0019	0.2249	407.6	11	431	27	490	130	407.6	11	100%	1
WPF41_8	602	602	0.0802	0.0053	0.0085917	0.482	0.036	0.045	0.0017	0.49115	283.9	11	398	24	1180	130	283.9	11	100%	1
WPF41_9	79.8	79.8	0.0676	0.0037	0.012762	0.648	0.045	0.069	0.002	0.31942	430.3	12	505	28	830	120	430.3	12	100%	1
WPF41_10	521	521	0.0547	0.0019	0.22699	0.462	0.024	0.0611	0.0017	0.72513	382.5	11	385.2	17	413	76	382.5	11	100%	1
WPF41_11	172	172	0.148	0.029	0.084419	1.45	0.3	0.0689	0.0029	0.081917	429	17	850	110	2090	320	429	17	100%	1
WPF41_12	110	110	0.0725	0.0039	0.40802	0.617	0.036	0.0612	0.0018	0.031634	383.2	12	490	21	1022	92	383.2	12	100%	1
WPF41_13	111.8	111.8	0.0566	0.002	0.06647	0.601	0.031	0.0771	0.0021	0.44401	478.8	13	477	20	469	80	478.8	13	100%	1
WPF41_14	87.1	87.1	0.055	0.0027	0.091095	0.504	0.03	0.0675	0.002	0.39665	421	12	413	20	430	120	421	12	100%	1
WPF41_15	188	188	0.0585	0.0022	0.33196	0.469	0.025	0.0586	0.002	0.62318	367	12	390	18	541	84	367	12	100%	1
WPF41_16	82.5	82.5	0.0562	0.0034	0.41022	0.505	0.031	0.065	0.0019	-0.12173	406	12	414	21	430	130	406	12	100%	1
WPF41_17	152	152	0.0538	0.0022	0.19294	0.518	0.028	0.06959	0.0016	0.28097	433.7	9.7	424	18	349	91	433.7	9.7	100%	1
WPF41_18	76	76	0.0566	0.004	-0.074499	0.565	0.046	0.072	0.0021	0.24673	448	13	452	28	430	140	448	13	100%	1
WPF41_19	186.8	186.8	0.0561	0.002	-0.16824	0.519	0.026	0.0674	0.0017	0.5712	420.3	10	424.4	17	450	79	420.3	10	100%	1
WPF41_20	301	301	0.0563	0.0021	0.12944	0.528	0.027	0.0685	0.0024	0.63877	427	15	426.8	18	455	82	427	15	100%	1
WPF41_21	206	206	0.0554	0.0023	0.35932	0.547	0.029	0.0733	0.0022	0.42354	456	13	443	19	419	93	456	13	100%	1
WPF41_22	66	66	0.0555	0.0032	0.14472	0.557	0.043	0.0714	0.0028	0.37895	445	17	447	27	480	140	445	17	100%	1
WPF41_23	33	33	0.0535	0.0043	0.0083751	0.43	0.038	0.0583	0.0019	0.18079	365.2	11	361	27	310	160	365.2	11	100%	1
WPF41_24	104	104	0.0542	0.0028	-0.12256	0.556	0.04	0.0752	0.0021	0.39109	467.5	13	447	27	363	110	467.5	13	100%	1
WPF41_25	94.6	94.6	0.0584	0.0031	0.25319	0.562	0.038	0.0683	0.0023	0.17162	426	14	451	24	520	120	426	14	100%	1
WPF41_26	76	76	0.0605	0.0043	0.2496	0.592	0.044	0.0684	0.002	0.11712	426.7	12	469	30	570	140	426.7	12	100%	1
WPF41_27	218	218	0.0582	0.0024	0.081195	0.568	0.032	0.0701	0.0022	0.49689	437	14	456	21	523	94	437	14	100%	1
WPF41_28	43.2	43.2	0.0664	0.0087	0.12164	0.64	0.084	0.0685	0.0023	0.053411	427	14	492	49	670	240	427	14	100%	1
WPF41_29	35.8	35.8	0.1198	0.0041	0.24968	5.88	0.29	0.3489	0.011	0.67346	1936	53	1956	43	1948	64	1948	64	99%	1
WPF41_30	149	149	0.0574	0.0028	0.15533	0.536	0.03	0.0675	0.002	0.20557	420.9	12	435	20	486	100	420.9	12	100%	1
WPF41_31	72.9	72.9	0.062	0.0035	0.011416	0.58	0.042	0.0668	0.0021	0.19875	416.7	12	463	26	615	95	416.7	12	100%	1
WPF41_32	394	394	0.1031	0.0039	0.48112	4.19	0.21	0.2986	0.01	0.57168	1683	50	1674	41	1683	76	1683	76	100%	1
WPF41_33	8.6	8.6	0.146	0.022	-0.031756	8	1.3	0.39	0.023	0.13514	2118	110	2105	70	2070	120	2070	120	102%	1
WPF41_34	161	161	0.0603	0.0031	0.24426	0.596	0.038	0.0703	0.0023	0.22382	438	14	473	24	591	110	438	14	100%	1
WPF41_35	356	356	0.0577	0.0025	0.0049231	0.574	0.034	0.0716	0.0023	0.41559	445	14	459	22	500	100	445	14	100%	1
WPF41_36	118.5	118.5	0.0581	0.0032	0.26699	0.515	0.032	0.0641	0.0018	0.0134	402.1	11	421	21	500	120	402.1	11	100%	1
WPF41_37	304	304	0.0587	0.002	0.4618	0.492	0.024	0.0609	0.0018	0.60159	380.9	11	405.9	17	559	81	380.9	11	100%	1
WPF41_38	52.2	52.2	0.0577	0.0043	-0.16402	0.534	0.051	0.0676	0.0025	0.3856	422	15	431	33	470	160	422	15	100%	1
WPF41_39	131	131	0.1191	0.004	0.45825	5.43	0.25	0.3387	0.0099	0.54076	1880	47	1889	39	1939	61	1939	61	97%	1
WPF41_40	116.2	116.2	0.0557	0.0035	-0.0096976	0.492	0.034	0.065	0.0021	0.19368	405.9	13	405	23	400	130	405.9	13	100%	1
WPF41_41	268	268	0.057	0.0021	0.17678	0.512	0.028	0.067	0.0021	0.55751	417.9	12	419	19	495	87	417.9	12	100%	1
WPF41_42	109.2	109.2	0.0585	0.003	0.14833	0.541	0.033	0.0683	0.0019	0.2065	426.1	12	438	22	520	120	426.1	12	100%	1
WPF41_43	54.9	54.9	0.0552	0.0033	0.11429	0.485	0.034	0.064	0.0019	0.33474	399.6	12	400	25	390	130	399.6	12	100%	1
WPF41_44	56.1	56.1	0.0556	0.003	-0.027894	0.516	0.034	0.0673	0.002	0.21336	419.8	12	421	22	410	120	419.8	12	100%	1
WPF41_45	101	101	0.0759	0.0029	0.59064	1.962	0.1	0.1906	0.007	0.79815	1124	38	1101	37	1083	77	1124	38	104%	1
WPF41_46	371	371	0.0566	0.0024	0.30004	0.501	0.026	0.0653	0.0019	0.2672	407.9	12	412	18	464	92	407.9	12	100%	1
WPF41_47	87	87	0.0545	0.003	0.1627	0.519	0.04	0.0674	0.0026	0.13242	421	16	423	25	360	120	421	16	100%	1
WPF41_48	79.2	79.2	0.0602	0.0051	0.20068	0.507	0.04	0.0644	0.0023	0.21407	402	14	414	30	540	170	402	14	100%	1
WPF41_49	78.1	78.1	0.0567	0.0032	0.49856	0.518	0.034	0.0659	0.0018	-0.18674	411.6	11	423	22	480	110	411.6	11	100%	1
WPF41_50	370	370	0.0558	0.0023	0.2419	0.462	0.024	0.0611	0.0019	0.53119	382	12	385	17	429	92	382	12	100%	1
WPF41_51	275	275	0.0546	0.0027	0.27447	0.458	0.029	0.0597	0.0019	0.21287	373.6	12	382	20	376	110	373.6	12	100%	1
WPF41_52	72.1	72.1	0.0776	0.0099	-0.23684	0.8	0.11	0.0745	0.0025	0.43531	463	15	589	58	1020	250	463	15	100%	1
WPF41_53	48.8	48.8	0.0543	0.0049	0.15947	0.532	0.061	0.0704	0.0023	0.0080779	439	14	430	32	330	180	439	14	100%	1
WPF41_54	141.6	141.6	0.0552	0.0026	-0.04324	0.511	0.03	0.0663	0.0018	0.41799	413.6	11	418	20	401	110	413.6	11	100%	1
WPF41_55	256	256	0.0559	0.0025	-0.038349	0.573	0.036	0.0726	0.0022	0.55467	452	13	458	24	432	100	452	13	100%	1
WPF41_56	30.1	30.1	0.1765	0.0061	0.27451	11.74	0.56	0.482	0.014	0.58337	2536	59	2581	51	2629	60	2629	60	96%	1
WPF41_57	277	277	0.0563	0.0022	0.29509	0.537	0.028	0.0697	0.002	0.44775	434.2	12	436	18	467	94	434.2	12	100%	1
WPF41_58	137.7	137.7	0.0582	0.0034	0.19792	0.532	0.034	0.0663	0.0018	0.012181	413.6	11	432	22	500	130	413.6	11	100%	1
WPF41_59	128.4	128.4	0.0544	0.0025	0.086703	0.412	0.026	0.0533	0.002	0.50978	334.4	12	349	20	370	100	334.4	12	100%	1
WPF41_60	229	229	0.0554	0.002	0.32279	0.497	0.025	0.0656	0.002	0.45982	409.8	12	409.5	17	418	82	409.8	12	100%	1
WPF41_61	56	56	0.0626	0.0045	-0.040778	0.81	0.092	0.0977	0.0062	0.62932	600	36	608	48	640	160	600	36	100%	1
WPF41_62	451	451	0.0561	0.0025	0.011567	0.438	0.027	0.0582	0.0016	0.34307	364.6	9.6	368	19	458	100	364.6	9.6	100%	1
WPF41_63	43.5	43.5	0.1639	0.0061	0.49496	10.21	0.51	0.454	0.015	0.56729	2421	67	2451	47	2498	68	2498	68	97%	1
WPF41_64	248	248	0.0569	0.0028	0.62322	0.524	0.027	0.0664	0.0022	0.38545	414	14	427	19	469	110	414	14	100%	1
WPF41_65	190	190	0.0561	0.0026	0.25463	0.569	0.034	0.0741	0.0022	0.1681	460.8	14	456	22	434	110	460.8	14	100%	1
WPF41_66	177	177	0.0556	0.0025	0.24903	0.48	0.028	0.0634	0.002	0.41184	396	12	397	19	420	100	396	12	100%	1
WPF41_67	55.1	55.1	0.0564	0.0044	0.38606	0.536	0.043	0.0695	0.0018	-0.21063	432.9	11	433	28	410	160	432.9	11	100%	1
WPF41_68	105	105	0.0531	0.0025	0.39357	0.514	0.031	0.0701	0.0019	0.0096152	436.9	12	420	21	313	110	436.9	12	100%	1
WPF41_69	524	524	0.055	0.0022	0.36947	0.502	0.027	0.0663	0.0022	0.45908	414	13	415	17	401	94	414	13	100%	1
WPF41_70	264	264	0.055	0.0023	0.31852	0.534	0.03	0.069	0.0025	0.52803	430	15	436	20	440	110	430	15	100%	1
WPF41_71	134	134	0.0546	0.0029	0.087696	0.578	0.042	0.0765	0.0034	0.56875	475	20	466	27	390	120	475	20	100%	1
WPF41_72	33.3	33.3	0.1109	0.0048	0.62739	4.93	0.26	0.3152	0.011	0.31904	1765	53	1805	44	1814	84	1814	84	97%	1
WPF41_73	73.2	73.2	0.1656	0.0058	0.0356	10.38	0.54	0.4593	0.012	0.62225	2436	51	2471	48	2509	61	2509	61	97%	1
WPF41_75	292	292	0.0541	0.0023	0.41278	0.534	0.028	0.0709	0.0022	0.45617	441	13	434	19	363	96	441	13	100%	1
WPF41_76	231	231	0.0575	0.0033	0.084745	0.336	0.025	0.042	0.0018	0.52346	265.2	11	297	17	480	120	265.2	11	100%	1
WPF41_77	218	218	0.0563	0.002	0.32168	0.518	0.031	0.0655	0.0031	0.78181	409	19	423	21	466	86	409	19	100%	1
WPF41_78	287	287	0.0557	0.0023	0.25334	0.519	0.03	0.0658	0.0021	0.25359	411	13	424	20	428	94	411	13	100%	1
WPF41_79	601	601	0.0637	0.0028	0.4389	0.599	0.034	0.0685	0.0023	0.34967	427	14	476	22	728	100	427	14	100%	1
WPF41_80	320.6	320.6	0.0637	0.005	-0.067084	0.529	0.048	0.0586	0.0017	0.28161	366.8	11	427	31	700	170	366.8	11	100%	1
WPF41_81	188	188	0.0549	0.0025	0.27152	0.537	0.033	0.0692	0.0019	0.21451	431.3	12	435	22	391	100	431.3	12	100%	1
WPF41_82	24.7	24.7	0.1163	0.0047	-0.15617	5.69	0.35	0.3505	0.01	0.64481	1936	48	1923	54	1890	77	1890	77	102%	1
WPF41_83	131	131	0.1193	0.0048	0.16238	5.84	0.31	0.3524	0.011	0.66232	1945	51	1949	46	1937	75	1937	75	100%	1
WPF41_84	39.9	39.9	0.0646	0.0073	0.039488	0.618	0.077	0.0689	0.0024	0.02947	429	15	480	47	640	230	429	15	100%	1
WPF41_85	1179	1179	0.069	0.0023	0.36136	1.128	0.054	0.1184	0.0039	0.66427	721	23	766	26	893	74	721	23	100%	1
WPF41_86	93	93	0.056	0.003	0.33112	0.5	0.032	0.065	0.0024	0.3162	406	14	410	22	470	130	406	14	100%	1
WPF41_87	187.2	187.2	0.0562	0.0024	0.29828	0.522	0.027	0.0687	0.0021	0.37572	428.5	13	429	18	441	100	428.5	13	100%	1
WPF41_88	95.5	95.5	0.0573	0.0041	0.26213	0.521	0.035	0.0681	0.0021	-0.066265	425	13	424	23	420	130	425	13	100%	1
WPF41_89	63.9	63.9	0.0579	0.0043	-0.39611	0.539	0.048	0.0685	0.0027	0.5508	427	16	435	30	470	150	427	16	100%	1
WPF41_90	100.9	100.9	0.0559	0.0027	0.1396	0.521	0.032	0.0677	0.0023	0.39321	422	14	425	21	445	120	422	14	100%	1
WPF41_91	549	549	0.0564	0.0022	0.66387	0.5036	0.023	0.0656	0.0019	0.22627	409.3	12	414	16	467	89	409.3	12	100%	1
WPF41_92	98.5	98.5	0.0598	0.0032	0.2797	0.562	0.034	0.0695	0.0019	0.074718	432.9	11	452	22	592	110	432.9	11	100%	1
WPF41_93	78	78	0.0602	0.0052	0.44474	0.57	0.055	0.0713	0.003	0.426	444	18	464	36	560	170	444	18	100%	1
WPF41_94	67.7	67.7	0.1176	0.0039	0.14832	5.45	0.26	0.3364	0.01	0.6402	1868	50	1890	43	1924	58	1924	58	97%	1
WPF41_95	61.3	61.3	0.123	0.014	-0.45806	1.03	0.16	0.058	0.0034	0.76043	363	21	690	78	1990	210	363	21	100%	1
WPF41_96	217	217	0.0555	0.0022	-0.057441	0.546	0.031	0.0727	0.0023	0.69437	452	14	442	20	435	93	452	14	100%	1
WPF41_97	237	237	0.196	0.02	0.042057	1.3	0.15	0.0484	0.0025	0.27086	305	15	829	68	2730	200	305	15	100%	1

Table 7: Kanayut Detrital Zircon U-Pb Data - 41DF15 - cont.

WPF41_98	116	116	0.0548	0.0027	0.36776	0.555	0.031	0.074	0.0026	0.3837	460	15	451	21	387	110	460	15	100%	1
WPF41_99	184	184	0.0786	0.0048	0.37785	0.573	0.036	0.0532	0.0016	0.088384	334.1	9.8	462	23	1130	120	334.1	9.8	100%	1
WPF41_100	392	392	0.0519	0.0022	0.1677	0.539	0.029	0.0741	0.0021	0.25834	460.8	12	433	19	272	93	460.8	12	100%	1
WPF41_101	67.5	67.5	0.0488	0.0038	0.19433	0.402	0.032	0.0594	0.002	-0.070142	371.7	12	341	23	130	150	371.7	12	100%	1
WPF41_103	60	60	0.0495	0.0041	0.39296	0.496	0.043	0.0742	0.0028	0.029715	461	17	412	29	190	170	461	17	100%	1
WPF41_104	50.2	50.2	0.0641	0.008	0.10255	0.64	0.076	0.0722	0.0025	0.18123	449	15	494	46	650	250	449	15	100%	1
WPF41_105	148.2	148.2	0.0548	0.0023	0.39644	0.525	0.027	0.0687	0.002	0.2415	428.4	12	430	17	406	100	428.4	12	100%	1
WPF41_106	588	588	0.0545	0.0021	0.27728	0.508	0.027	0.0656	0.0021	0.51909	409.5	13	417	18	382	88	409.5	13	100%	1
WPF41_107	191	191	0.054	0.0024	-0.12324	0.553	0.036	0.0734	0.0027	0.49831	457	16	445	24	354	100	457	16	100%	1
WPF41_108	47.3	47.3	0.048	0.0044	0.23133	0.477	0.05	0.0716	0.0025	0.010183	445	15	393	34	130	190	445	15	100%	1
WPF41_109	142	142	0.0581	0.0036	0.061101	0.552	0.044	0.0679	0.0024	0.34294	424	15	444	28	490	130	424	15	100%	1
WPF41_110	790	790	0.0563	0.0019	0.18943	0.542	0.028	0.0701	0.0025	0.76168	436	14	439	19	458	77	436	14	100%	1
WPF41_111	141.8	141.8	0.1153	0.0044	0.453	5.28	0.24	0.3275	0.011	0.59162	1825	55	1864	41	1876	74	1876	74	97%	1
WPF41_112	52.6	52.6	0.0592	0.0046	-0.013661	0.593	0.053	0.0712	0.0024	0.30152	443	14	469	34	580	180	443	14	100%	1
WPF41_113	490	490	0.055	0.0024	0.20207	0.539	0.03	0.0704	0.0027	0.53825	438	16	437	20	396	98	438	16	100%	1
WPF41_114	67	67	0.0562	0.0038	0.48564	0.491	0.033	0.0623	0.0022	-0.033385	390	13	404	21	480	150	390	13	100%	1
WPF41_115	165	165	0.0541	0.0027	0.091987	0.516	0.034	0.0685	0.0023	0.33628	427	14	421	23	354	110	427	14	100%	1
WPF41_116	83.7	83.7	0.0733	0.005	0.25901	0.731	0.052	0.0711	0.0032	0.22446	443	19	553	35	970	150	443	19	100%	1
WPF41_117	81.9	81.9	0.1637	0.0054	0.39209	10.92	0.51	0.476	0.016	0.66715	2507	69	2519	41	2497	57	2497	57	100%	1
WPF41_118	45.1	45.1	0.0576	0.006	0.021933	0.557	0.061	0.0693	0.0022	0.13247	432	13	433	39	380	180	432	13	100%	1
WPF41_119	84.2	84.2	0.0611	0.0043	0.10623	0.566	0.041	0.0681	0.0021	0.14273	424.7	12	453	26	560	130	424.7	12	100%	1
WPF41_120	74.3	74.3	0.0581	0.0042	0.32474	0.548	0.04	0.0674	0.0026	-0.17092	420	16	442	26	480	150	420	16	100%	1
WPF41_121	195	195	0.0818	0.0029	0.44322	1.824	0.089	0.1606	0.0051	0.57975	960	28	1053	33	1233	75	960	28	78%	1
WPF41_122	38.2	38.2	0.0534	0.0037	0.46485	0.506	0.036	0.0676	0.0028	0.068867	422	17	414	24	310	150	422	17	100%	1
WPF41_123	218	218	0.0576	0.0024	0.35939	0.597	0.031	0.0746	0.0024	0.31303	464	15	477	20	514	110	464	15	100%	1
WPF41_124	85.5	85.5	0.0621	0.0048	-0.015428	0.612	0.055	0.0711	0.0022	0.18085	443	13	472	34	610	160	443	13	100%	1
WPF41_125	298	298	0.0574	0.0021	0.26815	0.461	0.024	0.0578	0.002	0.57022	362	12	385	16	512	89	362	12	100%	1
WPF41_126	42.7	42.7	0.0592	0.0049	0.22618	0.58	0.057	0.0682	0.0028	0.088715	425	17	459	36	550	190	425	17	100%	1
WPF41_127	363	363	0.0612	0.0027	-0.066664	0.564	0.033	0.0659	0.0023	0.66773	411	14	453	22	641	110	411	14	100%	1
WPF41_128	67.9	67.9	0.0627	0.0044	0.026413	0.552	0.042	0.0638	0.0021	0.29122	399	13	444	30	670	160	399	13	100%	1
WPF41_129	72	72	0.0556	0.0029	0.1052	0.444	0.028	0.0572	0.0018	0.29143	358.5	11	376	18	470	110	358.5	11	100%	1
WPF41_130	91	91	0.0575	0.003	0.52536	0.532	0.03	0.0678	0.0023	-0.10593	423	14	433	20	510	110	423	14	100%	1
WPF41_2	9.7	9.7	0.668	0.03	-0.30799	32.5	4.4	0.347	0.039	0.87528	1890	190	3500	160	4663	69	4663	69	41%	0
WPF41_102	55.4	55.4	0.1077	0.004	0.34662	5.06	0.25	0.334	0.0096	0.42719	1857	46	1832	42	1756	69	1756	69	106%	0

Table 8: Hunt Fork Detrital Zircon U-Pb Data - 26DF15

						Isotope ratios					Apparent ages (Ma)									
Analysis	U (ppm)	U/Th	207Pb/206Pb	± 2 sigma	error corr.	207Pb/235U	± 2 sigma	206Pb/238U	± 2 sigma	error corr.	206Pb/238U	± (Ma)	207Pb/235U	± (Ma)	206Pb/207Pb	± (Ma)	Best age (Ma)	± (Ma)	Ef. Conc (%)	Use? (1-y; 0-n)
26DF15 n = 86/115						use prop uncertainty														
WPF26_2	288	4.14	0.0545	0.0053	-0.17369	0.556	0.079	0.0723	0.0066	0.92822	449	39	442	51	369	220	449	39	100%	1
WPF26_4	73.4	2.14	0.1007	0.0099	-0.00070824	4.3	0.61	0.306	0.029	0.93763	1710	140	1663	110	1635	190	1635	190	105%	1
WPF26_5	67.9	1.73	0.109	0.01	-0.097187	4.9	0.56	0.324	0.022	0.89527	1800	110	1784	100	1772	170	1772	170	102%	1
WPF26_6	352	2.83	0.0551	0.0054	-0.25969	0.52	0.066	0.0694	0.0052	0.80744	432	31	421	43	390	210	432	31	100%	1
WPF26_7	165	2.61	0.1695	0.016	0.071945	11.6	1.6	0.508	0.049	0.92466	2620	210	2539	130	2541	160	2541	160	103%	1
WPF26_8	87.7	1.71	0.1177	0.011	-0.33407	5.76	0.77	0.35	0.03	0.92758	1930	140	1936	110	1926	180	1926	180	100%	1
WPF26_9	514	2.48	0.0523	0.0049	-0.41161	0.523	0.07	0.0697	0.0053	0.95039	433	32	422	46	297	220	433	32	100%	1
WPF26_11	505	10.7	0.0529	0.0051	-0.067245	0.44	0.058	0.0601	0.0052	0.88112	375	31	366	40	307	210	375	31	100%	1
WPF26_12	325	3.86	0.0564	0.0056	0.0279	0.524	0.066	0.0666	0.0049	0.80374	415	29	423	43	442	220	415	29	100%	1
WPF26_13	177	6.6	0.0725	0.008	-0.038563	0.72	0.097	0.0725	0.0059	0.73191	451	36	552	59	1010	230	451	36	100%	1
WPF26_14	530	3.58	0.086	0.008	-0.093794	2.64	0.34	0.22	0.012	0.62717	1292	66	1328	90	1332	170	1292	66	97%	1
WPF26_16	177	3.14	0.055	0.0053	-0.090359	0.517	0.061	0.0701	0.0045	0.88322	436	27	425	42	406	210	436	27	100%	1
WPF26_17	22.5	2.2	0.1577	0.015	-0.21757	10	1.4	0.46	0.043	0.93587	2410	190	2397	130	2429	170	2429	170	99%	1
WPF26_18	463	2.27	0.0538	0.0051	-0.22382	0.525	0.069	0.0682	0.0054	0.92494	425	32	424	45	349	210	425	32	100%	1
WPF26_20	176	93	0.1335	0.014	-0.307	7.06	1	0.388	0.036	0.86153	2090	170	2100	150	2110	190	2110	190	99%	1
WPF26_21	298	5.65	0.0545	0.0052	0.00034667	0.434	0.055	0.0581	0.0043	0.91674	364	26	368	39	378	210	364	26	100%	1
WPF26_22	601	2.67	0.0534	0.0051	-0.23521	0.535	0.066	0.0724	0.0049	0.91357	456	31	437	45	328	210	456	31	100%	1
WPF26_23	401	2.01	0.0534	0.005	-0.038283	0.488	0.059	0.0676	0.0054	0.91266	421	33	400	41	331	210	421	33	100%	1
WPF26_25	39.8	3.91	0.0995	0.0096	-0.32806	3.97	0.52	0.292	0.023	0.92071	1660	120	1631	110	1600	180	1600	180	104%	1
WPF26_26	234	2.74	0.0902	0.0087	0.22582	3.2	0.42	0.257	0.025	0.90781	1480	130	1433	99	1427	190	1427	190	104%	1
WPF26_27	284	2.58	0.0595	0.0057	-0.11689	0.559	0.069	0.068	0.0048	0.87833	424	29	446	44	580	210	424	29	100%	1
WPF26_28	112	5.7	0.0548	0.0056	-0.11859	0.538	0.08	0.071	0.0068	0.92617	441	41	430	51	370	220	441	41	100%	1
WPF26_29	50.5	6.3	0.0541	0.0053	0.18446	0.524	0.071	0.0707	0.0068	0.88068	439	41	423	46	354	210	439	41	100%	1
WPF26_30	343	2.88	0.0532	0.0052	-0.21516	0.451	0.065	0.0587	0.0052	0.91406	367	32	372	44	333	220	367	32	100%	1
WPF26_31	29.7	1.82	0.0795	0.0086	-0.21409	1.86	0.28	0.162	0.013	0.77214	964	73	1041	97	1150	210	964	73	84%	1
WPF26_33	71.9	3.27	0.0545	0.0056	0.059709	0.549	0.081	0.0685	0.0066	0.88436	426	39	437	51	400	230	426	39	100%	1
WPF26_34	226	2.01	0.1171	0.011	-0.040388	5.92	0.76	0.361	0.03	0.9396	1970	140	1935	110	1912	160	1912	160	103%	1
WPF26_35	302	1.93	0.0544	0.0052	0.19502	0.522	0.069	0.0692	0.0068	0.90843	430	41	421	45	398	230	430	41	100%	1
WPF26_36	380	9.2	0.113	0.011	-0.41827	5.23	0.63	0.333	0.022	0.91744	1850	100	1835	100	1837	170	1837	170	101%	1
WPF26_38	47.2	4.13	0.1053	0.01	-0.20122	4.67	0.68	0.313	0.031	0.92223	1740	150	1742	120	1705	180	1705	180	102%	1
WPF26_39	494	1.03	0.0604	0.0059	-0.16219	0.782	0.1	0.0936	0.0069	0.90337	575	41	586	58	611	210	575	41	100%	1
WPF26_40	1270	6.4	0.0543	0.0052	0.17846	0.521	0.067	0.0687	0.006	0.93066	427	36	421	44	379	220	427	36	100%	1
WPF26_43	755	3.25	0.0555	0.0054	0.058226	0.508	0.065	0.0666	0.0056	0.9069	415	34	413	43	409	220	415	34	100%	1
WPF26_47	89	5.69	0.0861	0.0083	-0.16632	2.37	0.33	0.208	0.019	0.91643	1210	99	1253	100	1338	180	1210	99	90%	1
WPF26_49	710	4.97	0.0541	0.0051	0.0038329	0.6	0.083	0.0797	0.0077	0.94692	493	46	470	51	387	230	493	46	100%	1
WPF26_50	817	2.62	0.0552	0.0051	-0.057009	0.536	0.055	0.0701	0.0029	0.87879	437	18	434	36	412	200	437	18	100%	1
WPF26_51	458	3.45	0.0565	0.0054	0.027131	0.517	0.063	0.0659	0.0051	0.89302	411	31	419	42	510	210	411	31	100%	1
WPF26_53	623	3.24	0.0603	0.0059	-0.032317	0.498	0.067	0.0609	0.0057	0.89157	380	34	406	44	612	200	380	34	100%	1
WPF26_54	265	4.6	0.0583	0.0057	-0.16609	0.6	0.087	0.0711	0.0066	0.9305	442	39	469	54	551	220	442	39	100%	1
WPF26_55	546	2.47	0.0556	0.0053	-0.044628	0.517	0.073	0.0666	0.0063	0.94184	423	40	417	47	417	210	423	40	100%	1
WPF26_56	315	7.3	0.0633	0.0061	-0.20984	0.634	0.085	0.074	0.0059	0.89564	460	36	491	53	700	210	460	36	100%	1
WPF26_59	296	8	0.0553	0.0053	0.059767	0.675	0.1	0.0839	0.0086	0.92259	518	51	514	58	423	210	518	51	100%	1
WPF26_60	91.9	3.95	0.0604	0.0058	-0.16806	0.875	0.11	0.1021	0.007	0.87758	626	41	630	60	635	210	626	41	100%	1
WPF26_61	177	2.72	0.0605	0.006	-0.029633	0.97	0.14	0.109	0.01	0.91823	664	59	682	74	609	210	664	59	100%	1
WPF26_62	432	1.64	0.0577	0.0057	-0.01804	0.75	0.099	0.0921	0.0072	0.88497	566	42	567	56	509	210	566	42	100%	1
WPF26_63	211	2.39	0.0573	0.0056	-0.019869	0.568	0.08	0.0718	0.0071	0.92201	446	43	450	51	480	220	446	43	100%	1
WPF26_64	297	2.55	0.054	0.0052	-0.044771	0.446	0.059	0.0594	0.005	0.9295	371	30	371	41	352	210	371	30	100%	1
WPF26_65	29.6	3.74	0.1643	0.016	0.35134	11.5	1.6	0.507	0.054	0.93605	2610	230	2522	130	2486	160	2486	160	105%	1
WPF26_66	801	2.51	0.0552	0.0052	0.0066264	0.466	0.057	0.0605	0.0047	0.89507	378	29	385	39	408	210	378	29	100%	1
WPF26_67	227	7	0.1003	0.0096	-0.14042	3.62	0.5	0.26	0.025	0.93124	1500	130	1536	110	1616	180	1616	180	93%	1
WPF26_68	49.2	1.33	0.1216	0.012	0.30247	6.2	0.77	0.364	0.028	0.84828	1990	130	1978	110	2002	180	2002	180	99%	1
WPF26_71	225	8	0.125	0.016	-0.42234	5.03	0.75	0.295	0.017	0.70414	1663	82	1790	110	1970	190	1970	190	84%	1
WPF26_72	480	2.64	0.0558	0.0056	-0.15907	0.491	0.064	0.065	0.005	0.88724	405	30	401	43	410	220	405	30	100%	1
WPF26_75	165	4.66	0.0573	0.0057	-0.052155	0.55	0.075	0.067	0.0058	0.8236	418	35	447	50	530	240	418	35	100%	1
WPF26_76	409	2.55	0.0738	0.0069	-0.27041	1.85	0.23	0.182	0.013	0.91973	1075	71	1057	81	1024	190	1075	71	105%	1
WPF26_77	118	4.83	0.0858	0.0086	-0.05014	2.75	0.39	0.231	0.022	0.84621	1350	120	1345	110	1347	210	1350	120	100%	1
WPF26_79	52.4	1.47	0.1745	0.017	0.001551	12.6	1.8	0.526	0.053	0.87872	2690	220	2620	130	2599	170	2599	170	104%	1
WPF26_80	698	2.4	0.0553	0.0054	0.022578	0.583	0.079	0.074	0.0068	0.91091	459	41	460	50	420	220	459	41	100%	1
WPF26_81	403	2.63	0.0557	0.0053	-0.17254	0.528	0.068	0.0676	0.0052	0.88825	421	31	426	44	438	220	421	31	100%	1
WPF26_82	336	3.43	0.0548	0.0053	-0.058697	0.515	0.07	0.0664	0.0059	0.90924	414	36	416	46	399	220	414	36	100%	1
WPF26_83	1410	61.1	0.0745	0.0072	-0.076759	1.86	0.23	0.18	0.013	0.88192	1077	76	1071	86	1036	190	1077	76	104%	1
WPF26_84	177	2.18	0.0542	0.0054	-0.28149	0.532	0.075	0.0689	0.0055	0.9177	429	33	427	49	350	220	429	33	100%	1
WPF26_85	276	2.95	0.0615	0.0073	-0.18138	0.6	0.096	0.0711	0.0065	0.73099	448	40	488	65	590	240	448	40	100%	1
WPF26_87	394	5.41	0.1144	0.011	-0.021585	5.2	0.61	0.33	0.022	0.86047	1830	110	1847	100	1854	180	1854	180	99%	1
WPF26_88	76.9	7.9	0.0589	0.0055	0.11051	0.675	0.086	0.0827	0.0071	0.92705	518	44	517	51	550	200	518	44	100%	1
WPF26_89	97	3.87	0.1189	0.013	-0.052556	5.08	0.9	0.286	0.041	0.80688	1600	200	1790	150	1910	180	1910	180	84%	1
WPF26_90	134	2.19	0.1853	0.017	0.0065834	13	1.6	0.508	0.041	0.93901	2630	170	2683	120	2700	160	2700	160	97%	1
WPF26_93	577	3.25	0.0633	0.0062	-0.28109	0.682	0.084	0.0756	0.0047	0.85222	470	28	522	50	724	210	470	28	100%	1
WPF26_94	150	2.78	0.1478	0.015	-0.22622	9.6	1.5	0.451	0.046	0.91068	2380	200	2350	140	2305	160	2305	160	103%	1
WPF26_95	278	2.68	0.0535	0.0051	-0.1634	0.472	0.064	0.063	0.0056	0.94421	393	34	388	43	350	220	393	34	100%	1
WPF26_96	248	10.7	0.1006	0.0097	-0.097548	4.29	0.57	0.299	0.025	0.9258	1700	120	1661	100	1620	180	1620	180	105%	1
WPF26_97	74.6	2.45	0.1156	0.012	0.16245	5.98	0.84	0.356	0.033	0.86814	1950	150	1952	120	1867	180	1867	180	104%	1
WPF26_98	726	2.17	0.057	0.0056	-0.14484	0.557	0.068	0.069	0.0041	0.82173	429	24	446	43	466	210	429	24	100%	1
WPF26_99	108.3	3.38	0.0715	0.007	-0.17728	1.67	0.22	0.17	0.013	0.87775	1007	72	989	82	964	200	1007	72	104%	1
WPF26_100	194	5.33	0.0537	0.0054	0.053437	0.513	0.07	0.0694	0.0064	0.88321	431	38	415	46	350	220	431	38	100%	1
WPF26_101	48.8	2.28	0.1141	0.011	-0.12972	5.8	0.8	0.355	0.031	0.90114	1950	140	1909	120	1875	190	1875	190	104%	1
WPF26_102	51.8	1.82	0.1711	0.017	-0.36153	12.2	1.5	0.515	0.033	0.91883	2670	140	2591	120	2565	160	2565	160	104%	1
WPF26_103	801	3.01	0.0566	0.0055	-0.13338	0.564	0.075	0.0698	0.0057	0.89837	434	34	448	48	490	210	434	34	100%	1
WPF26_105	623	7.8	0.0548	0.0054	0.18585	0.465	0.062	0.0626	0.006	0.90293	391	36	389	43	384	210	391	36	100%	1
WPF26_106	359	1.13	0.0533	0.005	0.10124	0.462	0.06	0.0639	0.0061	0.94704	398	37	382	41	342	220	398	37	100%	1
WPF26_108	361	5.51	0.0841	0.0079	-0.10952	2.66	0.36	0.226	0.019	0.92368	1306	98	1305	98	1297	190	1306	98	101%	1
WPF26_109	178	4.13	0.0576	0.0055	0.36704	0.57	0.068	0.0735	0.0064	0.89447	456	38	454	43	517	200	456	38	100%	1
WPF26_110	250	2.08	0.0573	0.0056	-0.009576	0.546	0.069	0.0682	0.0052	0.82534	425	31	437	44	479	210	425	31	100%	1
WPF26_111	491	8.3	0.0532	0.0053	0.11845	0.465	0.065	0.0604	0.0054	0.90399	378	32	383	44	330	220	378	32	100%	1
WPF26_112	930	3.86	0.054	0.0054	0.13847	0.487	0.066	0.0648	0.006	0.90567	404	36	398	44	340	210	404	36	100%	1
WPF26_114	79	1.99	0.1329	0.012	-0.083606	7.76	1.1	0.421	0.038	0.95314	2240	170	2181	120	2137	160	2137	160	105%	1
WPF26_1	43	3.8	0.0778	0.0074	-0.060239	2.22	0.32	0.207	0.022	0.95634	1200	110	1164	96	1129	190	1200	110	106%	0
WPF26_3	520	8.2	0.0894	0.009	0.14283	3.67	0.56	0.293	0.036	0.91295	1630	170	1540	120	1390	180	1390	180	117%	0
WPF26_10	69	2.24	0.1904	0.018	-0.19623	15.8	2.2	0.599	0.055	0.94328	3050	210	2830	140	2746	150	2746	150	111%	0
WPF26_15	56.9	0.81	0.706	0.068	-0.30797	41.2	6	0.415	0.04	0.94576	2220	180	3760	150	4750	150	4750	150	47%	0
WPF26_19	36	0.526	0.666	0.064	-0.03807	29.8	4.2	0.318	0.029	0.93772	1760	140	3430	130	4659	150	4659	150	38%	0
WPF26_24	194	8.1	0.0916	0.0085	-0.096534	3.68	0.43	0.288	0.019	0.92253	1624	94	1551	93	1459	180	1459	180	111%	0
WPF26_32	234	4.17	0.0805	0.0078	-0.20097	2.44	0.32	0.219	0.018	0.89196	1268	95	1232	92	1192	190	1268	95	106%	0
WPF26_37	326	5.4	0.0904	0.0083	-0.21952	3.52	0.45	0.275	0.022	0.95369	1570	110	1508	100	1428	180	1428	180	110%	0
WPF26_41	498	5.05	0.0543	0.0053	0.093184	0.578	0.084	0.076	0.008	0.94325	471	48	456	52	361	210	471	48	100%	0

Table 8: Hunt Fork Detrital Zircon U-Pb Data - 26DF15 - cont.

WPF26_42	236	12.5	0.0699	0.0067	0.0048951	1.63	0.23	0.169	0.016	0.93741	1018	95	975	88	908	200	1018	95	112%	0
WPF26_44	141	6.9	0.1179	0.011	0.014669	6.06	0.84	0.371	0.034	0.93432	2010	160	1947	120	1910	170	1910	170	105%	0
WPF26_45	2.83	0.392	0.685	0.072	0.34201	42.9	7.3	0.44	0.064	0.92402	2370	300	3780	170	4700	170	4700	170	50%	0
WPF26_46	188	2.37	0.0549	0.0054	-0.03738	0.562	0.086	0.0721	0.0081	0.93201	447	48	444	54	400	230	447	48	100%	0
WPF26_48	126	2.74	0.0754	0.0074	0.077172	2.13	0.3	0.209	0.023	0.90531	1210	120	1150	97	1076	200	1210	120	112%	0
WPF26_52	123	3.08	0.1122	0.011	0.28645	5.54	0.73	0.351	0.034	0.90189	1920	160	1875	110	1817	180	1817	180	106%	0
WPF26_57	46.5	2.66	0.0897	0.009	0.061731	3.27	0.47	0.261	0.027	0.91783	1480	130	1440	110	1397	190	1397	190	106%	0
WPF26_58	51.6	0.54	0.689	0.068	-0.022985	44.6	7.1	0.434	0.048	0.94319	2300	210	3830	160	4711	150	4711	150	49%	0
WPF26_69	118	5.81	0.0866	0.0083	-0.21	3.22	0.42	0.277	0.024	0.9273	1570	120	1451	100	1349	190	1349	190	116%	0
WPF26_70	555	8.1	0.0823	0.008	-0.12986	2.76	0.39	0.243	0.024	0.92152	1390	120	1349	110	1236	180	1390	120	112%	0
WPF26_73	57.5	0.65	0.499	0.05	-0.10482	19.8	3.1	0.278	0.032	0.90299	1600	170	3040	150	4224	140	4224	140	38%	0
WPF26_74	51	6.5	0.0548	0.0055	-0.039162	0.579	0.087	0.0754	0.0082	0.89593	467	49	464	57	420	240	467	49	100%	0
WPF26_78	201	6.5	0.0623	0.0065	-0.21841	0.722	0.12	0.0798	0.0084	0.87463	493	50	538	67	660	230	493	50	100%	0
WPF26_86	167	5.1	0.0724	0.0072	-0.19805	1.74	0.26	0.173	0.017	0.92932	1025	95	1000	98	972	200	1025	95	105%	0
WPF26_91	235	15.3	0.0703	0.0069	-0.23072	1.67	0.24	0.172	0.015	0.91287	1018	84	975	86	915	200	1018	84	111%	0
WPF26_92	413	29	0.0695	0.0068	-0.26981	1.79	0.24	0.182	0.014	0.90226	1071	76	1022	85	892	210	1071	76	120%	0
WPF26_104	236	5.3	0.0968	0.0094	-0.11888	4.18	0.58	0.313	0.03	0.93381	1740	150	1650	110	1560	180	1560	180	112%	0
WPF26_107	269	3.43	0.084	0.018	-0.16098	0.9	0.25	0.0728	0.0096	0.58705	452	58	630	120	1240	380	452	58	100%	0
WPF26_113	280	6.2	0.1075	0.011	0.14762	5.15	0.71	0.335	0.032	0.91371	1880	160	1810	120	1752	180	1752	180	107%	0
WPF26_115	322	5.5	0.0573	0.0058	0.11032	0.572	0.09	0.0691	0.008	0.8962	429	48	449	56	490	230	429	48	100%	0